Image Reconstruction of Low Conductivity Material Distribution using Magnetic Induction Tomography

A thesis submitted to the University of Manchester for the degree of
Doctor of Philosophy in the Faculty of Engineering and Physical
Sciences

2010

Bachir Dekdouk

School of Electrical and Electronic Engineering

Table of Contents

List of figures

List of tables

List of abbreviations

CG	Conjugate Gradient
CSF	Cerebral Spinal Fluid
DGN-KM	Damped Gauss Newton Krylov Method
DGNM	Damped Gauss Newton Method
DoF	Degree of Freedom
ECG	Electrocardiogram
ECT	Electrical Capacitance Tomography
EIT	Electrical Impedance Tomography
FEM	Finite Element Method
FIT	Finite Integration Technique
GSVD	Generalised Singular Value Decomposition
GCV	Generalised Cross Validation
gT	Generalised Tikhonov regularisation
ICG	Impedance cardiography
KCL	Kirchhoff's current law
KVL	Kirchhoff's voltage law
LMM	Levenberg Marquardt Method
MAP	Maximum a-posteriori estimate
MIT	Magnetic Induction Tomography
MRI	Magnetic Resonance Imaging
NDT	Non Destructive Testing
NHS	National Health Service
PDLM	Powell's Dog Leg Method
RGNM	Regularised Gauss Newton Method

rms	Root Mean Square
SPFD	Scalar Potential Finite Difference
sT	Standard Tikhonov regularisation
SVD	Ordinary Singular Value Decomposition
TGSVD	Truncated Generalised Singular Value Decomposition
TSVD	Truncated Singular Value Decomposition
TV	Total Variation

List of symbols

$\boldsymbol{A}$	magnetic vector potential
$\boldsymbol{A}$	Gauss Newton approximate Hessian
$\boldsymbol{A}_0$	primary magnetic vector potential
$\boldsymbol{A}_\mathrm{r}$	reduced magnetic vector potential
$\boldsymbol{B}$	magnetic field density
$\boldsymbol{B}_0$	primary magnetic field density
$\boldsymbol{C}$	discrete curl operator in the grid
$\boldsymbol{C}_t$	constraint operator
$\widetilde{\boldsymbol{C}}$	discrete curl operator in the dual grid
$\boldsymbol{corr}_\sigma$	correlation
$\boldsymbol{D}$	measured/simulated data
$\boldsymbol{d}$	search direction (step)
$\boldsymbol{d}_d$	damping step
$\boldsymbol{d}_{dGN}$	damped Gauss Newton step
$\boldsymbol{d}_{LM}$	Levenberg Marquardt step
$\boldsymbol{d}_N$	Newton step
$\boldsymbol{d}_{rGN}$	regularised Gauss Newton step
$\boldsymbol{d}_{rLM}$	regularised Levenberg Marquardt step
$\boldsymbol{d}_{\boldsymbol{sd}}$	steepest descent step
$\boldsymbol{d}_{\boldsymbol{tr}}$	trust region step
$\boldsymbol{d}_{trPDL}$	trust region Powell Dog Leg step
$\boldsymbol{d}_{dGN\text{-}K}$	Krylov damped Gauss Newton step
dl	element of length
dv	element of volume

$\boldsymbol{E}$	electric field intensity
E	expected value function
emf	electromotive force
$\boldsymbol{F}$	forward model function
F	objective function
$\widetilde{F}$	approximate objective function
f	filter factor
f	frequency
$\boldsymbol{G}$	quasi-Newton approximation
$\boldsymbol{g}$	gradient of the approximate objective function
$\boldsymbol{H}$	magnetic field intensity
$\boldsymbol{H}$	Hessian or an approximation to it
$\boldsymbol{H}_{dGN}$	damped Gauss Newton approximate Hessian
$\boldsymbol{H}_{rGN}$	regularised Gauss Newton approximate Hessian
$\boldsymbol{H}_{rLM}$	regularised Levenberg Marquardt approximate Hessian
$\boldsymbol{H}_{trPDL}$	trust region Powell Dog Leg approximate Hessian
$\boldsymbol{I}$	identity
$\boldsymbol{I}_{branch}$	branch current
$\boldsymbol{I}_{loop}$	loop current
I_n	Bessel function of the first kind
I_0	excitation current magnitude in the coil
$\boldsymbol{J}$	Jacobian (sensitivity)
$\boldsymbol{J}^{\dagger}$	Moore-Penrose generalised inverse of $\boldsymbol{J}$
$\boldsymbol{\mathsf{J}}$	electric current density
$\boldsymbol{\mathsf{J}}_{\mathrm{S}}$	excitation current density in the coil
K	subspace

K_n	Bessel function of the second kind
k	iteration index
k_{max}	maximum number of iterations
$\boldsymbol{L}$	penalty operator
$\boldsymbol{L}_1$	approximate first derivative operator (Neighbouring)
$\boldsymbol{L}_2$	approximate second derivative operator
L	sobolev norm, (smoothing seminorm)
L_{TV}	total variation function
M	quadratic model function
$\boldsymbol{m}$	mean
m	number of collected measurements
$\boldsymbol{n}$	noise
n	number of elements in the object
$\boldsymbol{P}$	voltage generator source
$\boldsymbol{p}$	search direction (Conjugate Gradient method)
p	probability density function
p_i	marginal density value
$\boldsymbol{R}$	resistance
$\boldsymbol{R}$	regularisation
r	distance, radius
r	rank
$\mathbf{r}$	residual function
r_0	coil radius
$\boldsymbol{S}$	discrete divergence operator in the grid
s	meshing resolution
tol	tolerance

$\boldsymbol{V}$	computed forward model data
$\boldsymbol{V_i}$	nodal scalar potential
$\boldsymbol{Var}$	variance
$\boldsymbol{W}$	variance of the residual data
$\boldsymbol{X}$	impedance coefficient
$\boldsymbol{Y}$	admittance
$\boldsymbol{Z}$	induced mutual impedance
$\mathbf{Z}$	impedance
α	step length (relaxation factor)
β_n	calibration scalar
β^{FR}	Fletcher and Reeves calibration scalar
β^{PR}	Polak and Ribiere calibration scalar
γ_i	generalised singular value
γ_k	damping parameter
δ	variance of measurement noise
Δ	trust region radius
$\Delta\boldsymbol{A}$	secondary magnetic potential
$\Delta\boldsymbol{B}$	secondary magnetic field density
$\Delta\boldsymbol{D}$	frequency or state differential data
$\Delta\boldsymbol{V}$	induced voltage due to the target
$\Delta\boldsymbol{Z}$	Induced mutual impedance due to the target
$\Delta\boldsymbol{\sigma}$	difference conductivity image
ε	electrical permittivity
ε_r	relative electrical permittivity
ε_0	electrical permittivity of vacuum
$\boldsymbol{\Theta}$	preconditioner vector

$\boldsymbol{\Theta_n}$	associated Legendre polynomials
θ	angle (or spherical elevation angle)
κ	complex electrical conductivity
λ	regularisation parameter
μ	magnetic permeability
μ_r	relative magnetic permeability
μ_0	magnetic permeability of vacuum
ρ	gain ratio
σ	electrical conductivity
σ_i	singular values
$\boldsymbol{\sigma_p}$	prior conductivity vector
$\boldsymbol{\sigma}_0$	initial conductivity map
$\boldsymbol{\sigma}^*$	reconstructed conductivity map
$\boldsymbol{\sigma}_{\mathrm{true}}$	true conductivity map
Ω	entire problem domain
Ω_{c}	eddy current problem region
Ω_{s}	current source region
ω	angular frequency

Word Count: 45 021

Abstract

Magnetic induction tomography (MIT) is a non-invasive, soft field imaging modality that has the potential to map the electrical conductivity (σ) distribution inside an object under investigation. In MIT, a number of exciter and receiver coils are distributed around the periphery of the object. A primary magnetic field is emitted by each exciter, and interacts with the object. This induces eddy currents in the object, which in turn create a secondary field. This latter is coupled to the receiver coils and voltages are induced. An image reconstruction algorithm is then used to infer the conductivity map of the object.

In this thesis, the application of MIT for volumetric imaging of objects with low conductivity materials (< 5 Sm^{-1}) and dimensions < 1 m is investigated**.** In particular**,** two low conductivity applications are approached: imaging cerebral stroke and imaging the saline water in multiphase flows. In low conductivity applications, the measured signals are small and the spatial sensitivity is critically compromised making the associated inverse problem severely non-linear and ill-posed.

The main contribution from this study is to investigate three non-linear optimisation techniques for solving the MIT inverse problem. The first two methods namely, regularised Levenberg Marquardt method and trust region Powell's Dog Leg method employ damping and trust region strategies respectively. The third method is a modification of the Gauss Newton method and utilises a damping regularisation technique. An optimisation in the convergence and stability of the inverse solution was observed with these methods compared to standard Gauss Newton method. For such non linear treatment, re-evaluation of the forward problem is also required. The forward problem is solved numerically using the impedance method and a weakly coupled field approximation is employed to reduce the computation time and memory requirements. For treating the ill-posedness, different regularisation methods are investigated. Results show that the subspace regularisation technique is suitable for absolute imaging of the stroke in a real head model with synthetic data. Tikhonov based smoothing and edge preserving regularisation methods also produced successful results from simulations of oil/water. However, in a practical setup, still large geometrical and positioning noise causes a major problem and only difference imaging was viable to achieve a reasonable reconstruction.

Publications

- **Chapter 3**

B. Dekdouk, C. Ktistis, D. W. Armitage and A. J. Peyton, "Application of the impedance method for computing the current density inside a 3D conductor for low conductivity Magnetic Induction Tomography", in *Proc. 5th International Symposium on Process Tomography*, ProcTom2008, Zakopane, Poland, 2008.

W. Yin, A. J. Peyton, G. Zysko, **B. Dekdouk**," Limits of the weakly coupled field assumption for low conductivity electromagnetic induction tomography.", in *Proc. 5th International Symposium on Process Tomography*, ProcTom2008, Zakopane, Poland, 2008.

B. Dekdouk, M. H. Pham, D. W. Armitage, C. Ktistis, M. Zolgharni and A. J. Peyton, "A feasibility study on the delectability of Edema using Magnetic Induction Tomography using an Analytical Model" *in Proc. 4th European Congress for Medical and Biomedical Engineering*, Belgium, 2008.

B. Dekdouk, W. Yin, C. Ktistis, D. W. Armitage and A. J. Peyton, "A method to solve the forward problem in Magnetic Induction Tomography based on the Weakly Coupled Field Approximation" *IEEE Trans on Biomedical Eng*, vol. 57, N^0. 4, 2010.

B. Dekdouk, C. Ktistis, D. W. Armitage and A. J. Peyton, "Assessing the feasibility of detecting a hemorrhagic type stroke using a 16 channel Magnetic Induction System" *in Proc. International Conference on Electrical Bioimpedance*, Florida, 2010.

- **Chapter 4**

B. Dekdouk, C. Ktistis, D. W. Armitage, and A. J. Peyton, "An investigation of smoothing and edge preserving regularisation operators in Magnetic Induction Tomography", *in Proc. 10th International Conference on Biomedical Applications of Electrical Impedance Tomography*, EIT, 2009.

C. Ktistis, **B. Dekdouk**, D. W. Armitage and A. J. Peyton, "The use of unconstrained optimisation techniques for image reconstruction in Magnetic Induction Tomography", *in Proc. 10th International Conference on Biomedical Applications of Electrical Impedance Tomography*, EIT, 2009.

B. Dekdouk, C. Ktistis, and A. J. Peyton, "Nonlinear optimization of the eddy current inverse problem using damping and trust region techniques for imaging low conductivity materials using Magnetic Induction Tomography", *to be submitted to Journal IEEE on Magnetics*.

- **Chapter 5**

S. Watson, C. Ktistis, **B. Dekdouk**, D. W. Armitage, A. J. Peyton, R. J. Williams, H. Griffiths, “Developments in Magnetic Induction Tomography for oil-industry applications”, *in Proc. 5th World Congress on Industrial Process Tomography*, pp 1045-1050, ISBN 978 0 85316 265 0, Bergen, Norway, 2007.

B. Dekdouk, C. Ktistis, W. Yin, D. W. Armitage and A. J. Peyton, “The application of a priori structural information based regularization in image reconstruction in Magnetic Induction Tomography”, *in Proc. International Conference on Electrical Bioimpedance*, Florida, 2010.

- **Chapter 6**

M. Zolgharni, P.D. Ledger, C. Ktistis, **B. Dekdouk**, H. Griffiths, “High-contrast frequency-difference imaging for Magnetic Induction Tomography”, *in Proc. 10th International Conference on Biomedical Applications of Electrical Impedance Tomography*, EIT, 2009.

- **Additional papers**

W. Yin, **B. Dekdouk**, C. Ktistis, A. J. Peyton, “Evaluation of the effects of the screen based on an analytical solution of a simplified MIT system”, *in Proc. International Conference on Electrical Bioimpedance*, Florida, 2010.

W. Yin, **B. Dekdouk**, A. J. Peyton,” Solution of 3D Electromagnetic flow meter equations based on a resistor network equivalent method”, *in Proc. 3rd international Workshop on Process Tomography*, Japan, 2009.

Declaration

No portion of the work referred to in the thesis has been submitted in support of an application for another degree or qualification of this or any other university or other institute of learning.

Copyright Statement

i. The author of this thesis (including any appendices and/or schedules to this thesis) owns certain copyright or related rights in it (the "Copyright") and s/he has given The University of Manchester certain rights to use such Copyright, including for administrative purposes.

ii. Copies of this thesis, either in full or in extracts and whether in hard or electronic copy, may be made only in accordance with the Copyright, Designs and Patents Act 1988 (as amended) and regulations issued under it or, where appropriate, in accordance with licensing agreements which the University has from time to time. This page must form part of any such copies made.

iii. The ownership of certain Copyright, patents, designs, trade marks and other intellectual property (the "Intellectual Property") and any reproductions of copyright works in the thesis, for example graphs and tables ("Reproductions"), which may be described in this thesis, may not be owned by the author and may be owned by third parties. Such Intellectual Property and Reproductions cannot and must not be made available for use without the prior written permission of the owner(s) of the relevant Intellectual Property and/or Reproductions.

iv. Further information on the conditions under which disclosure, publication and commercialisation of this thesis, the Copyright and any Intellectual Property and/or Reproductions described in it may take place is available in the University IP Policy (see http://www.campus.manchester.ac.uk/medialibrary/policies/intellectual-property.pdf), in any relevant Thesis restriction declarations deposited in the University Library, The University Library's regulations (see http://www.manchester.ac.uk/library/aboutus/regulations) and in The University's policy on presentation of Theses

To my Mother

Acknowledgments

I wish to express my gratitude to my supervisors Prof Tony Peyton and Dr David Armitage for their support and encouragement. Especially, I am deeply indebted to my supervisor Prof Tony Peyton for excellent guidance, fruitful discussions during this work, as well as for his admirable motivation to challenge me and his willingness to support me inside and outside work.

I would like to give my personal thanks to my close partner in this project Dr Christos Ktistis from the University of Manchester for his valuable suggestions, and with whom I shared constructive discussions and criticism and professional collaboration which helped the project to succeed and for all moments of friendship. Special thanks to Prof Wuliang Yin from the University of Manchester for his interest in the project, productive discussions and for the collaboration opportunities he provided me and for his critical reading and helpful suggestions for my thesis.

I am also thankful for all the staff and colleagues from the Swansea University, University of Glamorgan and Phillips medical research centre GmbH previously based in Aachen for the productive regular meeting, valuable discussion and constructive criticism. I would also like to acknowledge Prof David S Holder from UCL for providing the head FEM mesh. I would like to express my appreciation to Dr Minh Pham for collaborating in this project.

I wish also to express my thanks to all my colleagues from the Sensing, Imaging and Signal Processing Research Group, and all my friends for the good moments we spent together.

My love and sincere gratitude go to my family, especially to my mother for her continuous support, encouragement, and for her kindness, patience, love and for everything.

1 Introduction

Magnetic induction tomography (MIT) which is also referred to as electromagnetic tomography, electromagnetic induction tomography and eddy current tomography is a non destructive electrical tomography technique for imaging the passive electrical properties namely electrical conductivity (σ), and magnetic permeability (μ) inside the volume of an object under examination. Reviews of MIT were given by [1-3]. Compared with its sister technique Electrical Impedance Tomography (EIT), MIT has the advantage that it does not require direct contact with the object but functions through an air gap using an array of coils. Similar behaviour is exhibited by ECT which operates effectively through an air gap for imaging of dielectric materials (electrical permittivity (ε)), but it is unsuitable for conductive materials ($\sigma >> \omega\varepsilon$) because the air layer dominates the response. Therefore, the contactless nature of MIT avoids the errors from which EIT suffer that are related to electrode contact impedances, and having the positions of the MIT sensors known and fixed also helps image reconstruction.

Fuelled by the rapid advances in eddy current Non Destructive Testing (NDT), MIT adopted the eddy current concept and with multiple transmitter and receiver sensors, MIT developed applications in industrial process monitoring. In particular, the metals industry was first approached with applications such as molten steel visualisation [4-7] and solidification monitoring for molten steel [8, 9] because their high conductivities cause a large flow of eddy currents that can be easily detectable. Later, the contactless characteristic of the technique made MIT attractive for medical imaging applications especially for those where the attachment of the electrodes is inconvenient. However, the development of MIT for biomedical use has been much more difficult because of the low conductivities of biological tissues (0.02-2 Sm^{-1}) that are many orders of magnitude lower than those of metals, and hence give much smaller signals. Nevertheless, with advances in sensor design and data acquisition, research in the field of MIT has shown that such technological difficulties can be overcome, signals are being measured and images are reconstructed at least for phantoms with simple representative material distributions. Among the medical applications that have been investigated using MIT include: detection of bleeding in the brain (cerebral stroke) [10, 11], body composition [12-14], monitoring of the heart, and lung activity [15] and wound healing. Some of the main research groups which featured strongly in medical MIT are Bioimpedance group in Graz, Electronic, Biomedical and Instrumentation group in Barcelona, Medical Electronics and Signal Processing Research group in South Wales and Philips Medical Research in Aachen. On the other hand, there is a number of low conductivity industrial applications where materials exhibit conductivities that do not exceed 5 Sm^{-1}. Some of them have materials which are similar to biological tissues like imaging of foodstuffs, while others have materials with relatively higher conductivity (approx 5 Sm^{-1}) such as the inspection of process water for offshore multiphase flows. This latter is characteristic of high contrast material distribution, whereas the medical applications are of lower contrast. In this thesis, two applications are targeted namely, imaging of cerebral stroke and the measurement of saline water in oil/saline water pipelines.

1.1 Principle of operation of MIT

The principle of operation of MIT can be illustrated as shown in Figure 1.1 with a human head representing the object under investigation. MIT requires an alternating magnetic excitation field $\boldsymbol{B}_0$ (orange loops) to be coupled from the excitation coil to the object. The complex conductivity distribution $\boldsymbol{\kappa} = \boldsymbol{\sigma} + \mathrm{j}\omega\varepsilon_0\boldsymbol{\varepsilon}_r$ or changes $\Delta\boldsymbol{\kappa}$ inside the object cause a secondary field perturbation $\Delta\boldsymbol{B}$ (blue loops) due to the induction of eddy currents in the volume of the object. This secondary field $\Delta\boldsymbol{B}$ is of interest and is measured in combination with the primary field $\boldsymbol{B}_0$ by receiver coils in the form of voltages or trans-impedances. In order to obtain sufficient information about the eddy current activity in the volume of the object, multiple independent measurements are collected by implementing numerous excitation and detection channels around the periphery of the object. The measured data are then passed to conditioning electronics, and transferred to a computer via a data acquisition board. A suitable image reconstruction algorithm is employed in order to recover the spatial distribution of the electrical conductivity in the target from the collected data. As mentioned earlier, MIT is also sensitive for permeability variations, and hence can be used for imaging this property. In this case, the interaction of the primary field $\boldsymbol{B}_0$ with the permeability $\boldsymbol{\mu}_r$ distribution produces magnetic dipoles in the volume, which generate a secondary perturbation field $\Delta\boldsymbol{B}$. Likewise to conductivity imaging this secondary field is measured and processed for eventually mapping the permeability distribution in the object under study. In this thesis, MIT is investigated for conductivity imaging due to the nature of the electromagnetic properties of the considered applications.

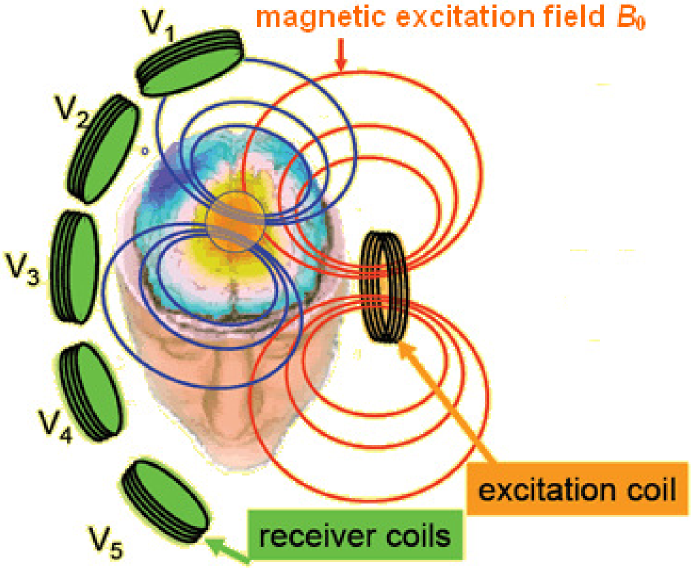

Figure 1.1: Principle of operation of MIT (based on schematic published by Scharfetter et al)

1.2 Electromagnetic effects in MIT

In MIT, when the excitation coils are energised, the spatial distribution of the magnetic flux inside the scanning region and hence the mutual coupling between the coils are altered when placing the object inside the region. The object material can be either ferro/ferri magnetic ($\mu_r > 1$) and/or has a high electrical conductivity. Compared to air, these materials typically cause the following electromagnetic effects which are represented below:

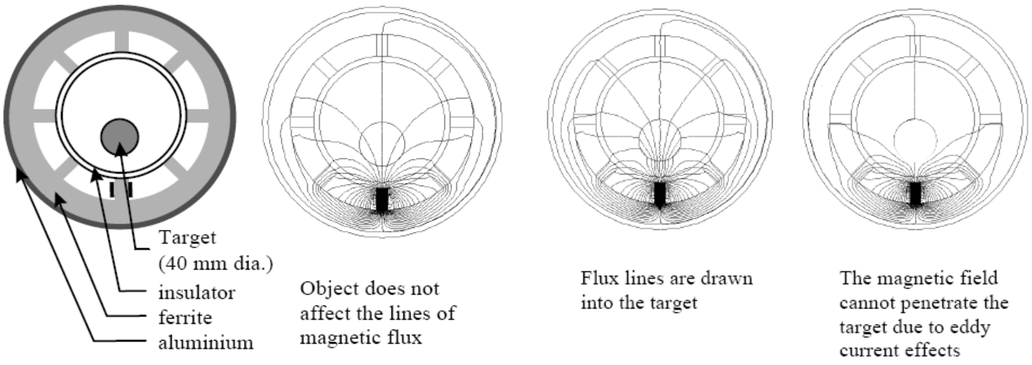

(a) Model **(b) Air target** **(c) Ferrite target** **(d) Aluminium target**

Figure 1.2: Schematic representation of the soft field effect [16].

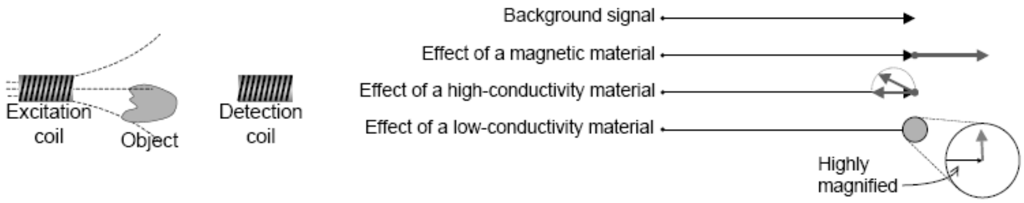

Figure 1.3: Phasor diagram demonstrating the electromagnetic effects of different material types in MIT [3]

From the figures shown above the following conclusions could be drawn:

- A permeable and non conducting object (ferrite) draws the magnetic flux lines into it, hence increasing the mutual coupling between some coil combinations as compared to others reflected by a rise in the detected signal as shown in Figure 1.2 (c). The secondary magnetic field coupled to the receiver coils is in phase with the primary field as illustrated by Figure 1.3.
- A very conducting, non magnetic object (Aluminium) tends to reduce the flux penetrating it due to the development of strong eddy currents inside the material which generate a secondary magnetic field opposing the source field as shown in the phasor diagram. This is known as the skin effect.
- For low conductive materials, which are the interest of this research, the phasor diagram shows the eddy current based magnetic field is perpendicular to the primary signal and its magnitude is very small. In order to be able to detect the corresponding induced voltages higher frequencies (up to 20 MHz) are generally favored compared to those used in metals inspection, because for

low conductivity applications the skin effect can be neglected, and hence the induced voltages are assumed to be proportional to frequency [17].

1.3 Image reconstruction in MIT: pitfalls, challenges and recent developments

Image reconstruction represents a significant hurdle for the future development of MIT. In contrast to hard field tomography modalities where the measured data depends only on the information along the well defined projected electromagnetic beam, in MIT the magnetic field lines are less definite and the measured data depend on the property variation in the whole volume of the target. Consequently, image reconstruction in MIT requires the treatment of a nonlinear inverse problem. Many workers in the field of MIT have reported the application of linear optimisation methods which usually produced qualitative images with limited resolution. From a mathematical point of view, linear approaches cannot be prescribed as a suitable treatment; instead non linear iterative schemes should be employed. In this iterative process, the conductivity map is updated in order to minimise an objective function represented with a least squares functional until some predefined convergence criteria is met. The solution should be able to produce the best fit between the measured data and the model. Two computational procedures are re-evaluated after each update of the image, namely the forward problem and the inverse problem. The forward problem can be defined as follows: given an object Ω with a known property (e.g. electrical conductivity $\boldsymbol{\sigma} \in \mathbb{R}^n$) distribution, and a mathematical model of the MIT system, calculate the measurement set $\boldsymbol{V} = \boldsymbol{F}(\boldsymbol{\sigma})$. On the other hand, the inverse problem is: given a measurement set of data $\boldsymbol{V} \in \mathbb{R}^m$ and sensitivity map $\boldsymbol{J} \in \mathbb{R}^{m \times n}$ of the object, derive the property distribution $\boldsymbol{\sigma} \subset \Omega$. In a nonlinear optimisation scheme, the sensitivity must be re-evaluated after each update of the conductivity map. Various nonlinear optimisation methods have been developed in numerical analysis but hardly have been applied in MIT since they require the re-evaluation of the 3D forward problem leading to very long computation time and demanding memory storage. The first results of a nonlinear treatment of the MIT inverse problem for conductivity imaging were published by Soleimani [18]. Moreover, the MIT inverse problem is ill-posed in the sense that small errors in the measured data may propagate with arbitrarily large errors in the estimate of the conductivity distribution. Two factors contribute to the ill-posedness of the MIT inverse problem. These are that the data is often contaminated with noise and the fact that MIT is substantially more sensitive to the periphery of the object than to the central region. In order to deal with the ill-posedness of the problem the application of regularisation schemes is required to stabilise the solution. Therefore, a penalty term which carries a priori information is added to the objective function to be minimised. Most groups have reported the application of generalised Tikhonov regularisation methods where the employed matrices are more or less *ad-hoc* and the implicit prior information is simple. For applications with complex internal structures like imaging cerebral stroke, these priors are not representative of the actual solution and may be inappropriate. An additional difficulty is related to low conductivity applications, where measured signals are usually small. In fact, although MIT systems designed for such applications operate at relatively higher frequencies in order to be able to measure the induced voltages, there is an upper bound when selecting the highest frequency in order to remain well below the resonant frequencies of the transmitter or receiver coils. In this situation, the image reconstruction algorithm would need to deal with systems of lower signal to noise ratios (SNR).

Image reconstruction in MIT can be divided into two main approaches: absolute imaging and difference imaging. In the former, a single projection of data is employed in the image reconstruction algorithm to yield a solution which represents the absolute conductivity distribution in the object. This approach requires a): an MIT system with high quality SNR and, b) a highly accurate forward model that can produce calculated data which can be fitted as well as possible to the measured data in the minimisation of the objective function. The second approach employs two data sets which can be taken for two different conductivity distributions. In biomedical MIT, biological tissues possess conductivities which change with frequency; hence difference imaging can be performed by using different frequencies. In industrial applications like in multiphase flow imaging, temporal difference imaging can be carried out since the fluid structure inside the pipe is continuously changing. Literature reported, difference imaging provide benefits in cancelling errors. However, image reconstruction using this approach is performed linearly and it is not clear yet how to derive a nonlinear approach.

1.4 Low conductivity applications for Magnetic Induction Tomography

Research into MIT has been established in the metal industry as a further development to inductive sensing based NDT for certain industrial applications where imaging of shapes or interior structures is desirable. MIT is attractive in this domain mainly because the metals are very good conductors. Over the last decade, work in MIT has been extended to investigate the possibility of using this modality for imaging biological tissues for medical applications. The associated motivation was that MIT shares similar principles of operation with its counterpart EIT in the sense that both translate a set of measured voltage data to a map of the electrical conductivity distribution in the object under investigation. Not only this but also some of the limitations from which EIT suffer such as being an invasive modality (electrode skin contact), electrode positioning and contact impedances constituted advantages for MIT. Initial reports published in the literature demonstrated with experiments conducted under simplified laboratory conditions that phantoms including perturbations with low conductivities that are characteristic of biological tissues can be imaged. This successful outcome not only led to the further investigation of MIT for imaging various pathophysiological conditions, but also to the rise of certain low conductivity industrial process applications.

In the medical field, the clinical use of MIT focused on some specific pathophysiological mechanisms causing physiological disturbances to biological tissues. In general broad perspective, these disturbances are manifested with changes in the normal physical and/or biochemical structure of body tissues, which produce changes in the tissue dielectric properties that can be determined with MIT. In the following, examples of some currently researched MIT clinical applications will be presented alongside with the MIT research groups involved and their progress so far. This presentation is preceded with a brief overview on the electric properties of biological tissues and their spectroscopic behaviour.

1.4.1 Tissue properties

The range of the dielectric properties of biological tissues and their variations with frequency represents an immense topic. The literature reveals that the interest into this domain has a long history, but from a practical perspective research into the specification of this range effectively started in the 1950s and 1960s with large amount of the work and findings produced by Schwan and his collaborators. Foster and Schwan [19] reviewed the basic concepts of the dielectric phenomena in biological tissues and explained them in terms of the interactions happening at the cellular level. Pethig and Kell [20] covered similar ground and provided an account of theories formulated to describe the dielectric properties in terms of the underlying molecular processes. Common to all these publications is undoubtedly a more or less a tabulation of the dielectric properties of tissues illustrating the theoretical findings of these authors. Excellent reviews and publications summarising the electrical properties of biological materials can be found in the literature by for instance Geddes and Baker [21], Stuchly and Stuchly [22], Durney *et al* [23] and Duck [24]. Although a great deal of research has been devoted to investigate the dielectric properties of tissues and quantify their behaviour with frequency variation, the findings showed that there exist inconsistencies in the estimation; hence no consensus on the dielectric data was achieved. In addition, there were some gaps in the range of the data meaning that the research was incomplete in some areas related to some particular types of tissues and frequency ranges. Recent experimental studies based on modern swept frequency techniques using impedance analysers carried out by Gabriel *et al* [25, 26] tried to address these issues by seeking the determination of dielectric properties of tissues over ten frequency decades (10 Hz to 20 GHz), hence bridging the gaps which were outstanding and also providing a basis for the evaluation and the analysis of the dielectric data that was already available. The research also led to the development of parametric models [27] that can be used to predict the frequency dependent behaviour of dielectric properties of tissues which is of great interest to electromagnetic dosimetry. This area of science deals with the simulation of electromagnetic exposure of biological structures to radiation and the calculation of the induced internal fields for various applications.

The dielectric properties of biological tissues can be described in terms of the complex conductivity (κ) written in the following form:

$$\kappa = \sigma + j\omega\varepsilon_r\varepsilon_0 \tag{1.1}$$

where σ is the electrical conductivity expressed in (Sm^{-1}) and ε_r is the relative permittivity (Fm^{-1}) and the angular frequency ω in radians per second. This electric expression can be justified in connection with the physiological structure of tissues that comprises of cells containing membranes, intracellular and extracellular fluids. The fluids provide the conductivity component, whereas the cell membranes are thin and have a high resistivity, hence electrically behaving like a small capacitor with a certain permittivity [28]. The complex tissue conductivity depends on the volumes of the intracellular and extracellular spaces and also on the overall tissue structure. If cells are randomly distributed within the extracellular space, then one value for the conductivity will be found but if the cells are grouped together to form sheets, then the tissue conductivity at low frequencies can drop rapidly because the current has to find its way through the sheets of cells. Hence the conductivity spectra changes with the tissue type.

When the electromagnetic radiation interacts with the constituents of a biological material, the tissue exhibits dielectric properties that change according to different biochemical mechanisms that happen as the frequency is increased from few Hz toward the GHz region. These mechanisms can be classified into three so called dispersions described as follows:

a) The low frequency α dispersion is associated with ionic diffusion processes at the site of cellular membrane.
b) The β dispersion, in the hundreds of kHz region, is caused mainly by the polarisation of cellular membranes which acts as barriers to the flow of ions between the intra and extra cellular media. Other contributions to the β dispersion come from the polarisation of protein and other organic macromolecules. This band is of interest in this thesis for the study of the cerebral stroke application as the employed frequencies fall in the range 1 MHz to 10 MHz in which large changes in tissue conductivity spectra are observed to be associated with malignant changes in tissue physiological structure caused by the stroke.

c) The γ dispersion, situated in the GHz band, is due to the polarization of water molecules.

For stroke imaging, if the stroke is caused by blood accumulation in the brain, spectroscopic induction measurements at frequencies covered within the β dispersion can be desirable since they may aid in distinguishing the blood among other head tissues [25]. Figure 1.4 shows a plot of the electrical conductivity of biological tissues in the head over two decades of frequency [100 kHz-10 MHz] comprised within the β dispersion region. The trends clearly show the blood has a relatively more significant change of conductivity compared to other tissues. Frequency differential imaging between two frequencies such as 1 MHz and 10 MHz (since the β dispersion of blood is centred at 3 MHz [29]) can therefore be a possible option for stroke detection. Table 1-1 below shows the dielectric properties of the head tissues at the pair of frequencies: 1 MHz and 10 MHz.

Table 1-1: Dielectric properties of head tissues at 1 MHz and at 10 MHz

Tissue type	Conductivity (Sm^{-1})@ 1 MHz	Relative permittivity (Fm^{-1}) @1 MHz	Conductivity (Sm^{-1})@10 MHz	Relative permittivity (Fm^{-1})@10 MHz
Scalp	0.50268	1836.4	0.6168	170.700
Skull	0.024353	144.51	0.0828	53.775
CSF	2	108.99	2.002	108.600
Grey matter	0.16329	860.42	0.2917	319.700
White matter	0.10214	479.79	0.1585	175.700
Ventricles	2	108.99	2.002	108.600
Spinal cord	0.13026	926.14	0.2251	247.700
Optic nerves	0.13026	926.14	0.2230	155.100
Eye Sclera	0.61882	2178.3	0.7984	208.25
Nasal cavity (air)	0	1	0	1
Ear canals (air)	0	1	0	1
Olfactory (air)	0	1	0	1
Blood	0.82211	3026.3	1.0967	280.03

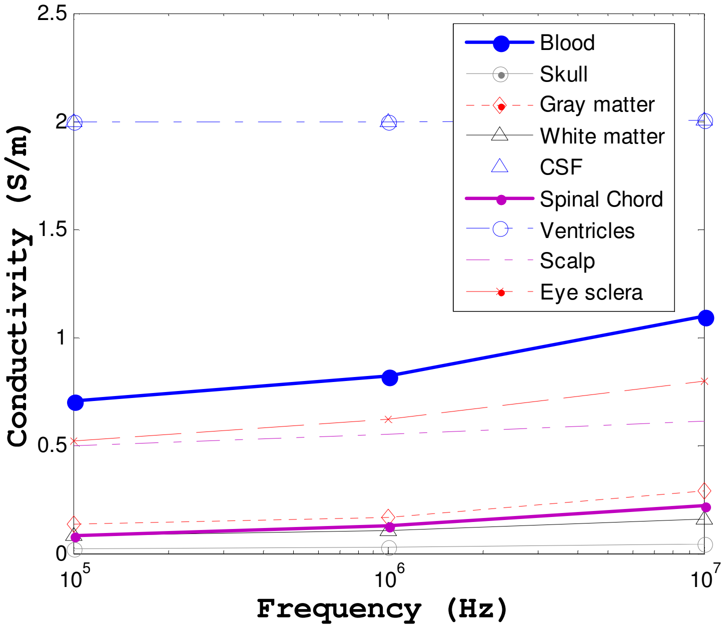

Figure 1.4: Plot of conductivity spectra for head tissues in the frequency range [1-10] MHz.

1.4.2 Cerebral stroke

Cerebral stroke is a life threatening pathological condition involving an accumulation of fluid in the brain. In the UK, a report by the National Health Service (NHS) Confederation [30] indicates every year an estimated 110,000 people in England suffer a stroke and the condition is the third largest cause of death. In addition to being described as a medical emergency, fatalities may not only result from the immediate brain injury; rather, progressive damage to brain tissue develops over time [31]. In fact, 30 % of affected people will suffer long term disability and 20 to 30 % will die within a month. It is also estimated that stroke costs the UK NHS about £2.8 billion p.a., which is about 66 % of the annual costs to the wider economy, associated with lost productivity, disability and informal care. Evidence shows that timely rapid diagnosis during the 24 hours following the stroke including first fast access to brain scanning and continuous monitoring of the lesion development can dramatically improve rates of survival and avoid associated potential neurological aggravations. Cerebral stroke can be broadly classified as extracellular vasogenic or intracellular cytotoxic in origin. The former, also called a "haemorrhage", happens when a blood vessel bursts due to breakdown of tight endothelial junctions which make the brain blood barrier. Cerebral haemorrhage can be classified as intracerebral if the blood artery ruptures inside the brain space, or subarachnoid if the blood is released in the subarachnoid space between the skull and the brain itself (Figure 1.5). In either case, the blood may cause a sudden pressure that can lead to a loss of blood supply to the affected tissue with resulting infarction, and the blood released by haemorrhage appears to have direct toxic effects on brain tissue and vasculature.

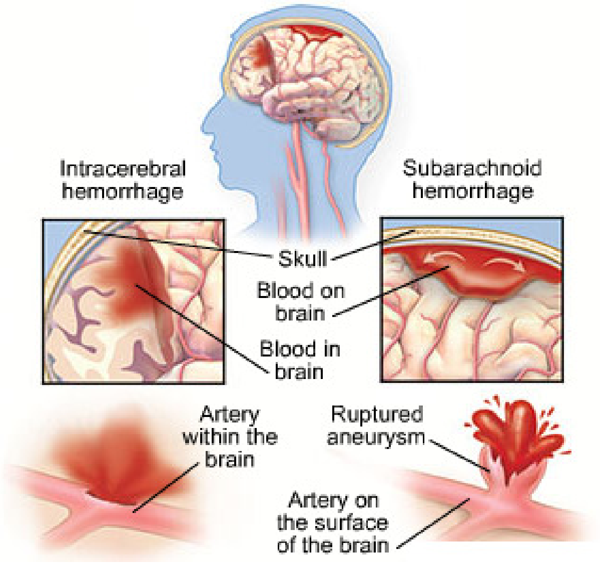

Figure 1.5: An ensemble of images illustrating Intracerebral and Subarachnoid Haemorrhage types and the causes leading to their occurrence (From [32]).

The other type of stroke is caused by “ischemia” which occurs when the blood supply to the brain cells is limited due to a partial or complete blockage of an artery that supplies the brain. In Figure 1.6, atherosclerosis in the carotid artery of the neck reduces blood flow to the brain. A rupture in the plaque can cause a blood clot to form. This clot may break loose and travel to an artery in the brain where it is trapped due to thin brain arteries (Figure 1.7) and hence resulting in blood blockage. At the cellular level, insufficient blood supply leads to inadequate functioning of the sodium and potassium pump in the cell membrane. As a result there is cellular retention of sodium and water leading to damage of brain tissues. Ischemic stroke is usually treated with thrombolytic drugs which operate by dissolving the blood clot to increase fluid circulation in the affected vessel. This treatment, however, increases the fatality of the hemorrhaged stroke by aiding in blood leakage. The two syndromes show the same symptoms and both require rapid medical intervention. Currently CT or MRI are used to diagnose the type of the stroke, however, access to these facilities is often limited. Furthermore, the condition also develops in delayed fashion and medical care ideally requires portable scanners which can be used at the patient bedside for frequent monitoring purposes.

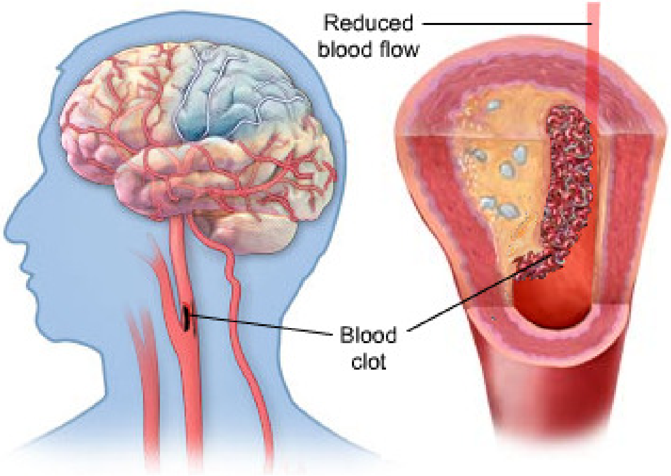

Figure 1.6: Ischemia type stroke visualised as a portion of a blood vessel leading to the brain where the blood flow has been obstructed due to the formation of a blood clot (From [32])

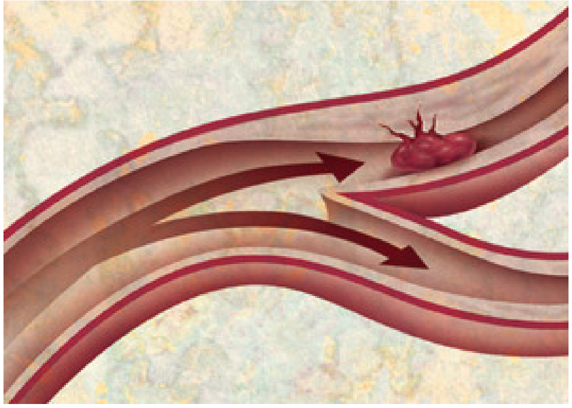

Figure 1.7: Image showing the early stage of ischemia development with a blood clot has been blocked in a narrow artery (From [32]).

In both types of the stroke (i.e. haemorrhage or ischemia) the local fluid accumulation in the brain space causes the composition of the tissues in the affected area to change leading to a change in associated electrical conductivity distribution. Tissue conductivity is known to be depressed in ischemia but the blood conductivity experiences a change that is five times higher than that of normal brain tissues in the frequency range of interest 1-10 MHz. EIT has been suggested as an alternative, more practicable, and low cost imaging modality for detecting both types of stroke and considerable amount of publications have been issued with much of the work dominated by Holder in UCL and his collaborators. However, the inconvenience of having to attach the electrodes to the scalp and the errors that can be caused by poor contact motivated research interest into investigating the possibility of using the contactless MIT for this application. Initial findings using MIT showed that a simulated haemorrhage in a phantom can be imaged, yet problems related to the low spatial resolution, shape, exact location of the stroke and quantitative estimation of its conductivity were still outstanding. Image reconstruction has a major impact in this issue and its development could certainly improve the results. This is an objective treated in this thesis. A haemorrhage may also be detectable by multi-frequency imaging since the gradient of the conductivity versus frequency curve is approximately 90% per decade and only 20% per decade for blood in the range 1 – 10 MHz [25]. Detecting ischemia by MIT might be more difficult since the change in tissue conductivity is less significant, and hence this thesis concentrates mainly on the detection or monitoring of haemorrhage based stroke.

1.4.3 Lung ventilation and heart rate monitoring

Another clinical application of vital importance where MIT has been proposed is the monitoring of lung and heart activity. Lung tissue has a conductivity which is about five times smaller than other soft tissues in the thorax. During the mechanical actions of the thorax, air which is an insulator is pumped into the lung through respiration, causing a change in the conductivity of the lung tissue. By imaging this change in conductivity using eddy current techniques the distribution of ventilation can be determined. In addition, it has been shown that cardiac related changes also affect the conductivity of the lung tissue. This is caused by the perfusion of blood, which is a conducting material, into the lungs. Hence MIT could potentially also be able to monitor heart rate. From the literature it has been shown that MIT can be a promising method for *in vivo* monitoring of heart rate [33] or lung activity [34]. More recent work by Steffen *et al* [15] based in the Philips Medical Research centre in Aachen demonstrated that respiration frequency can be well correlated to the demodulated inductive signal taken from newborn animals as illustrated in Figure 1.8. On human adults they showed measurement changes in frequency domain demonstrating lung and heart activity under maintained respiration.

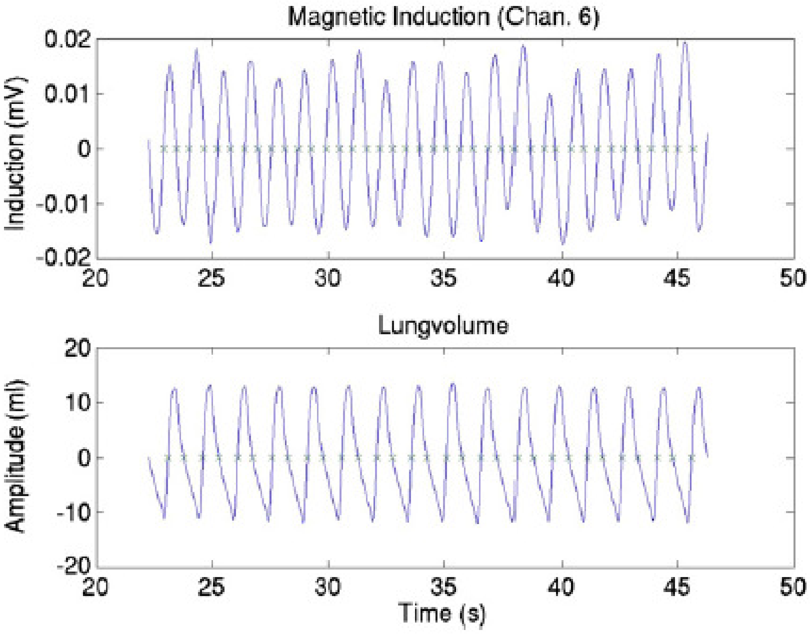

Figure 1.8: Comparison of air flow in the lung and magnetic induction (From [15])

EIT has also been proved as a feasible imaging method for monitoring pulmonary activity in the lungs but again the use of electrodes is an inconvenience since unwanted side effects such as skin irritation, difficult application or additional cabling may occur. Not only does EIT suffer from this problem but also existing clinical techniques already in use for this application such as the electrocardiogram (ECG), impedance cardiography (ICG) and pulse oximetry. The related side effects appear to be a concern for the very sensitive skin of infants, which can be irritated or even damaged by the removal of electrodes. Overall MIT is an attractive imaging modality for monitoring various diseases where contactless measurements are preferred. Obviously the research spectrum and the clinical applications investigated using its sister technique EIT are relatively much broader and diverse and as a point of conjecture, MIT may approach similar problems in the near future. As an example, in pulmonary related diseases, EIT has not only been investigated with lung activity and heart activity but other areas have been approached like detection of pulmonary oedema. EIT has also been investigated as possible screening method for detecting tumors notably breast cancer in women where there has been known to be a significant difference between normal breast tissues and tumors.

In industrial process inspection applications, there is only a few problems involving materials with low conductivity as opposed to medical MIT where all tissues are mainly dielectric. In this thesis, we will approach a low conductivity application in the oil industry, and below is a brief introduction explaining the application and the results of the initial investigation carried with inductive sensors. Other low conductivity industrial applications that have been targeted recently by MIT include imaging food products and inspection of fractures in carbon fibre based materials.

1.4.4 Oil/Gas/Water industrial process application

In off-shore oil production, measurement of the sea water fraction (water cut) in multiphase flow in pipelines and separators is important for controlling productivity. Various commercial sensors are available employing capacitance, microwaves, ultrasound or γ rays, but their accuracy has been limited by factors such as scaling of the pipes, a limited range and the gas content of the mixture. Eddy current techniques have been suggested as a complementary method because they would be sensitive only to the conductive component of the mixture, i.e. the process water, which has a typical conductivity of 5 Sm^{-1}. Furthermore, the use of several coils would enable the conductivity of the process water to be determined. Alberchtsen *et al* [35] demonstrated an experimental system using a single excitation coil with phantoms simulating different flow regimes. With non-cylindrically-symmetrical flow (e.g. stratified), the derived water fraction depended strongly on the position of the coil relative to the water/oil interface; the authors concluded that to overcome this problem, a tomographic system should be developed. More recent work by another Norwegian research group using a single channel inductive system has also concluded that the work should be extended to tomography. No one has yet constructed an MIT system for this application but our existing technology may be adapted for this purpose. Indeed, because the conductivity of the process water is generally higher than that of biological tissues the signals are larger and easier to measure, giving signal to noise ratios that may be sufficient for high frame rates.

1.5 Achievements

This project ran as part of a collaborative research programme funded by the Engineering and Physical Sciences Research Council (EPSRC) and called LCOMIT “Low Conductivity Imaging using Magnetic Induction Tomography”. This programme brings together three of the world’s leading groups in MIT in Manchester, Swansea and Glamorgan universities as well as an industrial contributor being Philips Medical Research; It is designed to approach the fundamental, theoretical and practical problems of making MIT operate effectively with low conductivity materials ($\sigma \leq 5$ Sm^{-1}).

Within this programme, this project aimed specifically to address the image reconstruction problem in MIT for low conductivity materials. Two applications have been approached, one of which is medical and consists of imaging cerebral stroke, and the second is industrial and aims to inspect multiphase flows for offshore oil/water applications. Overall, the thesis has concentrated on absolute imaging for both applications. For the stroke application, frequency difference has also been examined since it has been reported to be promising for imaging biological tissues. In addition, state difference imaging has also been an option to implement in the oil/water application. In this thesis, image reconstruction has also taken a solid step forward by considering imaging of more representative multi-layer head models which are the first kinds of their application in MIT. On the other hand, the practical results obtained from the industrial application also constitute the first findings of the possible implementation of MIT for this application.

For absolute imaging, efficient algorithms have been designed for the forward and inverse problems. In the former, the objective was to develop a custom software in MATLAB for simulating MIT measurement data for three dimensional eddy current problems. The solver has been tested to be able to deliver a fast and memory efficient solution to the forward problem in MIT compared to conventional finite element (FE) software packages. This constituted an essential prerequisite for implementing nonlinear iterative image reconstruction algorithms which require the re-evaluation of the forward problem in every iteration of the minimisation procedure. The forward problem has been solved using the impedance method. Since only low conductivity applications are considered, which require medium frequencies within the RF band, the application of a quasi static approximation has been implemented and examined. Because the MIT inverse problem is nonlinear, iterative techniques are commonly suggested. One of the first reports on nonlinear solution of the MIT inverse problem using the conventional Gauss Newton method was produced by [36]. Driven with the aim to achieve a better optimisation and stability of the MIT solution, work here has taken a further step by implementing more sophisticated nonlinear reconstruction methods. It has also delivered a comparative analysis on the resulting performance against that of previously reported method in MIT. For the biomedical application, imaging the stroke inside a realistic head model is classified as a large scale problem in conductivity, (i.e. a problem with a large number of degrees of freedom). The solution of the inverse problem using the direct inversion based Newton method is computationally expensive. In order to deal with this issue, the computationally robust Conjugate Gradient method based on the Krylov Subspace technique has been implemented in MIT for this application.

Another important study was to investigate the incorporation of different priors that are used to regularise, and consequently stabilise the solution. In this respect, the performance of three forms of regularisation priors has been examined in the framework of the targeted biomedical and industrial application. These are represented with smoothing operators, edge preserving regularisation and structural information based prior. This latter was found more suitable for the medical application where advanced high resolution scanners like MRI or CT can provide images showing the initial state of the stroke lesion. By exploiting these images as a prior in the image reconstruction, MIT can be used for post diagnosis rather than for detection of the cerebral stroke.

In difference imaging, the spectral behaviour of biological tissues has been employed in image reconstruction. The objective was to investigate the quality of the reconstructed images for the stroke using this approach. For the oil/ process water application, state difference imaging has been implemented and results appear promising.

1.6 Thesis organisation

The thesis is divided into seven chapters. In Chapter 2, a brief introduction of the MIT image reconstruction problem is presented starting from a statistical point of view. A short background about the commonly used linear and nonlinear image reconstruction algorithms and regularisation methods is reviewed. In Chapter 3, the forward problem in MIT is approached. Starting with a review about the commonly used numerical methods for modelling the eddy current problem such as FEM, the chapter continues to present the application of the impedance method for generating the 3D electromagnetic forward solution of the MIT measurements. Then, the principal weakly coupled field assumption adopted in the calculation of the forward solution is examined against full wave analytical and numerical software packages. The benefits of the synthesised custom forward solver related to the computational time and memory demands as well as to the tolerance errors are quantified for validation purposes. For the biomedical application, the feasibility of detecting stroke is investigated in two phases:

a) An analytical solution of the MIT forward problem is presented for a multilayer head model incorporating a stroke and employed to estimate the smallest detectable size above noise levels which are characteristic of current MIT systems
b) A custom forward solver is employed as a numerical means together with realistic head model incorporating a large peripheral stroke to quantify the magnitude of the measured signal due to the stroke and compare it against the mechanical errors due to movement of the head and the coils. The process is carried out for both absolute and frequency difference imaging.

Chapter 4 starts with a literature review on the fundamental optimisation methods namely the steepest descent method and Newton method. Then, a special class of nonlinear optimisation methods that are regarded as more efficient than conventional approaches such as Gauss Newton method are derived. These methods employ the concept of trust region and damping mechanisms which are presented and discussed. Using a simple test phantom with a single inclusion, which are assigned conductivities corresponding to white matter and stroke respectively, the efficiency and the benefits of these methods are analysed and compared against the performance of the conventional Gauss Newton method. In the last section, one of the proposed optimisation methods is modified to incorporate Krylov subspace techniques. This is presented in the framework of large scale problems encountered in the medical application. Chapter 5 starts with a brief introduction to different regularisation schemes that can be applied in MIT. Based upon the solution we obtain, the quality of such priors is examined in the context of the medical and industrial applications. In the medical application, since we are only interested in recovering the stroke among the complex structure of the head, a structural information prior comprising knowledge of the distribution of the head tissues is presented as a potential robust regularisation approach. Assuming this prior can be developed based upon a pre-diagnosis made by MRI or CT which accurately maps the initial state of the stroke together with the distribution of the other tissues, MIT could be used for post-diagnosis i.e. for monitoring the progress of the stroke condition at the bed side of the patient. In Chapter 6, a set of simulations is carried out to investigate the suitability of frequency difference imaging for MIT. Simulated image reconstructions start with simple conductivity distribution crudely approximating the head with the stroke and continue to more realistic head model extracted from MRI data. In the last chapter, conclusions about the work and the results obtained in this thesis as well as the areas of research suggested to approach as a future work are discussed.

2 Background

Image reconstruction in MIT is realised via the solution of an inverse conductivity problem that is both nonlinear and ill-posed. Being nonlinear, this inverse problem is usually evaluated iteratively by minimising a least squares functional. The ill-posedness of the problem is treated using regularisation by introducing a penalty functional. This latter is used either to de-correlate the noise signals from the measurements, or to correlate the property values of the elements in the image according to some prior knowledge about the assumed solutions. In a probabilistic (statistical) setting, this penalty functional is referred to as "a prior".

For the solution of the inverse problem deterministic or probabilistic methods can be employed although the former is more commonly used. However, the concept of minimisation and the prior knowledge implemented in deterministic methods are in fact derived from theoretical probabilistic principles which provide a unifying analysis of general ill-posed problems. Hence, a starting point is to illustrate the link between probability theory and the general MIT deterministic minimisation problem. Then, a literature review on the most commonly applied image reconstruction deterministic methods is presented. In order to clarify how regularisation is implemented within these algorithms, the basic analytical tool of singular value decomposition is utilised.

2.1 Probabilistic and deterministic approaches

The main difference between probabilistic and deterministic methods is that in the former the unknown conductivity vector is characterised as a set of random variables with a probability density whereas in the latter the variables are non-random. Let us first present some notation about the basic tools used in probability theory.

For a vector $\boldsymbol{\sigma} \in \mathbb{R}^n$ of n random variables, the marginal density of σ_i can be given by:

$$p_i(\sigma_i) = \int_{-\infty}^{\infty} \ldots \int_{-\infty}^{\infty} p(\boldsymbol{\sigma})\, d\sigma_1 d\sigma_2 \ldots d\sigma_{i-1} d\sigma_{i+1} \ldots d\sigma_{n-1} d\sigma_n \tag{2.1}$$

where $p(\boldsymbol{\sigma})$ is the probability density function of the random vector $\boldsymbol{\sigma}$

The mean or expected value $\boldsymbol{m}_\sigma \in \mathbb{R}^n$ of $\boldsymbol{\sigma}$ can be defined as:

$$\boldsymbol{m}_\sigma = E(\boldsymbol{\sigma}) = \int_{-\infty}^{\infty} \boldsymbol{\sigma}\, p(\boldsymbol{\sigma})\, d\boldsymbol{\sigma} \tag{2.2}$$

The correlation matrix of the n random variables $\boldsymbol{\sigma}$ is an n×n symmetric matrix written as:

$$\boldsymbol{corr}_\sigma = E\left(\boldsymbol{\sigma}\boldsymbol{\sigma}^{\mathrm{T}}\right) = \begin{pmatrix} E(\sigma_1\sigma_1) \cdots E(\sigma_1\sigma_n) \\ \vdots \quad \ddots \quad \vdots \\ E(\sigma_n\sigma_1) \cdots E(\sigma_n\sigma_n) \end{pmatrix} \tag{2.3}$$

The variance of $\boldsymbol{\sigma}$ is the correlation of the random vector $(\boldsymbol{\sigma} - \boldsymbol{m}_\sigma)$ given by:

$$\boldsymbol{Var}_\sigma = E\left((\boldsymbol{\sigma} - \boldsymbol{m}_\sigma)(\boldsymbol{\sigma} - \boldsymbol{m}_\sigma)^{\mathrm{T}}\right) = E\left(\boldsymbol{\sigma}\boldsymbol{\sigma}^{\mathrm{T}}\right) - \boldsymbol{m}_\sigma \boldsymbol{m}_\sigma^{\mathrm{T}} \tag{2.4}$$

The conditional density of $\boldsymbol{\sigma}$ given the vector $\boldsymbol{D}$ is defined as follows:

$$p(\boldsymbol{\sigma} \mid \boldsymbol{D}) = \frac{p(\boldsymbol{\sigma}, \boldsymbol{D})}{p(\boldsymbol{D})} \tag{2.5}$$

whenever $p(\boldsymbol{D}) \neq 0$, otherwise $p(\boldsymbol{\sigma} \mid \boldsymbol{D}) = 0$. Similarly we can write:

$$p(\boldsymbol{D} \mid \boldsymbol{\sigma}) = \frac{p(\boldsymbol{\sigma}, \boldsymbol{D})}{p(\boldsymbol{\sigma})} \tag{2.6}$$

Hence,

$$p(\boldsymbol{\sigma} \mid \boldsymbol{D})\, p(\boldsymbol{D}) = p(\boldsymbol{D} \mid \boldsymbol{\sigma})\, p(\boldsymbol{\sigma}) \tag{2.7}$$

This is called Bayes' theorem.

In MIT the vector $\boldsymbol{D}$ consisting of m measured data, can be related to the conductivity $\boldsymbol{\sigma}$ using the following model:

$$\boldsymbol{D} = \boldsymbol{F}(\boldsymbol{\sigma}) + \boldsymbol{n} \tag{2.8}$$

where $\boldsymbol{n}$ is the noise distribution vector and $\boldsymbol{\sigma}$ is unknown. Assuming $\boldsymbol{\sigma}$ and $\boldsymbol{n}$ are random sets, and the model $\boldsymbol{F}(\boldsymbol{\sigma})$ and $\boldsymbol{n}$ are independent, the conditional probability density of the measurements $\boldsymbol{D}$ given $\boldsymbol{\sigma}$ also referred to as the "likelihood" is written as:

$$p(\boldsymbol{D}|\boldsymbol{\sigma}) = p(\boldsymbol{F}(\boldsymbol{\sigma})+\boldsymbol{n}|\boldsymbol{\sigma}) = \underbrace{p(\boldsymbol{F}(\boldsymbol{\sigma})|\boldsymbol{\sigma})}_{=1}\, p(\boldsymbol{n}|\boldsymbol{\sigma}) = p(\boldsymbol{n}|\boldsymbol{\sigma}) \tag{2.9}$$

Assuming the probability density function of the random parameter $\boldsymbol{n}$ is Gaussian, $p(\boldsymbol{n}|\boldsymbol{\sigma})$ can be written as:

$$p(\boldsymbol{n}|\boldsymbol{\sigma}) = \frac{1}{(2\pi)^{n/2}\det(\boldsymbol{Var_n})}\, exp\left(-\frac{1}{2}(\boldsymbol{n}-\boldsymbol{m_n})^{\mathrm{T}}\boldsymbol{Var_n}^{-1}(\boldsymbol{n}-\boldsymbol{m_n})\right) \tag{2.10}$$

where $\det(\boldsymbol{Var_n})$ denotes the determinant of $\boldsymbol{Var_n}$. Assuming that $\boldsymbol{n}$ is Gaussian with zero mean $\boldsymbol{m_n}$ and variance $\boldsymbol{Var_n}$, from (2.9), (2.10) and (2.8) we can write:

$$\begin{aligned} p(\boldsymbol{D}|\boldsymbol{\sigma}) &\propto exp\left(-\frac{1}{2}(\boldsymbol{n})^{\mathrm{T}}\boldsymbol{Var_n}^{-1}(\boldsymbol{n})\right) \\ &\propto exp\left(-\frac{1}{2}(\boldsymbol{D}-\boldsymbol{F}(\boldsymbol{\sigma}))^{\mathrm{T}}\boldsymbol{Var_n}^{-1}(\boldsymbol{D}-\boldsymbol{F}(\boldsymbol{\sigma}))\right) \end{aligned} \tag{2.11}$$

Following similar Gaussian assumptions, the *prior* density $p(\boldsymbol{\sigma})$ can be written as:

$$p(\boldsymbol{\sigma}) \propto exp\left(-\frac{1}{2}(\boldsymbol{\sigma}-\boldsymbol{m_\sigma})^{\mathrm{T}}\boldsymbol{Var_\sigma}^{-1}(\boldsymbol{\sigma}-\boldsymbol{m_\sigma})\right) \tag{2.12}$$

From (2.11), (2.12), and using Bayes' theorem (2.7) one can obtain the conditional density of $\boldsymbol{\sigma}$ given $\boldsymbol{D}$ as:

$$\begin{aligned} p(\boldsymbol{\sigma}|\boldsymbol{D}) &\propto \frac{1}{p(\boldsymbol{D})} exp\left(-\frac{1}{2}(\boldsymbol{D}-\boldsymbol{F}(\boldsymbol{\sigma}))^{\mathrm{T}}\boldsymbol{Var_n}^{-1}(\boldsymbol{D}-\boldsymbol{F}(\boldsymbol{\sigma}))\right) * \\ &\qquad exp\left(-\frac{1}{2}(\boldsymbol{\sigma}-\boldsymbol{m_\sigma})^{\mathrm{T}}\boldsymbol{Var_\sigma}^{-1}(\boldsymbol{\sigma}-\boldsymbol{m_\sigma})\right) \\ &\propto exp\left(\underbrace{-\frac{1}{2}(\boldsymbol{D}-\boldsymbol{F}(\boldsymbol{\sigma}))^{\mathrm{T}}\boldsymbol{Var_n}^{-1}(\boldsymbol{D}-\boldsymbol{F}(\boldsymbol{\sigma}))}_{P1}\underbrace{-\frac{1}{2}(\boldsymbol{\sigma}-\boldsymbol{m_\sigma})^{\mathrm{T}}\boldsymbol{Var_\sigma}^{-1}(\boldsymbol{\sigma}-\boldsymbol{m_\sigma})}_{P2}\right) \end{aligned} \tag{2.13}$$

The conditional density $p(\boldsymbol{\sigma} \mid \boldsymbol{D})$ is also called the "posterior density" since it gives the probabilities for the random parameters $\boldsymbol{\sigma}$'s after the measurement data $\boldsymbol{D}$, unlike the prior $p(\boldsymbol{\sigma})$ which assumes the probabilities for $\boldsymbol{\sigma}$'s before the measurements. Clearly the prior information is split into two parts:

a) The a-priori information about the noise which is embodied within the variance $\boldsymbol{Var_n}$ can be used to de-correlate the noise from the measurements.

b) The a-priori information about the parameter distribution represented by $\boldsymbol{Var_\sigma}$ and the expectation $\boldsymbol{m_\sigma}$ which can be employed to impart knowledge about the correlation of the conductivity voxel values and provide an initial prior respectively.

In probability theory, the maximum a posteriori estimate (MAP) is the conductivity vector $\boldsymbol{\sigma}$ that maximises the posterior density (2.13). This is equivalent to solving for the vector $\boldsymbol{\sigma}$ that minimises the functional:

$$\begin{aligned} F(\boldsymbol{\sigma}) &= -\frac{1}{2}\left(\boldsymbol{D}-\boldsymbol{F}(\boldsymbol{\sigma})\right)^{\mathrm{T}} \boldsymbol{Var_n^{-1}} \left(\boldsymbol{D}-\boldsymbol{F}(\boldsymbol{\sigma})\right) - \frac{1}{2}\left(\boldsymbol{\sigma}-\boldsymbol{m_\sigma}\right)^{\mathrm{T}} \boldsymbol{Var_\sigma^{-1}} \left(\boldsymbol{\sigma}-\boldsymbol{m_\sigma}\right) \\ &= -\frac{1}{2}\left\|\boldsymbol{D}-\boldsymbol{F}(\boldsymbol{\sigma})\right\|^2_{\boldsymbol{Var_n^{-1}}} - \frac{1}{2}\left\|\boldsymbol{\sigma}-\boldsymbol{m_\sigma}\right\|^2_{\boldsymbol{Var_\sigma^{-1}}} \end{aligned} \tag{2.14}$$

Assuming $\boldsymbol{Var_n^{-1}}$ and $\boldsymbol{Var_\sigma^{-1}}$ are positive definite, the square root $\boldsymbol{Var_n^{-1/2}}$ and $\boldsymbol{Var_\sigma^{-1/2}}$ are well defined. Hence, in this case, (2.14) is identical to the generalised Tikhonov problem (also known as "ridge regression" in the probability literature [37]) given by:

$$\boldsymbol{F(\sigma)} = -\frac{1}{2}\left\|\left(\boldsymbol{D}-\boldsymbol{F}(\boldsymbol{\sigma})\right)\right\|_2^2 - \frac{1}{2}\lambda\left\|\boldsymbol{L}\left(\boldsymbol{\sigma}-\boldsymbol{\sigma}_p\right)\right\|_2^2 \tag{2.15}$$

where $\boldsymbol{Var_\sigma^{-1/2}} = \sqrt{\lambda}\boldsymbol{L}$, $\boldsymbol{m_\sigma} = \boldsymbol{\sigma}_p$ is the initial prior and $\boldsymbol{Var_n^{-1/2}} = \boldsymbol{I}$. This latter setting is an assumption which infers that all the measurements are equally affected by noise. This is idealistic, which may be approximated with sensors, electronics and data acquisition circuit of high specifications that could sustain constant variance of noise. Otherwise, if the variance matrix $\boldsymbol{W}$ exists such that $\boldsymbol{W}^{-1} = \boldsymbol{Var_n^{-1/2}}$, then the residual can be scaled by the variance matrix accordingly. This scaling will amount to an additional computational cost which depends on the structure of $\boldsymbol{W}$, but as long the variance matrix is diagonal or banded (which is often the case in practice), then the cost of scaling will only contribute marginally to the total cost of the algorithm.

The parameter λ is called the regularisation parameter which is used to control the amount of the regularisation (prior) imposed on the solution. Increasing λ would mean reducing the variance $\boldsymbol{Var}_{\sigma}$ and thereby reducing the size of the $\boldsymbol{Var}_{\sigma}^{-1}$ normed distance between $\boldsymbol{\sigma}$ and $\boldsymbol{\sigma}_p$. Hence, this can be interpreted as reinforcing the prior.

If the conductivity vector is assumed to be not random, the minimisation problem can be solved deterministically. Using this approach, we seek the conductivity solution that best minimises the discrepancy between the data and the forward solution while keeping a reasonable proximity to the estimated prior. Using the generalised form (2.15), the Tikhonov method has two formulations which can be used to evaluate the solution:

$$
\begin{gathered}
(\boldsymbol{J}^{\mathrm{T}}\boldsymbol{J}+\lambda\boldsymbol{L}^{\mathrm{T}}\boldsymbol{L})\boldsymbol{\sigma}=-\boldsymbol{J}^{\mathrm{T}}\boldsymbol{D}\ -\lambda\boldsymbol{L}^{\mathrm{T}}\boldsymbol{L}\boldsymbol{\sigma}_p \\
\text{and} \\
\min\left\|\begin{pmatrix}\boldsymbol{J}\\ \sqrt{\lambda}\boldsymbol{L}\end{pmatrix}\boldsymbol{\sigma}-\begin{pmatrix}\boldsymbol{D}\\ \sqrt{\lambda}\boldsymbol{L}\boldsymbol{\sigma}_p\end{pmatrix}\right\|_2
\end{gathered}
\tag{2.16}
$$

where $\boldsymbol{J}\in\mathbb{R}^{m\times n}$ is called the Jacobian or the Sensitivity matrix which quantifies the sensitivity of measured data to small perturbations in property values inside the object. The former linear Tikhonov formulation is of interest in this thesis since the theoretical basis to its derivation will form the groundwork for the optimisation methods investigated in Chapter 4.

2.2 Image reconstruction methods

On the whole, image reconstruction algorithms find a solution ($\boldsymbol{\sigma}$) to the MIT conductivity problem by constructing a discrete linear problem of the form:

$$\Delta\boldsymbol{D}=\boldsymbol{J}\,\Delta\boldsymbol{\sigma} \tag{2.17}$$

This could be interpreted as seeking the absolute or the difference image from the difference of two sets of data, where one set can typically be linked to empty space for absolute imaging, or to homogenous background for state difference imaging. It could also refer to a linearised step within an iterative nonlinear optimisation protocol, where each iterate solution is calculated recursively from previous iterates.

For this section, we will drop the symbol Δ and consider the simplified notation:

$$\boldsymbol{D} = \boldsymbol{J}\,\boldsymbol{\sigma} \tag{2.18}$$

The main problem with the MIT discrete inverse problem is that the Jacobian $\boldsymbol{J} \in \mathbb{R}^{m \times n}$ is ill-conditioned and under-determined ($m \ll n$). This section will review several computational tools and algorithms reported for analysis and treatment of such problem.

2.2.1 SVD and GSVD

The ordinary singular value decomposition (SVD) and its generalization (GSVD) form powerful numerical tools for analysis of general discrete ill-posed problems. For the MIT inverse problem, in particular, the SVD of the Jacobian ***J*** can reveal all the difficulties associated with the ill-conditioning of this matrix, while the GSVD of the pair (***J***, ***L***) can yield insights into the regularisation methods which can be implemented for the evaluation of the problem. Detailed theory on the use of SVD, GSVD and other canonical decompositions for the study and analysis of general discrete ill-conditioned problems can be found in [38, 39].

Given the Jacobian $\boldsymbol{J} \in \mathbb{R}^{m \times n}$ being a rectangular matrix with $m \ll n$, and rank *r* the SVD of ***J*** is a decomposition of the form:

$$\boldsymbol{J} = \boldsymbol{U}\boldsymbol{\Sigma}\boldsymbol{V}^{\mathrm{T}} = \sum_{i=1}^{m} \upsilon_i\, \sigma_i\, \nu_i^{\mathrm{T}} \tag{2.19}$$

where $\boldsymbol{U} = (\upsilon_1, \ldots, \upsilon_m) \in \mathbb{R}^{m \times m}$ and $\boldsymbol{V} = (\nu_1, \ldots, \nu_n) \in \mathbb{R}^{n \times n}$ are unitary matrices with columns that are orthonormal, i.e. $\boldsymbol{U}^{\mathrm{T}}\boldsymbol{U} = \boldsymbol{V}^{\mathrm{T}}\boldsymbol{V} = \boldsymbol{I}$, and are called left and right singular vectors respectively, and the diagonal matrix $\boldsymbol{\Sigma} \in \mathbb{R}^{m \times n}$ includes the singular values $\mathrm{diag}(\sigma_1, \ldots, \sigma_r)$, with *r* = rank (***J***), which are arranged in a non-increasing order such that:

$$\sigma_1 \geq \sigma_2 \geq \ldots \geq \sigma_r \geq 0 \tag{2.20}$$

It is important to bear in mind the similarity in the notation σ_i assigned to the ordinary singular values of $\boldsymbol{J}$ and to the discrete conductivity elements of the object. However, in the sequel it will always be clear from the context which of them is being described.

The GSVD of the pair of matrices ($\boldsymbol{J}$, $\boldsymbol{L}$) is a matrix decomposition more general than the ordinary SVD, in the sense that it can be used to study the conditioning of $\boldsymbol{J}$ as well as the regularisation techniques used for treating the ill-conditioning of $\boldsymbol{J}$. In Tikhonov type regularisation (2.15), the matrix $\boldsymbol{L}$ can typically be either, the identity matrix, a diagonal weighting matrix or a discrete differential operator. For all these operators the general dimension of $\boldsymbol{L}$ can be exposed for simplicity as $\boldsymbol{L} \in \mathbb{R}^{p \times n}$, where $r = \operatorname{rank}\begin{pmatrix} \boldsymbol{J} \\ \boldsymbol{L} \end{pmatrix}$ with $r \leq m$ and $p > m$. In this case, the GSVD of the pair ($\boldsymbol{J}$, $\boldsymbol{L}$) is a decomposition in the form:

$$\boldsymbol{J} = \boldsymbol{U}\begin{pmatrix} \boldsymbol{\Sigma} & \boldsymbol{I}_{n-r} \end{pmatrix}\boldsymbol{X}^{-1} \qquad \boldsymbol{L} = \boldsymbol{V}\begin{pmatrix} \boldsymbol{H} & 0 \end{pmatrix}\boldsymbol{X}^{-1} \tag{2.21}$$

where the unitary matrices $\boldsymbol{U} \in \mathbb{R}^{m \times m}$ and $\boldsymbol{V} \in \mathbb{R}^{p \times p}$ have orthonormal columns, and $\boldsymbol{X} \in \mathbb{R}^{n \times n}$ is nonsingular with columns that are $\boldsymbol{J}^{\mathrm{T}}\boldsymbol{J}$ orthogonal. Moreover, $\boldsymbol{\Sigma}$ and $\boldsymbol{H}$ are $r \times r$ diagonal matrices defined by $\operatorname{diag}(\sigma_i)$ and $\operatorname{diag}(\eta_i)$ respectively. The diagonal elements of $\boldsymbol{\Sigma}$ and $\boldsymbol{H}$ are positive and ordered as follows:

$$0 \leq \sigma_1 \leq \sigma_2 \leq \ldots \leq \sigma_r \leq 1 \qquad \text{and} \qquad 1 \geq \eta_1 \geq \eta_2 \geq \ldots \geq \eta_r \geq 0 \tag{2.22}$$

The generalized singular values of the pair ($\boldsymbol{J}$, $\boldsymbol{L}$) are then defined as the ratios $\gamma_i = \sigma_i / \eta_i$ and $\sigma_i^2 + \eta_i^2 = 1$; hence, they appear in a non-decreasing order.

Suppose that the matrix $\boldsymbol{J}$ is invertible (nonsingular), then its inverse can be computed in SVD terms as: $\boldsymbol{J}^{-1} = \sum_{i=1}^{m} v_i \sigma_i^{-1} \upsilon_i^{\mathrm{T}}$ and an exact solution $\boldsymbol{\sigma}$ to the system $\boldsymbol{J\sigma} = \boldsymbol{D}$ can be achieved as:

$$\boldsymbol{\sigma} = \sum_{i=1}^{m} \sigma_i^{-1}\left(\upsilon_i^{\mathrm{T}}\boldsymbol{D}\right)v_i \tag{2.23}$$

In the MIT inverse problem $\boldsymbol{J}$ is however, singular and such an approach cannot be applied. Hence, a possible road to take is to compute a pseudo inverse which is also referred to as "Moore-Penrose generalized inverse" $\boldsymbol{J}^{\dagger}$ as: $\boldsymbol{J}^{\dagger} = \sum_{i=1}^{\mathrm{rank}(\boldsymbol{J})} v_i \sigma_i^{-1} \upsilon_i^{\mathrm{T}}$ and obtain a least squares solution $\boldsymbol{\sigma}_{LS}$ to the least squares functional $\min \|\boldsymbol{J\sigma} - \boldsymbol{D}\|_2$ given by:

$$\boldsymbol{\sigma}_{LS} = \boldsymbol{J}^{\dagger}\boldsymbol{D} = \sum_{i=1}^{\mathrm{rank}(\boldsymbol{J})} \sigma_i^{-1}\left(\upsilon_i^{\mathrm{T}}\boldsymbol{D}\right)v_i \tag{2.24}$$

Unfortunately, because the Jacobian $\boldsymbol{J}$ in MIT is ill-posed, the minimum norm solution $\boldsymbol{\sigma}_{LS}$ will not be unique. In addition, the solution will be instable and very sensitive to perturbations and errors in the Jacobian $\boldsymbol{J}$ and the data $\boldsymbol{D}$. For instance, this can be visualised with small changes in the data $\boldsymbol{D}$ leading to large changes in the solution.

In order to explore the appropriate numerical treatment for the MIT inverse problem it should be necessary to first study the ill-conditioning of the Jacobian $\boldsymbol{J}$, which enable us to pinpoint the problematic features which prevent us from achieving the desired unique, stable solution. For this purpose, the numerical decomposition tools, namely the SVD and the GSVD can be used.

In connection with the ill-posedness of the MIT inverse problem, the SVD of the Jacobian $\boldsymbol{J}$ can show three important characteristic features:

a) The singular values σ_i decay gradually to zero as the index *i* increases.

b) The left and right singular vectors υ_i and v_i tend to have more sign changes in their elements as the index *i* increases, i.e. as σ_i deceases.

c) The Fourier coefficients $\left|(\upsilon_i)^{\mathrm{T}}\boldsymbol{D}\right|$ decay to zero as least as fast as the singular values σ_i

Another important observation can be extracted from the SVD of $\boldsymbol{J}$ if the collected measurement data are not independent, for example if some of the sampled voltages can be determined by reciprocity. These voltages are subsequently redundant, and such dependencies within the measurement dataset will then transfer to linear relations between the rows of $\boldsymbol{J}$. In this case, the matrix $\boldsymbol{J}$ is classified as rank-deficient where the rank of $\boldsymbol{J}$ is a scalar which quantifies the amount of independent information in the matrix $\boldsymbol{J}$. The SVD spectrum will show a well determined gap which separates two clusters of positive and zero singular values. The independent information is then represented with the former cluster of positive values.

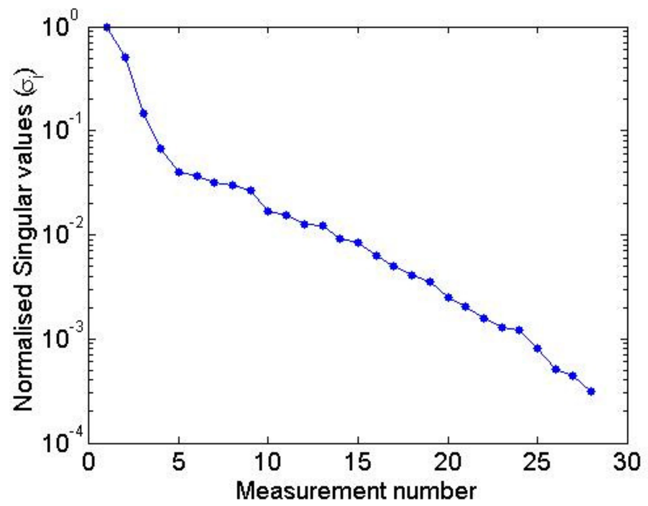

Figure 2.1: Plot of the singular values of the Jacobian of an ill-posed MIT problem

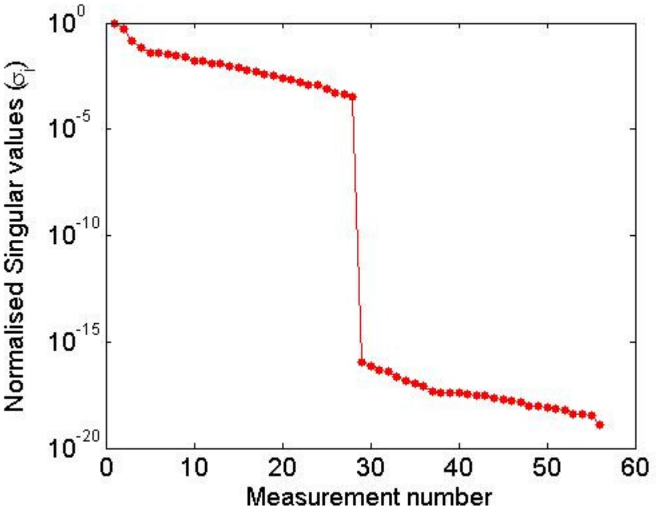

Figure 2.2: Plot of the singular values of the Jacobian of a rank-deficient MIT problem

It is important to mention the features related to the ill-posedness and rank-deficiency of the MIT discrete problem as described earlier can only apply to a system without perturbations and errors. In practice, the components $\boldsymbol{J}$ and $\boldsymbol{D}$ can be subject to several sources of errors. One source relates to the discretisation process involved in setting up the system of equations and corresponding approximation errors affect both $\boldsymbol{J}$ and $\boldsymbol{D}$. Another source of errors stems from the measurement system tolerances which obviously influence only $\boldsymbol{D}$. Lastly, errors produced from computational rounding approximations which involve both $\boldsymbol{J}$ and $\boldsymbol{D}$ can also be taken into account. In light of these errors, some interesting observations can be made with regard to the SVD features of the ill-posed and may be rank-deficient $\boldsymbol{J}$. If the Jacobian $\boldsymbol{J}$ incorporates redundant information, it can never be called exactly rank-deficient, but instead numerically rank deficient, in the sense that it will have a cluster of small but non-zero singular values (Figure 2.2). These components should be ignored in the regularised solution, since otherwise, small perturbations in $\boldsymbol{J}$ and $\boldsymbol{D}$ will appear with large errors in the solution i.e. the reconstructed image. On the other hand, the effect of the errors on the ill-posed $\boldsymbol{J}$ will be that the singular values σ_i and the Fourier coefficients $(v_i)^{\mathrm{T}} \boldsymbol{D}$ will not decay exactly to zero, but will decrease until they settle to different levels $\tau_{\boldsymbol{J}}$ and $\tau_{\boldsymbol{D}}$ respectively (Figure 2.1). These levels are, in effect, determined by the errors in $\boldsymbol{J}$ and $\boldsymbol{D}$ and hence can be used to determine how much useful information can be extracted from the ideal error-free MIT system ($\boldsymbol{J\sigma} = \boldsymbol{V}$). The typical situation is that the measurement errors in $\boldsymbol{D}$ are larger than the other types of errors in $\boldsymbol{J}$ and $\boldsymbol{D}$ especially if extra care is taken in the discretisation procedure and rounding errors are minimized with the use of high precision advanced computer. In this case, the coefficients $\left|(v_i)^{\mathrm{T}} \boldsymbol{D}\right|$ level off at $\tau_{\boldsymbol{D}}$ before the σ_i values level off at $\tau_{\boldsymbol{J}}$. If the coefficients $\left|(v_i)^{\mathrm{T}} \boldsymbol{D}\right|$ are assumed to settle at $\tau_{\boldsymbol{D}}$ when the index $i \geq i_{\boldsymbol{D}}$, and the singular values σ_i settle at $\tau_{\boldsymbol{J}}$ for $i \geq i_{\boldsymbol{J}}$, then the most of the useful information we seek to recover is comprised in the first $i_{\boldsymbol{D}}$ components of the solution. Clearly, the remaining $(m - i_{\boldsymbol{D}})$ SVD components which also include the $(m - i_{\boldsymbol{J}})$ elements will be dominated by noise, and therefore they should be filtered out in the regularised solution in the same way as described for the numerically rank deficient problem. In the following, the Jacobian $\boldsymbol{J}$ is assumed to be mainly ill-posed, since the collected measurements are considered to be linearly independent, and hence $\boldsymbol{J}$ is unlikely to be numerically rank deficient. Various common regularisation or filtering approaches will be described via the implementation of the “filter factors” in the regularised solution which provide answers to the following questions: a) *Which SVD components could be considered erroneous and hence should be filtered out*, and b) *how to filter them out*. Using the concept of the filter factors, the regularised solution takes the following form:

$$\boldsymbol{\sigma} = \boldsymbol{V\Phi\Sigma}^{-1}\boldsymbol{U}^{\mathrm{T}}\boldsymbol{D} \qquad \text{, or} \qquad \boldsymbol{\sigma} = \boldsymbol{X\Phi}\left(\boldsymbol{\Sigma}^{-1} \quad \boldsymbol{I}_{n-r}\right)\boldsymbol{U}^{\mathrm{T}}\boldsymbol{D} \tag{2.25}$$

which is generated using the SVD of $\boldsymbol{J}$ and GSVD of ($\boldsymbol{J}$, $\boldsymbol{L}$) respectively. This implementation is common to the regularised reconstruction methods presented below, expect that the filter function $\boldsymbol{\Phi}$ varies accordingly.

2.2.2 TSVD

Truncated SVD (TSVD) is the simplest method which can be used in the regularisation of the MIT inverse problem. By means of this method, the ill-conditioning of the matrix $\boldsymbol{J}$ is treated by explicitly truncating (ignoring) the last (m-k) SVD components of $\boldsymbol{J}$. This leads to a regularised solution which can be written as:

$$\boldsymbol{\sigma}^{\mathrm{TSVD}} = \sum_{i=1}^{m} f_i \frac{\left(\upsilon_i^{\mathrm{T}}\boldsymbol{D}\right)}{\sigma_i} v_i = \sum_{i=1}^{k} \frac{\left(\upsilon_i^{\mathrm{T}}\boldsymbol{D}\right)}{\sigma_i} v_i \tag{2.26}$$

where the filter factors f_i can be defined as a piecewise function which simply consists of zeros and ones:

$$f_i = \begin{cases} 1, & i \le k, \\ 0, & i > k, \end{cases} \tag{2.27}$$

The TSVD can be found suitable for regularising rank-deficient problems where the truncation level k is well defined and corresponds to the rank of the system matrix. However, since the MIT system $\boldsymbol{J}$ is ill-posed, there is no gap in the spectrum of singular values on the one hand, and on the other hand, the level at which the erroneous SVD components settle is not obvious for an accurate truncation to be applied. There exists also a TGSVD version for the GSVD, which can be applied in a similar fashion to the SVD. Due to its simple regularising properties, EIT is already familiar with TSVD and in MIT it has been implemented by [40] and [11]. However, although TSVD and TGSVD are proved theoretically to lead to a valid regularised solution, they are not favourably applied in practice in MIT inverse problems since their corresponding decompositions are very expensive to calculate and the cost is prohibitive for large matrices $\boldsymbol{J}$. However, from a theoretical point of view, they are useful and simple to analyse.

2.2.3 Tikhonov regularisation method

Tikhonov regularisation method is the most universally used regularisation tool for solving discrete ill-posed problems and has been extensively applied in EIT [41, 42] , ECT [43] and MIT [11]. Unlike the TSVD, the method provides stability to the ill-posed least squares problem by damping or filtering the unwanted small singular values in an implicit fashion. As can be seen from the generalised Tikhonov formulation (2.15), this is effectively implemented by incorporating a penalty term, in the form of the smoothing seminorm $L(\boldsymbol{\sigma})$ written in the discrete case as:

$$L(\boldsymbol{\sigma}) = \frac{1}{2}\lambda \left\| \boldsymbol{L}\left(\boldsymbol{\sigma} - \boldsymbol{\sigma}_p\right) \right\|_2^2 \tag{2.28}$$

In the literature, this form of the penalty functional $L(\boldsymbol{\sigma})$ is also referred to as the "Sobolev norm". Here the penalty operator, $\boldsymbol{L}$, carries a-priori information about the smoothness of the desired solution (see Chapter 5 for more details and examples on penalty operators), and λ controls the weight given to the minimisation of the solution regularisation term, relative to the minimisation of the data least squares functional. For a more general exposure of the penalty functional formulation, $\boldsymbol{\sigma}_p$ has also been inserted to denote a-priori estimate of the solution. In practice, it is difficult to obtain the prior $\boldsymbol{\sigma}_p$ which approximately reflects the true internal structure of the test object, hence users sometimes choose a homogenous distribution as a prior. Otherwise, $\boldsymbol{\sigma}_p$ can be chosen equal to zero, i.e. empty space is considered.

The regularised solution $\boldsymbol{\sigma}$ to the linear formulation of the generalised Tikhonov (gT) problem given by equation (2.16) can be written in terms of the GSVD of ($\boldsymbol{J}$, $\boldsymbol{L}$) in the following form:

$$\boldsymbol{\sigma}^{\mathrm{gT}} = \sum_{i=1}^{r} \left(f_i \frac{\upsilon_i^{\mathrm{T}} \boldsymbol{D}}{\sigma_i} + \left(1 - f_i\right) \boldsymbol{K}_i^{\mathrm{T}} \boldsymbol{\sigma}_p \right) x_i + \sum_{i=r+1}^{m} \upsilon_i^{\mathrm{T}} \boldsymbol{D} x_i \tag{2.29}$$

where $\boldsymbol{K}_i$ is the i-th row of $\boldsymbol{X}^{-1}$. The filter factors f_i can be defined as:

$$f_i = \frac{\gamma_i^2}{\gamma_i^2 + \lambda} \qquad (2.30)$$

When choosing $\boldsymbol{L}$ to be the identity matrix, i.e. $L(\boldsymbol{\sigma}) = (1/2)\lambda \left\| \boldsymbol{\sigma} - \boldsymbol{\sigma}_p \right\|_2^2$, the generalised Tikhonov method reduces to its standard form (sT) which can simply be written as:

$$(\boldsymbol{J}^{\mathrm{T}}\boldsymbol{J} + \lambda \boldsymbol{I})\,\boldsymbol{\sigma} = -\boldsymbol{J}^{\mathrm{T}}\boldsymbol{D} \ -\lambda \boldsymbol{\sigma}_p \qquad (2.31)$$

Similarly, with this specific form of Tikhonov regularisation (sT), we can write the regularised solution in terms of the SVD of $\boldsymbol{J}$ in the following generic form:

$$\boldsymbol{\sigma}^{\mathrm{sT}} = \sum_{i=1}^{m} \left(f_i \frac{\boldsymbol{v}_i^{\mathrm{T}}\boldsymbol{D}}{\sigma_i} + \left(1 - f_i\right) v_i^{\mathrm{T}} \boldsymbol{\sigma}_p \right) v_i \qquad (2.32)$$

where the corresponding filter factors are formulated as:

$$f_i = \frac{\sigma_i^2}{\sigma_i^2 + \lambda} \qquad (2.33)$$

One important piece of insight that we can draw from equations (2.29) and (2.32) is the way Tikhonov regularisation is used to damp the contributions to the solution associated with the unwanted small singular components of the Jacobian $\boldsymbol{J}$. The key mechanism is to have the filter factors close to 1 for large singular values σ_i and much smaller than 1 for small σ_i. This is implemented via the formulations for the filter factors as presented by (2.30) and (2.33) where we notice the filtering effectively sets in for those GSVD/SVD components for which $\gamma_i < \sqrt{\lambda}$ and $\sigma_i < \sqrt{\lambda}$ respectively. Hence, one should be prudent to select a reasonable value of the regularisation parameter λ so as the cluster of erroneous singular values levels just below $\sqrt{\lambda}$. Otherwise, if λ is badly chosen, such as $\sqrt{\lambda} < \gamma_1$ or $\sqrt{\lambda} < \sigma_m$, Tikhonov regularisation is virtually negligible since all the filter factors are approximately equal to 1 and the basis vectors x_i or v_i related to the erroneous singular values will unfortunately propagate in the solution.

Another important insight relates to the way the filter factors, and hence the regularisation parameter, control the influence of the a-priori information (the prior

$\boldsymbol{\sigma}_p$ and the penalty operator $\boldsymbol{L}$) on the regularised solution. Equations (2.29) and (2.32) show that, for those GSVD/SVD components of the regularised solution resulting in filter factors (f_i) near one, and thus for $\sqrt{\lambda} < \gamma_i$ or $\sqrt{\lambda} < \sigma_i$, the basis vectors x_i or v_i of the regularised solution are essentially dominated by contributions from the left hand side term ($\boldsymbol{D}$). However, for the other GSVD/SVD components where the filter factors (f_i) are close to zero, or equivalently $\sqrt{\lambda} > \gamma_i / \sqrt{\lambda} > \sigma_i$, then the basis vectors x_i or v_i are influenced by contributions from the right hand side coefficient including the a-priori estimate $\boldsymbol{\sigma}_p$. Hence, the role of the regularisation parameter in controlling the balance or the trade off between providing the good fit to the data and the good correlation to the prior is clear. Therefore, one should seek the optimum regularisation parameter which results in a regularised solution that is as close as possible to the true solution. The task of selecting the optimum regularisation parameter is challenging, which is reflected in literature with a range of parameter selection methods that have been devised for this purpose, namely:

a) *The Discrepancy Principle* [44]: is based on the assumption that the variance value of the measurement noise δ is known. In this case the regularisation parameter is chosen to so that:

$$\left\| \boldsymbol{J\sigma} - \boldsymbol{D} \right\| = \varepsilon\delta \tag{2.34}$$

where $\varepsilon > 1$ is some predefined value.

b) *The L-curve*: does not depend on a-priori knowledge of the noise level in the data. The method requires the plot of the "log" of the squared norm of the regularised solution against the squared norm of the residual for a range of values of regularisation parameter. This curve typically has an L shape. The L curve criterion for regularisation is to pick the parameter value corresponding to the "corner" of this curve. For examples and implementation details for this method, see [39, 45]

c) *The Generalised Cross Validation method* [46]: also does not require prior information of the variance of the noise δ. To apply this method, one selects the regularisation parameter that minimises the GCV functional:

$$GCV(\lambda) = \frac{\left\| \mathbf{r}_\lambda \right\|^2}{trace\left(\boldsymbol{C}_\lambda - \boldsymbol{I} \right)^2} \tag{2.35}$$

where $\mathbf{r}_\lambda = \boldsymbol{J}\boldsymbol{\sigma}_\lambda - \boldsymbol{D} = \left(\boldsymbol{C}_\lambda - \boldsymbol{I}\right)\boldsymbol{D}$ is the regularised residual.

Although these methods have been theoretically validated, they did not find their way to practice for a number of reasons: a) they are found to successfully work for a limited number of applications, b) some of them rely on prior knowledge of the noise which cannot be estimated in practice, and c) some of them are expensive to calculate especially in the framework of nonlinear optimisation.

Another useful tool of regularisation or prior information can be implemented in the form of adding constraints to the Tikhonov method. For example, in MIT image reconstruction, negative values in the regularised solution are not admissible since physically negative conductivity elements do not exist. Hence, these negative elements are truncated using the inequality condition:

$$\boldsymbol{\sigma} \geq 0 \quad \text{(non-negativity)} \tag{2.36}$$

In literature, other forms of constraints have been reported, which include monotonicity and convexcity and their inequality formulations are, respectively given by:

$$\boldsymbol{L}_1 \boldsymbol{\sigma} \geq 0 \quad \text{(monotonicity)} \tag{2.37}$$

$$\boldsymbol{L}_2 \boldsymbol{\sigma} \geq 0 \quad \text{(convexcity)} \tag{2.38}$$

where $\boldsymbol{L}_1$ and $\boldsymbol{L}_2$ approximate the first and second derivative operators, respectively. In MIT, non negativity constraining is normally applied. These constraints can also be combined in a matrix $\boldsymbol{C}_t$. Thus, the inequality constrained Tikhonov solution solves the problem:

$$(\boldsymbol{J}^{\mathrm{T}}\boldsymbol{J} + \lambda \boldsymbol{L}^{\mathrm{T}}\boldsymbol{L})\boldsymbol{\sigma} = -\boldsymbol{J}^{\mathrm{T}}\boldsymbol{D} \ -\lambda \boldsymbol{L}^{\mathrm{T}}\boldsymbol{L}\boldsymbol{\sigma}_p \qquad \text{subject to:} \quad \boldsymbol{C}_t\boldsymbol{\sigma} \geq 0 \tag{2.39}$$

The constraints can, of course, be explicitly implemented to other regularisation methods.

2.2.4 Other direct reconstruction methods

Rutishauser [47] suggested a modification to Tikhonov's method for achieving a regularised solution with sharper filter factors. In the standard form case this method amounts to solving the following system of equations:

$$(\boldsymbol{J}^{\mathrm{T}}\boldsymbol{J} + \lambda\boldsymbol{I} + \lambda(\boldsymbol{J}^{\mathrm{T}}\boldsymbol{J} + \lambda\boldsymbol{I})^{-1})\boldsymbol{\sigma} = \boldsymbol{J}^{\mathrm{T}}\boldsymbol{D} \tag{2.40}$$

The corresponding filter factors are:

$$f_i = \frac{\sigma_i^2}{\sigma_i^2 + \lambda + \lambda \big/ \left(\sigma_i^2 + \lambda\right)} \tag{2.41}$$

Beyond the classical 2-norm Tikhonov's method, regularisation in other norms has also been investigated by solving problems of the general form:

$$\min\left\{\left\|(\boldsymbol{D} - \boldsymbol{J\sigma})\right\|_q^2 - \lambda\left\|\boldsymbol{L\sigma}\right\|_p^p\right\} \tag{2.42}$$

where $1 \le q < \infty$ and $1 \le p < \infty$. Regarding the residual norm, the choice $1 \le q \le 2$ is favourable since it leads to an estimation that takes into account possible outliers in the measured data. For the regularisation term, the 1-norm $\left\|\boldsymbol{L\sigma}\right\|_1$ attracted a special attention in applied mathematics for some applications where one is interested in recovering the separation between high contrast materials (e.g. monitoring molten steel flow in pipes and imaging metals). While the Tikhonov 2-norm introduces smoothing a-priori information which penalises extreme variations in material properties (for example conductivities), the 1-norm is found to produce regularised solutions which reveal steep conductivity gradients and even mark discontinuities. The class of methods sharing this characteristic are known as "*edge preserving regularisation methods*". Direct (single step) solutions using these regularisation methods are nonlinear unlike their counterpart Tikhonov method, (see section 5.2 for illustration). An example of a classical method in this range is "total variation (TV)". For a one dimensional continuous $\boldsymbol{\sigma}$, the TV penalty functional is defined as:

$$L_{TV}(\boldsymbol{\sigma}) = \int_0^1 \left|\frac{d\boldsymbol{\sigma}}{dt}\right| dt \tag{2.43}$$

and for a general discrete problem with an object (Ω) in the multidimensional case:

$$L_{TV}(\boldsymbol{\sigma}) = \sum_{i=1}^{n} \left|\nabla\boldsymbol{\sigma}\right| = \left\|\boldsymbol{L}_1\boldsymbol{\sigma}\right\|_1 \tag{2.44}$$

where $\boldsymbol{L}_1$ is a discrete approximation to a 1st order difference operator with each row (*i*) including only two nonzero coefficients, 1 and -1, e.g. row(*i*) = [0 0..1..0 0..-1..0], which occur in the columns corresponding to two adjacent conductivity elements sharing an edge or a facet (*i*). TV regularisation method has been applied in EIT by Borsic [48], ECT by [49, 50], and in MIT [51]. Another edge preserving regularisation method with special features is investigated using MIT in Chapter 5.

A further set of direct nonlinear methods include shape reconstruction algorithms designed to be implemented for specific applications where the values of the materials inside the test object are already known, but their shapes, boundaries and their geometry are unknown. An introduction study to this type of shape reconstruction methods was presented by Kolehmainen *et al* [52], and examples of such methods include the monotonicity method [53], the linear sampling method [54] and the level set technique [55]. The monotonicity method is a pixel based shape reconstruction method which relies in principle on the monotonicity of the mapping function $\boldsymbol{J}:\boldsymbol{\sigma}\rightarrow\boldsymbol{V}$. The method has the merit of being computationally efficient since it involves the computation of the singular values of relatively small matrices. The linear sampling method, which is also a pixel based shape reconstruction technique, shares similar advantages and time complexity as to the monotonicity method in the sense it can be applied for any number of perturbations with different conductivity values, as long as they are separated from each other by the background. In medical imaging, for instance, these methods can be applied for detection and shape reconstruction of anomalies inside approximately homogeneous tissues such as breast tumours. The third method, namely the level set technique, differs from its former counterparts in being an interface reconstruction technique. While being applied for piecewise conductivity distributions, this method seeks to recover the interface between two materials by shrinking the search to a narrow band area surrounding the interface to solve the associated inverse problem. Consequently the method is claimed to be more computationally cheap and able to provide an accurate estimation of the interfaces. This method could be very suitable for applications including two component phases where the goal is to recover the interface between two high contrast smooth regions. Overall, the limitation which could become critical for this class of methods is that they assume the materials and the background are idealistically smooth and their conductivities are known, which cannot be true in practice. For further details on implementation of such methods in ECT, EIT and MIT the reader can also refer to [18].

2.2.5 Iterative methods

For the solution of the discrete MIT ill-posed inverse problem, the application of iterative methods can be favourable than direct methods in two respects:

a) For large scale problems, (i.e. inverse problems involving large number of degrees of freedom) direct methods are not desirable since they lead to the formation of an immense coefficient matrix $\boldsymbol{H} = (\boldsymbol{J}^{\mathrm{T}}\boldsymbol{J} + \lambda \boldsymbol{L}^{\mathrm{T}}\boldsymbol{L})$ that is difficult to store in memory on the one hand, and on the other hand the required inversion $\boldsymbol{H}^{-1}$ is computationally expensive. Iterative methods have been designed to achieve an equivalent solution to that of a direct inversion method, in a way that the explicit formation of the coefficient matrix is avoided, and the algebraic operations do not go beyond matrix vector multiplications with $\boldsymbol{J}$ and $\boldsymbol{J}^{\mathrm{T}}$.

b) Because of the nonlinear relationship between the conductivity and the measurement data, it is almost impossible to find an accurate solution via a direct method. To improve the quality of the image reconstruction, iterative methods are a straightforward option in the framework of nonlinear optimisation. It is important to be aware that iterative schemes devised for nonlinear optimisation are not automatically suited for large scale problems and vice versa, although it is possible to merge both types of iterative schemes to generate specialised optimisation with combined features.

For the iterative methods typically suitable for large scale problems, the methods generally amount to the regularised solution of the problem given by:

$$\min \left\| (\boldsymbol{D} - \boldsymbol{J}\,\boldsymbol{\sigma}) \right\|_2 \qquad \text{subject to:} \qquad \boldsymbol{\sigma} \in K_k \tag{2.45}$$

where K_k is the k-th dimensional subspace and k is the regularisation parameter. One of the classical iterative methods which follows this form (2.45) is the Landweber method commonly applied in ECT [43, 56]. The recursive formulation for the Landweber iterate takes the form:

$$\boldsymbol{\sigma}_{k+1} = \boldsymbol{\sigma}_k + \alpha \boldsymbol{J}^{\mathrm{T}}(\boldsymbol{J}\boldsymbol{\sigma} - \boldsymbol{D}) \tag{2.46}$$

where $\boldsymbol{\sigma}_0$ is the starting vector (often $\boldsymbol{\sigma}_0 = 0$) and the fixed scalar α is the relaxation factor. In this formulation, the Landweber iterate employs only first order derivative information stipulated by the Jacobian $\boldsymbol{J}$, Hence the solution iterate can be computed fast and with low memory accommodation unlike the linearised Tikhonov step where second order information is utilised. Clearly, for large problems with a large number of unknown parameters, this is an advantage. Another observation relates to the fact that the Jacobian $\boldsymbol{J}$ is not updated in the iterative procedure making the Landweber method a purely linear iterative method. For the nonlinear MIT inverse problem, the Landweber method might not be suitable for highly nonlinear problems as in those including complex distributions or high contrast material parameters. Only in cases where the material distribution is simple or low contrast, such method can be produce successful reconstruction. With regard to regularisation, while the Tikhonov method generates a regularised solution by explicitly inserting a penalty functional, Landweber method applies regularisation to the solution in an implicit way. To illustrate this fact, the filter factors associated with the Landweber method can be given by:

$$f_i = 1 - \left(1 - \alpha\sigma_i^2\right)^k \tag{2.47}$$

As can be seen, the iteration k determines the filter factors and thus it plays the role of the regularisation parameter. A critical drawback of the Landweber method is that it usually requires a large number of iterations and hence its convergence characteristics are poor compared to its sister, the CG method described below. In order to improve its convergence quality, the basic Landweber method can be augmented with a projection to give the so called "projected Landweber iteration" written as:

$$\boldsymbol{\sigma}_{k+1} = \boldsymbol{P}\left(\boldsymbol{\sigma}_k + \alpha \boldsymbol{J}^{\mathrm{T}}(\boldsymbol{J\sigma} - \boldsymbol{D})\right) \tag{2.48}$$

where the projection $\boldsymbol{P}$ represents the "hard constraints" by which additional a-priori information about the solution is incorporated in the regularisation such as non-negativity or upper boundary limitation. In addition to ECT, this method has also been applied in MIT for a high contrast application related to imaging process water in oil/gas pipelines by [57]. Unfortunately, results were not encouraging and own observations by the authors concluded not only the method is slow to converge but is not suitable for highly nonlinear problems.

A more sophisticated alternative to the Landweber method is the *Conjugate Gradient* (CG) method, which make use of the conjugate direction [58]. In origin, the method was designed to solve linear systems of equations, but later the method has undergone several modifications to adapt it for nonlinear optimisation, a case which corresponds to the MIT inverse problem. Within these modifications, a great deal of research was devoted to derive robust preconditioners in order to enhance the convergence properties of the method. Overall, the method converges more quickly than the Landweber method and is widely applied in optimisation. In Chapter 4 on the MIT inverse problem, an elaborative description of the method is presented, which leads to an interesting implementation in MIT for large scale biomedical problems.

Let us recall that the regularised solution obtained using either the standard or the generalised Tikhonov formula (2.16), (2.31) assumes the MIT ill-posed problem to be linear. The Tikhonov method can be modified to provide a solution to the nonlinear MIT problem by using a nonlinear iterative process which typically requires an evaluation of a series of linearised Tikhonov steps. Once the initial conductivity vector is estimated, for instance via a direct Tikhonov method, then the nonlinear Tikhonov solution can be obtained after recursively evaluating *k* iterate estimates, $\boldsymbol{\sigma}_k$, using the formula given by:

$$\boldsymbol{\sigma}_{k+1} = \boldsymbol{\sigma}_k + \left(\boldsymbol{J}_k^{\mathrm{T}} \boldsymbol{J}_k + \lambda \boldsymbol{L}^{\mathrm{T}} \boldsymbol{L}\right)^{-1} \boldsymbol{J}_{\mathrm{k}}^{\mathrm{T}} \left(\boldsymbol{D} - \boldsymbol{J}_k \boldsymbol{\sigma}_k\right) \qquad (2.49)$$

This iterative scheme is also known as the “modified Newton Raphson method” or the “Regularised Gauss Newton method”. Workers in the field of tomography found that updating the Jacobian matrix $\boldsymbol{J}_k$ at every iteration for the nonlinear treatment of the MIT problem is very time consuming. This is because the general numerical methods that have been designed so far for the evaluation of the forward problem and hence the computation of the Jacobian require a considerable deal of computation power to generate a solution. Therefore, a fixed Jacobian is usually used from the beginning of the iteration process, and the simulated voltages are simply calculated by multiplying the Jacobian with the current conductivity vector. Hence, equation (2.49) is approximated to

$$\boldsymbol{\sigma}_{k+1} = \boldsymbol{\sigma}_k + \left(\boldsymbol{J}^{\mathrm{T}} \boldsymbol{J} + \lambda \boldsymbol{L}^{\mathrm{T}} \boldsymbol{L}\right)^{-1} \boldsymbol{J}^{\mathrm{T}} \left(\boldsymbol{D} - \boldsymbol{J} \boldsymbol{\sigma}_k\right) \qquad (2.50)$$

In the literature about ill-posed problems, this linear iterative method is called “iterative Tikhonov regularisation” [39]. This method can produce an improved solution to the direct Tikhonov method only if the first estimate is not far from the true (desired) conductivity distribution.

3 Forward problem in Magnetic Induction Tomography

3.1 Introduction

Image reconstruction in MIT constitutes of two computational problems, namely: the forward problem and the inverse problem. In the forward problem a mathematical model of the MIT physical system is constructed. Electromagnetic field equations are applied with specific boundary conditions to calculate the eddy currents in an object of a given conductivity distribution and to determine the induced potentials in the receiver coils or the mutual impedances. These received signals are used in the inverse problem to recover the conductivity distribution inside the object. Image reconstruction still represents a major difficulty to the development of MIT due to the following reasons: a) the loosely termed soft field effect characterising the forward problem where the physical relationship between the conductivity distribution and the received induced voltages is nonlinear [36]; b) the inverse problem is ill-posed and under-determined because of the limited number of independent measurements with respect to the unknown conductivity cells. Therefore, an appropriate treatment suggests that the solution of the conductivity distribution should be obtained using an iterative scheme whereby the forward and inverse problems are re-evaluated for a number of times to find the best fit of the simulated data to the measured physical data. Because the inverse problem is ill-posed, a small error in estimating the induced voltage change in the receiver coils will lead to a large error in predicting the image. Hence, for an accurate MIT reconstruction, a forward model capable of accurately calculating the voltages in the coils is required, especially in applications involving non-homogenous objects with irregular shapes such as the human head.

Analytical methods have been employed to solve the forward problem in MIT (for example [59-61]) but their application is restricted to objects with simple conductivity distributions. Analytical methods may be used for problems with irregular boundaries at least in two dimensions using conformal mapping but such application is far from easy. In the last decade, numerical techniques have been used to solve the eddy current problem in MIT and proved to be efficient for treating objects with complex shapes and interior material distributions. Of these methods, two techniques play a substantial role in computational modelling, namely the finite element method (FEM) and the finite difference method (FDM). FEM has been extensively implemented for solving the partial differential equations in EIT and MIT [62-66]. In this method, the problem domain is discretised into a mesh of irregular tetrahedra (often called finite elements FEs) and the method has the advantage that it is capable of easily modelling curved boundaries of objects by fitting irregular shaped FEs. On the other hand, FDM has also been applied mainly in NDT and MIT [67, 68]. Using the FDM, the problem is meshed with lines parallel to the Cartesian coordinate system, creating a grid of uniform sized voxels. The FDM has the advantage that regular grids can be easily generated. Other methods that have also been employed to model the forward problem in MIT include the boundary element method (BEM) and transmission line matrix method (TLM) ([69-71]). The BEM method is relatively fast and memory efficient compared to FEM or FDM since it discretises only the boundaries and therefore reduces the problem dimension by one. The BEM is however, only suitable for problem domains which consist of a few inhomogeneities. Using integral expressions derived at the interfaces and appropriate boundary conditions magnetic induction measurements can be calculated. In the TLM method, the MIT problem is decomposed into an array of transmission lines and excitation signals are modelled by Gaussian pulses which propagate through the grid. Since MIT systems usually operate at a single frequency, a Fast Fourier Transform (FFT) is required to calculate the sensor induced voltages. In this thesis, the author presents a method based on the FDM which is coined the term “the impedance method” or “the custom forward solver”. This method employs techniques from circuit theory analysis to solve the forward problem.

The forward problem in MIT is an eddy current boundary value problem which is formulated in terms of magnetic vector and scalar potentials. When using FEM to evaluate the forward problem, Biro [72, 73] showed that edge based FEM has advantages over nodal FEM in approximating the magnetic vector potential. In MIT, edge FEM has been implemented by [65, 66, 74] and the eddy current boundary value problem was solved using an $\boldsymbol{A}_r$, $\boldsymbol{A}_r$-$\boldsymbol{V}$ formulation. This means, the electric field in the conductive object is expressed as the sum of the primary magnetic vector potential

$\boldsymbol{A_s}$, the eddy current based magnetic vector potential $\boldsymbol{A_r}$, and the scalar potential $\boldsymbol{V}$. Using this approach the entire problem domain including the conductive target and the surrounding empty space needs to be discretised into finite elements, which usually leads to large system of linear equations. For high conductivity applications (for example molten steel visualisation [51]) one needs to follow this formulation in order to produce a reliable forward model. However, the corresponding computation and memory costs become expensive and a nonlinear iterative image reconstruction of three dimensional objects is far from being practical [11, 75] in real time. In the biomedical field and low conductivity process applications where the conductivity of materials does not exceed a few Siemens per metre, a weakly coupled field approximation can be considered in MIT. The approximation basically ignores the skin effect (i.e. the diffusion effect) by assuming the incident primary magnetic field remains unaffected by the scattered secondary field caused by the eddy currents. Hence, the electric field in the conductive target is described only in terms of the primary vector potential $\boldsymbol{A_s}$ and the scalar potential $\boldsymbol{V}$. In setting the condition for this approximation, Griffiths [2] stated that if the skin depth of the penetrating electromagnetic wave is larger than the dimension of the target, then the measured secondary field is proportional to the operating frequency of the primary field and the conductivity of the target under investigation, i.e. $\Delta\boldsymbol{B}/\boldsymbol{B} \propto \omega(\omega\varepsilon_0\varepsilon_r - \mathrm{j}\sigma)$. Hence, in addition to low conductivity materials, only low frequency excitation signals can be employed for the approximation to be valid since the skin depth is also inversely proportional to the square root of the frequency. In the scope of this thesis the weakly coupled field approximation is implemented in the solution of the eddy current problem. In particular, two low conductivity applications are considered: the first is medical characterized as a low contrast application ($\sigma \le 2\,\mathrm{Sm}^{-1}$ at 10 MHz [26]) and involves imaging stroke in the head. The second is a relatively high contrast case ($\sigma \le 5\,\mathrm{Sm}^{-1}$) and consists of inspecting the water fraction in oil/water pipelines. The assumption is carefully examined via analytical and numerical means. In effect, by means of simulations the range of frequencies over which the approximation is admissible is evaluated in the framework of the medical application.

In literature, the weakly coupled field approximation was implemented by Gencer and Tek [40] who presented a numerical solution of magnetic induction measurements using FEM. Another record of its application can be found in [67, 68] where an iterative method based on the so called "successive over relaxation technique" was employed to solve the forward problem. In the synthesis of the custom forward solver, the approximation is implemented using the impedance method whereby a linear system of equations is assembled and direct inversion is used to evaluate the forward solution. In order to verify the correctness and accuracy of the solver, analytical and numerical solutions of the eddy current problem for simple homogenous objects are employed for comparison. The forward solver is further tested on irregular shaped objects with complex structure and a good example in this respect is a realistic shaped head model. The computational efficiency attained by such solver is benchmarked against that of a commercial FE software package. Following the validation process, the forward solver is used in addition to the commercial FE software and an analytical derived expression to evaluate the sensitivity of a 16 channel MIT system prototype to a stroke, a step which is helpful to examine the required performance of MIT systems as well as the feasibility of stroke detection under predefined system performance criteria.

3.2 Approaches

3.2.1 Finite Element Method

In this section the solution of the eddy current boundary value problem using FEM is considered in the general case where the diffusion effect cannot be ignored. In this case, the problem domain is split into two sub-domains as shown in Figure 3.1. One of which is the non-conducting region Ω_n where a stationary field is assumed and the other is the conducting object Ω_c comprising eddy currents. The $\boldsymbol{A}_r$, $\boldsymbol{A}_r$-$\boldsymbol{V}$ formulation reviewed in [72] employs a reduced magnetic vector potential $\boldsymbol{A}_r$ valid in the entire problem region, a modified scalar potential $\boldsymbol{V}$ applied in the conducting region, and an impressed magnetic vector potential $\boldsymbol{A}_s$ being the field produced by the coils in the infinite space when no material is present.

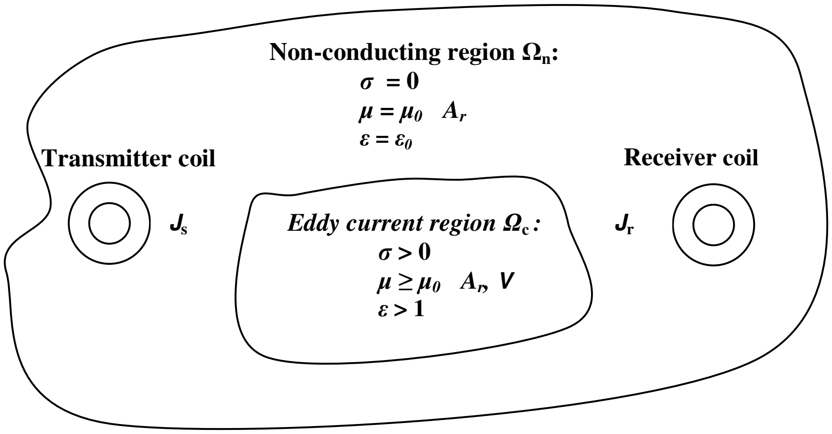

Figure 3.1: Eddy current boundary value problem

Assuming time harmonic fields with an angular frequency ω, we have:

$$\nabla \times \boldsymbol{H} = (\sigma + \mathrm{j}\omega\varepsilon)\boldsymbol{E} + \boldsymbol{J}_\mathrm{s} \ , \tag{3.1}$$

$$\nabla \bullet (\sigma + \mathrm{j}\omega\varepsilon)\boldsymbol{E} = 0 \tag{3.2}$$

where ***H*** and ***E*** are the magnetic field intensity and the electric field intensity. Vector $\boldsymbol{J}_\mathrm{s}$ is the electric current density in the excitation coil and $(\sigma + \mathrm{j}\omega\varepsilon)$ is the complex conductivity distribution in the object. The electric field intensity in the problem domain is described as:

$$\boldsymbol{E} = -\mathrm{j}\omega\boldsymbol{A} - \nabla \boldsymbol{V} \tag{3.3}$$

Biro [76] and Chari [77] suggested expressing the electric scalar potential as a time derivative, similar to the magnetic vector potential in order to introduce symmetry in the derived integral Galerkin equations. Hence equation (3.3) is modified into the following form:

$$\boldsymbol{E} = -\mathrm{j}\omega\boldsymbol{A} - \mathrm{j}\omega\nabla \boldsymbol{V} \tag{3.4}$$

where: $\boldsymbol{A} = \boldsymbol{A}_r + \boldsymbol{A}_s$. Given that: $\boldsymbol{B} = \nabla \times \boldsymbol{A}$ and substituting equation (3.4) into (3.1) and (3.2) we obtain the following equations that model the eddy current boundary value problem in MIT as:

$$\nabla \times (\nu \nabla \times \boldsymbol{A}) + \mathrm{j}\omega\kappa(\boldsymbol{A} + \nabla \boldsymbol{V}) = \boldsymbol{J}_\mathrm{s} \ , \tag{3.5}$$

$$\mathrm{j}\omega\nabla \bullet \kappa(\boldsymbol{A} + \nabla \boldsymbol{V}) = 0 \tag{3.6}$$

where $\nu = 1/\mu$ (μ : magnetic permeability) and $\kappa = \sigma + \mathrm{j}\omega\varepsilon$.

After generating a tetrahedral mesh for the problem domain, edge FEM can be used to solve the eddy current problem described by equations (3.5), (3.6) and appropriate boundary conditions. For first order finite elements, the magnetic vector potential between edge nodes (*i*, *j*) is approximated by an edge basis function $\boldsymbol{N}_{ij}$ given by:

$$\boldsymbol{N}_{ij} = \boldsymbol{L}_i \nabla \boldsymbol{L}_j - \boldsymbol{L}_j \nabla \boldsymbol{L}_i \tag{3.7}$$

where $\boldsymbol{L}_i$, $\boldsymbol{L}_j$ are nodal basis functions. Applying the finite element Galerkin technique using edge basis functions we obtain the following equations:

$$\int_{\Omega} (\nabla \times \boldsymbol{N}\nu \bullet \nabla \times \boldsymbol{A})\, dv + \int_{\Omega_c} (\mathrm{j}\omega\kappa \boldsymbol{N} \bullet (\boldsymbol{A} + \nabla \boldsymbol{V})\, dv = \int_{\Omega_s} (\boldsymbol{N} \bullet \boldsymbol{J}_s)\, dv \tag{3.8}$$

$$\int_{\Omega_c} (\mathrm{j}\omega\kappa \nabla \boldsymbol{L} \bullet (\boldsymbol{A} + \nabla \boldsymbol{V})\, dv = 0 \tag{3.9}$$

where $\boldsymbol{N}$ is any linear combination of edge basis functions, Ω is the entire problem domain, Ω_c is the eddy current region and Ω_s is the current source region. By discretising equations (3.8) and (3.9) a linear system of equations is assembled and solved using suitable numerical technique. The induced voltage (***V***) in the receiver coils can then be evaluated as follows:

$$\boldsymbol{V} = -\mathrm{j}\omega \int_{\Omega_s} (\boldsymbol{A} \bullet \boldsymbol{J}_0)\, \mathrm{d}v \tag{3.10}$$

where $\boldsymbol{J}_0$ is a unit current density applied to the receiver coil.

For further details about the application of edge FEM for solving the eddy current problem in MIT the reader might refer to ([18], [66], [65])

3.2.2 Finite Difference Method

FDM is an alternative numerical technique to FEM. The main difference between the two numerical approaches being that the FDM is used to model the forward problem using regular grids. This is regarded advantageous in the sense that more efficient solvers can be implemented at the expense of the difficulty in accurately representing curved boundaries or smooth interior structures. However, treatment for such problem has been demonstrated in [78] whereby peripheral voxels are trimmed to approximate the exact shape of curved boundaries. In this section the application of the FDM in MIT using the "the successive over relaxation method" is briefly reviewed. For more details [67] provides a fuller description of the method. Furthermore, the derivation will be presented based on the weakly coupled field approximation which neglects the skin effect. This approximation will be rigorously approached later in this chapter. Note when using this approximation only the conductive volume within the scanning region is discretised.

When meshing the problem the object space is divided into cubic voxels with the nodes of the finite difference mesh at the voxel centres. A constant material conductivity κ is assigned to every voxel. The equations describing the current density ($\boldsymbol{J}$) are:

$$\begin{aligned} &\nabla \bullet \boldsymbol{J} = 0 \\ &\boldsymbol{J} = \kappa \boldsymbol{E} \qquad\qquad \kappa = \sigma + \mathrm{j}\omega\varepsilon \\ &\boldsymbol{E} = -\nabla \boldsymbol{V} - \mathrm{j}\omega \boldsymbol{A} \end{aligned} \tag{3.11}$$

Figure 3.2 shows a single cell electrically connected to its six nearest neighbouring cells via an admittance $\boldsymbol{Y}$ and a voltage generator $\boldsymbol{P}$ representing the induced electric field, where:

$$\begin{aligned} &\boldsymbol{Y} = s\,\boldsymbol{\kappa} \\ &\boldsymbol{P} = -\mathrm{j}\omega \boldsymbol{A}\, s \end{aligned} \tag{3.12}$$

and s is the internode spacing.

The scalar potential $\boldsymbol{V}_0$ at the cell node is solved using the successive over relaxation method. In this process the voltage at the node $\boldsymbol{V}_0$ is updated iteratively using knowledge of the potentials at the neighbouring nodes and the connecting impedances and voltage sources. The system of equations is given by:

$$\begin{aligned} &\Delta \boldsymbol{V}_i = \frac{\sum_{i=1}^{6} \boldsymbol{Y}_i \left(\boldsymbol{V}_i + \boldsymbol{P}_i \right)}{\sum_{i=1}^{6} \boldsymbol{Y}_i} - \boldsymbol{V}_0 \\ &\boldsymbol{V}_0' = \boldsymbol{V}_0 + \lambda \Delta \boldsymbol{V}_i \end{aligned} \tag{3.13}$$

where $\boldsymbol{V}_0$ and $\boldsymbol{V}_0'$ are the old and the updated potential values at the cell node and λ is an acceleration factor that determines the rate of convergence.

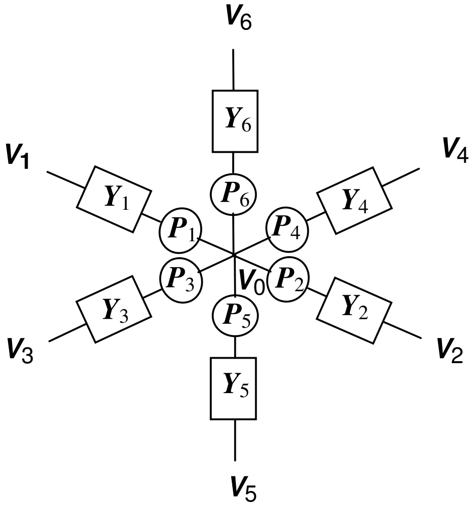

Figure 3.2: Three dimensional cell connected electrically to its six nearest neighbours

The secondary magnetic potential ($\Delta \boldsymbol{A}$) caused by the eddy current flow in the mesh elements .i.e. the branches between adjacent nodes of the conductive object is calculated by:

$$\Delta \boldsymbol{A} = \frac{\mu_0}{4\pi} \int_{\Omega_c} \frac{\boldsymbol{J}}{r} dv \tag{3.14}$$

where r is the distance from the mesh element to the point in space at which the field is calculated. The induced voltage in the receiver coil due to the target ($\Delta \boldsymbol{V}$) is obtained by integrating the secondary magnetic potential around the coil as shown by the equation below:

$$\Delta \boldsymbol{V} = -\mathrm{j}\omega \oint \Delta \boldsymbol{A}.dl \tag{3.15}$$

where dl being defined as an element length within the coil

The same result could be obtained by calculating the secondary magnetic field density using the Biot-Savart law and then carrying out a surface integration over the coil to obtain the induced voltage.

3.3 MIT system and coil sensitivity

In this section, the simulation arrangement used to develop the forward model and calculate the simulated data is based on the Mark 1 which is a 16 channel MIT system made by [79]. As shown in Figure 3.3, the MIT system comprises a cylindrical conductive shield and a circular coil array. The sensor array consists of 16 excitation coils and 16 receiver coils, which are coaxially positioned and arranged in two concentric circles of radii 141.5 mm and 131.5 mm respectively. Each coil is made of two turns of 1 mm thickness copper wire with 50 mm diameter. A cylindrical aluminium screen with diameter 350 mm and height 250 mm surrounds the object space. The screen is intended to shield the system electromagnetically from external interferences and provides a ground termination for the electric field produced by the coils, which reduces the effects of capacitive coupling.

Commercial FE software packages namely Maxwell 3D by Ansoft Corp and COMSOL by Multiphysics have been employed to model the tomography system. There have been some differences in the strategies adopted to model the system efficiently on these software platforms. In Maxwell, the coils have been modelled as cylindrical rings made of stranded copper with an inner diameter of 50 mm and height of 2 mm. A uniform current density has been assigned to the excitation coils. The screen, with 2.5 mm thickness, was simulated using a perfect electrical conducting (PEC) material which does not require FE discretisation. In COMSOL, however, it appeared to be efficient to design the coils as filamentary. The shield was modelled as a cylinder and a magnetic insulation boundary condition was applied. For simulations carried out in this chapter the excitation coil was driven with a unit current for simplicity and the operating frequency was 10 MHz. In order to discretise the problem domain adaptive meshing has been used in Maxwell simulations whereby the finite element mesh is iteratively refined as the field solution converges to a predefined error. This meshing protocol operates by increasing the mesh density in regions with high field strengths and keeping it coarser in other regions where the field is gently perturbed. In COMSOL simulations, the problem domain is directly meshed and mesh refinement tools are provided to increase the resolution in particular sub-domains.

It has been mentioned in section (3.1) that the custom forward problem solver developed by the author employs a weakly coupled field approximation. In this case the eddy current distribution in the object is determined using the primary magnetic vector potential computed in empty space when no material is present. For simulated problems described in this chapter the primary field in the target region is calculated numerically by COMSOL. As we will see in this chapter, there are eddy current problems for which analytical solutions have been derived. For such cases the screen is not modelled, hence a far field boundary condition by considering that the tangential component of the magnetic vector potential ($\hat{\mathbf{n}} \times \boldsymbol{A} = 0$, with normal $\hat{\mathbf{n}}$) vanishes on some larger enclosing surface has been applied.

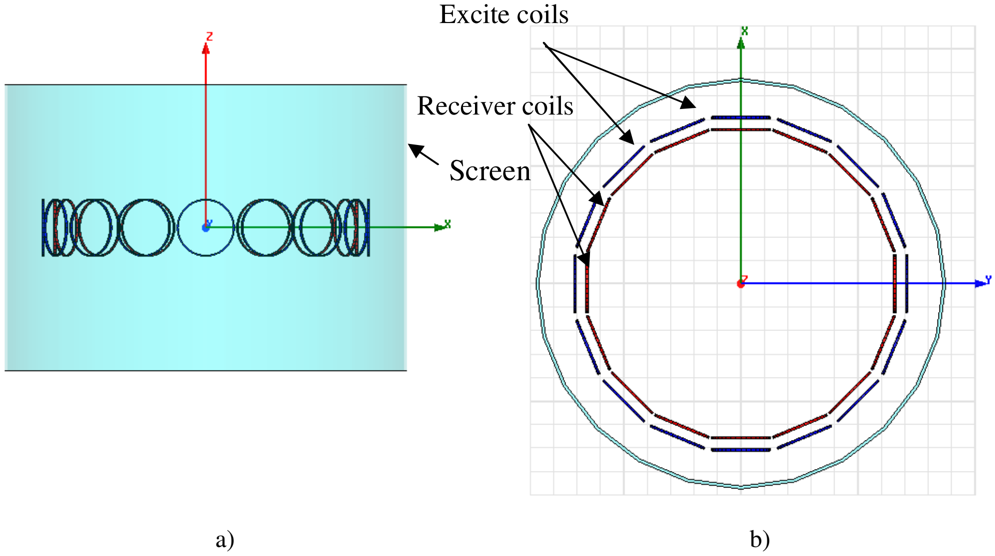

Figure 3.3: Simulated 16 channel MIT system. a) Side view. b) Top view

In addition to simulating the induced voltages by the MIT coil array the spatial sensitivity map has to be determined. In this process, the sensitivity of an excite-detect coil pair to a small change in the conductivity of the object is evaluated. In what follows, the main steps in the derivation of an efficient formula for the sensitivity, which involves only the dot product of the electric fields of the excitation and detection coils, is briefly presented. This formula is used in the thesis to calculate the sensitivity matrix (i.e. the Jacobian) employed in image reconstruction. An elaborate description of the sensitivity analysis in MIT can be found in [80].

The electromagnetic field interaction in MIT is described by Maxwell's equations, which for time harmonic fields with angular frequency ω are given by:

$$\nabla\times\boldsymbol{E} = -\mathrm{j}\omega\mu\boldsymbol{H}, \qquad \nabla\bullet\mu\boldsymbol{H} = 0 \tag{3.16}$$

$$\nabla\times\boldsymbol{H} = \kappa\boldsymbol{E} + \boldsymbol{J}_{\mathrm{S}}, \qquad \nabla\bullet\varepsilon\boldsymbol{E} = 0 \tag{3.17}$$

where $\boldsymbol{H}$ and $\boldsymbol{E}$ are the magnetic field intensity and the electric field intensity. Vector $\boldsymbol{J}_{\mathrm{S}}$ represent the current passing in the excitation coil, κ and ε are respectively the complex conductivity and the permittivity of the object . When combining (3.16) and (3.17) we obtain the equation:

$$\nabla\times\left(\nu\nabla\times\boldsymbol{E}\right) + \mathrm{j}\omega\kappa\boldsymbol{E} = -\mathrm{j}\omega\boldsymbol{J}_{\mathrm{S}} \tag{3.18}$$

Let us assume a small perturbation in the conductivity of the object $\kappa' = \kappa + \delta\kappa$ results in a perturbation of the electric field $\boldsymbol{E}' = \boldsymbol{E} + \delta\boldsymbol{E}$ while the excitation current is held constant. A parameterisation of the sensitivity can be obtained by finding the corresponding linearised change in the voltage induced in the coil. Substituting $\boldsymbol{E}' = \boldsymbol{E} + \delta\boldsymbol{E}$ into equation (3.18) and subtracting from (3.18) while ignoring higher order terms we obtain:

$$\nabla\times\left(\nu\nabla\times\delta\boldsymbol{E}\right) + \mathrm{j}\omega\left(\delta\kappa\boldsymbol{E} + \kappa\delta\boldsymbol{E}\right) = 0 \tag{3.19}$$

Taking the dot product with $\boldsymbol{E}$ gives:

$$\nu\boldsymbol{E}\bullet\nabla\times\left(\nabla\times\delta\boldsymbol{E}\right) + \mathrm{j}\omega\delta\kappa\boldsymbol{E}\bullet\boldsymbol{E} + \mathrm{j}\omega\kappa\boldsymbol{E}\bullet\delta\boldsymbol{E} = 0 \tag{3.20}$$

Using the identity vector:

$$\nabla\bullet\left(\boldsymbol{E}\times\nabla\times\delta\boldsymbol{E}\right) = -\boldsymbol{E}\bullet\nabla\times\nabla\times\delta\boldsymbol{E} + \left(\nabla\times\boldsymbol{E}\right)\bullet\left(\nabla\times\delta\boldsymbol{E}\right) \tag{3.21}$$

Swapping $\boldsymbol{E}$ and $\delta\boldsymbol{E}$ in (3.21) and using equation (3.18) we obtain:

$$\begin{aligned}\nabla\bullet\left(\delta\boldsymbol{E}\times\nabla\times\boldsymbol{E}\right) &= -\delta\boldsymbol{E}\bullet\nabla\times\nabla\times\boldsymbol{E} + \left(\nabla\times\delta\boldsymbol{E}\right)\bullet\left(\nabla\times\boldsymbol{E}\right) \\ &= \mathrm{j}\omega\mu\kappa\delta\boldsymbol{E}\bullet\boldsymbol{E} + \mathrm{j}\omega\mu\delta\boldsymbol{E}\bullet\boldsymbol{J}_{\mathrm{S}} + \left(\nabla\times\delta\boldsymbol{E}\right)\bullet\left(\nabla\times\boldsymbol{E}\right)\end{aligned} \tag{3.22}$$

Subtracting (3.21) from (3.22):

$$\nabla\bullet\left(\delta\boldsymbol{E}\times\nabla\times\boldsymbol{E} - \boldsymbol{E}\times\nabla\times\delta\boldsymbol{E}\right) = \boldsymbol{E}\bullet\nabla\times\nabla\times\delta\boldsymbol{E} + \mathrm{j}\omega\mu\kappa\delta\boldsymbol{E}\bullet\boldsymbol{E} + \mathrm{j}\omega\mu\delta\boldsymbol{E}\bullet\boldsymbol{J}_{\mathrm{S}} \tag{3.23}$$

Assigning the subscripts (1) and (2) which respectively relates to the excitation and detection coil pair to equations (3.23) and (3.20) and using the reciprocity theorem [81]:

$$\nabla \bullet \left(\boldsymbol{E}_1 \times \nabla \times \delta \boldsymbol{E}_2 - \delta \boldsymbol{E}_1 \times \nabla \times \boldsymbol{E}_2 \right) = 0 \tag{3.24}$$

We deduce:

$$\delta \boldsymbol{E}_1 \bullet \boldsymbol{J}_{S2} = \delta \kappa \boldsymbol{E}_1 \bullet \boldsymbol{E}_2 \tag{3.25}$$

Taking the integrand over the domain (Ω) we obtain:

$$\int_{\Omega} \delta \boldsymbol{E}_1 \bullet \boldsymbol{J}_{S2} dv = \int_{\Omega} \delta \kappa \boldsymbol{E}_1 \bullet \boldsymbol{E}_2 dv \tag{3.26}$$

where:

$$\begin{aligned} \int_{\Omega} \delta \boldsymbol{E}_1 \bullet \boldsymbol{J}_{S2} dv &= \int_{\Omega} \delta \boldsymbol{E}_1 dl \bullet \boldsymbol{J}_{S2} da \\ &= \Delta \boldsymbol{V}_2 \, \boldsymbol{I}_2 \end{aligned} \tag{3.27}$$

Therefore the sensitivity of the detection coil (coil 2) to a small change in conductivity is simply the multiplication of the electric field distribution due to the exciter (coil 1) and receiver (coil 2) provided they have been driven with the same current.

3.4 Impedance method

To solve the eddy current problem the impedance method is employed, which effectively treats the test object as an electrical network of passive and active electrical components and uses circuit analysis tools to translate the electromagnetic behaviour of the network into a linear system of equations which is solved to determine the unknown quantities. In fact, the impedance method has previously been implemented for estimation of the induced electric fields in the human body, for example from electronic article surveillance devices and portable appliances as well as from exposure to MRI and magnetic walk through metal detectors [82-85]. However, the impedance method has been implemented in different ways depending on the chosen circuit analysis technique. In what follows, three methods are investigated namely: the branch current method, mesh analysis and nodal analysis. The derivation of each method will be illustrated in accordance with Maxwell’s laws describing the electromagnetic problem.

At the start, the impedance method is devised to compute the eddy currents in a test object modelled as a two dimensional (2D) grid of regular sized pixels. The rationale is to keep the structure fairly simple to facilitate the validation process and the inter-comparison procedure to whichever method can be promoted to solve three dimensional problems. Figure 3.4 shows an example of a grid with $m \times n$ cells, each of which is assigned a constant conductivity value and altogether forming an electrical network of lumped impedances. Each edge impedance is calculated by taking the impedance contributions by the neighbouring cells in parallel. For example, the edge impedance along the x direction of cell (i, j) is given by:

$$Z_x^{i,j} = \frac{\Delta x}{\Delta y\left(\sigma_{i,j} + \sigma_{i,j-1}\right)} \tag{3.28}$$

where $\Delta x = \Delta y$ are the dimensions of the cell in the x, y direction; $\sigma_{i,j}, \sigma_{i,j-1}$ denote the conductivities of the cells sharing the impedance of interest.

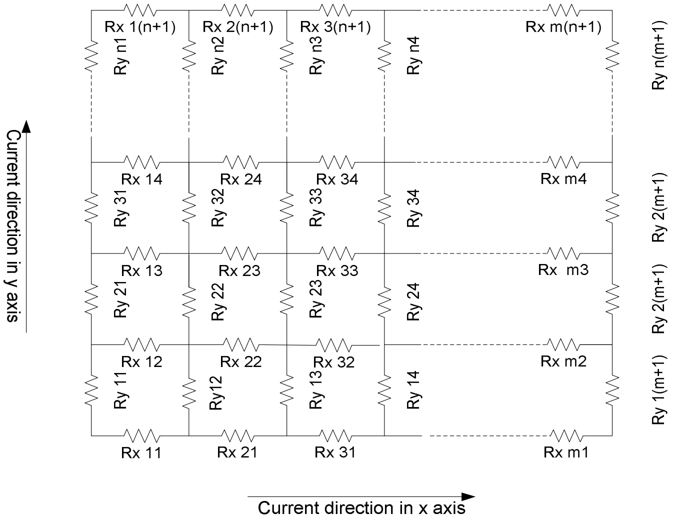

Figure 3.4: *m*×*n* 2D model

In order to test the performance of the impedance method implemented with the three different circuit analysis techniques, the following 2D test samples shown in Figure 3.5, which comprise a **U** shaped object and a circular disc with a homogenous conductivity (σ=1 Sm^{-1}), were modelled. These test samples are assumed to extend to a depth of 1 m in the z direction for current density calculation.

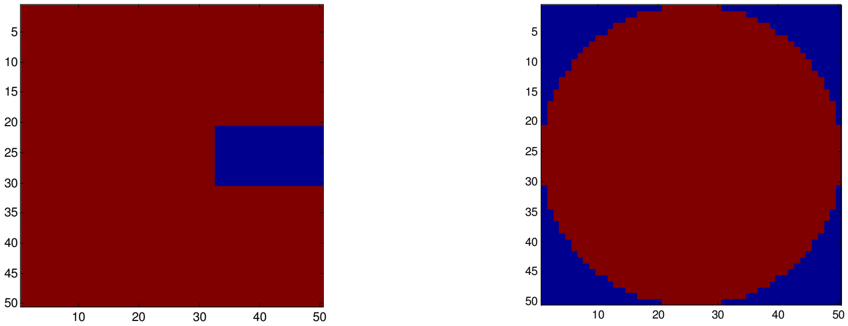

a) b)

Figure 3.5: 2D test models: a) Horse shoe, b) Circular disc

For simulations, the test objects were subject to a uniform time varying alternating magnetic field normal to the plane surface in the z direction ($\boldsymbol{B}_z$) with magnitude of 1 Tesla and angular frequency ($\omega = 2\pi \times 10\,\mathrm{MHz}$). This field distribution can be approximated to that produced by a relatively large coil surrounding the test objects.

3.4.1 Finite Integration Technique

Recalling that the eddy current problem is described by the frequency dependent curl and divergence continuous equations from Maxwell's laws illustrated as follows:

$$\begin{cases} \nabla \times \boldsymbol{E} = -\mathrm{j}\omega\mu_0\boldsymbol{H}, & (\mathrm{a}) \\ \nabla \times \boldsymbol{H} = \boldsymbol{J} + \mathrm{j}\omega\varepsilon\boldsymbol{E}, & (\mathrm{b}) \\ \nabla \bullet \boldsymbol{J} = 0, & (\mathrm{c}) \end{cases} \tag{3.29}$$

where $\boldsymbol{E}$ is the electric field, $\boldsymbol{H}$ is the magnetic field, $\boldsymbol{J}$ is the current density, ε and μ_0 denote the permittivity and the permeability. In order to solve Maxwell's equations on the discretised problems, the impedance method employs the Finite Integration Technique (FIT). FIT is a generalisation of the Finite Difference Time Domain (FDTD) method and is used to transform Maxwell's equations originally expressed in integral continuous form to a discrete form suitable for mapping onto discrete problems [78]. Using (3.29), Maxwell's equations in discrete form, also known as Maxwell's grid equations are obtained below.

$$\begin{cases} \boldsymbol{C}\,\boldsymbol{E} = -\mathrm{j}\omega\mu_0 \boldsymbol{H}, & \text{(a)} \\ \widetilde{\boldsymbol{C}}\,\boldsymbol{H} = \mathrm{j}\omega\varepsilon \boldsymbol{E} + \boldsymbol{J}, & \text{(b)} \\ \boldsymbol{S}\,\boldsymbol{J} = 0, & \text{(c)} \end{cases} \tag{3.30}$$

where $\boldsymbol{E}$, $\boldsymbol{H}$ are integral quantities corresponding respectively to the electric voltage along the pixel edges and the magnetic voltage on the pixel facets. Vector $\boldsymbol{J}$ is the charge current on the edges. The field quantities $\boldsymbol{E}$ and $\boldsymbol{H}$ are mapped on two different grids. These grids are dual to each other. The discrete curl and div operators are described by the coefficient matrices $\boldsymbol{C}$ and $\boldsymbol{S}$ in the grid and by $\widetilde{\boldsymbol{C}}$ in the dual grid.

At an operating frequency of 10 MHz a weakly coupled field approximation can be assumed under quasi-static conditions in which the secondary field due to the skin effect can be ignored. In addition, $\omega\varepsilon$ is sufficiently small so as the displacement currents in the imaginary part of equation (3.30(b)) can also be neglected.

3.4.2 Branch current method

In the branch current method a current is assigned to each branch (edge) of the network (see Figure 3.4). Kirchhoff's voltage law (KVL) equations are written for each closed, independent loop and Kirchhoff's current law (KCL) equations are applied to the minimum number of nodes that will include all the branch currents of the network [86-88]. In theory, KVL and KCL are directly derived from the physical laws described by Maxwell's equations in discrete form, where KVL is a simplification of the Faraday induction law and KCL can be found by taking the divergence of the eddy charge current $\boldsymbol{J}$ induced by the primary magnetic field. Therefore it can be seen that:

$$\begin{cases} \boldsymbol{C}\,\boldsymbol{E} = -\mathrm{j}\omega\mu_0 \boldsymbol{H} & \rightarrow \sum\limits_{facet} \boldsymbol{I}_{branch}\,\boldsymbol{Z} = emf \\ \boldsymbol{S}\,\boldsymbol{J} = 0 & \rightarrow \sum\limits_{node} \boldsymbol{I}_{branch} = 0 \end{cases} \tag{3.31}$$

A linear system of simultaneous equations is assembled in a matrix format as ***XI=Q***, where ***X***, ***I*** and ***Q*** are the impedance matrix, the unknown branch current vector and the vector comprising the results on the right hand side of KVL and KCL equations.

For high resolution grids, the impedance matrix incorporates a high density of zero valued cells which are redundant in the computation procedure and overload the memory storage of the computer. In order to deal with this problem, sparse matrix technique is deployed which effectively stores only the non-zero elements together with their indices and eliminate operations on zero valued elements. The constructed sparse linear system is then solved in MATLAB using direct inversion which employs LU factorization and back-substitution since the impedance matrix is square but non-symmetrical. Subsequently, the current density $\boldsymbol{J}$ is computed for each pixel as two components ($\boldsymbol{J}_x$, $\boldsymbol{J}_y$) relative to the (x, y) Cartesian coordinates system per unit length in the z direction.

The eddy current solution results are presented in Figure 3.6 which visualises the current flow direction in vector notation on the plane surface of the samples. As expected, the eddy currents flow in loops normal to the field orientation and parallel to the excitation current flow in the coil, which agrees with theory. The current magnitude appears to be larger near the periphery due to larger flux coupling.

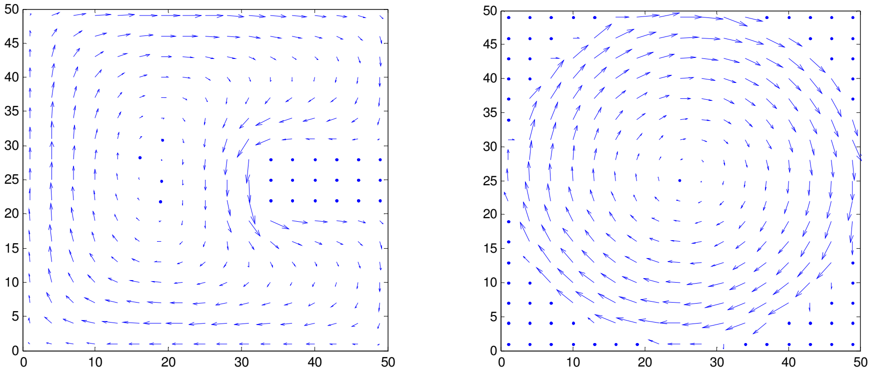

Figure 3.6: Eddy current flow on the 2D test models calculated by the branch current method.

3.4.3 Mesh analysis

The mesh current method, also known as the loop current method, uses the concept of artificial currents which are assigned to the closed loops in the network and configured to circulate according to a user specified uniform direction. These loop currents are solved and their results are then used to determine the real currents in the network branches. In fact, this approach is an optimisation of the branch current method, where the need to substitute the results of KCL into the equations derived from KVL is eliminated. Hence the simultaneous linear system of equations is formed by only applying KVL to every closed loop incorporating an unknown loop current in the network. This systemic approach is computationally efficient compared to the branch current method in the sense that the system comprises less equations and hence less unknown variables. The only drawback is that this circuit analysis technique can only be applied to planar networks with no impedance crossovers. The system of equations $\boldsymbol{XI}=\boldsymbol{Q}$ is written following the formula shown below:

$$\boldsymbol{C}\,\boldsymbol{E} = -\mathrm{j}\omega\mu_0\boldsymbol{H} \rightarrow \sum_{facet}\boldsymbol{I}_{loop}\boldsymbol{Z} = -\mathrm{j}\omega\mu_0\boldsymbol{H} \tag{3.32}$$

The impedance matrix $\boldsymbol{X}$ generated by the mesh analysis is a symmetric, positive definite sparse matrix. In this case, Cholesky factorisation is employed in the inversion process which effectively returns an upper triangular matrix $\boldsymbol{R}$ so that $\boldsymbol{X}= \boldsymbol{R}^{\mathrm{T}}\boldsymbol{R}$, where $\boldsymbol{R}^{\mathrm{T}}$ is the transpose of $\boldsymbol{R}$, and back substitution is used to calculate the loop currents. Subsequently, KCL can be applied to extract the branch currents from the loop currents.

To investigate the mesh analysis performance, the same test procedure was repeated and the eddy currents were computed. As can be seen from Figure 3.7 the eddy currents circulate in the same fashion as observed by the branch current method.

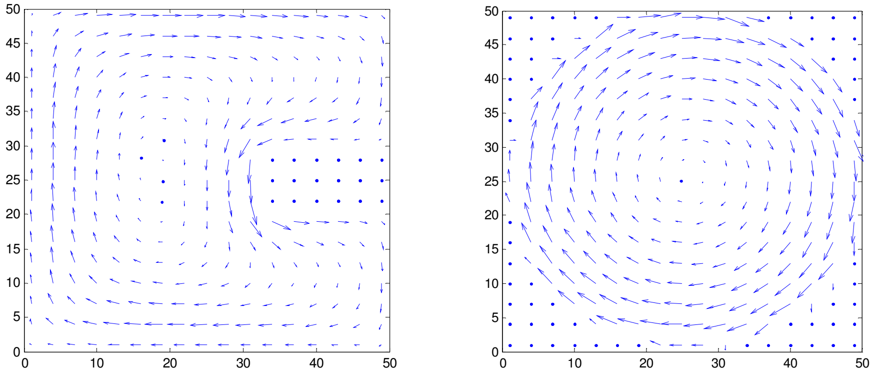

Figure 3.7: Eddy current flow on the 2D test models calculated by the mesh analysis.

3.4.4 Nodal analysis

Another method in circuit theory analysis is nodal analysis which has also been referred to in numerical methods as the scalar potential finite difference (SPFD) method [89, 90]. In contrast to the branch and loop current methods, nodal analysis employs the magnetic vector potential (***A***) as the external applied magnetic field. The electromagnetic problem in MIT is described by Maxwell's equations as illustrated by the system of equations (3.29). Given that: $\boldsymbol{B}=\mu_0\boldsymbol{H}$ and $\nabla\times\boldsymbol{A}=\boldsymbol{B}$ and when substituting the magnetic field density ***B*** by ***A***, equation (a)) becomes:

$$\nabla\times(\boldsymbol{E}+\mathrm{j}\omega\boldsymbol{A})=0 \tag{3.33}$$

which infers that:

$$\boldsymbol{E}=-\nabla\boldsymbol{V}-\mathrm{j}\omega\boldsymbol{A} \tag{3.34}$$

where ***V*** is the electric scalar potential. The Kirchhoff's current equation (c)) is transformed into scalar potential form by substituting the electric field ***E*** from equation (3.34).

$$\nabla\bullet(\sigma\nabla\boldsymbol{V})=\nabla\bullet(-\mathrm{j}\omega\sigma\boldsymbol{A}) \tag{3.35}$$

The resulting differential continuous equation is then mapped onto the 2D electrical network of discrete pixels where ***V*** is now defined at the nodes (i.e. junctions) of the network. As a consequence, the edge current in every branch is expressed in terms of the difference between the nodal voltages associated with the branch and the magnetic vector potential ***A*** that is evaluated half way of the branch length. In a similar fashion to the branch current and loop current methods a linear system of equations is synthesized of the form ***XV*=*P***, where ***X***, ***V*** and ***P*** are the impedance matrix, the unknown nodal voltages and the magnetically induced voltage vector respectively. The system is solved directly using the Cholesky factorization and back-substitution which enables optimized inversion [91]. Once the nodal voltages are determined, Ohm's law is applied to compute the current density (***J***) for each pixel.

The same simulations made in the previous sections were carried out with nodal analysis. In order to produce a uniform magnetic field with a density of 1 Tesla, the ***A*** field was chosen to vary according to the function $\boldsymbol{A}(x)=0.5x+1$; $\boldsymbol{A}(y)=0.5\mathrm{y}+1$, where $\boldsymbol{A}(x)$ and $\boldsymbol{A}(y)$ are the ***A*** field components in the $(x,\ y)$ coordinate system.

Figure 3.8 below depicts the current flow direction on the two test planes, which appears to agree with the results from the previous applied circuit theory methods.

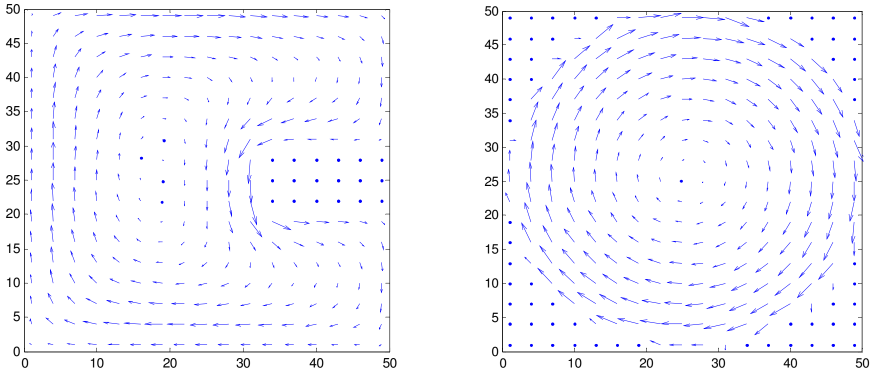

Figure 3.8: Eddy current flow on the 2D test models calculated by the nodal analysis

In summary, this section has described the solution of the eddy current problem in MIT, which involves the coupling between the excitation source and the target. The solution was demonstrated by means of the impedance method. Circuit analysis tools including the branch current method, mesh analysis and nodal analysis were introduced and their correlation with electromagnetic field principles describing the MIT problem was illustrated. Eddy current simulations were presented using 2D samples to test the performance of the algorithms which appear to produce similar results. As noted in section (3.4.3) the mesh analysis method applies only to planar networks. Hence in the following sections, where mainly 3D eddy current problems are considered, work continues with the impedance method based on the branch current and the nodal analysis techniques

3.5 Evaluation with analytical and numerical methods

The impedance method based on the branch current and nodal analysis techniques have been extended to solve 3D eddy current problems. In order to evaluate the method a test problem was devised, which seeks to determine the eddy current density in a sphere with homogenous conductivity distribution and subject to magnetic field from a circular filamentary coil of 50 mm diameter. The coil is positioned so it is symmetrical about the z axis and is 141.5 mm away from the origin. These dimensions were chosen to conform to the 16 channel MIT system specifications elaborated in section (3.3). The model schematic is shown in Figure 3.9 including a sphere of 60 mm radius, conductivity ($\sigma =$ 1Sm^{-1}) and permeability ($\mu = \mu_0$, air). Unit current excitation was passed around the coil and the operating frequency was set to 10 MHz. The solution of the eddy current problem was first generated by the impedance method.

In order to test the eddy current results, the same problem was re-evaluated using analytical and numerical methods. For the analytical case, equation (3.36) given below describes the electric field in the conducting sphere [92]. Due to the geometrical homogeneity of the sphere and symmetry of the coil arrangement only the φ component of the electric field is used among the spherical coordinates (r, θ, φ).

$$\boldsymbol{E}_{\varphi}\left(r,\theta\right)=\frac{j\omega\mu_0 I_0 r_0 \sin\theta_0}{\sqrt{ar}}\sum_{n=1}^{\infty}\frac{I_{n+1/2}\left(\alpha r\right)}{\alpha a I_{n-1/2}\left(\alpha a\right)}\left(\frac{a}{r_0}\right)^{n+1}\boldsymbol{\Theta}_n\left(\theta\right)\boldsymbol{\Theta}_n\left(\theta_0\right) \tag{3.36}$$

where μ_0 is the permeability of free space, (r_0, θ_0) are the coordinates specifying the coil position, a is the sphere radius, $\alpha = \left(1+\mathrm{j}\right)\sqrt{\omega\mu\sigma/2}$. Here, $I_{n+1/2}(\alpha r)$ are modified Bessel functions of the first kind with order (n+1/2) and $\boldsymbol{\Theta}_n\left(\theta\right)$ are the associated Legendre polynomials. I_0 is the excitation current and ($r_0 \sin\theta_0$) is the radius of the coil. For conductivity of 1 Sm^{-1} the current density $\boldsymbol{J}_{\varphi}$ and the electric field $\boldsymbol{E}_{\varphi}$ are equated according to the definition: $\boldsymbol{J}_{\varphi} = \sigma \boldsymbol{E}_{\varphi}$.

For numerical simulations Maxwell, COMSOL and TLM were used. The first two solvers account for the skin effect and displacement currents in the solution process. On the other hand, TLM solves the full wave Maxwell's equations including wave propagation effects and is also intended to reflect the impact of the wave propagation assumption on measurements. For simulation results, Figure 3.10 depicts a map of the eddy current density distribution on the (x, z) plane. The eddy currents appear to be stronger in general near the periphery of the sphere and notably in the upper half close to the excitation. We also notice the symmetry of the eddy current distribution around the coil axis which can be explained by the symmetry of the problem.

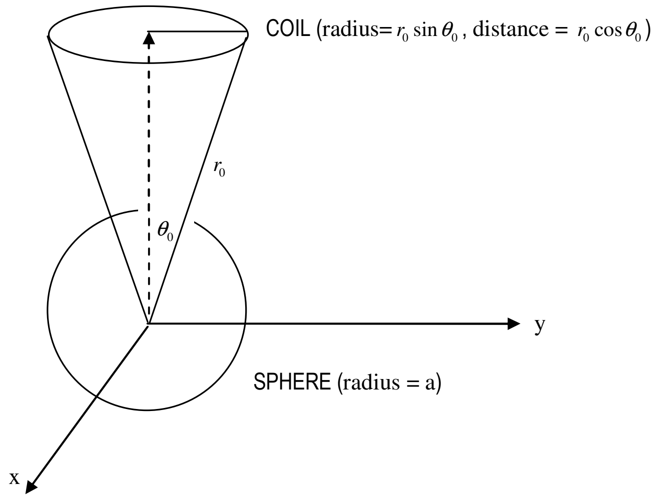

Figure 3.9: Model schematic for eddy current simulation

Figure 3.11 plots the current density as calculated by the different solvers against the angle θ along the periphery of the sphere. As can be seen, the results show a very good agreement between the solvers. A small mismatch can be identified about $\theta = 40^0$ where the eddy current flow exhibits a peak magnitude. This may be attributed to the discrepancy in the meshing mechanism adopted by the solvers based on either tetrahedra FEs or voxels. Figure 3.12 also shows the eddy current distribution along the *y* axis computed by the solvers. In addition to the quality of agreement, the eddy current flow conforms to the theory with stronger eddy currents circulating near the periphery of the sphere.

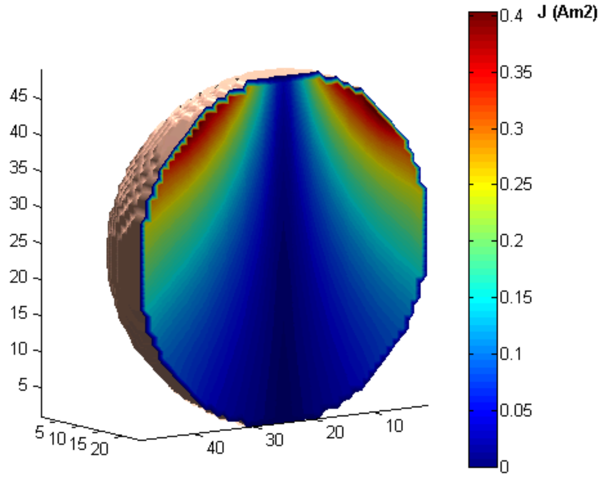

Figure 3.10: Map of the eddy current distribution on the (*x*, *z*) plane

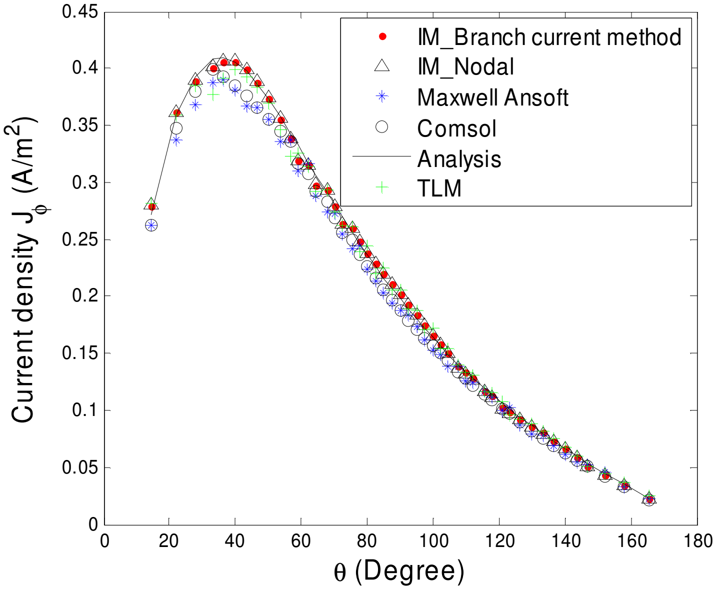

Figure 3.11: Eddy current on the surface as a function of θ

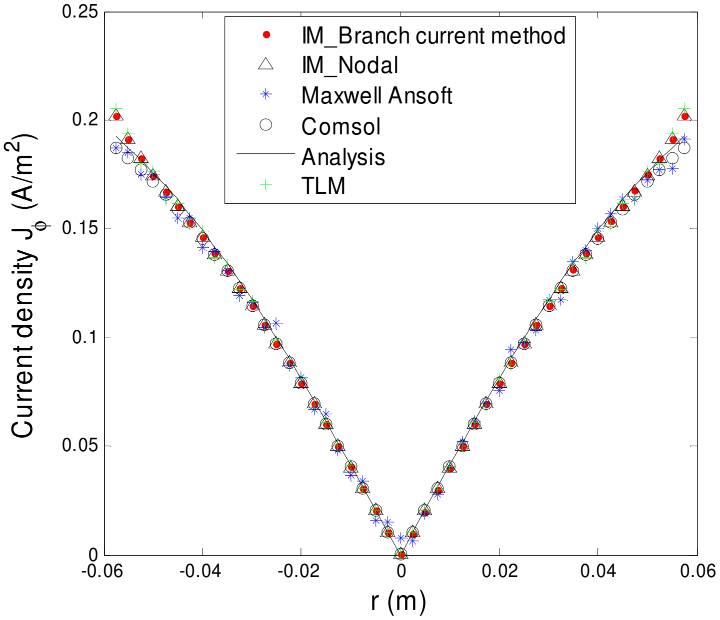

Figure 3.12: Eddy current along the x axis as a function of r. (y=0, z=0)

3.6 Weakly coupled field approximation in MIT forward solution

This section focuses on evaluating the impact of the weakly coupled field approximation (i.e. neglecting the skin effect) in the solution of the MIT forward problem. The investigation will be divided in two stages. In the first part, a theoretical analysis of the approximation is presented using an analytical expression derived from full wave theory for an impedance change in a coil pair near an infinitely large flat conductor. This expression is used to quantify the error due to the approximation for a range of radio frequencies ($f \leq 10\text{MHz}$) [93]. In addition, the work purposely seeks the highest frequency based upon a nominal allowable error margin of 1%. This frequency figure is desirable for image reconstruction in order to increase the magnitude of eddy current based induced voltage above systematic noise levels. In the second part of this investigation numerical tools are employed where frequencies within the specified range are then used with the impedance method and the error is re-evaluated against a commercial FE solver (COMSOL) for a range of conductivities related to biological tissues.

3.6.1 Theoretical analysis

In this theoretical analysis two integral expressions for the impedance change of a coil pair due to a target are presented for the simple model shown in Figure 3.13. The magnetic induction set up includes a coaxial excitation and detection coil pair which are modelled as circular and filamentary, and a conductive non-magnetic plate that is infinitely large and parallel to the coil surface. For the analysis of the weakly coupled field approximation, one analytical expression is derived to calculate the induced mutual impedance change in the coil pair when such approximation is considered, whereas the second expression takes into account the skin effect in the solution. The results are compared and the corresponding error is quantified.

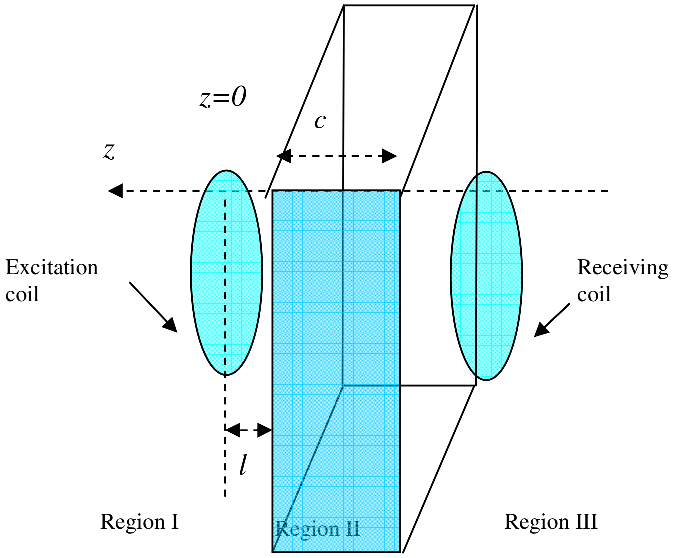

Figure 3.13: Simplified MIT model for evaluating the skin effect

The solution to the problem starts with the diffusion equation which describes the behaviour of the vector potential ($\boldsymbol{A}$) in an isotropic, linear and inhomogeneous object due to an applied current density J_0 as given by [15]:

$$\nabla^2 \boldsymbol{A} = -\mu \boldsymbol{J}_0 + \mu\sigma \frac{\mathrm{d}\boldsymbol{A}}{\mathrm{d}t} + \mu\varepsilon \frac{\mathrm{d}^2\boldsymbol{A}}{\mathrm{d}t^2} + \mu\nabla\left(1/\mu \right)\times(\nabla\times\boldsymbol{A}) \tag{3.37}$$

where, σ, ε and μ are the conductivity, permittivity and permeability of the medium respectively. For operating frequencies below 10 MHz, $\mu\varepsilon\,\mathrm{d}^2\boldsymbol{A}/\mathrm{d}t^2$ is much smaller than $\mu\sigma\,\mathrm{d}\boldsymbol{A}/\mathrm{d}t$ and thus can be ignored.

Solution of the differential equation yields integral equations of the magnetic vector potential in the regions I, II, and III which are shown in Figure 3.13. The magnetic vector potential in each region is expressed as follows:

$$\begin{aligned}\boldsymbol{A}^{(1)}(r,z) = {} & \frac{\mu_0 I_0 r_0}{2}\int_0^\infty I_1(\alpha r_0)\cdot I_1(\alpha r)e^{-\alpha_0|l-z|}\frac{\alpha d\alpha}{\alpha_0} \\ & +\frac{\mu_0 I r_0}{2}\int_0^\infty I_1(\alpha r_0) I_1(\alpha r)e^{-(\alpha_0 l+\alpha_0 z)}\cdot \\ & \frac{(\alpha_0+\alpha_1)(\alpha_1-\alpha_2)+(\alpha_0-\alpha_1)(\alpha_1+\alpha_2)e^{2\alpha_1 c}}{(\alpha_0-\alpha_1)(\alpha_1-\alpha_2)+(\alpha_0+\alpha_1)(\alpha_1+\alpha_2)e^{2\alpha_1 c}}\frac{\alpha d\alpha}{\alpha_0}\end{aligned} \tag{3.38}$$

$$\boldsymbol{A}^{(2)}(r,z)=\mu_0 I_0 r_0\int_0^{\infty} I_1(\alpha r_0)I_1(\alpha r)e^{-\alpha_0 l}\alpha \frac{(\alpha_1+\alpha_2)e^{2\alpha_1 c}e^{\alpha_1 z}+(\alpha_1-\alpha_2)e^{-\alpha_1 z}}{(\alpha_0-\alpha_1)(\alpha_1-\alpha_2)+(\alpha_0+\alpha_1)(\alpha_1+\alpha_2)e^{2\alpha_1 c}}\frac{\alpha d\alpha}{\alpha_0} \tag{3.39}$$

$$\boldsymbol{A}^{(3)}(r,z)=\mu_0 I_0 r_0\int_0^{\infty} I_1(\alpha r_0)I_1(\alpha r)e^{-\alpha_0 l}\alpha \frac{2\alpha_1 e^{(\alpha_1+\alpha_2)c}e^{\alpha_2 z}}{(\alpha_0-\alpha_1)(\alpha_1-\alpha_2)+(\alpha_0+\alpha_1)(\alpha_1+\alpha_2)e^{2\alpha_1 c}}\frac{\alpha d\alpha}{\alpha_0} \tag{3.40}$$

where μ_0 is the permeability of free space, l denotes the distance of the coil to the parallel plate surface; and c characterizes the thickness of the plate. $\alpha_0=\alpha$, $\alpha_1=\sqrt{\alpha^2+j\sigma\mu_1\omega}$, $\alpha_2=\alpha$. $I_1(x)$ is a first order Bessel function of the first kind. I_0 is the excitation current and r_0 is the radius of the coils. The induced mutual impedance in the receiver coil in the presence of the object is given by:

$$\boldsymbol{Z}=\mathrm{j}\omega 2\pi r_0^{\,2}\mu_0\int_0^{\infty} I_1(\alpha r_0)I_1(\alpha r_0)e^{-\alpha_0 l}\alpha \frac{2\alpha_1 e^{(\alpha_1+\alpha_2)c}e^{\alpha_2 z}}{(\alpha_0-\alpha_1)(\alpha_1-\alpha_2)+(\alpha_0+\alpha_1)(\alpha_1+\alpha_2)e^{2\alpha_1 c}}\frac{\alpha d\alpha}{\alpha_0} \tag{3.41}$$

Whereas in empty space the mutual impedance of the coil channel is:

$$\boldsymbol{Z}_{air}=\mathrm{j}\omega 2\pi r_0^{\,2}\mu_0\int_0^{\infty} I_1(\alpha r_0)I_1(\alpha r_0)e^{-\alpha_0 l}\alpha\frac{e^{\alpha_0 z}}{2\alpha_0}\frac{\alpha d\alpha}{\alpha_0} \tag{3.42}$$

Hence the change in the mutual impedance due to the conducting plate is obtained by simply taking the difference between equations (3.41) and (3.42):

$$\Delta\boldsymbol{Z}=\mathrm{j}\omega 2\pi r_0^{\,2}\mu_0\int_0^{\infty} I_1(\alpha r_0)I_1(\alpha r_0)e^{-\alpha_0 l}\alpha \left(\frac{2\alpha_1 e^{(\alpha_1+\alpha_2)c}e^{\alpha_2 z}}{(\alpha_0-\alpha_1)(\alpha_1-\alpha_2)+(\alpha_0+\alpha_1)(\alpha_1+\alpha_2)e^{2\alpha_1 c}}-\frac{e^{\alpha_0 z}}{2\alpha_0}\right)\frac{\alpha d\alpha}{\alpha_0} \tag{3.43}$$

Now, the weakly coupled field approximation which is also referenced as the Born or the low diffusion approximation is applied. Considering the fact that in the low frequency limit $\sigma\mu_0\omega$ is infinitely small and $\alpha_1=\sqrt{\alpha^2+\mathrm{j}\sigma\mu_0\omega}$ can be approximated as: $\alpha_1=\alpha_0+\mathrm{j}\sigma\mu_0\omega/2\alpha_0$ equation (3.43) simplifies to:

$$
\begin{aligned}
\widetilde{\Delta \mathbf{Z}} &= \mathrm{j}\omega 2\pi r_0^{\ 2}\mu_0 \int_0^\infty I_1(\alpha r_0) I_1(\alpha r_0) e^{-\alpha_0 l} \alpha [-\mathrm{j}\frac{\omega\sigma c\mu_0}{8\alpha^3{}_0}] \frac{\alpha d\alpha}{\alpha_0} \\
&= \omega^2 \sigma c 2\pi r_0^{\ 2}\mu_0 \int_0^\infty I_1(\alpha r_0) I_1(\alpha r_0) e^{-\alpha_0 l} \alpha \frac{\mu_0}{8\alpha^3{}_0} \frac{\alpha d\alpha}{\alpha_0}
\end{aligned} \tag{3.44}
$$

In the simulations, the coil dimensions and current excitation were set according to the MIT system specification described in section (3.3), (i.e. the coil diameter was set to 50 mm, the exciter and receiver coils are 141.5 mm away from the origin and a unit current is passed in the exciter coil). The conductive plate thickness *c* was selected to be 140 mm.

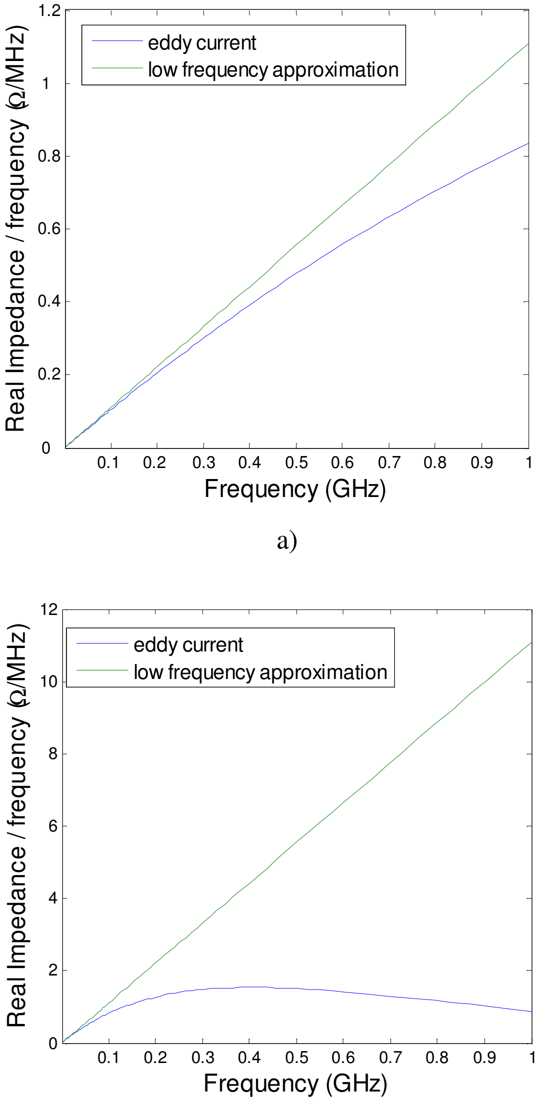

a)

b)

Figure 3.14: The mutual impedance between the excitation and the detection coil at different frequencies for saline solutions (a) $\sigma = 0.01$ Sm^{-1}; (b) $\sigma = 0.1$ Sm^{-1}; using solutions (1) and (2)

Figure 3.14 shows the change in the mutual impedance of the excite-detect coil pair due to the object once by taking into account the skin effect (solution (1)) and the other by assuming the low diffusion approximation (solution (2)). As the frequency increases the mutual impedance measurements from solution (1) deviate progressively from those of solution (2) which exhibit a linear relationship with frequency. In addition, as the object conductivity rises from $\sigma = 0.01$ to $\sigma = 0.1$ Sm^{-1} the skin effect becomes more pronounced.

In order to define the highest frequency at which the skin effect can reasonably be ignored, the plate conductivity was allowed to take values up to 1 Sm^{-1}. For each conductivity co-ordinate, the corresponding frequency was selected so as the error between solutions (1) and (2) is 1 %. From Figure 3.15 it can be seen that at an operating frequency of 1MHz, the saline conductivity of the homogenous plate is 1Sm^{-1}, whereas at 10 MHz the conductivity of the plate drops to 0.1 Sm^{-1}. However, since most biological tissues are well below 1 Sm^{-1} according to [26] and the analysis considered here imposes an exaggerating geometrical definition which considers the plate to be infinitely large, hence we feel comfortable extending the range of acceptable frequencies up to 10 MHz at which the approximation can be valid, expecting the error will reduce with a finite volume object as will be shown in the following section.

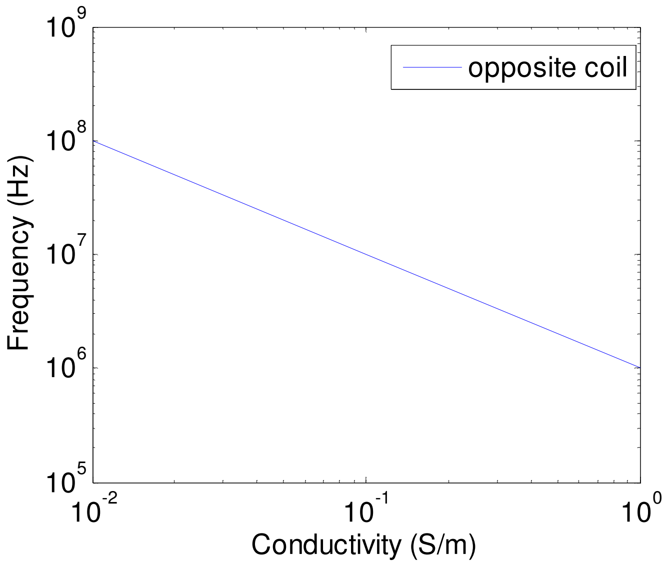

Figure 3.15: Frequency versus conductivity with the error due to ignoring skin effects is 10%

3.6.2 Numerical analysis

In section (3.4) the branch current and the nodal analysis methods have been described as circuit analysis tools that can be used to synthesise the impedance method for solution of 3D electromagnetic problems. It was also noted that the nodal analysis method is superior to the branch current method since for the same problem it requires far less equations and produces a symmetrical linear system of equations that can be solved efficiently. Hence in the following numerical simulations the impedance method is developed based on nodal analysis.

In the numerical analysis of the weakly coupled field approximation, the multi-channel MIT set up (Mark 1) depicted in Figure 3.16 (a) was modelled in COMSOL. The model consists of an array of excitation and detection coils, a screening shield and a conductive rectangular object. The dimensions and current excitation of a single channel are similar to those of the analytical model illustrated in the previous section (3.6.1). Here, the electromagnetic field problem is numerically solved by COMSOL and the impedance method for three different coil combinations namely, adjacent, orthogonal, and the opposite cases as shown in Figure 3.16 (b) to examine the weakly coupled field approximation adopted by the impedance method solution at different sensor channels since MIT requires multiple sensor pick ups for image reconstruction. In order to calculate the induced voltages in the receiver coils due to the target using the impedance method, the tangential component of the secondary magnetic vector potential ($\Delta \boldsymbol{A}$) is integrated around the coil as expressed by equation (3.45), where $\Delta \boldsymbol{A}$ is calculated using the Biot-Savart law in discrete form by integrating $\boldsymbol{J}$ over the conductive object volume Ω as displayed by equation (3.46)

$$\Delta \boldsymbol{V} = -\mathrm{j}\omega \oint \Delta \boldsymbol{A}.dl \tag{3.45}$$

$$\Delta \boldsymbol{A} = \frac{\mu_0}{4\pi} \sum_{n=1}^{\Omega_c} \frac{\boldsymbol{J}_n}{r_n} \tag{3.46}$$

where $\boldsymbol{J}_n$ is the current density calculated at the centre of voxel (n) and r_n is the distance between the corresponding voxel centre and the elemental length dl of the coil . The skin effect error is estimated from the two solutions for each coil pair at two frequencies namely, 10 MHz and 1 MHz. For the impedance method, the object was discretised into 44×28×42 cubic voxels with 5 mm^3 resolution. The object was assigned a range of conductivities up 2 Sm^{-1} similar to those encountered in biological tissues.

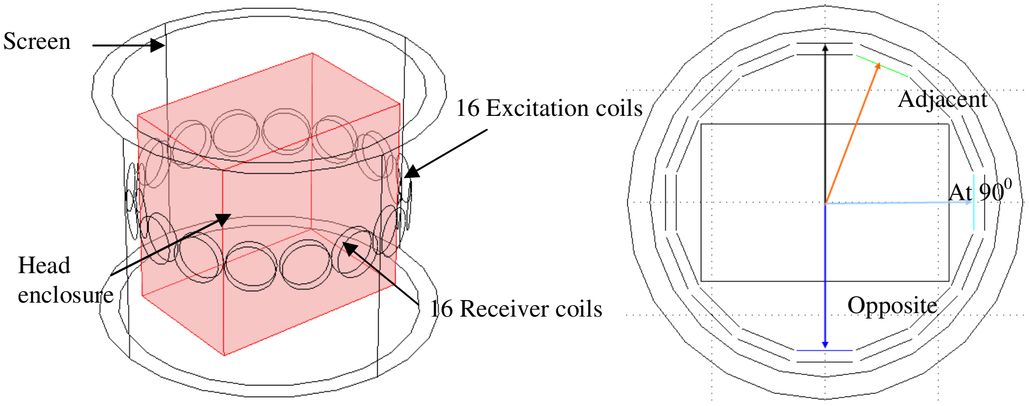

a) b)

Figure 3.16: a) 16 channel MIT system with conductive box. b) Coil combinations

Figure 3.17 (a) and (b) show the error due to neglecting the skin effect in the impedance method by comparing the induced voltage measurements against COMSOL. The simulated measurements were computed at frequencies 10 MHz and 1MHz for three coil combinations. As can be seen, for conductivities below 2 Sm^{-1} the largest error at 10 MHz is recorded for the opposite coil with 6 %, where the field is assumed to interact with a greater volume of the object making the case most prone to the diffusion effect. However, in the anatomical structure of the head, it is only the cerebral spinal fluid (CSF) whose conductivity is 2 Sm^{-1} and it is represented with a very thin layer, whereas all other tissues which occupy a substantial volume of the head including the white and grey matter, muscle corresponding conductivities do not exceed 0.5 Sm^{-1} at 10 MHz [26]. Taking this into account, the worst skin effect error at 10 MHz for the opposite coil does not exceed 0.4 % as illustrated by Figure 3.17 (a). Image reconstruction using MIT in medical applications can be done differentially since all conductivities of all biological tissues exhibit frequency dependency. Since 10 MHz has been proven to be about the upper limit for such approximation, the skin effect error was evaluated at another lower frequency 1 MHz. In this case, Figure 3.17 (b) shows the error in the extreme case is about 0.1 % when the whole volume of the target is considered to have a conductivity of 2 Sm^{-1}.

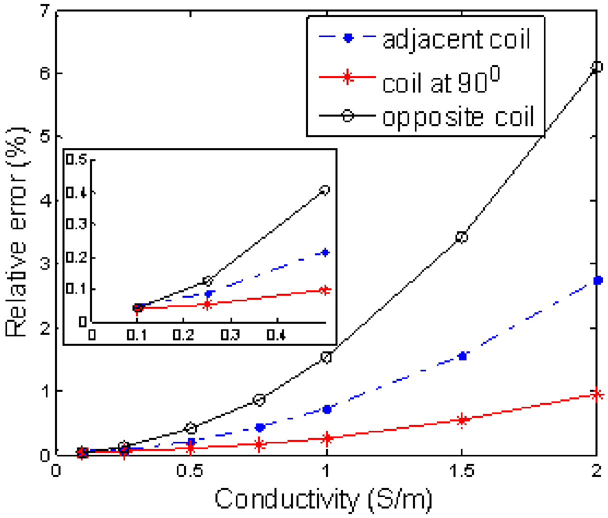

a)

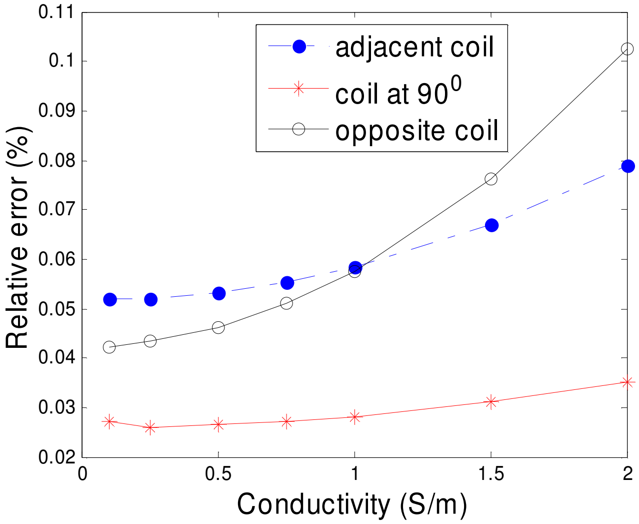

b)

Figure 3.17: Plot of the error due to neglecting the skin effect between the Impedance method and COMSOL at the adjacent, perpendicular and the opposite coils at a) 10MHz, b) 1MHz

3.7 Eddy current simulations with realistic head model

Biomedical MIT is an important area where the application of the custom forward solver employing the impedance method and the weakly coupled field approximation can be suitable, since all biological tissues belong to the low conductivity range. In this section the operation of the custom forward solver is tested on an irregular shaped phantom with a complex structure represented with a realistic head model. A set of simulations is performed to examine the changes in eddy current distribution when a stroke is included inside the brain. The forward solution is used to examine the sensitivity of a single MIT channel to the position of stroke. The gain in the computational power saving achieved with the custom forward solver is also investigated against COMSOL.

3.7.1 Computational experiments

An anatomically realistic multilayer head model was used to test the functionality of the custom forward solver. The FE meshed head model (supplied courtesy of Holder *et al*) was originally developed from segmented Magnetic Resonance (MR) data [94] and has been used for several EIT studies related to cerebral stroke and neurological imaging [95-98]. The head model comprised scalp, skull, CSF, grey matter, white matter, ventricles, spinal cord, eyes, optic nerves, and ear canals and nasal cavity. The head FE mesh consisted of 53,336 tetrahedra, where each tetrahedron was assigned one of the mentioned tissue types, and every tissue type was designated with its corresponding electrical conductivity (see Table 1-1). The dielectric properties of tissues were sourced from measurements in [26]. The FE mesh was then converted into a cubic mesh suitable for the impedance method with a resolution of 3.5 mm^3 and mapped into a rectangular enclosure with dimensions of 62×45×63 voxels.

Figure 3.18 (a, b and c) shows a 3D view of the head model with a cutaway plane displaying the conductivity distribution for the head with the following pathological cases:

a) Healthy head: with normal tissues

b) External intraparenchymal haemorrhage: a large stroke occupying a spherical region in the periphery of the left hemisphere of the brain and affecting the grey and white matter. 75 % of its volume consists of blood.

c) Internal intraparenchymal haemorrhage: a small spherical stroke in the inner part of the brain falling in the white matter with bleeding taking up three quarters of the volume.

The stroke is modelled by altering the conductivity of the affected tissue (grey and/or white matter) to account for the conductivity of the invasive blood which is 1.097Sm^{-1}

at frequency of 10 MHz.

In order to test the performance of the custom electromagnetic solver the following simulations have been devised:

a) The head model was exposed to a time varying sinusoidal magnetic field generated by driving a single coil of the MIT system depicted in Figure 3.16 (a) with a unit current. The induced eddy currents in a healthy head and a head with large stroke volumes were calculated and corresponding eddy current flow maps on coronal and sagittal planes of the head were produced.

b) The sensitivity of a single MIT measurement channel to the cerebral stroke was examined. In doing this, an internal small stroke (Figure 3.18 (c)) was moved horizontally parallel to the co-ordinate y axis towards the periphery in steps of 3.5 mm. The induced voltage change ($\Delta \boldsymbol{V}$) due to the head as function of the stroke position was examined.

c) The gain in the computational power saving was tested for this forward problem solver. A test object consisting of a simplified head modelled as a multi-shell sphere with layered tissue conductivities was solved both with COMSOL and our custom forward solver. Using this latter, the head was meshed to a fine resolution of 2 mm^2 as encountered in medical applications quantifying for 260k conductive tissue cells. This results in about 280k unknown voltage nodes or degrees of freedom (DoF's) to be solved using direct inversion. In COMSOL, the AC/DC module was used which ignores the propagation effects, but still accounts for the skin effect, and hence requires a full meshing of the problem including the head, the MIT system, and the problem region. The entire problem was discretised into 160k quadratic tetrahedra, which amount to 1013k DoFs, but for the sake of comparison, the head was allocated 46k elements yielding a comparable number of DoFs to the impedance method. Boundary conditions were set so as to magnetically isolate the problem region from external interferences. The problem was solved both directly and iteratively with a stopping tolerance of 10^{-6}.

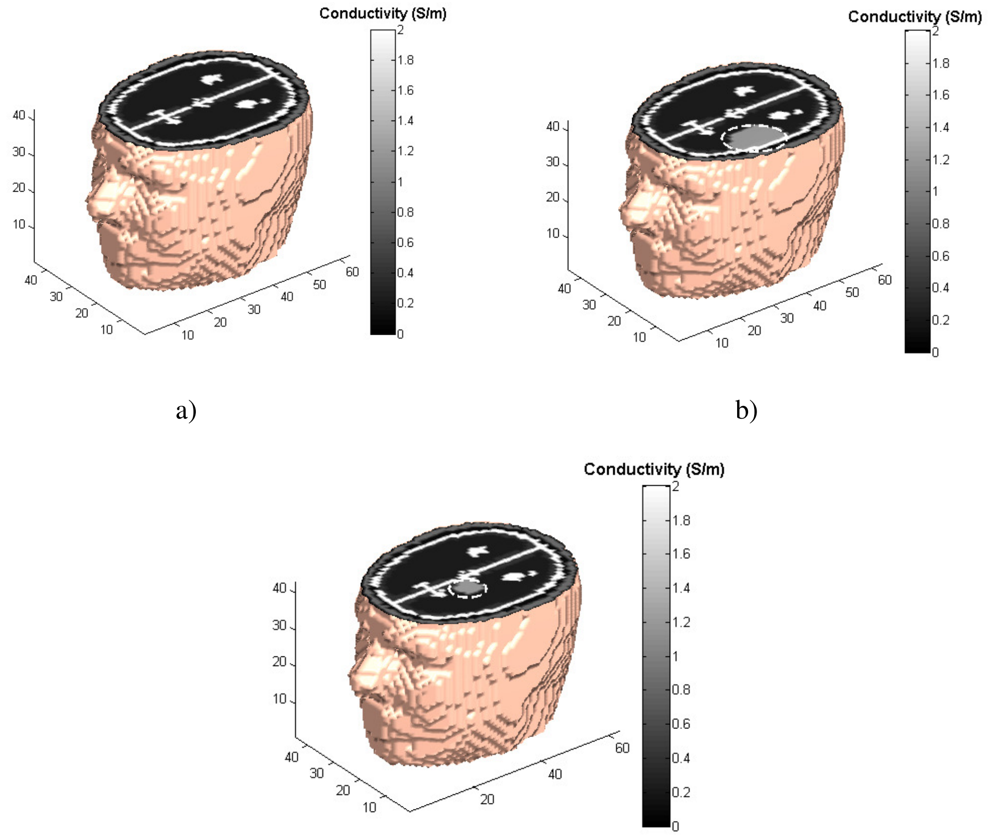

a)

b)

c)

Figure 3.18: Head model with coronal cutaway plane showing conductivity distribution for a) normal head b) head with external large intraparenchymal haemorrhage c) head with internal intraparenchymal haemorrhage

3.7.2 Results and discussion

The induced current density (***J***) was evaluated in normal and different state pathological cases of the human head with stroke using the custom electromagnetic field solver based on the weakly coupled field approximation. Figure 3.19 depicts the ***J*** distribution on coronal and sagittal cross sectional planes of the head. As expected, the current flow is highest in regions with relatively high conductivities notably in the CSF layer as well as near the excitation coil where the flux density is strong. The eddy currents also tend to circulate in loops parallel to the current flow in the excitation coil as shown in Figure 3.20. In order to visualize the effect of the induced current density for a head with a stroke Figure 3.21 shows the current density distribution in the presence of a large external intraparenchymal haemorrhage. The result is described by a relative rise in the current flow due to blood ingress in the very low conductive grey and white matter.

To investigate the MIT measurement channel sensitivity to the cerebral stroke, Figure 3.22 shows the induced voltage change (ΔV) in the opposite receiver coil as the external stroke is moved parallel to the coil axis. When qualitatively interpreted, the trend shows the measured signal due to the head decreases as the stroke is moved towards the centre. However, from a quantitative point of view, the relative signal change between the two extreme positions of the stroke is very small ($\approx$ 0.3%) inferring the signal proportion due to the stroke contributes weakly to the total signal.

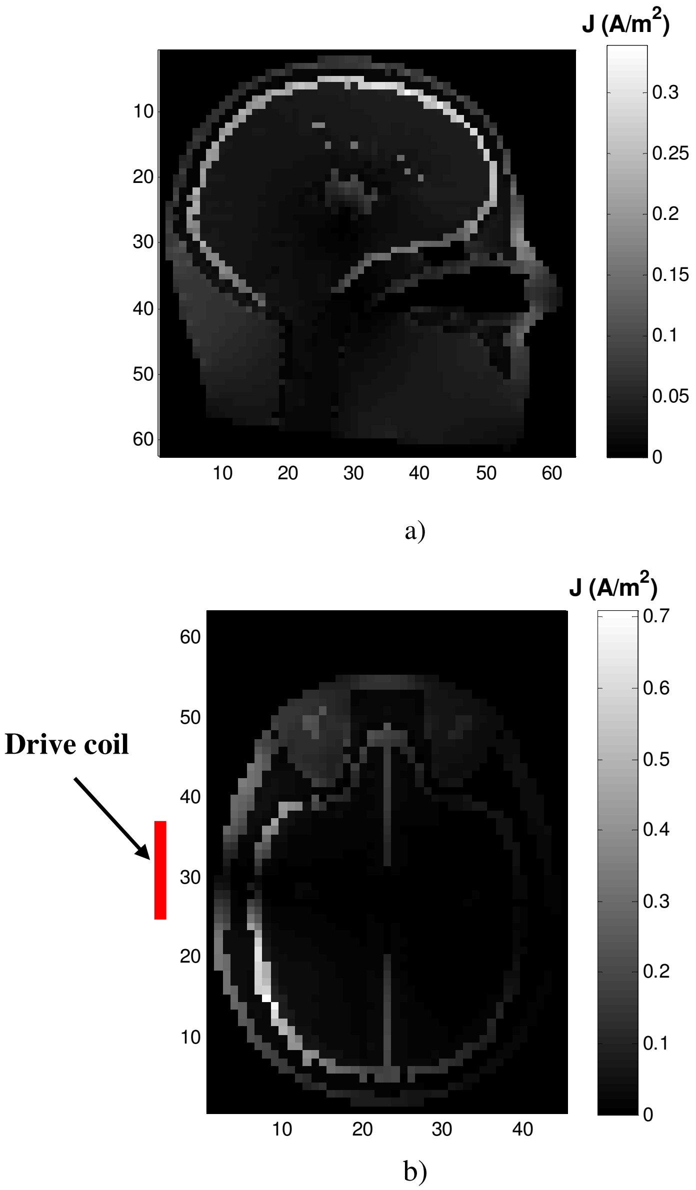

a)

b)

Figure 3.19: Plot of the current density on a) sagittal b) coronal sectional planes of the head

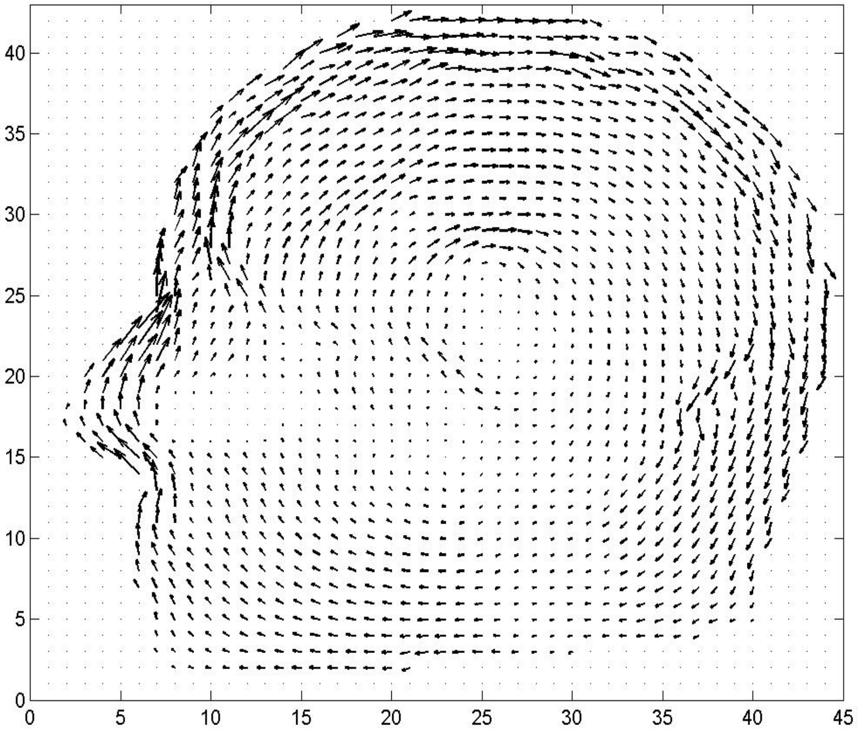

Figure 3.20: The direction of the current density on a sagittal sectional view

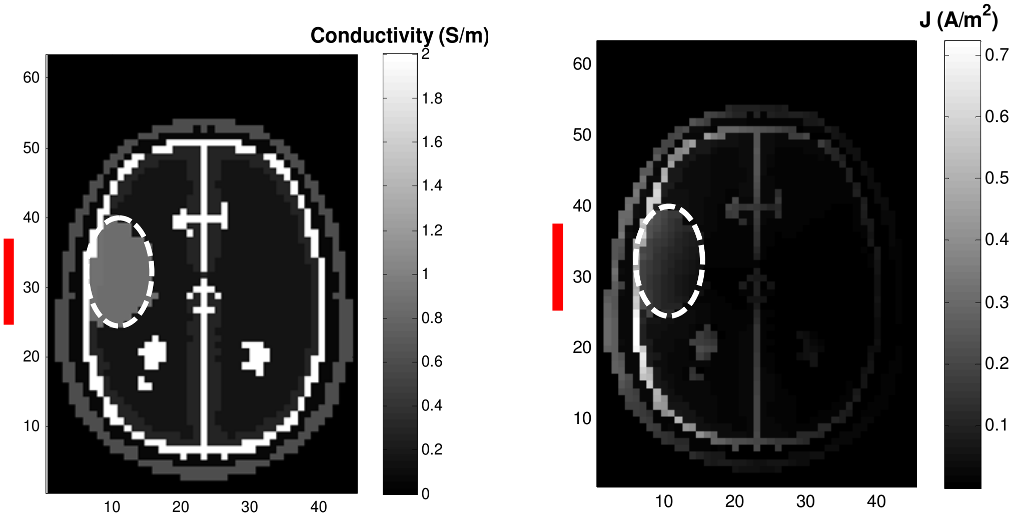

a) b)

Figure 3.21: a) Conductivity distribution b) Current density mapping of head with large peripheral stroke on coronal sectional plane.

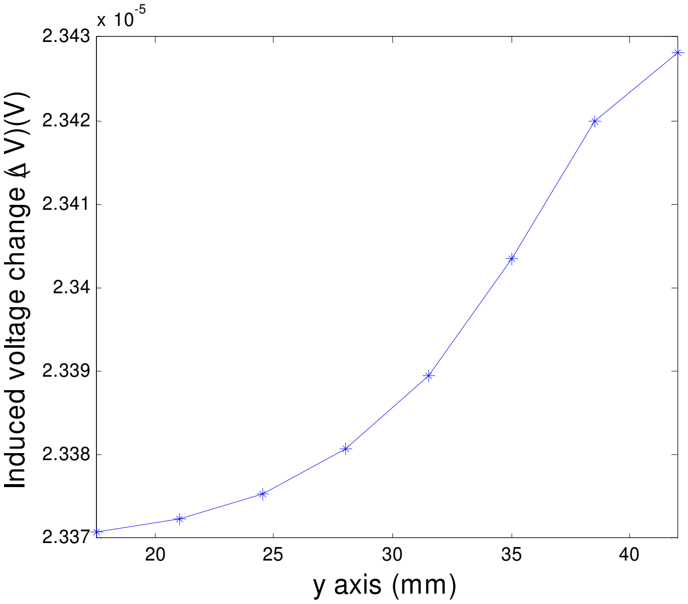

Figure 3.22: MIT channel sensitivity profile along the coil axis (*y* axis)

In the last test where the computational demands of the custom forward solver are compared with COMSOL, the results showed the electromagnetic field problem for the spherical head model was solved using a direct inversion in MATLAB in 3 minutes 30 seconds and the peak memory capacity needed was about 4 GB on a Quadro 2.5 GHz CPU, 32 GB RAM workstation. However, using the COMSOL direct solver, the problem went out of memory and a solution was not possible. In an attempt to obtain a solution, an iterative solver scheme was employed and the problem was solved in 26 minutes and required a comparable memory of 4 GB, but at the expense of a tolerance error. Clearly, the impedance method proved to be fast and memory efficient and this is mainly attributed to the implementation of the weakly coupled field approximation which requires only the target to be meshed as opposed to FE based COMSOL. Such approximation is proved to be very much implementable for medical applications.

3.8 Feasibility of stroke detection using an analytical model

The previous section demonstrated that the most difficult case to detect is when the stroke lies in the centre of the MIT scanning region where the signal sensitivity is minimum. So far, two methods of image reconstruction in MIT have been investigated, difference imaging and absolute imaging. The latter method suffers low sensitivity to the biological perturbation and systematic noise problems. In this section the limits of absolute imaging in detecting a central cerebral stroke will be investigated. For this purpose, an MIT system with a single measurement channel is used and an analytical solution is derived for an axial symmetrical head model. The sensitivity of the MIT channel to various sizes of stroke is analysed for two cases: (a) the background signal is measured and (b) the background field is cancelled out. For image reconstruction, a priori knowledge of the shape boundary of the head is useful and therefore the analysis extends to consider the sensitivity of the MIT channel to changes in the diameter of the head model as an indication of the dimensional accuracy required from the shape scanning system.

3.8.1 Model and validation

A multi-shell head model was used, which consisted of a sphere with an axial changing piecewise conductivity profile (radii a_k; conductivity σ_k; $0 \le k \le K+1$) simulating tissue layers: scalp, skull, cerebral spinal fluid (CSF), grey matter, white matter, and inner sphere representing the stroke. The excitation and receiver coils were modelled as filamentary circular elements, (rad. 25 mm) and positioned 141.5 mm and 131.5 mm respectively to the origin as shown in Figure 3.23. The excitation current was sinusoidal with 1 A amplitude at a frequency of 10 MHz. Note, the channel dimensions and excitation frequency correspond to the 16 channel MIT system prototype described in section (3.3). The electrical parameters and the radii of the tissue layers are extracted from [26] and displayed in the table below. The conductivity of the stroke was computed from the white matter and the blood conductivities assuming the leakage blood occupies 3/4 of the affected tissue. Permeabilities are assumed to be the same for all layers for the sake of simplicity. Electromagnetic field coupling due to tissue permittivities is minute at this operating frequency and hence was neglected.

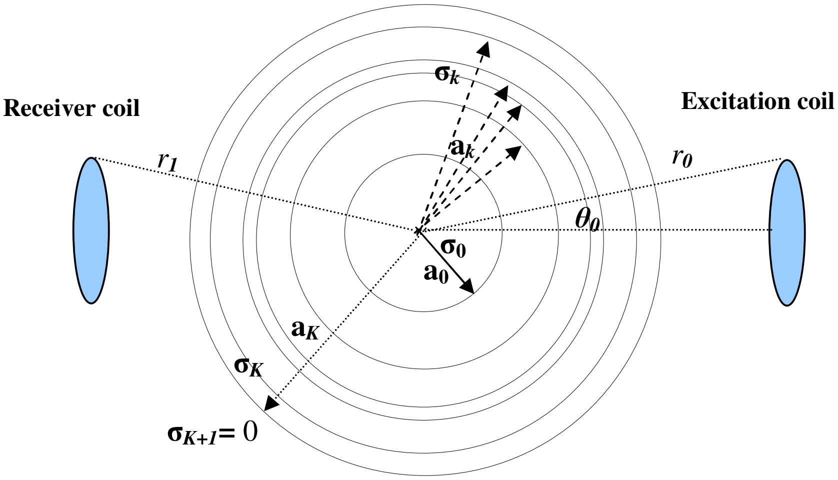

Figure 3.23: MIT channel and Analytical head model

Table 3-1: Electrical properties and dimensions of human head tissues

Tissue	*k*	Conductivity (Sm^{-1})	Radius (mm)
Stroke	0	0.8624	<=40
White matter	1	0.1582	54
Grey matter	2	0.2917	66
CSF	3	2.002	62
Skull	4	0.0828	74
Scalp	*K*	0.6168	80
Outside	*K+1*	0	>80

The electromagnetic field problem is described by the basic Maxwell's equations and the constitutive laws of electromagnetism which are combined into a Poisson's equation written in spherical coordinates (r, θ, φ) as:

$$\frac{1}{r}\frac{\partial^2\left(r\boldsymbol{E}_\varphi\right)}{\partial r^2}+\frac{1}{r^2}\frac{\partial}{\partial\theta}\left(\frac{1}{\sin\theta}\frac{\partial\left(\sin\theta\boldsymbol{E}_\varphi\right)}{\partial\theta}\right)=j\omega\mu\sigma\boldsymbol{E}_\varphi \tag{3.47}$$

Using the method of separation of variables, the general solution of (3.47) is given by:

$$\boldsymbol{E}_{\varphi}(r,\theta)=\sum_{n=1}^{\infty}\boldsymbol{R}_n(r)\boldsymbol{\Theta}_n(\theta) \tag{3.48}$$

where $\boldsymbol{R_n}$ and $\boldsymbol{\Theta_n}$ are written in terms of modified Bessel functions and associated Legendre polynomials

$$\boldsymbol{R}_n(r)=\frac{\boldsymbol{A}_n}{\sqrt{r}}I_{n+1/2}(\alpha r)+\frac{\boldsymbol{B}_n}{\sqrt{r}}K_{n+1/2}(\alpha r) \tag{3.49}$$

$$\boldsymbol{\Theta}_n(\theta)=\sqrt{\frac{2n+1}{2n(n+1)}}\boldsymbol{P}_n^1(\cos(\theta)) \tag{3.50}$$

where $\alpha=(1+\mathrm{j})\sqrt{\omega\mu\sigma/2}$. The limit of equation (3.49) when $\sigma = 0$ is given by:

$$\boldsymbol{R}_n(r)=\boldsymbol{A}_n r^n+\frac{\boldsymbol{B}_n}{r^{n+1}} \tag{3.51}$$

Solution (3.51) only satisfies homogeneous equation. In the presence of a source $-\mathrm{j}\omega\mu I_0\delta(r-r_0)\delta(\theta-\theta_0)$, the Green function associated with this source can be shown to be:

$$\boldsymbol{G}(r,r_0,\theta,\theta_0)=\sum_{n=1}^{\infty}\frac{\gamma}{2n+1}\frac{r_<^n}{r_>^{n+1}}\boldsymbol{\Theta}_n(\theta)\boldsymbol{\Theta}_n(\theta_0) \tag{3.52}$$

where $\gamma=\mathrm{j}\omega\mu I_0 r_0\sin\theta_0$, $r_>=\max(r,r_0)$ and $r_<=\min(r,r_0)$. Since $I_{n+1/2}(\infty)$ and $K_{n+1/2}(0)$ diverge, component $\boldsymbol{R}_n(r)$ of solutions in each region is given by:

$$\boldsymbol{R}_n^0(r)=\frac{\boldsymbol{A}_n^0}{\sqrt{r}}I_{n+1/2}(\alpha_0 r) \tag{3.53}$$

$$\boldsymbol{R}_n^k(r)=\frac{\boldsymbol{A}_n^k}{\sqrt{r}}I_{n+1/2}(\alpha_k r)+\frac{\boldsymbol{B}_n^k}{\sqrt{r}}K_{n+1/2}(\alpha_k r),\quad 1\le k\le K \tag{3.54}$$

$$\boldsymbol{R}_n^{K+1}(r)=\frac{\boldsymbol{B}_n^{K+1}}{r^{n+1}}+\frac{\gamma}{2n+1}\frac{r_<^n}{r_>^{n+1}}\boldsymbol{\Theta}_n(\theta_0) \tag{3.55}$$

From (3.48), (3.52) and (3.55) the field outside the conductor is given by:

$$\begin{aligned} \boldsymbol{E}_{\varphi}(r,\theta) &= \sum_{n=1}^{\infty}\left(\frac{\boldsymbol{B}_n^{K+1}}{r^{n+1}} + \frac{\gamma}{2n+1}\frac{r_<^n}{r_>^{n+1}}\right)\boldsymbol{\Theta}_n(\theta)\boldsymbol{\Theta}_n(\theta_0) \\ &= \sum_{n=1}^{\infty}\left(\frac{\boldsymbol{B}_n^{K+1}}{r^{n+1}}\right)\boldsymbol{\Theta}_n(\theta)\boldsymbol{\Theta}_n(\theta_0) + \sum_{n=1}^{\infty}\left(\frac{\gamma}{2n+1}\frac{r_<^n}{r_>^{n+1}}\right)\boldsymbol{\Theta}_n(\theta)\boldsymbol{\Theta}_n(\theta_0) \end{aligned} \tag{3.56}$$

To compute the voltage change, the scattered field due to the target is integrated, which is the first term on the right hand side of the above equation. The scattered field is given by:

$$\boldsymbol{E}_{sc}(r,\theta) = \sum_{n=1}^{\infty}\left(\frac{\boldsymbol{B}_n^{K+1}}{r^{n+1}}\right)\boldsymbol{\Theta}_n(\theta)\boldsymbol{\Theta}_n(\theta_0) \tag{3.57}$$

$$\begin{aligned} \Delta\boldsymbol{V} &= \oint_{C(\text{Receiver})} \boldsymbol{E}_{sc}(r,\theta)\,dl = \int_0^{2\pi} \boldsymbol{E}_{sc}(r_1,\theta_1)\, r_1 \sin\theta_1 d\varphi \\ &= 2\pi r_1 \sin\theta_1 \boldsymbol{E}_{sc}(r_1,\theta_1) \end{aligned} \tag{3.58}$$

where the coordinates (r_1, θ_1) denotes the location of the receiver coil. In order to validate the analytical solution, a finite element model of the MIT model was constructed using COMSOL. The problem was meshed with 168,000 FEs approximated with quadratic shape functions. The change in the induced voltage due to the head was calculated analytically and numerically. The resulted error was estimated as 7.5 %. This level of error could be due to numerical solution associated with meshing quality.

3.8.2 Results and discussion

For a first analysis, the aim is to analyse the sensitivity of the measurement channel to various sizes of the central stroke and compare the results with noise levels exhibited by the currently developed MIT instrumentation; thus, the smallest radius of the stroke that could be resolved in absolute imaging could be deduced. Two cases were analysed:

a) when the background field is not cancelled and the induced voltage comprises $\boldsymbol{V}_0+\Delta\boldsymbol{V}$. The sensitivity of the channel to the stroke with respect to the background signal is expressed as:

$$\text{(Signal/Background Ratio) } SBR = \frac{\Delta \boldsymbol{V}_2 - \Delta \boldsymbol{V}_1}{\boldsymbol{V}_0} \tag{3.59}$$

where $\boldsymbol{V}_0$ is the induced voltage correlated to the primary field and $\Delta \boldsymbol{V}_2 / \Delta \boldsymbol{V}_1$ denote the induced voltages due to the head with/without stroke respectively. As expected, Figure 3.24 shows the sensitivity increases with the radius of the stroke. This is explained by stronger induced eddy currents increasing the coupled perturbation field.

b) when the primary field is assumed to be perfectly eliminated. The signal to target ratio (STR) is evaluated with respect to the induced voltage due to the unhealthy head as:

$$STR = \frac{\Delta \boldsymbol{V}_2 - \Delta \boldsymbol{V}_1}{\Delta \boldsymbol{V}_2} \tag{3.60}$$

The simulation results depicted in Figure 3.24 show the channel sensitivity to the stroke has considerably improved. Taking the Mark 1 as a reference MIT system with a reported signal to noise ratio (SNR = ΔV_2/noise) of 40dB a stroke of 27 mm radius and 5.45 contrast to the background potentially could be resolved. From a clinical perspective a stroke with such volume is too large which infers that current MIT system specifications need to be improved in order to increase the possibility of detecting a stroke within practical limits. However, it is expected that relatively smaller stroke could theoretically be detected with future MIT systems such as the new Mark 2 which is being developed in Glamorgan University as part of this LCOMIT programme.

In a second analysis, the MIT sensitivity to noise caused by error in shape scanning of the head boundary is analysed. This analysis seeks to obtain a view of the impact of the shape scan noise on MIT measurements of the head and helps in defining the criteria for design requirements of the optical shape scanner. In this investigation we assumed the background can be eliminated and the SNR was simulated for different radii of the head. The results displayed by Figure 3.25 indicate a spatial deviation of 1.2 mm is equivalent to the system noise exhibited by the Mark 1.

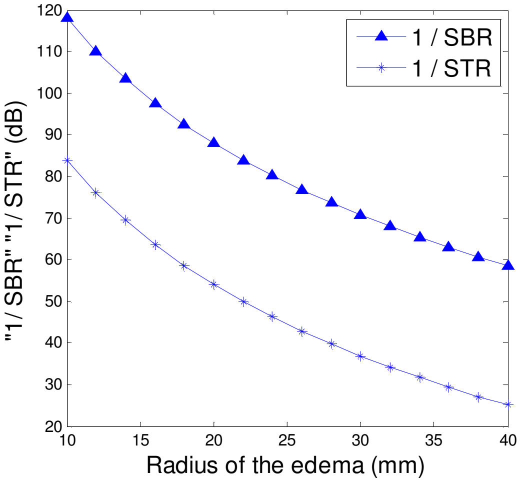

Figure 3.24: (1/SBR) and (1/STR) versus radius of the stroke

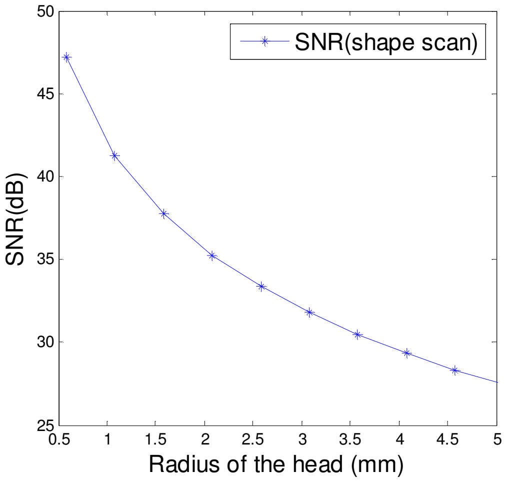

Figure 3.25: Simulated SNR from shape scanner versus radius of the head

3.9 Feasibility of stroke detection using a numerical model

In this section, the possibility of detecting a haemorrhage type stroke is investigated by examining the signal due to the stroke against that of systematic errors that can happen in a real MIT system.

3.9.1 Results and discussion

Figure 3.26 (a) and (b) shows the simulation arrangement which includes a head model and an MIT system. This latter is a model of the Mark 1 system simulated in COMSOL. The excitation coil was driven with unit current and induced voltages were measured through the receiver coils. A realistic multilayer head model (Figure 3.26 (a)) consisting 7 biological tissues (Scalp, Skull, CSF, grey matter, white matter, spinal/optic nerves, and Eye balls) was placed in the scanning region so as the stroke line up with the sensor plane. The electrical conductivities for the corresponding tissues were obtained from Table 1-1. The voltages induced on the receiver coils were computed using our custom eddy current software which employs a pre-computed primary field $\boldsymbol{A}_0$ by an FE package (e.g. COMSOL) and solves the MIT forward problem using the impedance method.

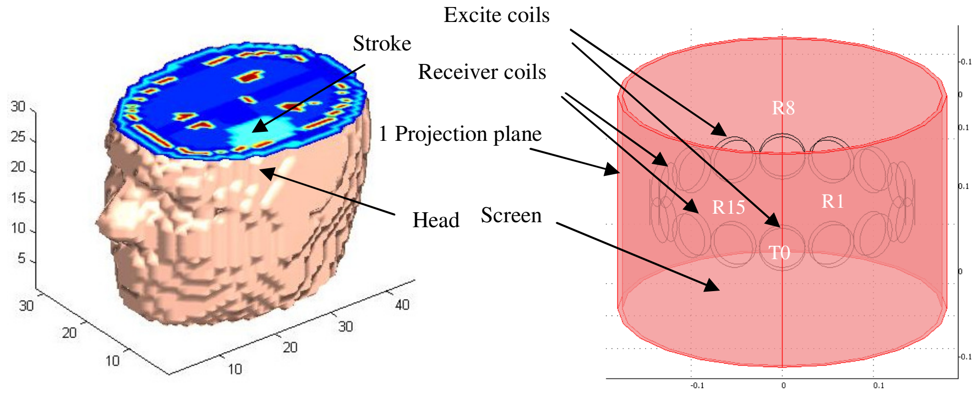

a) b)

Figure 3.26: MIT system with a) Simulated Target (Head and stroke), and b) MIT coil array

In a first analysis, one transmitter was excited and the differences in the voltage induced because of the presence of the head between the transmitter being in the correct orientation (solution (1)) and the transmitter being rotated by one and two degrees (solution (2)) were calculated for every receiver channel (equation (3.61)). The values were normalized to the rms of the induced voltages produced by the noise free case and plotted against the channel number (Figure 3.27 (a)). Receiver coil numbers are in order; number R1 and R15 are adjacent to transmitter T0, and R8 is the opposite receiver.

$$dV = \frac{\Delta \boldsymbol{V}_{\text{solution1}} - \Delta \boldsymbol{V}_{\text{solution2}}}{\text{rms}(\Delta \boldsymbol{V}_{\text{solution2}})} \qquad (3.61)$$

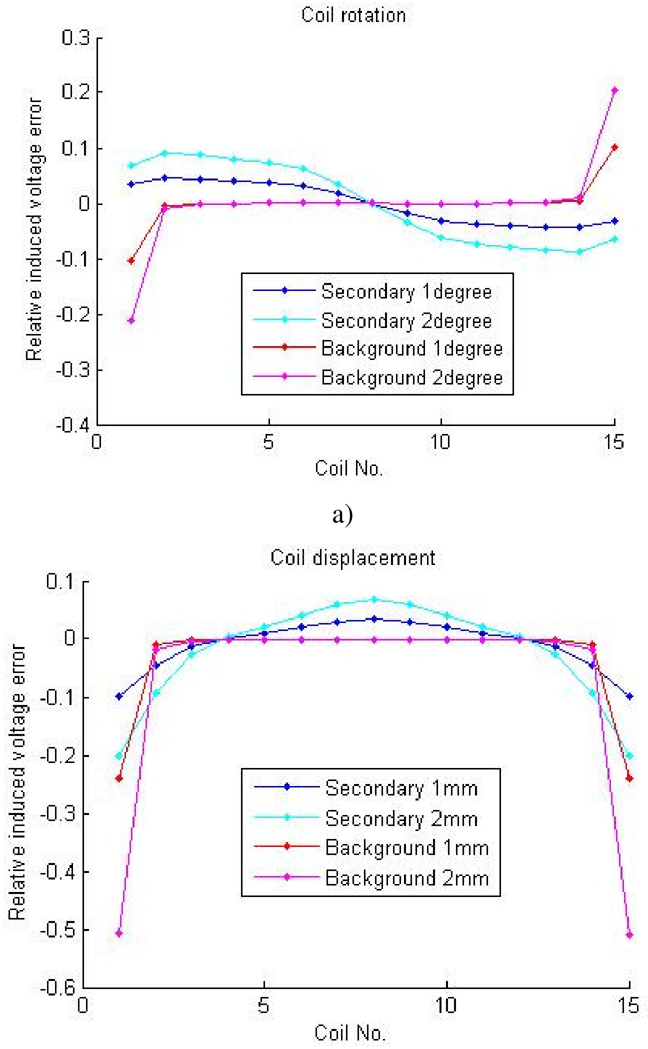

a)

b)

Figure 3.27: Relative voltage errors caused by the coil rotation/displacement

From the graph (Figure 3.27 (a)), we can see that the worst effected coils are the coils near the transmitter where the opposite coil has nearly zero error. On the same graph, the voltages induced by the background magnetic field are also plotted. The relative changes in the background measurements are smaller than the error in the secondary induced voltages except for the adjacent coils. The lines do not follow the same trend; hence it is difficult to use the background to compensate for the error on the secondary field.

On the other hand, Figure 3.27 (b) presents the results of the simulations for displacing the transmitter coil by 1 and 2 mm along its axis towards the centre of the object space. As can be seen, similar observations made for the mis-ortientation of the coil earlier remain valid for when the transmitter coil is displaced. In a second simulation, the effect of the displacement of the head to measurements differences is quantified. The head is moved by 2 mm and the relative voltage differences are plotted on the graph below (Figure 3.28). In this case, MIT appears to be not as sensitive to the movement of the head as to the movement of the coils. The changes of the signal caused by the 50 ml stroke (inclusion) are also mapped in the figure for comparison. The relative signal from the stroke is in the same order of magnitude compared to the relative voltage errors caused by the movements of the coil and the head. This means that for a system that is built with these tolerances it will be very difficult to reconstruct the stroke.

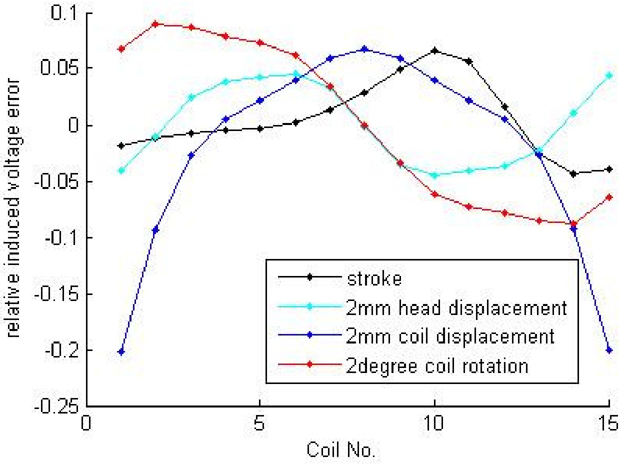

Figure 3.28: Comparison of the errors with the signal from a 50 ml stroke

Recently frequency difference imaging has been suggested as attractive for imaging the stroke since biological tissues exhibit conductivity changes with frequency. Workers in the field of MIT reported this procedure whereby dual frequency measurements are used can reduce systematic errors investigated above [99]. In order to test if frequency difference can reduce the error caused by coil positioning, the following computational experiment was conducted. The induced voltages due to the presence of the head were computed at frequencies of 1 and 10 MHz for the case when the transmitter was in the correct position (solution (1)) and displaced (i.e. rotated/moved - solution (2)). The voltage differences were calculated in a similar fashion to the absolute case and have been normalized to the rms value of the frequency difference measurements for the correct position according to the equation given below:

$$dV = \frac{(\Delta \boldsymbol{V}_{\mathrm{f}_1} - (\mathrm{f}_1/\mathrm{f}_2)^2 \Delta \boldsymbol{V}_{\mathrm{f}_2})_{\mathrm{solution1}} - (\Delta \boldsymbol{V}_{\mathrm{f}_1} - (\mathrm{f}_1/\mathrm{f}_2)^2 \Delta \boldsymbol{V}_{\mathrm{f}_2})_{\mathrm{solution2}}}{\mathrm{rms}((\Delta \boldsymbol{V}_{\mathrm{f}_1} - (\mathrm{f}_1/\mathrm{f}_2)^2 \Delta \boldsymbol{V}_{\mathrm{f}_2})_{\mathrm{solution1}})} \tag{3.62}$$

In Figure 3.29 (a) the results show that there is no improvement on the relative error caused by the movement of the coil.

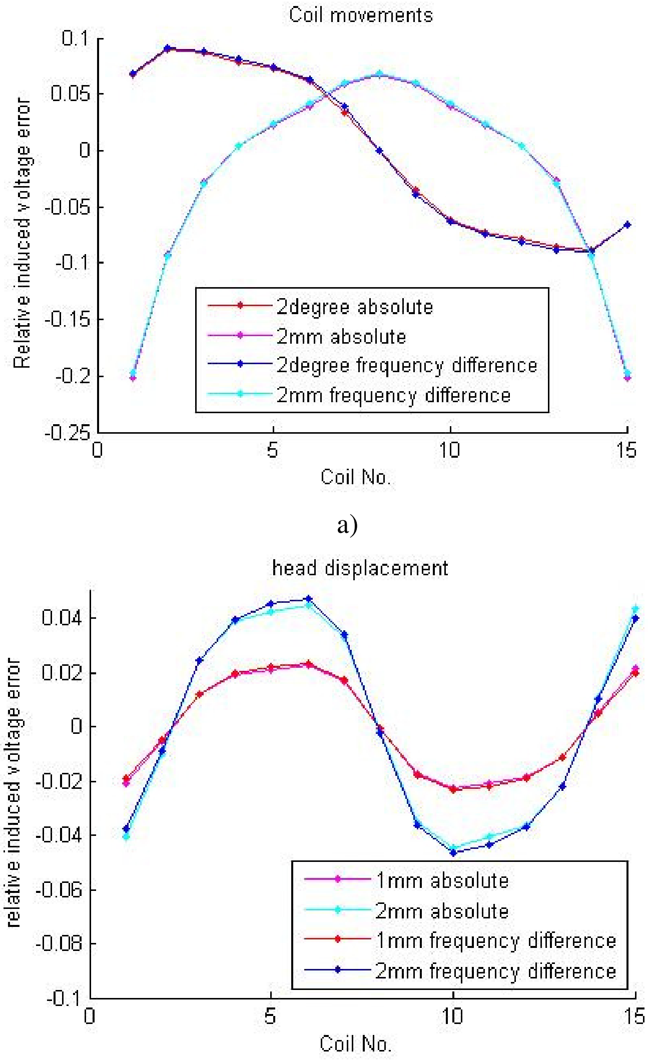

a)

b)

Figure 3.29: Comparison of errors between absolute and frequency difference measurements

The error cancelation when frequency difference measurements are used is also tested for head displacement (Figure 3.29 (b)). Interestingly, the absolute and frequency difference relative error show similar pattern, which infers that there is no advantage of using frequency difference for head displacement error cancelation.

4 Inverse problem in Magnetic Induction Tomography

4.1 Introduction

Image reconstruction in MIT aims to estimate the conductivity distribution within an object given a measurement set of induced voltages or mutual-impedances taken around the periphery of the object. Image reconstruction is performed via the solution of an inverse problem that is ill-posed and nonlinear with respect to conductivity distribution. The nonlinearity stems from the fact that a local change in conductivity affects all measurement channels and the measurement sensitivity of a single channel to a local conductivity perturbation depends also on the conductivity variation in the background. For a given MIT mapping, with Jacobian $\boldsymbol{J}:\boldsymbol{\sigma}\rightarrow\boldsymbol{D}$, the MIT system $\boldsymbol{J}\boldsymbol{\sigma}=\boldsymbol{D}$ is regarded ill-posed if one of the Hadamard conditions are not met namely: a) Existence: a solution $\boldsymbol{\sigma}$ exists; b) Uniqueness: the solution is unique; and c) Stability: the solution is continuously dependent on the observed data. In MIT, the first two criteria could be fulfilled by imposing some constraints on the solution. The third condition is, however, the most problematic, whereby small changes in measurement data could often result in large reconstructed conductivity changes. One method to quantify the severity of the instability of the MIT inverse problem is by the condition number of the Jacobian matrix $\boldsymbol{J}$, which represents the ratio of the largest singular value to the smallest singular value. For the MIT inverse problem which is unstable and hence ill-posed, the singular values of the Jacobian $\boldsymbol{J}$ tend to decay quickly towards zero giving large condition number. Furthermore, the MIT inverse problem is underdetermined which implies that a limited number of measurements, m, are usually used to reconstruct a large number of unknown conductivity elements, n, ($m<<n$).

Numerical analysis often suggests solving the MIT inverse problem through minimization of a least squares functional given by the system of equations:

$$\boldsymbol{\sigma}^* = \mathop{\mathbf{argmin}}_{\sigma \in R^n} \{F(\boldsymbol{\sigma})\} \tag{4.1}$$

$$F(\boldsymbol{\sigma}) = \frac{1}{2}\sum_{i=1}^{m} \mathrm{r}_i(\sigma) = \frac{1}{2}\|\mathbf{r}(\boldsymbol{\sigma})\|^2 = \frac{1}{2}\mathbf{r}(\boldsymbol{\sigma})^{\mathbf{T}} * \mathbf{r}(\boldsymbol{\sigma}) \tag{4.2}$$

$$\mathbf{r}(\boldsymbol{\sigma}) = \boldsymbol{F}(\boldsymbol{\sigma}) - \boldsymbol{D} \tag{4.3}$$

i.e. the task is to find the argument conductivity vector $\boldsymbol{\sigma}^* \in \mathbb{R}^n$ that minimises the objective function $F: \mathbb{R}^{\mathrm{n}} \to \mathbb{R}$, $i = 1, \ldots, m$ and $m < n$. Here the vector function $\mathbf{r} : \mathbb{R}^{\mathbf{n}} \to \mathbb{R}^{\mathbf{m}}$ is called the residual. $\boldsymbol{F} : \mathbb{R}^{\mathbf{n}} \to \mathbb{R}^{\mathbf{m}}$ denotes the forward operator and $\boldsymbol{D} \in \mathbb{R}^m$ is the measurement data. In nonlinear optimisation, the MIT inverse problem is usually solved in an iterative scheme by solving a series of linearised inverse solutions ($\boldsymbol{\sigma}_1, \boldsymbol{\sigma}_2, \boldsymbol{\sigma}_3, \ldots, \boldsymbol{\sigma}^*$). For every conductivity update, one needs to re-compute the forward problem and recalculate the Sensitivity (the Jacobian). Because of the computation demands associated with a nonlinear treatment of the problem, many workers in the field of MIT solve the problem (4.1) by considering a linear approximation of the residual given by:

$$\mathbf{r}(\boldsymbol{\sigma}) = \boldsymbol{J}\boldsymbol{\sigma} - \boldsymbol{D} \tag{4.4}$$

where the Jacobian, $\boldsymbol{J}$, is usually computed in empty space or a homogenous conductivity distribution. Theoretically this linear approximation should work fairly well for objects with very simple internal structures and small conductivity variations, i.e. for less nonlinear problems. For instance, in medical imaging authors [11, 75, 100, 101] reported differential single step reconstructions of a perturbation placed inside conductive background crudely approximating the shape and the structure of the head including a stroke. Results showed the perturbation can be reconstructed, but the images were over blurred and quantitatively unrepresentative of actual values of the tissues, which could possibly be improved via nonlinear reconstruction schemes. In some NDT applications [102, 103], where fast data acquisition and image reconstruction is essential, linear iterative reconstruction methods produced more or less satisfactory results since the tested objects involved conductivity distributions that are relatively simple. However, in [57] where similar methods were used to reconstruct experimental and simulated phantoms representative of multiphase flow patterns in the oil industry, linear algorithms failed to recover the internal conductivity distribution especially for annular and bubble flow where the nonlinearity of the problem is obvious. Therefore, in order to improve image reconstruction in these applications, the associated inverse problem should preferably be approached in a nonlinear framework.

Starting with an initial guess $\boldsymbol{\sigma}_0$, the nonlinear method produces a series of conductivity updates $\{\boldsymbol{\sigma}_k \mid k = 1,2,3,...\}$ which desirably should converge toward the minimiser $\boldsymbol{\sigma}^*$ (also termed a "local minimiser") of the given objective function *F*. These conductivity updates are obtained using the recurrence relation:

$$\boldsymbol{\sigma} = \boldsymbol{\sigma} + \alpha \boldsymbol{d} \tag{4.5}$$

where the vector $\boldsymbol{d}$, which is termed the "search direction", is computed with the constrain to produce the descending condition for the objective function given by:

$$F(\boldsymbol{\sigma} + \alpha \boldsymbol{d}) < F(\boldsymbol{\sigma}) \tag{4.6}$$

An optimisation method which enforces this condition in its iterative procedure is called a "descent method". Given the half line starting from $\boldsymbol{\sigma}$ in the direction of $\boldsymbol{d}$, the scalar $\alpha > 0$ determines how much we need to move along the direction $\boldsymbol{d}$ to achieve an optimum decrease in the objective function as:

$$\alpha^* = \underset{\alpha>0}{\mathbf{argmin}}\left\{F(\boldsymbol{\sigma}+\alpha \boldsymbol{d})\right\} \tag{4.7}$$

This process of evaluating the step factor α^* is performed using a line search algorithm. In practice, the line search sub-problem (4.7) need not to be solved to a high degree of accuracy, which is important from the standpoint of computational cost. What is usually required is a sufficient decrease in the objective function F. For references on available strategies of line search, the reader could refer to [104, 105]. The optimisation methods presented in this chapter employ special techniques to simultaneously determine the search direction $\boldsymbol{d}$ and the step factor α. Hence, the conductivity vector is updated by the search direction without the need for explicitly evaluating the step factor α.

In order to calculate the search direction two widely known methods are usually used: the steepest descent direction and Newton's method. These methods form the foundations for the derivation of the special optimisation methods which will be investigated later in this chapter. A brief insight into the derivation of these fundamental methods is presented below.

4.1.1 Steepest descent method

The steepest descent method, also known as the gradient method is the simplest method in optimisation. Given the objective function F, the first order Tailor series expansion of F around the solution $\boldsymbol{\sigma}$ yields:

$$\begin{aligned} F(\boldsymbol{\sigma}+\alpha\boldsymbol{d}) &= F(\boldsymbol{\sigma})+\alpha\boldsymbol{d}^{\mathrm{T}}\nabla F(\boldsymbol{\sigma})+O(\alpha^2) \\ &\approx F(\boldsymbol{\sigma})+\alpha\boldsymbol{d}^{\mathrm{T}}\nabla F(\boldsymbol{\sigma}) \quad \text{for } \alpha \text{ for sufficietly small.} \end{aligned} \tag{4.8}$$

where $\nabla F(\boldsymbol{\sigma}) = \left[\partial F(\boldsymbol{\sigma})/\partial\sigma_i\right]$ is the gradient ($\boldsymbol{g}$). From (4.8) another special property of descent methods can be derived if $\boldsymbol{d}$ is a decent direction or equivalently condition (4.6) is satisfied:

$$F(\boldsymbol{\sigma}+\alpha\boldsymbol{d}) < F(\boldsymbol{\sigma}) \iff \boldsymbol{d}^{\mathrm{T}}\nabla F(\boldsymbol{\sigma}) < 0 \tag{4.9}$$

Using equation (4.8), when the conductivity vector is updated with a step $\alpha\boldsymbol{d}$, the relative gain in the reduction of the objective function is given by:

$$\lim_{\alpha\to 0}\frac{F(\boldsymbol{\sigma}) - F(\boldsymbol{\sigma}+\alpha\boldsymbol{d})}{\alpha\|\boldsymbol{d}\|} = -\frac{1}{\|\boldsymbol{d}\|}\boldsymbol{d}^{\mathrm{T}}\nabla F(\boldsymbol{\sigma}) = -\|\nabla F(\boldsymbol{\sigma})\|\cos\theta \tag{4.10}$$

where θ is the angle between the vectors $\boldsymbol{d}$ and $\nabla F(\boldsymbol{\sigma})$. It is clear that the largest gain (reduction in F) is achieved when θ is equal to π. Hence, the steepest direction $\boldsymbol{d}_{sd}$ is obtained by choosing $\boldsymbol{d}_{sd} = -\nabla F(\boldsymbol{\sigma})$. Using this method, the conductivity update can be written in the form:

$$\begin{aligned} \boldsymbol{\sigma} &= \boldsymbol{\sigma}+\alpha\boldsymbol{d}_{sd} \\ &= \boldsymbol{\sigma}-\alpha\nabla F(\boldsymbol{\sigma}) \end{aligned} \tag{4.11}$$

This method requires only the calculation of the gradient to determine the descending direction in each iterate of the optimisation. Since only first order derivative information of the objective function is used the convergence of this method is very slow. Nevertheless, for many inverse problems the method exhibit quite good convergence in the initial stage of the iterative process [106].

4.1.2 Newton's method

Another fundamental approach in optimisation techniques is Newton's Method. This method can be derived by first approximating the objective function F with its second order Tailor series around the iterate $\boldsymbol{\sigma}$ as:

$$\begin{aligned} F(\boldsymbol{\sigma}+\boldsymbol{d}) &= F(\boldsymbol{\sigma})+\boldsymbol{d}^{\mathrm{T}}\nabla F(\boldsymbol{\sigma}) + \frac{1}{2}\boldsymbol{d}^{\mathrm{T}}\nabla^2 F(\boldsymbol{\sigma})\boldsymbol{d}+O(\|\boldsymbol{d}\|^3) \\ &= F(\boldsymbol{\sigma})+\boldsymbol{d}^{\mathrm{T}}\nabla F(\boldsymbol{\sigma}) + \frac{1}{2}\boldsymbol{d}^{\mathrm{T}}\nabla^2 F(\boldsymbol{\sigma})\boldsymbol{d}, \text{ for small} \|\boldsymbol{d}\|^3 \end{aligned} \tag{4.12}$$

where $\nabla^2 F(\boldsymbol{\sigma}) = \left[\partial^2 F(\boldsymbol{\sigma}) / \partial\sigma_i \partial\sigma_j\right]$ is the Hessian (***H***). As can be seen, for small step lengths $\|\boldsymbol{d}\|$ higher order terms become insignificant in the series and approximating the objective function with a quadratic form is adequate. Then, the task is to find the local minimiser ($\boldsymbol{\sigma}^*$) of the approximate objective function F in the small neighbourhood of $\boldsymbol{\sigma}$. The minimiser $\boldsymbol{\sigma}^*$ must satisfy $\nabla F(\boldsymbol{\sigma}^*)=0$. Using equation (4.12) we have:

$$\nabla F(\boldsymbol{\sigma}+\boldsymbol{d}) = \nabla F(\boldsymbol{\sigma}) + \nabla^2 F(\boldsymbol{\sigma})\boldsymbol{d} = 0 \tag{4.13}$$

Assuming that the Hessian (***H***) is invertible, the Newton's search direction $\boldsymbol{d}_N$ can be obtained by rearranging equation (4.13) as follows:

$$\boldsymbol{H}\ \boldsymbol{d}_N = -\nabla F(\boldsymbol{\sigma}) \Leftrightarrow \boldsymbol{d}_N = -\boldsymbol{H}^{-1}\nabla F(\boldsymbol{\sigma}) \tag{4.14}$$

where $\boldsymbol{H} = \nabla^2 F(\boldsymbol{\sigma})$. Using this approach the conductivity update is formulated as:

$$\begin{aligned} \boldsymbol{\sigma} &= \boldsymbol{\sigma} + \boldsymbol{d}_N \\ &= \boldsymbol{\sigma} - \boldsymbol{H}^{-1}\nabla F(\boldsymbol{\sigma}) \end{aligned} \tag{4.15}$$

where it can be seen that a full step is taken by considering $\alpha = 1$ when using this method.

If the Hessian ***H*** is positive definite, which means that ***H*** is non-singular and for any nonzero vector $\boldsymbol{v}$: $\boldsymbol{v}^{\mathrm{T}}\boldsymbol{H}\,\boldsymbol{v} > 0$, then by multiplying both sides of equation (4.14) by $\boldsymbol{d}_N^{\mathrm{T}}$, one obtains:

$$\boldsymbol{d}_N^{\mathrm{T}}\boldsymbol{H}\,\boldsymbol{d}_N = -\boldsymbol{d}_N^{\mathrm{T}}\nabla F(\boldsymbol{\sigma}) > 0 \tag{4.16}$$

This shows that whenever the Hessian is positive definite, the Newton's direction vector $\boldsymbol{d}_N$ is a descent direction as illustrated by equation (4.9).

Newton's method employs second order derivative information in evaluating the direction step by which the conductivity is updated. Whilst the steepest descent method is robust in the initial stage of the iterative image reconstruction protocol, Newton's method is fast convergent in the final stage of the iterative procedure when $\boldsymbol{\sigma}$ approaches the local minimiser $\boldsymbol{\sigma}^*$. During the iteration if $\boldsymbol{\sigma}$ is in the close vicinity of $\boldsymbol{\sigma}^*$ and the Hessian $\boldsymbol{H}$ is positive definite, then a quadratic convergence toward $\boldsymbol{\sigma}^*$ can be achieved, Otherwise, if $\boldsymbol{H}$ is close to be singular then the method diverges away from $\boldsymbol{\sigma}^*$ [107].

In the following section, two special optimisation methods, which provide a mechanism to combine the steepest descent method and Newton's method in a single iterative optimisation process, will be presented. These hybrid methods are the Levenberg-Marquardt and the Trust Region. During optimisation, they switch to Newton's method whenever the system is stable and $\boldsymbol{\sigma}$ is close to the local minimiser $\boldsymbol{\sigma}^*$, and employ the steepest descent direction whenever the system becomes unstable or the current iterate $\boldsymbol{\sigma}$ is far from the solution $\boldsymbol{\sigma}^*$. When operating in Newton's mode, it will be shown that these methods tend to take longer steps making the process fast converging, whereas in the steepest descent method they reduce the step size. These hybrid methods employ so called damping and trust region techniques to control which of the aforementioned parent methods i.e. the steepest descent method and Newton's method should be used, and hence manipulate the size and the direction of the step to achieve good stability and convergence of the algorithm in every iterate.

Another special method based on Newton's optimisation, which has been termed the Damped Gauss Newton method, is also investigated and proposed for the first time in the framework of MIT. The method employs similar damping process as for the Levenberg Method but uses it in the framework of controlling the amount of regularisation. The performance of the proposed methods is compared against that of standard Gauss Newton method. In this comparison, they will be judged upon different issues which are critical for image reconstruction. Stability of the optimisation process, type of regularisation or equivalently the conformity of the a-priori information with the problem, the choice of the regularisation parameter and the reliability of the stopping criteria are among these issues which form the basis to analyse these methods.

Moreover, for large scale problems as in the medical application approached in this thesis, where enormous number of degrees of freedom can be encountered, the corresponding Hessian can be large. Therefore, a direct inverse of the Hessian becomes impractical due to the computational and memory costs. In this situation, Krylov sub-space methods can be regarded computationally cost effective to generate an implicit inverse of the Hessian. Therefore, one of the proposed optimisation algorithms is modified to incorporate the Krylov sub-space efficiency in producing an approximate for the inverse of the Hessian and is tested on MIT for head imaging.

4.2 *Nonlinear optimisation methods*

Non linear treatment of the inverse problem in MIT has already been presented using regularised Gauss Newton method. Examples of conductivity imaging using this approach in medical applications include [108] and in industrial process applications involve [36]. In this section, special methods that are more efficient will be approached. Some of these methods have already been applied in EIT, but to the author's knowledge, this is the first time they have been implemented in the field of MIT. In the following subsection, the techniques employed by these methods in determining the search direction and the step length simultaneously will be described.

4.2.1 Damping and trust region techniques

Assume that the objective function F can be represented with a quadratic model M which approximates its behaviour in the neighbourhood of the current iterate ($\boldsymbol{\sigma}$) as follows:

$$M(\boldsymbol{d}) = F(\boldsymbol{\sigma}) + \boldsymbol{d}^{\mathrm{T}} \nabla F(\boldsymbol{\sigma}) + \frac{1}{2} \boldsymbol{d}^{\mathrm{T}} \boldsymbol{H}\, \boldsymbol{d} \tag{4.17}$$

where $\boldsymbol{H} \in \mathbb{R}^{n \times n}$ is a symmetric matrix which can be the Hessian $\nabla^2 F(\boldsymbol{\sigma})$ or an approximation to it. Note that when $\boldsymbol{H} = \nabla^2 F(\boldsymbol{\sigma})$, the model M is identical to the first three terms of the Tailor series expansion of F as illustrated on the right hand side of equation (4.12). In this case, the error difference between $M(\boldsymbol{d})$ and $F(\boldsymbol{\sigma}+\boldsymbol{d})$ is $O(\|\boldsymbol{d}\|^3)$, so the approximation error is small when $\|\boldsymbol{d}\|^3$ is small. Hence, the model M is a good approximation to $F(\boldsymbol{\sigma}+\boldsymbol{d})$ only when the step $\boldsymbol{d}$ is small. Based on this model two techniques can be introduced which compute the step $\boldsymbol{d}$ that minimises M but also adhere to additional constrains.

Using the damping technique the step is determined as:

$$\boldsymbol{d} = \boldsymbol{d}_d = \mathbf{argmin}_d \left\{ M(\boldsymbol{d}) + \frac{1}{2}\gamma \boldsymbol{d}^{\mathrm{T}} \boldsymbol{d} \right\} \tag{4.18}$$

where the scalar $\gamma > 0$ is a damping parameter. As can be seen, the term $\frac{1}{2}\gamma \boldsymbol{d}^{\mathrm{T}} \boldsymbol{d} = \frac{1}{2}\gamma \|\boldsymbol{d}\|^2$ imposes a constraint, and in this form is seen to penalise large magnitudes of the step $\boldsymbol{d}$.

In the trust region technique, a positive number $\Delta > 0$ is defined, which represents the radius of a sphere (i.e. a trust region) inside which the model is considered accurate (or equivalently trusted), and the step size $\boldsymbol{d}$ is computed as:

$$\boldsymbol{d} = \boldsymbol{d}_{tr} = \mathbf{argmin}_d \{ M(\boldsymbol{d}) \}, \quad \text{s.t.} \|\boldsymbol{d}\| \le \Delta \tag{4.19}$$

The central part in the algorithms of the hybrid optimisation methods described later satisfies the following form:

```
Calculate $\boldsymbol{d}$ by (4.18), or (4.19)
if $F(\boldsymbol{\sigma}+\boldsymbol{d}) < F(\boldsymbol{\sigma})$
    $\boldsymbol{\sigma} = \boldsymbol{\sigma} + \boldsymbol{d}$;                                  (4.20)
Update $\gamma$ or $\Delta$
```

If the step $\boldsymbol{d}$ is a descent direction, the conductivity $\boldsymbol{\sigma}$ is updated with a full step, i.e. by taking the step factor $\alpha = 1$; Otherwise, if a descending condition is not satisfied, $\boldsymbol{d}$ is rejected ($\alpha = 0$) and we do not move from the iterate $\boldsymbol{\sigma}$. This does not mean an end to the iterative optimisation process since the problem can be treated by modifying the damping parameter γ or the trust region radius Δ and recalculating the step with the hope that a descent direction will be achieved in the next iterate.

The process of updating γ or Δ is controlled by the gain ratio (ρ) which features the quality of the model function *M* or equivalently determines how much the model *M* agrees with the objective function *F*. After calculating the step ***d***, the gain ρ can be evaluated using the following formula:

$$\rho = \frac{F(\boldsymbol{\sigma}) - F(\boldsymbol{\sigma} + \boldsymbol{d})}{M(0) - M(\boldsymbol{d})} \tag{4.21}$$

where the denominator defines the predicted reduction in the objective function whereas the numerator evaluates the actual reduction in the function value.

By construction the denominator is positive. Hence, based on the value of the gain ratio three cases can be identified:

a) If ρ is negative, it means the numerator is negative, which infers that the step ***d*** was not descent and must be rejected. Hence, it is necessary to constrain the step to be smaller and repeat the iteration.
b) If ρ is positive and smaller than 1, the penalty should be increased on the magnitude of the step in the next iteration.
c) If ρ is close to 1, the model function is a good approximation of the objective function, and taking a larger step in the next iteration would be recommended.

Both damped and trust region methods provide means to implement these conditions. In a damped method, a small value of the gain ρ indicates that the parameter γ should be increased in the next iteration, which effectively reduce the step size; whereas a large value of ρ shows that the model *M* matches very well the behaviour of the objective function *F*, which suggests to decrease γ in the next iteration. Marquardt [109] proposed a strategy to monitor the value of γ, which has the form:

```
if $\rho < 0.25$
    $\gamma = \gamma * 2$;
else if $\rho > 0.75$
    $\gamma = \gamma / 3$;
```
(4.22)

Experience shows that the choice of thresholds 0.25 and 0.75 works fine for many problems but minor changes to these values will not affect the method. However, the method is quite sensitive to the numbers $m_1 = 2$, and $m_2 = 3$ since computational experiments show that considerably unstable inverse problems would require modification to these values. In this thesis, the following values have been selected, $m_1 = m_2 = 2$. Nielsen [110] mentioned that the discontinuity of the values of γ across 0.25 and 0.75 produces a flutter as demonstrated in Figure 4.1 and recommended the following strategy which we adopted throughout the thesis:

```
if $\rho > 0$
  $\gamma = \gamma * \max(0.5, 1-(2\rho-1)^3)$;
  $\eta$=2;
else
   $\gamma = \gamma * \eta$;   $\eta = \eta * 2$;
   if $\eta > 32$ exit
```

(4.23)

Note that a stopping condition has been added to Nielsen's method if the method fails to produce a descending condition after five consecutive trials.

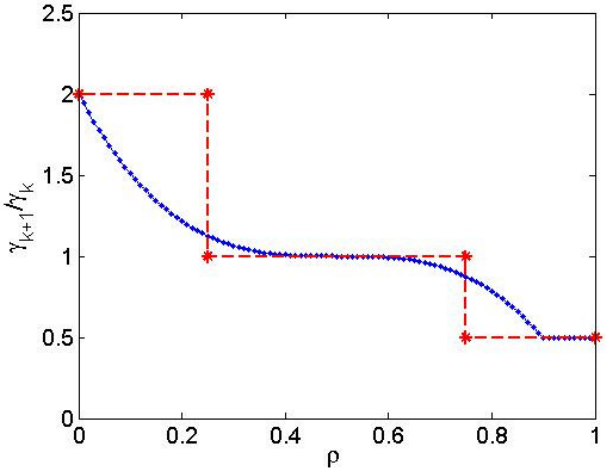

Figure 4.1: Updating of the damping parameter (γ) by (4.23) (blue line) and by Marquardt method (4.22) (red line)

With regard to the trust region based method, the step length ***d*** is controlled by the size of the radius Δ. The following strategy is adopted in this thesis:

```
if $\rho < 0.25$
    $\Delta = \|d\| / 2$;
else
    if $\rho > 0.75$
        $\Delta = \max(\Delta, 2*\|d\|)$;
    else
        $\Delta = \Delta$;
```

(4.24)

4.2.2 Regularised Gauss Newton method

The Gauss Newton method is the basis of Newton type methods used for solving non-linear least squares problems. In order to derive the equations for this method, one first needs formulas for the gradient ∇F and the Hessian $\nabla^2 F$ of the objective function F. Using the integral expression of the objective function in equation (4.2), the derivatives of F can be derived and expressed in terms of the Jacobian $\boldsymbol{J}$ (an $m \times n$ matrix representing the first order partial derivative of the residual function $\mathbf{r}$ with respect to conductivity variables (equation (4.3))) defined by:

$$\boldsymbol{J} = \left[\frac{\partial r_i}{\partial \sigma_j} \right]_{\substack{i=1,\dots,m \\ j=1,\dots,n}} \tag{4.25}$$

Hence:

$$\nabla F(\boldsymbol{\sigma}) = \sum_{i=1}^{m} \mathrm{r}_i(\boldsymbol{\sigma}) \nabla \mathrm{r}_i(\boldsymbol{\sigma}) = \boldsymbol{J}(\boldsymbol{\sigma})^{\mathrm{T}} \mathbf{r}(\boldsymbol{\sigma}) \tag{4.26}$$

$$\begin{aligned} \nabla^2 F(\boldsymbol{\sigma}) = \boldsymbol{H} &= \sum_{i=1}^{m} \nabla \mathrm{r}_i(\boldsymbol{\sigma}) \nabla \mathrm{r}_i(\boldsymbol{\sigma})^{\mathrm{T}} + \sum_{i=1}^{m} \mathrm{r}_i(\boldsymbol{\sigma}) \nabla^2 \mathrm{r}_i(\boldsymbol{\sigma}) \\ &= \boldsymbol{J}(\boldsymbol{\sigma})^{\mathrm{T}} \boldsymbol{J}(\boldsymbol{\sigma}) + \sum_{i=1}^{m} \mathrm{r}_i(\boldsymbol{\sigma}) \nabla^2 \mathrm{r}_i(\boldsymbol{\sigma}) \\ &= \boldsymbol{J}(\boldsymbol{\sigma})^{\mathrm{T}} \boldsymbol{J}(\boldsymbol{\sigma}) + \boldsymbol{Q}(\boldsymbol{\sigma}) \end{aligned} \tag{4.27}$$

By substituting (4.26), (4.27) into (4.14) and using (4.3), the equations for the standard Newton's method described in section (4.1.2) can be written as:

$$\boldsymbol{H}\, \boldsymbol{d}_N = -\nabla F(\boldsymbol{\sigma}) \Leftrightarrow (\boldsymbol{J}^{\mathrm{T}} \boldsymbol{J} + \boldsymbol{Q}) \boldsymbol{d}_N = -\boldsymbol{J}^{\mathrm{T}} (\boldsymbol{F}(\boldsymbol{\sigma}) \text{-} \boldsymbol{D}) \tag{4.28}$$

$$\boldsymbol{\sigma} = \boldsymbol{\sigma} + \boldsymbol{d}_N \tag{4.29}$$

where $\boldsymbol{D} \in \mathbb{R}^m$ is the measurement data set. If we exclude the second order term, $\boldsymbol{Q}$, from the Hessian $\nabla^2 F(\boldsymbol{\sigma})$, Newton's method simplifies to the Gauss Newton method with the following equations:

$$(\boldsymbol{J}^{\mathrm{T}} \boldsymbol{J}) \boldsymbol{d}_{GN} = -\boldsymbol{J}^{\mathrm{T}} (\boldsymbol{F}(\boldsymbol{\sigma}) \text{-} \boldsymbol{D}) \tag{4.30}$$

$$\boldsymbol{\sigma} = \boldsymbol{\sigma} + \boldsymbol{d}_{GN} \tag{4.31}$$

The motivation for deriving the Gauss Newton method is that considerable computational saving can be achieved by ignoring the $\boldsymbol{Q}$ term, as this computation requires the specification and calculation of $mn(n+1)/2$ second order derivative terms $\nabla^2 r_i$. In MIT, as for other electrical tomography modalities, it is often straightforward to form the Jacobian $\boldsymbol{J}$ from calculations of first order partial derivatives, which is used to compute the gradient ∇F. Hence, by knowing the Jacobian the approximate Hessian as adopted in the Gauss Newton method can be obtained directly with a simple matrix multiplication. When using this approximation, however, it can be seen that the Hessian is expressed only in terms of first order derivatives. The question is then, under which conditions can this approximation be considered valid. It is clear from the structure of $\boldsymbol{Q}$ in formula (4.27) that this simplification can be performed only when r_i is small (i.e. for problems with small residuals) or when r_i is nearly a linear function (i.e. $\nabla^2 r_i(\boldsymbol{\sigma})$ is small). In practice, many least squares problems have small residuals at the solution, and in such cases Gauss Newton method can give performance similar to Newton's method. However, for large residual problems where the considered assumption cannot be justified and if the second order term $\boldsymbol{Q}$ cannot be exactly determined, Quasi-Newton methods also termed "variable metric" methods can be a possible solution. Using these methods, the term $\boldsymbol{Q}$ can be replaced with a Quasi-Newton approximation matrix $\boldsymbol{G}$ and the search direction is calculated as follows:

$$(\boldsymbol{J}^{\mathrm{T}}\boldsymbol{J}+\boldsymbol{G})\boldsymbol{d}_{qN}=-\boldsymbol{J}^{\mathrm{T}}(\boldsymbol{F}(\boldsymbol{\sigma})\text{-}\boldsymbol{D}) \tag{4.32}$$

Two popular methods for constructing the matrix $\boldsymbol{G}$ are the Davidon-Fletcher-Powel DFP procedure [111], and the Broyden-Fletcher-Goldfarb-Shanno BFGS method [112-115].

Since the MIT inverse problem is ill-posed and underdetermined, the Jacobian $\boldsymbol{J}$ is ill-conditioned as described in section (3.1). There are number of factors contributing to the ill-conditioning of the Jacobian. First, the measurement sensitivity near the periphery of a test object with a homogenous conductivity is much larger compared to the central region [36], hence the secondary inductive signal coupled to the coils is mainly dominated by the contribution from the conductive elements near the periphery of the object space. Second, the measured data is contaminated with hardware and arithmetic noise which is transferred to the Jacobian. In this case, the minimization problem would attempt to recover the conductivity that fits the noise as well. Another problem is that $\boldsymbol{J}$ is a rectangular ($m \times n$) matrix where the collected number of measurements m is usually less than the number of unknown conductivity elements n. While the Jacobian is ill-conditioned (i.e. $\boldsymbol{J}$ has a large condition number) the system $\boldsymbol{J}^{\mathrm{T}}\boldsymbol{J}$ used in (4.30) to approximate the Hessian in the Gauss Newton method will be even more ill-conditioned because it will have twice the condition number of $\boldsymbol{J}$. A direct consequence of this condition is the conductivity solution will be very prone to noise and will not be unique.

A common way to stabilize the solution and allow for uniqueness is to use regularisation. This topic will be investigated and discussed in depth in the next chapter. For now, the topic of interest is the nonlinear optimization method, and hence a simple common and popular regularisation method will be employed namely Tikhonov smoothing regularisation. Using this regularisation method, instead of minimizing the original objective function F, an approximate objective function $\widetilde{F}$ will be adopted, as defined by:

$$\widetilde{F}(\boldsymbol{\sigma}) = \underbrace{\frac{1}{2}\|\mathbf{r}(\boldsymbol{\sigma})\|^2}_{F(\sigma)} + \underbrace{\frac{1}{2}\lambda\|\boldsymbol{L\sigma}\|^2}_{P(\sigma)} \tag{4.33}$$

where $P(\boldsymbol{\sigma})$ is a 2-norm penalty functional imposing a smoothing constraint on the conductivity distribution by means of a regularisation operator $\boldsymbol{L}$ and a regularisation parameter also termed a “hyper-parameter”. The task is therefore to seek the argument $\boldsymbol{\sigma}$ that minimizes the original objective function F, and at the same time, reduces the magnitude of the penalty P. The hyper parameter λ is chosen to control the weighting of the regularisation imposed on the solution. By following the same procedure in deriving expressions for the gradient $\nabla\widetilde{F}$ and the Hessian $\nabla^2\widetilde{F}$, a regularised version of the Gauss Newton method can be constructed, which has the equations:

$$(\boldsymbol{J}_k{}^{\mathrm{T}}\boldsymbol{J}_k + \lambda\boldsymbol{L}^{\mathrm{T}}\boldsymbol{L})\boldsymbol{d}_{rGN} = -\boldsymbol{J}_k{}^{\mathrm{T}}(\boldsymbol{F}(\boldsymbol{\sigma}_k)\text{-}\boldsymbol{D}) - \lambda\boldsymbol{L}^{\mathrm{T}}\boldsymbol{L}\boldsymbol{\sigma}_k \tag{4.34}$$

$$\boldsymbol{\sigma}_{k+1} = \boldsymbol{\sigma}_k + \boldsymbol{d}_{rGN} \tag{4.35}$$

In (4.34) and (4.35), the subscript k has been added to show the terms that are updated for every iteration of the optimisation procedure. Using the regularised Gauss Newton method, the regularisation parameter λ is kept constant throughout and can be selected using an empirical method or an appropriate parameter selection algorithm. Some workers in the field of MIT have used this standard Gauss Newton method as a nonlinear optimisation strategy for solving the conductivity inverse problem. Soleimani [36] combined this method with a line search strategy to further optimise reduction in the objective function especially when the starting guess is far from the solution. Using this approach an appropriate step length α should be computed and the conductivity is updated with $\alpha\boldsymbol{d}_{rGN}$ instead of full step $\boldsymbol{d}_{rGN}$. In this thesis however, the method is used in its standard form described by (4.34)-(4.35) as a comparison tool for evaluating the performance of the special methods based on the damping and trust region techniques. Figure 4.3 shows the image reconstruction algorithm for this method.

As illustrated in Figure 4.3, the initial guess $\boldsymbol{\sigma}_0$ is computed via a direct reconstruction method such as linear regularised Tikhonov method with a smoothing operator ($\boldsymbol{R} = \boldsymbol{L}^{\mathrm{T}}\boldsymbol{L}$) and a regularisation parameter λ_0. This latter was chosen based on the order of magnitude of the elements in $\left[\boldsymbol{J}_0{}^T\boldsymbol{J}_0\right]$ as in [107], where $\boldsymbol{J}_0$ is the Jacobian computed by assuming a homogenous conductivity distribution (e.g, σ = 1 Sm^{-1}) in the object under investigation. Hence, this gives:

$$\lambda_0 = \varepsilon_1 * \max_{i=1,\ldots,n}\left(\left[\boldsymbol{J}_0{}^T\boldsymbol{J}_0\right]_{(i,i)}\right) \tag{4.36}$$

where ε_1 is chosen by the user. In this thesis, for conductivity problems with noise free measurement data, less regularisation is required so a small value of λ_0 is preferred by setting $\varepsilon_1 = 1$, whereas for noise contaminated data, a larger value of λ_0 is a safe choice (for example: $\varepsilon_1 = 10^2$ or even $\varepsilon_1 = 10^3$). By knowing λ_0, the regularisation parameter λ used in the iterative cycles is selected as follows:

$$\lambda = \varepsilon_2 * \lambda_0 \tag{4.37}$$

where ε_2 is a user specified factor (eg. $\varepsilon_2 \in \left[10^{-3}, 1\right]$). Additional constraints are applied on elements with negative values and on elements with conductivities larger than the assumed maximum conductivity in the target in order to stabilize the solution.

The stopping criterion for this method is chosen so as to terminate the iteration when the following descending condition for the objective function $\widetilde{F}$ is <u>not</u> met:

$$\widetilde{F}(\boldsymbol{\sigma}_{k+1}) < \widetilde{F}(\boldsymbol{\sigma}_k) \tag{4.38}$$

As an example of the performance of this nonlinear optimization method, consider the simulated simple phantom (P1) approximating a head with a stroke region shown in Figure 4.2. The phantom consists of a background cylinder (diameter: 20 cm; height: 16 cm) centred at the origin, and a cylindrical perturbation (diameter: 4 cm; height: 8 cm) centred at (0, 0, 5) cm in the (x, y, z) co-ordinate space. The phantom has been discretised into 5056 cubic voxels of 10x10x10 mm^3 resolution, of which 96 elements were allocated to the perturbation. Notice the blocky form of the edges of the background and the perturbation, which do not conform to the smooth cylindrical boundaries of the real objects. This is a problem from which this type of regular cubic discretisation suffers, especially at low resolutions. However, in this study the interest lies in the performance of several optimization methods using a phantom of a given structure, and the treatment of the edges is not the immediate topic of investigation here. The background and the perturbation were assigned conductivities of 0.16 Sm^{-1} and , 1.1 Sm^{-1} respectively corresponding to reported values for biological tissues of white matter and blood [26]. The MIT system used in this computational experiment is depicted in Figure 4.2 and is the same model presented in (section 3.3), which consists of 16 pairs of exciter and receiver coils arranged in two circles of radii 141.5 mm and 131.5 mm respectively. The excitation coils are sequentially driven with a time varying sinusoidal unit current for simplicity. The system has been modelled in a commercial FE software (COMSOL by Multiphysiscs), and a simulation with empty space (i.e. no target) is performed to compute the primary magnetic vector potential $\boldsymbol{A}_0$ in the space designated for the phantom. The forward problem is solved using the custom eddy current solver based on the impedance method presented in Chapter 3. The excitation frequency is set to 10 MHz. In order to increase the number of measurements, 9 planes of projections were taken by displacing the coil array along the z direction in steps of 20 mm over the interval $z \in [-80, 80]$ mm. The multiple measurement planes also provide more eddy current information to be obtained from the volume of the phantom. In total, 2304 independent simulated measurement data were collected and no noise has been added to the data. The same mesh for solving the forward problem was employed for the inverse problem. The regularised Gauss Newton method is used to find the conductivity map that minimizes the difference between the simulated measured voltages and the calculated data using the forward model. Figure 4.4 shows the reduction of the objective function $\widetilde{F}$ during the iterative process. The image reconstruction results are shown in Figure 4.6 with vertical and different horizontal conductivity maps along the z axis. The results can be compared against the true conductivity maps shown in Figure 4.5.

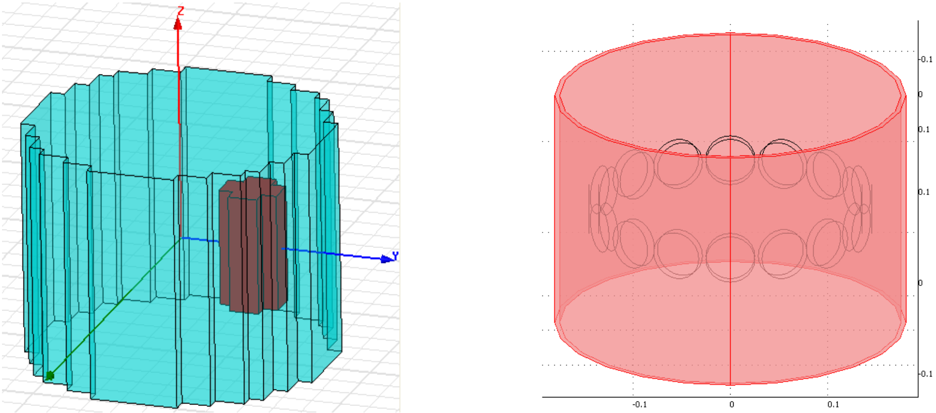

a) b)

Figure 4.2: Phantom (P1) and the MIT system model

```
Problem: $\underset{\sigma \in R^n}{\operatorname{argmin}} \left\{ \widetilde{F}(\boldsymbol{\sigma}) \right\}$; $\widetilde{F}(\boldsymbol{\sigma}) = \frac{1}{2}\left\| \boldsymbol{F}(\boldsymbol{\sigma}) - \boldsymbol{D} \right\|^2 + \frac{1}{2}\lambda \left\| \boldsymbol{L}\boldsymbol{\sigma} \right\|^2$
Algorithm:
Select the regularisation parameter
$\lambda_0 = \varepsilon_1 * \max_{i=1,\dots,n}\left( \left[ \boldsymbol{J}_0^{\ T}\boldsymbol{J}_0 \right]_{(i,i)} \right)$; where $\boldsymbol{J}_0$: Jacobian calculated for homogenous $\boldsymbol{\sigma}$
Find $\boldsymbol{\sigma_0}$ using single step reconstruction:
$\boldsymbol{\sigma}_0 = -(\boldsymbol{J}_0^{\mathrm{T}}\boldsymbol{J}_0 + \lambda_0 \boldsymbol{L}^{\mathrm{T}}\boldsymbol{L})^{-1}\boldsymbol{J}_0^{\mathrm{T}}\boldsymbol{D}$;
Evaluate the objective function:
$\widetilde{F}(\boldsymbol{\sigma}_0) = \frac{1}{2}\left\| \boldsymbol{F}(\boldsymbol{\sigma}_0) - \boldsymbol{D} \right\|^2 + \frac{1}{2}\lambda_0 \left\| \boldsymbol{L}\boldsymbol{\sigma}_0 \right\|^2$;
Compute the gradient: $\boldsymbol{g} = \boldsymbol{J}(\boldsymbol{\sigma}_0)^{\mathrm{T}}(\boldsymbol{F}(\boldsymbol{\sigma}_0) - \boldsymbol{D}) + \lambda_0 \boldsymbol{L}^{\mathrm{T}}\boldsymbol{L}\boldsymbol{\sigma}_0$;
Calculate: $\boldsymbol{A} = \boldsymbol{J}(\boldsymbol{\sigma}_0)^{\mathrm{T}}\boldsymbol{J}(\boldsymbol{\sigma}_0)$;
Set $\lambda = \varepsilon_2 * \lambda_0$; $k = 0$; set $k_{max}$; $exit$ = false;
while $k < k_{max}$ and $exit \neq$ true
        Compute the Hessian: $\boldsymbol{H}_{rGN} = \boldsymbol{A} + \lambda \boldsymbol{L}^{\mathrm{T}}\boldsymbol{L}$;
        Calculate the step: $\boldsymbol{d}_{rGN} = -\boldsymbol{H}_{rGN}^{\ \ -1}\boldsymbol{g}$;
        Update the conductivity map: $\boldsymbol{\sigma}_{New} = \boldsymbol{\sigma}_k + \boldsymbol{d}_{rGN}$ ;
        Constrain the conductivity map: $\begin{cases} i = 1{:}n \,|\, (\boldsymbol{\sigma}_{New}(i) < 0) = \tau \simeq 0 \\ i = 1{:}n \,|\, (\boldsymbol{\sigma}_{New}(i) > \boldsymbol{\sigma}_{\max}) = \boldsymbol{\sigma}_{\max} \end{cases}$
        Evaluate the objective function: $\widetilde{F}(\boldsymbol{\sigma}_{New}) = \frac{1}{2}\left\| \boldsymbol{F}(\boldsymbol{\sigma}_{New}) - \boldsymbol{D} \right\|^2 + \frac{1}{2}\lambda \left\| \boldsymbol{L}\boldsymbol{\sigma}_{New} \right\|^2$;
        if $\widetilde{F}(\boldsymbol{\sigma}_{New}) < \widetilde{F}(\boldsymbol{\sigma}_k)$
            $\boldsymbol{\sigma}_{k+1} = \boldsymbol{\sigma}_{New}$;
            $\boldsymbol{g} = \boldsymbol{J}(\boldsymbol{\sigma}_{k+1})^{\mathrm{T}}(\boldsymbol{F}(\boldsymbol{\sigma}_{k+1}) - \boldsymbol{D}) + \lambda \boldsymbol{L}^{\mathrm{T}}\boldsymbol{L}\boldsymbol{\sigma}_{k+1}$;
            $\boldsymbol{A} = \boldsymbol{J}(\boldsymbol{\sigma}_{k+1})^{\mathrm{T}}\boldsymbol{J}(\boldsymbol{\sigma}_{k+1})$;
        else
            $exit$ = true ;
        end
        $k = k+1$;
end
```

Figure 4.3: Regularised Gauss Newton Algorithm

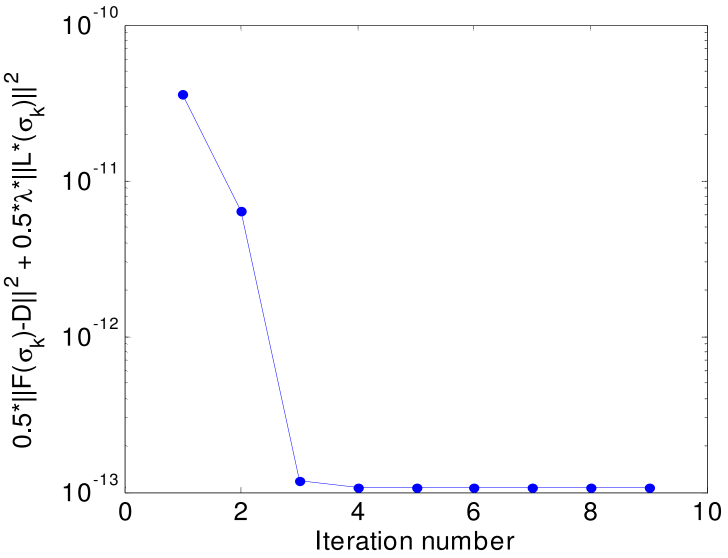

Figure 4.4: Convergence plot illustrating the minimisation of the objective function using the regularised Gauss Newton method.

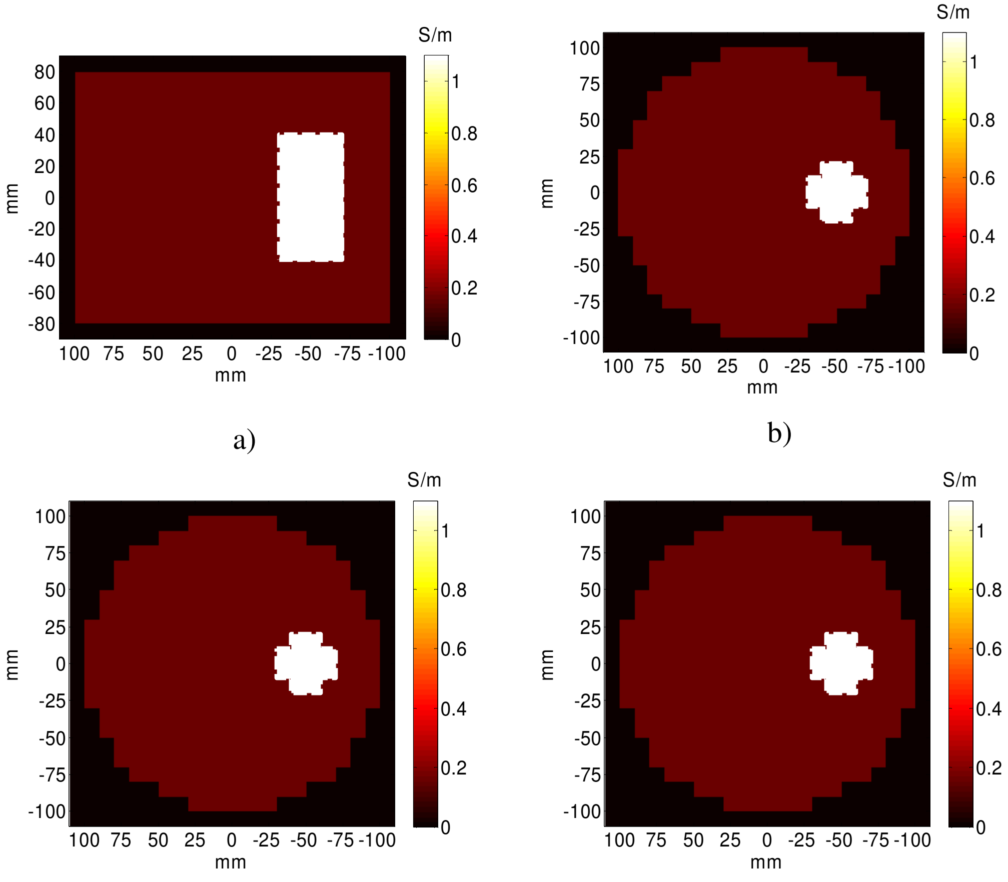

a)

b)

c)

d)

Figure 4.5: True conductivity maps for a) vertical slice (*x*=0) mm, b) horizontal slices in different *z* levels (*z*=-40*;* *z*=0*;* *z*=40) mm

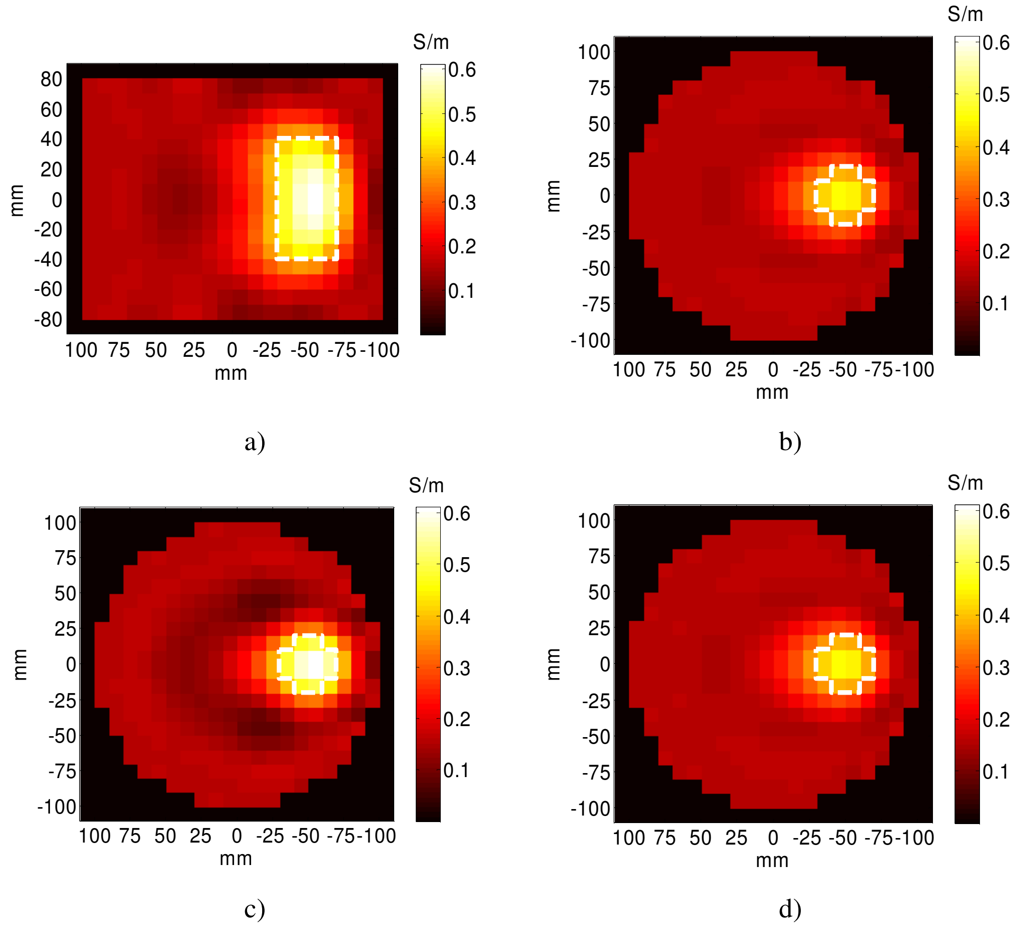

a) b) c) d)

Figure 4.6: Reconstruction of conductivity distribution showing a) vertical slice (x=0) mm, b) horizontal slices in different z levels (z=-40; z=0; z=40) mm with No noise added to the data.

4.2.3 Regularised Levenberg Marquardt method

Levenberg [116] and Marquardt [109] suggested a modification to the Gauss Newton method by implementing the damping technique described in (section 4.2.1) to calculate the step vector $\boldsymbol{d}_{LM}$. The basic iteration using this method can be given by the equations:

$$(\boldsymbol{J}^{\mathrm{T}}\boldsymbol{J}+\gamma\boldsymbol{I})\boldsymbol{d}_{LM} = -\boldsymbol{J}^{\mathrm{T}}(\boldsymbol{F}(\boldsymbol{\sigma})\text{-}\boldsymbol{D}) \tag{4.39}$$

$$\boldsymbol{\sigma} = \boldsymbol{\sigma} + \boldsymbol{d}_{LM} \tag{4.40}$$

Notice that the difference between the Gauss Newton and the Levenberg Marquardt (LM) methods is the new term $\gamma\boldsymbol{I}$ which introduces the following effects:

a) For γ sufficiently positive, the term $\gamma\boldsymbol{I}$ can act as a regularisation operator, and hence can make the coefficient matrix ($\boldsymbol{J}^{\mathrm{T}}\boldsymbol{J}+\gamma\boldsymbol{I}$) positive definite. This ensures that $\boldsymbol{d}_{LM}$ is a descent direction.

b) For very large values of γ, the effect of the term $\gamma\boldsymbol{I}$ dominates that of $\boldsymbol{J}^{\mathrm{T}}\boldsymbol{J}$ in determining the step $\boldsymbol{d}_{LM}$, so that:

$$\boldsymbol{d}_{LM} \approx -\frac{1}{\gamma}\boldsymbol{J}^{\mathrm{T}}(\boldsymbol{F}(\boldsymbol{\sigma})\text{-}\boldsymbol{D}) = -\frac{1}{\gamma}\boldsymbol{g} = -\frac{1}{\gamma}\boldsymbol{d}_{sd} \tag{4.41}$$

which represents a step $\alpha = 1/\gamma$ of the steepest descent method (see section 4.1.1).

c) When γ is too small compared to the elements in the coefficient matrix ($\boldsymbol{J}^{\mathrm{T}}\boldsymbol{J}$), $\boldsymbol{d}_{LM}$ is effectively close to the Gauss Newton step.

In the iterative optimization process of the LM method, the damping parameter γ can be decreased or increased depending on the value of the gain ratio ρ which reflects how good the reduction in the objective function F compares with that of the quadratic model M (see section 4.2.1). Usually one starts with a large value of γ, which can make the steepest descent method more influential than the Gauss Newton method in determining the step $\boldsymbol{d}_{LM}$. This is a sensible approach especially if the first guess is far from the solution $\boldsymbol{\sigma}^*$. Through the iterations, γ is reduced whenever the objective function records a descending direction compatible with that of the model M. This is intended to push the algorithm towards the Gauss Newton method as we approach the final stage of the interation. When the iterate solution attains the local minimiser $\boldsymbol{\sigma}^*$, the LM method switches to the steepest descent method whereby γ is increased to penalise large magnitudes of the step $\boldsymbol{d}_{LM}$. This is meant to prevent the algorithm from a possible unwanted divergence away from the minimiser $\boldsymbol{\sigma}^*$. Thus, it is clear that the LM method can be considered as a hybrid method switching between a dominant steepest descent method and a dominant Gauss Newton method. This can be considered a good optimization strategy since the steepest descent method can offer efficient stability and the Gauss Newton method can provide fast convergence properties, which can be combined and employed in a sophisticated manner inside a single optimisation scheme.

An alternative version of the LM method has been suggested for the EIT ill-posed problem by attempting to apply the damping procedure to the regularised Gauss Newton method described by equations (4.34) and (4.35) [117, 118]. Hence the LM iteration is adapted as follows:

$$(\boldsymbol{J}_k^{\mathrm{T}}\boldsymbol{J}_k + \gamma_k \boldsymbol{I} + \lambda \boldsymbol{L}^{\mathrm{T}}\boldsymbol{L})\boldsymbol{d}_{rLM} = -\boldsymbol{J}_k^{\mathrm{T}}(\boldsymbol{F}(\boldsymbol{\sigma}_k)\text{-}\boldsymbol{D}) - \lambda \boldsymbol{L}^{\mathrm{T}}\boldsymbol{L}\boldsymbol{\sigma}_k \tag{4.42}$$

$$\boldsymbol{\sigma}_{k+1} = \boldsymbol{\sigma}_k + \boldsymbol{d}_{rLM} \tag{4.43}$$

The rational behind this modification is to be able to supply prior information about the solution through the regularisation operator $\boldsymbol{L}$ and the hyper-parameter λ in addition to the regularisation properties provided by the identity matrix $\boldsymbol{I}$ within the damping term.

The LM method described by equations (4.42) and (4.43) has been implemented in this thesis. While the regularisation parameter λ is kept fixed, the damping parameter γ is updated as illustrated in section 4.2.1. The updating is monitored via the gain ratio ρ given by:

$$\rho = \frac{\widetilde{F}(\boldsymbol{\sigma}_k) - \widetilde{F}(\boldsymbol{\sigma}_k + \delta\boldsymbol{\sigma}_k)}{M(0) - M(\delta\boldsymbol{\sigma}_k)} \tag{4.44}$$

where $\widetilde{F}$ is the approximate Tikhonov objective function described by equation (4.33). Note that the step $\boldsymbol{\delta\sigma}_k$ is used instead of $\boldsymbol{d}_{rLM}$ in the above formula. The reason is that after updating the current iterate $\boldsymbol{\sigma}_k$ with the step $\boldsymbol{d}_{rLM}$ as in (4.43), additional regularisation in the form of non-negativity constraining is applied and the conductivity vector $\boldsymbol{\sigma}_{k+1}$ can further be updated if it contains negative conductivities. Hence, the non-negativity constrained $\boldsymbol{\sigma}_{k+1}$ is validated as the updated conductivity vector, and the actual step used to produce this vector can be computed by:

$$\delta\boldsymbol{\sigma}_k = \boldsymbol{\sigma}_{k+1} - \boldsymbol{\sigma}_k \tag{4.45}$$

The denominator in (4.44) is the reduction in the quadratic model (4.17) where:

$$\nabla\widetilde{F}(\boldsymbol{\sigma}_k) = \boldsymbol{g}_k = \boldsymbol{J}_k^{\mathrm{T}}(\boldsymbol{F}(\boldsymbol{\sigma}_k)\text{-}\boldsymbol{D}) + \lambda \boldsymbol{L}^{\mathrm{T}}\boldsymbol{L}\boldsymbol{\sigma}_k \tag{4.46}$$

and

$$\boldsymbol{H}_k = \boldsymbol{J}_k{}^{\mathrm{T}}\boldsymbol{J}_k + \lambda \boldsymbol{L}^{\mathrm{T}}\boldsymbol{L} \tag{4.47}$$

Therefore:

$$M(0) - M(\delta\boldsymbol{\sigma}_k) = -\delta\boldsymbol{\sigma}_k{}^{\mathrm{T}}\boldsymbol{g}_k - \frac{1}{2}\delta\boldsymbol{\sigma}_k{}^{\mathrm{T}}\boldsymbol{H}_k\delta\boldsymbol{\sigma}_k \tag{4.48}$$

A large value of ρ indicates that $M(\delta\boldsymbol{\sigma}_k)$ is a good approximation to $\widetilde{F}(\boldsymbol{\sigma}_k + \delta\boldsymbol{\sigma}_k)$, and hence we can reduce γ so that the next LM step is closer to the Gauss Newton step. If ρ is small, then $M(\delta\boldsymbol{\sigma}_k)$ is a poor approximation, so we should increase γ with the aim to approach the steepest descent direction and penalize (i.e. reduce) the step length $\|\delta\boldsymbol{\sigma}_k\|$. The strategy used in this chapter for updating the value of γ has been given by the algorithm in (4.23).

The following criterion was used to stop the iterative minimization procedure [107]:

$$\|\boldsymbol{\sigma}_{k+1} - \boldsymbol{\sigma}_k\| < \varepsilon_3\left(\|\boldsymbol{\sigma}_k\| + \varepsilon_3\right) \tag{4.49}$$

i.e. when the change in $\boldsymbol{\sigma}_k$, $\delta\boldsymbol{\sigma}_k$, is very small. Here, ε_3 is a small positive number specified by the user. Using this criterion, the algorithm stops either when $\delta\boldsymbol{\sigma}_k$ is smaller than ε_3 times $\|\boldsymbol{\sigma}_k\|$ if this latter is large, or smaller than ε_3^2 if $\|\boldsymbol{\sigma}_k\|$ is close to zero. As mentioned earlier, in the final stage of the iterative process, the LM algorithm reaches a point where it switches back to the steepest descent method since the Gauss Newton step is not anymore a good step. Hence, this is seen in γ being increased continuously in an attempt to produce a step that yields a large ρ (i.e. a good fit between the gain in the model M and the reduction in $\widetilde{F}$). Consequently, this augmentation of γ leads to a continuous reduction in the step size $\boldsymbol{d}_{rLM}$, resulting in small $\|\delta\boldsymbol{\sigma}_k\|$, and the process will be terminated by (4.49).

The complete algorithm is presented below. The algorithm is not very sensitive to the choice of the initial value of γ as long as it is sufficiently large. In this chapter, $\gamma = 10^{-3}\lambda_0$ is selected, where λ_0 is the regularisation parameter used to produce the initial guess $\boldsymbol{\sigma}_{\mathbf{0}}$. The regularisation parameter (λ), however, is chosen in similar way to the Gauss Newton method. In order to test the performance of the algorithm in

MIT, 3D image reconstruction was carried out with the same example (P1) as in section (4.2.2). Recall, the measured data used for image reconstruction is free of noise. The convergence of the objective function $\widetilde{F}$ is shown in Figure 4.8. Image reconstruction results are depicted in Figure 4.9.

```
Problem: $\underset{\sigma\in R^n}{\operatorname{argmin}}\left\{\widetilde{F}(\boldsymbol{\sigma})\right\}$; $\widetilde{F}(\boldsymbol{\sigma})=\frac{1}{2}\left\|\boldsymbol{F}(\boldsymbol{\sigma})-\boldsymbol{D}\right\|^2+\frac{1}{2}\lambda\left\|\boldsymbol{L\sigma}\right\|^2$
Select the regularisation parameter
$\lambda_0=\varepsilon_1*\max_{i=1,\ldots,n}\left(\left[\boldsymbol{J}_0{}^T\boldsymbol{J}_0\right]_{(i,i)}\right)$; where $\boldsymbol{J}_0$: Jacobian calculated for homogenous $\boldsymbol{\sigma}$
Find $\boldsymbol{\sigma_0}$ using single step reconstruction:
$\boldsymbol{\sigma_0}=-(\boldsymbol{J}_0{}^{\mathrm{T}}\boldsymbol{J}_0+\lambda_0\boldsymbol{L}^{\mathrm{T}}\boldsymbol{L})^{-1}\boldsymbol{J}_0{}^{\mathrm{T}}\boldsymbol{D}$;
Evaluate the objective function:
$\widetilde{F}(\boldsymbol{\sigma}_0)=\frac{1}{2}\left\|\boldsymbol{F}(\boldsymbol{\sigma}_0)-\boldsymbol{D}\right\|^2+\frac{1}{2}\lambda_0\left\|\boldsymbol{L\sigma}_0\right\|^2$;
Compute the gradient: $\boldsymbol{g}=\boldsymbol{J}(\boldsymbol{\sigma}_0)^{\mathrm{T}}(\boldsymbol{F}(\boldsymbol{\sigma}_0)-\boldsymbol{D})+\lambda_0\boldsymbol{L}^{\mathrm{T}}\boldsymbol{L\sigma}_0$;
Calculate: $\boldsymbol{A}=\boldsymbol{J}(\boldsymbol{\sigma}_0)^{\mathrm{T}}\boldsymbol{J}(\boldsymbol{\sigma}_0)$;
Set $\lambda=\varepsilon_2*\lambda_0$; $\gamma=10^{-3}\times\lambda_0$; $k=0$; set $k_{max}$; $exit$ = false;

while $k<k_{max}$ and $exit\neq$ true
    Compute the Hessian: $\boldsymbol{H}_{rLM}=\boldsymbol{A}+\gamma\boldsymbol{I}+\lambda\boldsymbol{L}^{\mathrm{T}}\boldsymbol{L}$;
    Calculate the step: $\boldsymbol{d}_{rLM}=-\boldsymbol{H}_{rLM}{}^{-1}\boldsymbol{g}$;
    Update the conductivity map: $\boldsymbol{\sigma}_{New}=\boldsymbol{\sigma}_k+\boldsymbol{d}_{rLM}$;
    Constrain the conductivity map: $\begin{cases} i=1{:}n\,|\,(\boldsymbol{\sigma}_{New}(i)<0)=\tau\simeq 0 \\ i=1{:}n\,|\,(\boldsymbol{\sigma}_{New}(i)>\boldsymbol{\sigma}_{\max})=\boldsymbol{\sigma}_{\max} \end{cases}$
    if $\left\|\boldsymbol{\sigma}_{New}-\boldsymbol{\sigma}_k\right\|<\varepsilon_3\left(\left\|\boldsymbol{\sigma}_k\right\|+\varepsilon_3\right)$
        $exit$ = true ;
    else
        Evaluate the objective function: $\widetilde{F}(\boldsymbol{\sigma}_{New})=\frac{1}{2}\left\|\boldsymbol{F}(\boldsymbol{\sigma}_{New})-\boldsymbol{D}\right\|^2+\frac{1}{2}\lambda\left\|\boldsymbol{L\sigma}_{New}\right\|^2$;
        Calculate the gain ratio: $\rho=\left(\widetilde{F}(\boldsymbol{\sigma}_k)-\widetilde{F}(\boldsymbol{\sigma}_{New})\right)\Big/\left(M(0)-M(\boldsymbol{\sigma}_{New}-\boldsymbol{\sigma}_k)\right)$;
        if $\rho>0$
            $\boldsymbol{\sigma}_{k+1}=\boldsymbol{\sigma}_{New}$;
            $\boldsymbol{g}=\boldsymbol{J}(\boldsymbol{\sigma}_{k+1})^{\mathrm{T}}(\boldsymbol{F}(\boldsymbol{\sigma}_{k+1})-\boldsymbol{D})+\lambda\boldsymbol{L}^{\mathrm{T}}\boldsymbol{L}\boldsymbol{\sigma}_{k+1}$;
            $\boldsymbol{A}=\boldsymbol{J}(\boldsymbol{\sigma}_{k+1})^{\mathrm{T}}\boldsymbol{J}(\boldsymbol{\sigma}_{k+1})$;
            $\gamma=\gamma*\max(0.5,1-(2\rho\text{-}1)^3)$; $\eta$=2;
        else
            $\gamma=\gamma*\eta$;
            $\eta=\eta*2$;
            if $\eta>32$ $exit$ = true; end
        end
    $k=k+1$;
end
```

Figure 4.7: Regularised Levenberg Marquardt Method

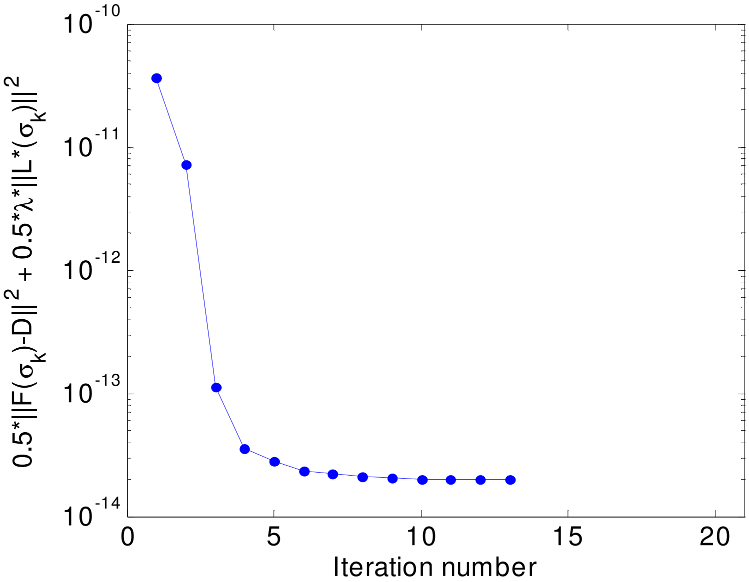

Figure 4.8: **Convergence plot illustrating the minimisation of the objective function using the regularised Levenberg Marquardt Method.**

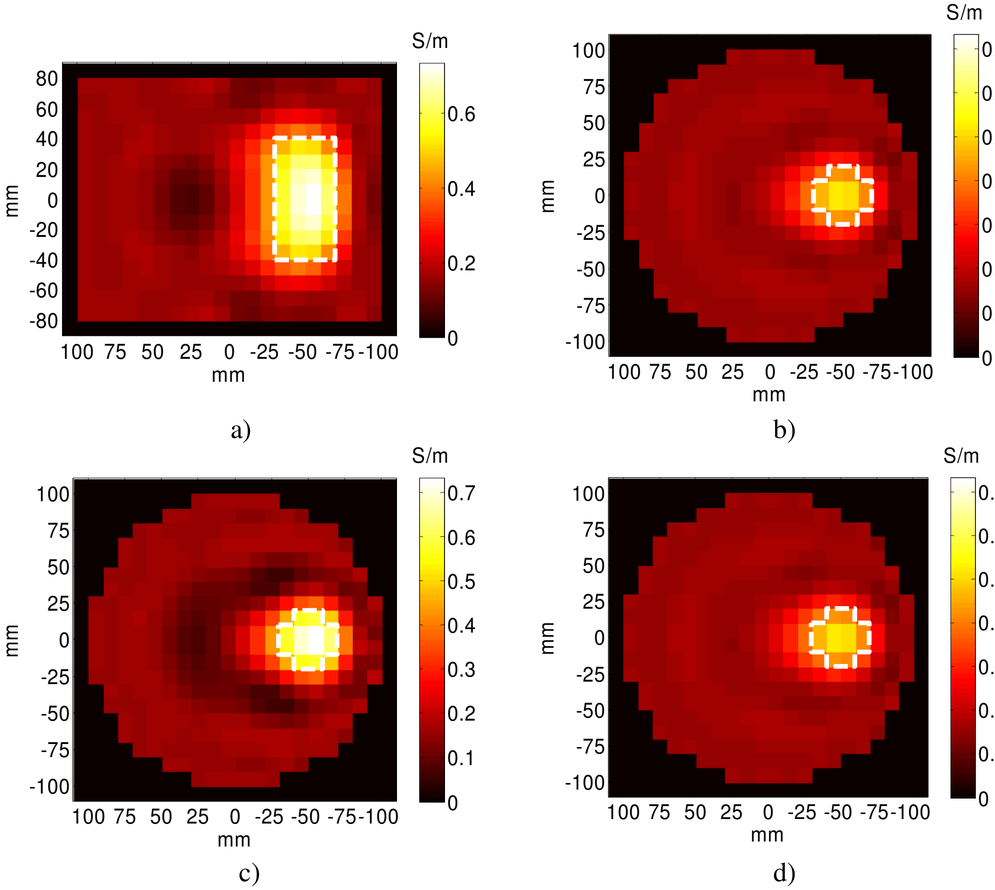

Figure 4.9: **Reconstruction of conductivity distribution showing a) vertical slice (*x*=0) mm, [b); c); d)] horizontal slices in different *z* levels (*z*=-40*;* *z*=0*;* *z*=40) mm with No noise added to the data.**

4.2.4 Damped Gauss Newton method

In the previous section, the LM method has been described as a modification of the Gauss Newton method which employs a damping mechanism in which the length and the search direction of the step $\boldsymbol{d}$ are simultaneously determined. This is done by inserting the term $\gamma_k \boldsymbol{I}$ into the regularised Gauss Newton Hessian, $\boldsymbol{H}_{rGN} = \boldsymbol{J}_k^{\mathrm{T}} \boldsymbol{J}_k + \lambda \boldsymbol{L}^{\mathrm{T}} \boldsymbol{L}$. Although the LM method is a special method which can produce good stability and convergence to the MIT inverse problem, some drawbacks can be observed, which are mainly related to the quality of employed regularisation.

First, the term $\gamma_k \boldsymbol{I}$ imposes regularisation effect on the elements in the coefficient matrix $\boldsymbol{J}_k^{\mathrm{T}} \boldsymbol{J}_k$ via the identity matrix which is referred to as a zero order type regularisation. This is a classical type of regularisation which employs uniform weights to penalize the diagonal of the Hessian $\boldsymbol{H}_{rGN}$. During the iterative process, if the term $\gamma_k \boldsymbol{I}$ is more significant than $\lambda \boldsymbol{L}^{\mathrm{T}} \boldsymbol{L}$, the sensitivity coefficient matrix $\boldsymbol{J}_k^{\mathrm{T}} \boldsymbol{J}_k$ will be mainly penalized by $\gamma_k \boldsymbol{I}$. MIT, like other electrical tomography techniques such as EIT and ECT, suffer from a poor sensitivity in the central region of the target compared to the periphery. Hence, the conductive elements in the centre of the object should preferentially be penalized less than those near the periphery. However, the term $\gamma_k \boldsymbol{I}$ does not conform to this prior information, which makes its application for such electrical modalities not very attractive. Common negative aspects associated with this type of regularisation are usually manifested with noise being reconstructed near the periphery, which is amplified as the iterative procedure progresses.

Second, if the regularisation term $\lambda \boldsymbol{L}^{\mathrm{T}} \boldsymbol{L}$ is on the other hand more influential than $\gamma_k \boldsymbol{I}$ in the iteration, then having a fixed weight of regularisation (i.e. λ remains unchanged) constantly imposed on $\boldsymbol{J}_k^{\mathrm{T}} \boldsymbol{J}_k$ will preserve the smoothness of the image especially if λ is large. As a result, this may prevent reconstruction of high frequency components of the image toward the final stage of the iterative process.

In this section an alternative optimisation approach called “damped Gauss Newton Method”, which aims to deal with the drawbacks associated with regularisation in the

LM method, is presented. The proposed method is a modification of the regularised Gauss Newton method and is described by the equations:

$$(\boldsymbol{J}_k{}^{\mathrm{T}}\boldsymbol{J}_k + \lambda_k \boldsymbol{L}^{\mathrm{T}}\boldsymbol{L})\boldsymbol{d}_{dGN} = -\boldsymbol{J}_k{}^{\mathrm{T}}(\boldsymbol{F}(\boldsymbol{\sigma}_k)\text{-}\boldsymbol{V}) - \lambda_k \boldsymbol{L}^{\mathrm{T}}\boldsymbol{L}\boldsymbol{\sigma}_k \tag{4.50}$$

$$\boldsymbol{\sigma}_{k+1} = \boldsymbol{\sigma}_k + \boldsymbol{d}_{dGN} \tag{4.51}$$

where the regularisation parameter λ_k is now adaptable and selected in an identical fashion to the damping parameter γ_k. In this way, the identity matrix and the extra regularisation parameter, which are found in the LMM, can be avoided. The regularisation term $\lambda_k \boldsymbol{L}^{\mathrm{T}}\boldsymbol{L}$ is now involved in a similar damping process as for the LMM. This modification produces the following effects:

a) The algorithm is not sensitive to the initial choice of the regularisation parameter λ_k compared to the LM or the Gauss Newton method. The image reconstruction can start with a large λ_k that produces a sufficiently smooth image, which is then gradually decreased to allow high frequency components of the image to be reconstructed.

b) In case of poor accord between the reduction in the model *M* and the objective function $\widetilde{F}$, the hyper-parameter λ_k is increased with the aim of enhancing the smoothing and restoring stability. This could result in a reduction of the step size $\boldsymbol{d}_{dGN}$, but does not necessarily switch to the steepest descent method.

In equation (4.50), the gradient can be seen to incorporate a penalty term $\lambda_k \boldsymbol{L}^{\mathrm{T}}\boldsymbol{L}\boldsymbol{\sigma}_k$ in addition to the first order derivative of the residual, $\nabla\mathbf{r}(\boldsymbol{\sigma})$ (see equation (4.33)). When Tikhonov smoothing priors $\boldsymbol{R} = \boldsymbol{L}^{\mathrm{T}}\boldsymbol{L}$ are used the key in the presence of the term $\lambda_k \boldsymbol{R}\boldsymbol{\sigma}_k$ is to find the smoothest solution that fits the measured data to within an acceptable tolerance rather than seeking the solution that fits the data as well as possible. In this case, this constraint is appropriate for applications where the experimental data are severely contaminated with noise. For imaging applications with low noise levels, omitting the term $\lambda_k \boldsymbol{L}^{\mathrm{T}}\boldsymbol{L}\boldsymbol{\sigma}_k$ can result in a better convergence. This chapter, however, deals with noise contaminated data; hence it is recommended to preserve this term in all algorithms that have been derived. This is in order to keep the system reasonably stable despite the fact that the spatial resolution can be compromised with the usage of smoothing Tikhonov priors. However, for some applications where prior information within the matrix ***R*** is more representative of the internal structure of the test object, the presence of the term can be very advantageous. For instance, in medical imaging of cerebral stroke, MIT can be used for monitoring further development of the stroke condition after having been detected using MRI or CT scans. Regularisation can be constructed from anatomical data available from the MRI or CT images, which can help the MIT image reconstruction. This type of regularisation is approached in more depth in the next chapter.

Like the LM method, the regularisation parameter λ_k can be updated based on the value of the gain ratio ρ between the model M and the objective function $\widetilde{F}$. The complete algorithm using this method is shown below in Figure 4.10. The image reconstruction results including the convergence of the objective function and the reconstructed conductivity maps for the example (P1) in different z levels are presented in Figure 4.11 and Figure 4.12 respectively.

```
Problem: $\mathop{\mathbf{argmin}}_{\sigma\in R^n}\left\{\widetilde{F}(\boldsymbol{\sigma})\right\}$; $\widetilde{F}(\boldsymbol{\sigma}) = \frac{1}{2}\left\|\boldsymbol{F}(\boldsymbol{\sigma})-\boldsymbol{D}\right\|^2 + \frac{1}{2}\lambda\left\|\boldsymbol{L}\boldsymbol{\sigma}\right\|^2$
Select the regularisation parameter
$\lambda_0 = \varepsilon_1 * \max_{i=1,\dots,n}\left(\left[\boldsymbol{J}_0^{\,T}\boldsymbol{J}_0\right]_{(i,i)}\right)$; where $\boldsymbol{J}_0$: Jacobian calculated for homogenous $\boldsymbol{\sigma}$
Find $\boldsymbol{\sigma}_0$ using single step reconstruction:
$\boldsymbol{\sigma}_\mathbf{0} = -(\boldsymbol{J}_0^{\mathbf{T}}\boldsymbol{J}_0 + \lambda_0\boldsymbol{L}^{\mathbf{T}}\boldsymbol{L})^{-1}\boldsymbol{J}_0^{\mathbf{T}}\boldsymbol{D}$;
Evaluate the objective function:
$\widetilde{F}(\boldsymbol{\sigma}_0) = \frac{1}{2}\left\|\boldsymbol{F}(\boldsymbol{\sigma}_0)-\boldsymbol{D}\right\|^2 + \frac{1}{2}\lambda_0\left\|\boldsymbol{L}\boldsymbol{\sigma}_0\right\|^2$;
Compute the gradient: $\boldsymbol{g} = \boldsymbol{J}(\boldsymbol{\sigma}_0)^{\mathrm{T}}(\boldsymbol{F}(\boldsymbol{\sigma}_0) - \boldsymbol{D}) + \lambda_0\boldsymbol{L}^{\mathrm{T}}\boldsymbol{L}\boldsymbol{\sigma}_0$;
Calculate: $\boldsymbol{A} = \boldsymbol{J}(\boldsymbol{\sigma}_0)^{\mathrm{T}}\boldsymbol{J}(\boldsymbol{\sigma}_0)$;
Set $\lambda = \lambda_0$; $k = 0$; set $k_{max}$; $exit$ = false;
while $k < k_{max}$ and $exit \neq$ true
    Compute the Hessian: $\boldsymbol{H}_{dGN} = \boldsymbol{A} + \lambda\boldsymbol{L}^{\mathrm{T}}\boldsymbol{L}$;
    Calculate the step: $\boldsymbol{d}_{dGN} = -\boldsymbol{H}_{dGN}^{\;-1}\boldsymbol{g}$;
    Update the conductivity map: $\boldsymbol{\sigma}_{New} = \boldsymbol{\sigma}_k + \boldsymbol{d}_{dGN}$;
    Constrain the conductivity map: $\begin{cases} i = 1{:}n \,|\, (\boldsymbol{\sigma}_{New}(i) < 0) = \tau \simeq 0 \\ i = 1{:}n \,|\, (\boldsymbol{\sigma}_{New}(i) > \boldsymbol{\sigma}_{\max}) = \boldsymbol{\sigma}_{\max} \end{cases}$

    Evaluate the objective function: $\widetilde{F}(\boldsymbol{\sigma}_{New}) = \frac{1}{2}\left\|\boldsymbol{F}(\boldsymbol{\sigma}_{New})-\boldsymbol{D}\right\|^2 + \frac{1}{2}\lambda\left\|\boldsymbol{L}\boldsymbol{\sigma}_{New}\right\|^2$;
    Calculate the gain ratio: $\rho = \left(\widetilde{F}(\boldsymbol{\sigma}_k) - \widetilde{F}(\boldsymbol{\sigma}_{New})\right) \big/ \left(M(0) - M(\boldsymbol{\sigma}_{New} - \boldsymbol{\sigma}_k)\right)$;
    if $\rho > 0$
        $\boldsymbol{\sigma}_{k+1} = \boldsymbol{\sigma}_{New}$;
        $\lambda = \lambda * \max(0.5, 1-(2\rho\text{-}1)^3)$; $\eta$=2;
        $\boldsymbol{g} = \boldsymbol{J}(\boldsymbol{\sigma}_{k+1})^{\mathrm{T}}(\boldsymbol{F}(\boldsymbol{\sigma}_{k+1}) - \boldsymbol{D}) + \lambda\boldsymbol{L}^{\mathrm{T}}\boldsymbol{L}\boldsymbol{\sigma}_{k+1}$;
        $\boldsymbol{A} = \boldsymbol{J}(\boldsymbol{\sigma}_{k+1})^{\mathrm{T}}\boldsymbol{J}(\boldsymbol{\sigma}_{k+1})$;
    else
        $\lambda = \lambda * \eta$;
        $\eta = \eta * 2$;
        if $\eta > 32$ $exit$ = true; end
    end
    $k = k+1$;
end
```

Figure 4.10: Damped Gauss Newton method

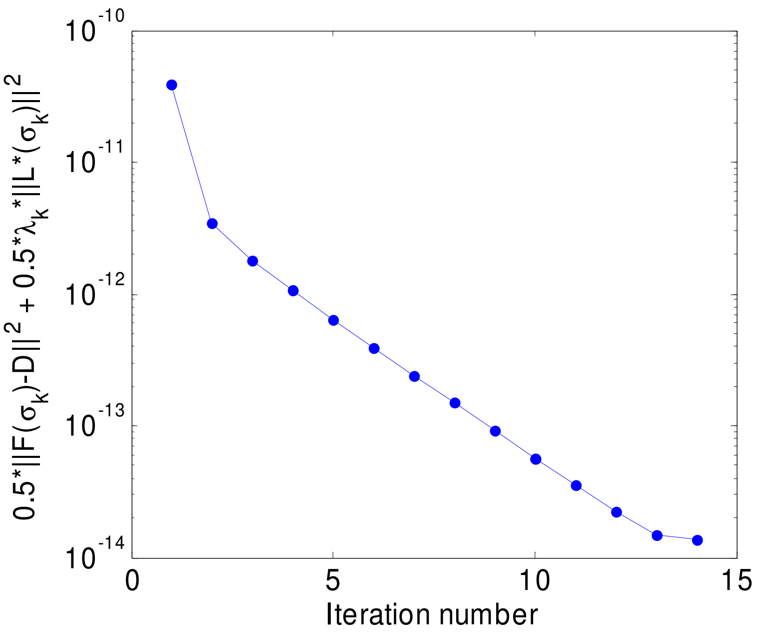

Figure 4.11: Convergence plot illustrating the minimisation of the objective function using the damped Gauss Newton method.

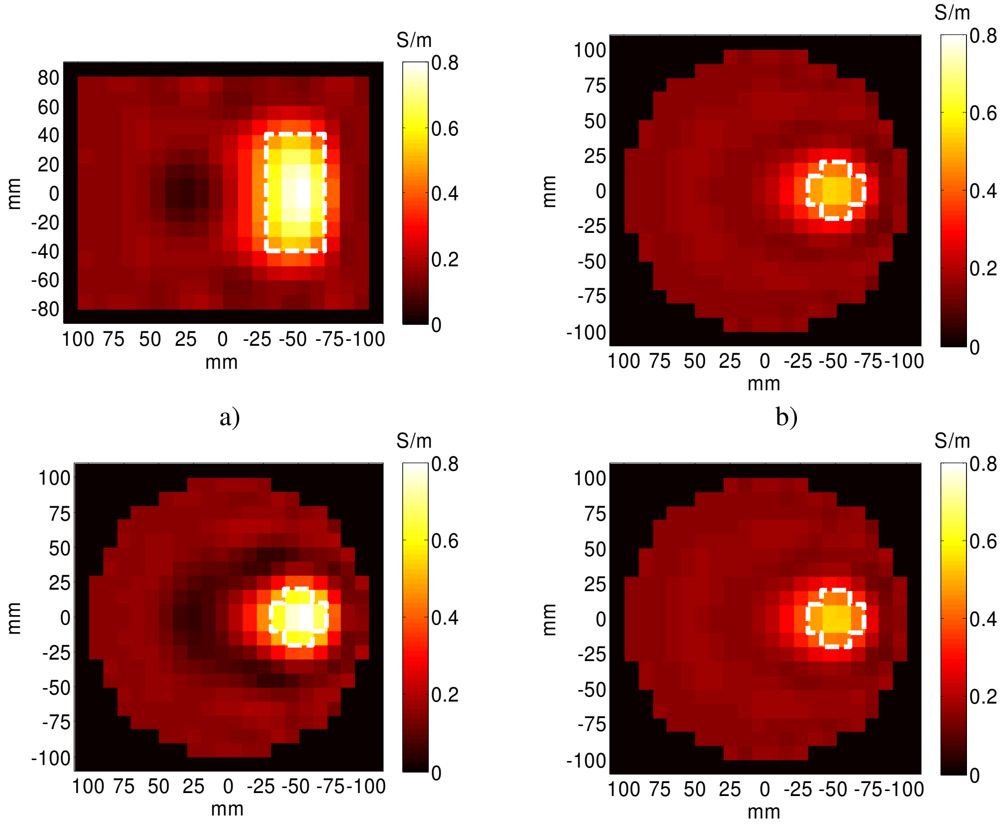

a)

b)

c)

d)

Figure 4.12: Reconstruction of conductivity distribution showing a) vertical slice (*x*=0) mm, [b); c); d)] horizontal slices in different *z* levels (*z*=-40*;* *z*=0*;* *z*=40) mm from noise free data.

4.2.5 Trust region Powell's Dog Leg method

While the LM method determines the length and the direction of the step by means of the damping process, the Powel's Dog Leg (PDL) method employs the trust region strategy described in (section 4.2.1). Using this method, the step size and direction are controlled explicitly via the radius of the trust region Δ. Like the LM method, the PDL method works in combination between the Gauss Newton method and the steepest descent method.

Recall from (4.19) that in a trust region strategy, the step $\boldsymbol{d}_{trPDL}$ is determined by solving the constrained optimisation problem:

$$\begin{aligned} &\boldsymbol{d}_{trPDL} = \mathbf{argmin}_{\boldsymbol{d}} \left\{ \underbrace{\widetilde{F}(\boldsymbol{\sigma}) + \boldsymbol{d}^{\mathrm{T}} \nabla \widetilde{F}(\boldsymbol{\sigma}) + \frac{1}{2} \boldsymbol{d}^{\mathrm{T}} \boldsymbol{H}\, \boldsymbol{d}}_{M(\boldsymbol{d})} \right\}, \\ &\text{s.t.} \left\| \boldsymbol{d}_{trPDL} \right\| \le \Delta \end{aligned} \tag{4.52}$$

where M is the model function, $\widetilde{F}$ is the approximate objective function as defined in equation (4.33), $\nabla \widetilde{F}$ is the gradient, and $\boldsymbol{H}$ is the approximate Hessian as employed in the regularised Gauss Newton method, and Δ is the radius of the trust region.

The trust region and the LM method are closely related. In fact, it has been shown in [106] that for a positive damping parameter ($\gamma > 0$), the computed LM step $\boldsymbol{d}_{rLM}$ satisfies:

$$\begin{aligned} &\boldsymbol{d}_{rLM} = \mathbf{argmin}_{\boldsymbol{d}} \left\{ \underbrace{\widetilde{F}(\boldsymbol{\sigma}) + \boldsymbol{d}^{\mathrm{T}} \nabla \widetilde{F}(\boldsymbol{\sigma}) + \frac{1}{2} \boldsymbol{d}^{\mathrm{T}} \boldsymbol{H}\, \boldsymbol{d}}_{M(\boldsymbol{d})} \right\}, \\ &\text{s.t.} \left\| \boldsymbol{d} \right\| \le \left\| \boldsymbol{d}_{rLM} \right\| \end{aligned} \tag{4.53}$$

However, there is no simple formula that illustrates the connection between the Δ and γ values.

Given the current iterate $\boldsymbol{\sigma}_k \in \mathbb{R}^n$, the step $\boldsymbol{d}$ needed to obtain the next iterate $\boldsymbol{\sigma}_{k+1}$ can be calculated by the regularised Gauss Newton method as follows:

$$\boldsymbol{H}_{rGN} \boldsymbol{d}_{rGN} = -\boldsymbol{g}_{rGN} \Leftrightarrow (\boldsymbol{J}_k{}^{\mathrm{T}} \boldsymbol{J}_k + \lambda \boldsymbol{L}^{\mathrm{T}} \boldsymbol{L}) \boldsymbol{d}_{rGN} = -(\boldsymbol{J}_k{}^{\mathrm{T}} (\boldsymbol{F}(\boldsymbol{\sigma}_k) \text{-} \boldsymbol{D}) + \lambda \boldsymbol{L}^{\mathrm{T}} \boldsymbol{L} \boldsymbol{\sigma}_k) \tag{4.54}$$

Or it can also be evaluated via the steepest descent method using the equation below:

$$\boldsymbol{d}_{sd} = -\boldsymbol{g}_{sd} \Leftrightarrow \boldsymbol{d}_{sd} = -\boldsymbol{J}_k{}^{\mathrm{T}}(\boldsymbol{F}(\boldsymbol{\sigma}_k)\text{-}\boldsymbol{D}) - \lambda \boldsymbol{L}^{\mathrm{T}}\boldsymbol{L}\boldsymbol{\sigma}_k \tag{4.55}$$

While the regularised Gauss Newton method takes full step ($\alpha = 1$) to obtain $\boldsymbol{\sigma}_{k+1}$, the steepest descent method needs to determine α. This latter can be computed by approximating the objective function $\widetilde{F}$ at the iterate $\boldsymbol{\sigma}_{k+1} = \boldsymbol{\sigma}_k + \alpha \boldsymbol{d}_{sd}$ using a linear model as follows:

$$\begin{aligned}
\widetilde{F}(\boldsymbol{\sigma}_k + \alpha \boldsymbol{d}_{sd}) &\simeq \underbrace{\frac{1}{2}\left\|\mathbf{r}(\boldsymbol{\sigma}_k) + \alpha \boldsymbol{J}_k \boldsymbol{d}_{sd}\right\|^2}_{F} + \underbrace{\frac{1}{2}\lambda\left\|\boldsymbol{L}\bullet(\boldsymbol{\sigma}_k + \alpha \boldsymbol{d}_{sd})\right\|^2}_{P} \\
&= \underbrace{\frac{1}{2}\left\|\mathbf{r}(\boldsymbol{\sigma}_k)\right\|^2 + \alpha \boldsymbol{d}_{sd}^{\mathrm{T}} \boldsymbol{J}_k^{\mathrm{T}} \mathbf{r}(\boldsymbol{\sigma}_k) + \frac{1}{2}\alpha^2 \left\|\boldsymbol{J}_k \boldsymbol{d}_{sd}\right\|^2}_{F} + \underbrace{\frac{1}{2}\left\|\boldsymbol{L}\bullet\boldsymbol{\sigma}_k\right\|^2 + \alpha\lambda \boldsymbol{d}_{sd}^{\mathrm{T}} \boldsymbol{L}^{\mathrm{T}} \boldsymbol{L}\boldsymbol{\sigma}_k + \frac{1}{2}\alpha^2\lambda\left\|\boldsymbol{L}\boldsymbol{d}_{sd}\right\|^2}_{P} \\
&= \underbrace{\frac{1}{2}\left\|\mathbf{r}(\boldsymbol{\sigma}_k)\right\|^2 + \frac{1}{2}\left\|\boldsymbol{L}\bullet\boldsymbol{\sigma}_k\right\|^2}_{\widetilde{F}(\boldsymbol{\sigma}_k)} + \alpha \boldsymbol{d}_{sd}^{\mathrm{T}} \boldsymbol{J}_k^{\mathrm{T}} \mathbf{r}(\boldsymbol{\sigma}_k) + \alpha\lambda \boldsymbol{d}_{sd}^{\mathrm{T}} \boldsymbol{L}^{\mathrm{T}} \boldsymbol{L}\boldsymbol{\sigma}_k + \frac{1}{2}\alpha^2\left\|\boldsymbol{J}_k \boldsymbol{d}_{sd}\right\|^2 + \frac{1}{2}\alpha^2\lambda\left\|\boldsymbol{L}\boldsymbol{d}_{sd}\right\|^2 \\
&= \widetilde{F}(\boldsymbol{\sigma}_k) + \alpha \boldsymbol{d}_{sd}^{\mathrm{T}} \underbrace{\left(\boldsymbol{J}_k^{\mathrm{T}} \mathbf{r}(\boldsymbol{\sigma}_k) + \lambda \boldsymbol{L}^{\mathrm{T}} \boldsymbol{L}\boldsymbol{\sigma}_k\right)}_{\boldsymbol{g}_{sd}} + \frac{1}{2}\alpha^2\left(\boldsymbol{d}_{sd}^{\mathrm{T}} \boldsymbol{J}_k^{\mathrm{T}} \boldsymbol{J}_k \boldsymbol{d}_{sd} + \lambda \boldsymbol{d}_{sd}^{\mathrm{T}} \boldsymbol{L}^{\mathrm{T}} \boldsymbol{L}\boldsymbol{d}_{sd}\right)
\end{aligned}$$

The function of α is minimal when:

$$\begin{aligned}
&\frac{\partial \widetilde{F}}{\partial \alpha} = 0 \Leftrightarrow \boldsymbol{d}_{sd}^{\mathrm{T}} \underbrace{\left(\boldsymbol{J}_k^{\mathrm{T}} \mathbf{r}(\boldsymbol{\sigma}_k) + \lambda \boldsymbol{L}^{\mathrm{T}} \boldsymbol{L}\boldsymbol{\sigma}_k\right)}_{\boldsymbol{g}_{sd}} + \alpha\left(\boldsymbol{d}_{sd}^{\mathrm{T}} \underbrace{(\boldsymbol{J}_k^{\mathrm{T}} \boldsymbol{J}_k + \lambda \boldsymbol{L}^{\mathrm{T}} \boldsymbol{L})}_{\boldsymbol{H}_{rGN}} \boldsymbol{d}_{sd}\right) = 0 \\
&\qquad \Leftrightarrow \alpha = -\frac{\boldsymbol{d}_{sd}^{\mathrm{T}} \boldsymbol{g}_{sd}}{\boldsymbol{d}_{sd}^{\mathrm{T}} \boldsymbol{H}_{rGN} \boldsymbol{d}_{sd}} = \frac{\left\|\boldsymbol{g}_{sd}\right\|^2}{\boldsymbol{g}_{sd}^{\mathrm{T}} \boldsymbol{H}_{rGN} \boldsymbol{g}_{sd}}
\end{aligned} \tag{4.56}$$

Now, given two step candidates for computing the next iterate vector $\boldsymbol{\sigma}_{k+1}$, namely: $\mathbf{a} = \alpha \boldsymbol{d}_{sd}$, and $\mathbf{b} = \boldsymbol{d}_{rGN}$, Powell proposed the following strategy for calculating the trust region step $\boldsymbol{d}_{trPDL}$, when the trust region has a radius Δ:

```
if $\|\boldsymbol{d}_{rGN}\| \le \Delta$
    $\boldsymbol{d}_{trPDL} = \boldsymbol{d}_{rGN}$;
elseif $\|\alpha \boldsymbol{d}_{sd}\| \ge \Delta$
    $\boldsymbol{d}_{trPDL} = \left(\Delta / \|\boldsymbol{d}_{sd}\|\right) * \boldsymbol{d}_{sd}$;                (4.57)
else
    $\boldsymbol{d}_{trPDL} = \alpha \boldsymbol{d}_{sd} + \zeta\left(\boldsymbol{d}_{rGN} - \alpha \boldsymbol{d}_{sd}\right)$; s.b.$\|\boldsymbol{d}_{trPDL}\| = \Delta$ .
```

The last case in the strategy is illustrated in Figure 4.13:

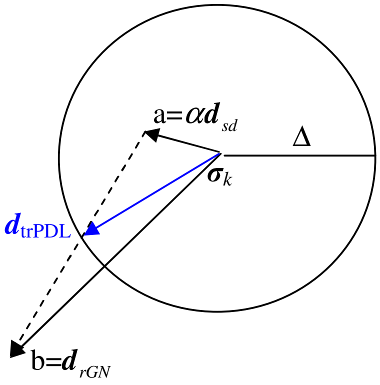

Figure 4.13: Trust region Powell's Dog Leg step

With **a** and **b** defined as above, and **c = a**$^{\mathrm{T}}$(**b - a**), the positive scalar $\zeta > 0$ can be computed by choosing the positive root of the quadratic equation in ζ defined by:

$$\begin{aligned} \varphi(\zeta) &= \left\| \mathbf{a}+\zeta\left(\mathbf{b}\text{-}\mathbf{a}\right)\right\|^2 - \Delta^2 \\ &= \left\|\mathbf{b}\text{-}\mathbf{a}\right\|^2 \zeta^2 + 2\mathbf{c}\,\zeta + \left\|\mathbf{a}\right\|^2 - \Delta^2 \end{aligned} \tag{4.58}$$

As in the LM method, the gain ratio ρ can be used to control the size of the trust region radius Δ.

$$\rho = \left(\widetilde{F}(\boldsymbol{\sigma}_k) - \widetilde{F}(\boldsymbol{\sigma}_k + \delta\boldsymbol{\sigma}_k)\right) \Big/ \left(M(0) - M(\delta\boldsymbol{\sigma}_k)\right)$$

where M is the quadratic model in $\delta\boldsymbol{\sigma}_k$, $\delta\boldsymbol{\sigma}_k = \boldsymbol{\sigma}_{k+1} - \boldsymbol{\sigma}_k$ and:

$$M(0)\text{-}M(\delta\boldsymbol{\sigma}_k) = -\delta\boldsymbol{\sigma}_k{}^{\mathrm{T}}\boldsymbol{g}_k - \frac{1}{2}\delta\boldsymbol{\sigma}_k{}^{\mathrm{T}}\boldsymbol{H}_k\delta\boldsymbol{\sigma}_k$$

Recall from previous sections on the LM method and damped Gauss Newton method that after calculating $\boldsymbol{\sigma}_{k+1} = \boldsymbol{\sigma}_k + \boldsymbol{d}_{trPDL}$, any negative elements within $\boldsymbol{\sigma}_{k+1}$ are constrained to positive values very near to zero (e.g. 1×10^{-4}) since negative conductivities do not exist in practice, which changes the vector $\boldsymbol{\sigma}_{k+1}$. Hence, the actual step is now $\delta\boldsymbol{\sigma}_k$ which is the difference between the constrained $\boldsymbol{\sigma}_{k+1}$ and the previous iterate $\boldsymbol{\sigma}_k$.

Similar to the LM method, the regularisation parameter is set to $\lambda = \varepsilon_2 * \lambda_0$, where ε_2 is specified by the user (e.g. $\varepsilon_2 \in [10^{-3}, 0.1]$), and λ_0 is selected according to equation (4.36), again ε_1 is a user specified constant (e.g. $\varepsilon_1 = 1$). The initial trust region radius can be selected as: $\Delta_0 = 1$. The same stopping criteria as for the LM method are applied here due the similarity in the convergence characteristics of both methods. The pseudo form of the algorithm is presented in Figure 4.14.

Again, in order to test the performance of this method the same example (P1) have been used for image reconstruction, with noise free data generated from the custom forward model. The plots of the convergence of the objective function are depicted in Figure 4.15. The image reconstruction results are shown in Figure 4.16.

```
Problem: argmin$_{\sigma \in R^n}\left\{\widetilde{F}(\boldsymbol{\sigma})\right\}$; $\widetilde{F}(\boldsymbol{\sigma}) = \frac{1}{2}\left\|\boldsymbol{F}(\boldsymbol{\sigma}) - \boldsymbol{D}\right\|^2 + \frac{1}{2}\lambda\left\|\boldsymbol{L}\boldsymbol{\sigma}\right\|^2$
$\lambda_0 = \varepsilon_1 * \max_{i=1,\ldots,n}\left(\left[\boldsymbol{J}_0^T \boldsymbol{J}_0\right]_{(i,i)}\right)$; where $\boldsymbol{J}_0$: Jacobian calculated for homogenous $\boldsymbol{\sigma}$
Find $\boldsymbol{\sigma_0}$ using single step reconstruction: $\boldsymbol{\sigma_0} = -(\boldsymbol{J}_0^{\mathrm{T}}\boldsymbol{J}_0 + \lambda_0 \boldsymbol{L}^{\mathrm{T}}\boldsymbol{L})^{-1}\boldsymbol{J}_0^{\mathrm{T}}\boldsymbol{D}$;
Evaluate the objective function: $\widetilde{F}(\boldsymbol{\sigma}_0) = \frac{1}{2}\left\|\boldsymbol{F}(\boldsymbol{\sigma}_0) - \boldsymbol{D}\right\|^2 + \frac{1}{2}\lambda_0\left\|\boldsymbol{L}\boldsymbol{\sigma}_0\right\|^2$;
Compute the gradient: $\boldsymbol{g} = \boldsymbol{J}(\boldsymbol{\sigma}_0)^{\mathrm{T}}(\boldsymbol{F}(\boldsymbol{\sigma}_0) - \boldsymbol{D}) + \lambda_0 \boldsymbol{L}^{\mathrm{T}}\boldsymbol{L}\boldsymbol{\sigma}_0$;
Calculate: $\boldsymbol{A} = \boldsymbol{J}(\boldsymbol{\sigma}_0)^{\mathrm{T}}\boldsymbol{J}(\boldsymbol{\sigma}_0)$;
Set $\lambda = \varepsilon_2 * \lambda_0$; Set $\Delta = \Delta_0$
Compute the Hessian: $\boldsymbol{H}_{rGN} = \boldsymbol{A} + \lambda\boldsymbol{L}^{\mathrm{T}}\boldsymbol{L}$;
Calculate the step: $\boldsymbol{d}_{rGN} = -\boldsymbol{H}_{rGN}^{-1}\boldsymbol{g}$;
Compute $\alpha$ by (4.56)
$k$ = 0; set $k_{max}$; $exit$ = false; $\eta = 0$;
while $k < k_{max}$ and $exit \neq$ true
        Compute $\boldsymbol{d}_{trPDL}$ by (4.57)
        Update the conductivity map: $\boldsymbol{\sigma}_{New} = \boldsymbol{\sigma}_k + \boldsymbol{d}_{trPDL}$;
        Constrain: $\{i = 1{:}n \mid (\boldsymbol{\sigma}_{New}(i) < 0) = \tau \simeq 0;\ i = 1{:}n \mid (\boldsymbol{\sigma}_{New}(i) > \boldsymbol{\sigma}_{\max}) = \boldsymbol{\sigma}_{\max}$
        if $\left\|\boldsymbol{\sigma}_{New} - \boldsymbol{\sigma}_k\right\| < \varepsilon_3\left(\left\|\boldsymbol{\sigma}_k\right\| + \varepsilon_3\right)$
            $exit$ = true ;
        else
            Evaluate the objective function: $\widetilde{F}(\boldsymbol{\sigma}_{New}) = \frac{1}{2}\left\|\boldsymbol{F}(\boldsymbol{\sigma}_{New}) - \boldsymbol{D}\right\|^2 + \frac{1}{2}\lambda\left\|\boldsymbol{L}\boldsymbol{\sigma}_{New}\right\|^2$;
            Calculate the gain ratio: $\rho = \left(\widetilde{F}(\boldsymbol{\sigma}_k) - \widetilde{F}(\boldsymbol{\sigma}_{New})\right) \big/ \left(M(0) - M(\boldsymbol{\sigma}_{New} - \boldsymbol{\sigma}_k)\right)$;
            if $\rho < 0.25$
                $\Delta = \Delta/2$;
            elseif $\rho > 0.75$
                $\Delta = \max\left(\Delta, 2 * \left\|\boldsymbol{d}_{trPDL}\right\|\right)$;
            end
            if $\rho > 0$
                $\boldsymbol{\sigma}_{k+1} = \boldsymbol{\sigma}_{New}$;
                $\boldsymbol{g} = \boldsymbol{J}(\boldsymbol{\sigma}_{k+1})^{\mathrm{T}}(\boldsymbol{F}(\boldsymbol{\sigma}_{k+1}) - \boldsymbol{D}) + \lambda\boldsymbol{L}^{\mathrm{T}}\boldsymbol{L}\boldsymbol{\sigma}_{k+1}$;
                $\boldsymbol{H}_{rGN} = \boldsymbol{J}(\boldsymbol{\sigma}_{k+1})^{\mathrm{T}}\boldsymbol{J}(\boldsymbol{\sigma}_{k+1}) + \lambda\boldsymbol{L}^{\mathrm{T}}\boldsymbol{L}$;
                Compute $\alpha$ by (4.56)
            else
                $\eta = \eta + 1$;
                if $\eta > 5$  $exit$ = true;  end
            end;   $k = k + 1$; $\eta = 0$;

end
```

Figure 4.14: Trust region Powell's Dog Leg algorithm

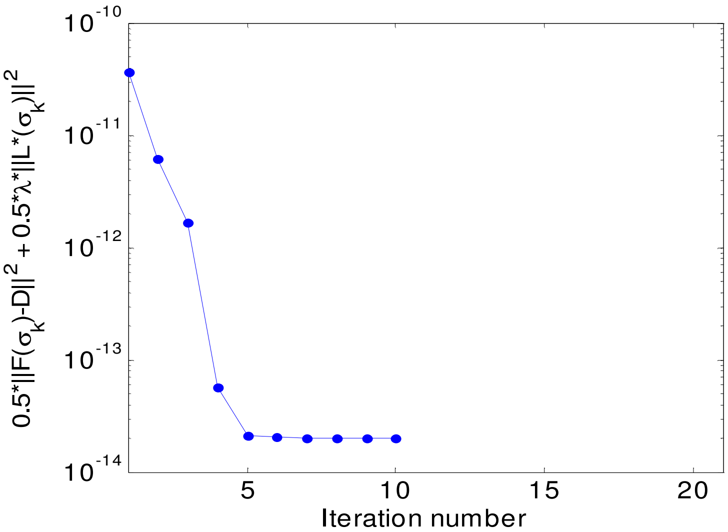

Figure 4.15: Convergence plot illustrating the minimisation of the objective function using the Powel Dog Leg method.

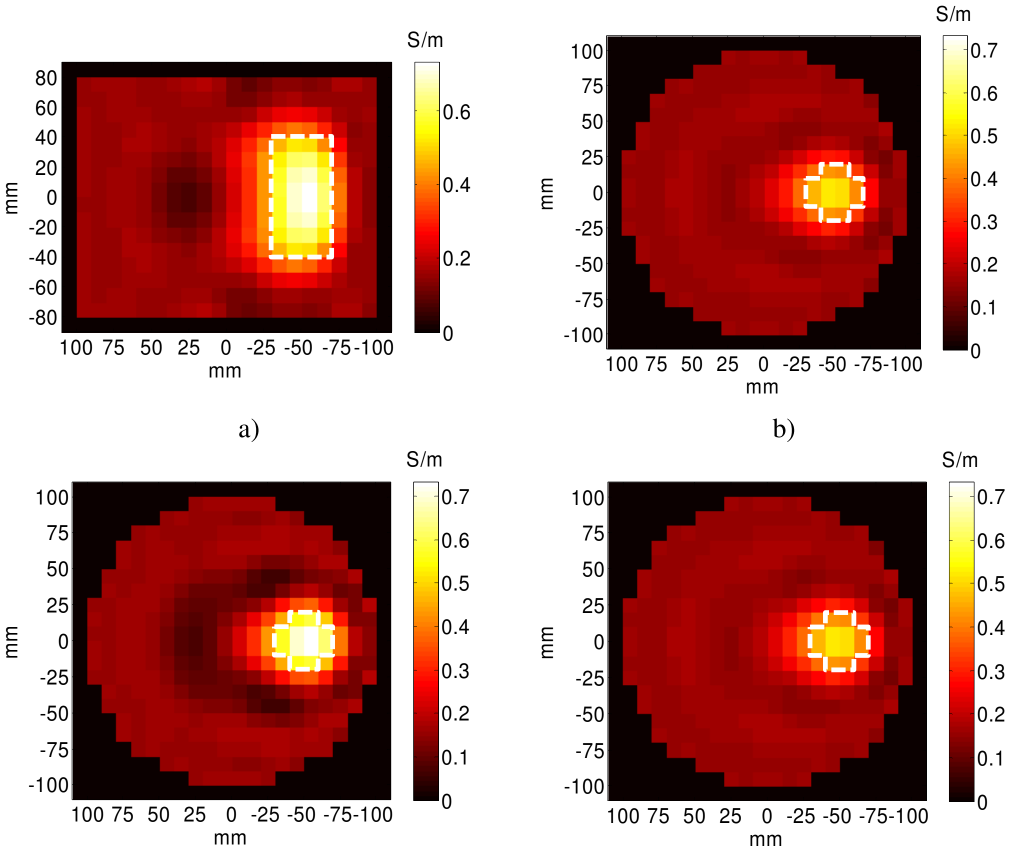

a)

b)

c)

d)

Figure 4.16: Reconstruction of conductivity distribution showing a) vertical slice (*x*=0) mm, [b); c); d)] horizontal slices in different z levels (*z*=-40*;* *z*=0*;* *z*=40) mm with No noise added to the data.

4.2.6 Simulations

In order to assess the efficiency of the proposed special optimisation methods namely Levenberg Marquardt method (LMM), trust region Powell Dog Leg method (PDLM) and damped Gauss Newton method (DGNM), their performance was examined against the conventional regularised Gauss Newton method (RGNM). The solvers were compared with respect to the following five criteria:

a) Convergence of the objective function $\widetilde{F}$,

b) Convergence of the solution (reconstructed conductivity) error $\left\|\boldsymbol{\sigma}_k - \boldsymbol{\sigma}_{true}\right\| / \left\|\boldsymbol{\sigma}_{true}\right\|$

c) Stability of the algorithm

d) Robustness of the selected stopping criteria

e) Sensitivity to the choice of the regularisation parameter.

In a first numerical experiment, the same example (P1) (Figure 4.2) was used with geometry and conductivity distribution described in section 4.2.2. Simulated measured data was generated from the custom forward solver. In real image reconstruction, data are always contaminated with noise caused by hardware and modelling inaccuracies. In order to account for the presence of noise, an additional 2 % of the rms of the secondary induced voltages was added to the simulated data as normally distributed or equivalently Gaussian noise. To put this figure in context, the modelled MIT system (Mark 1) used in this chapter for image reconstruction was developed at Glamorgan University, our academic partner in this research project, and reported in [79] to have a signal to noise ratio (SNR = $\boldsymbol{D}$/noise) of 40 dB which is equivalent of 1% percent added noise. Again, 3D image reconstruction was carried out with 5056 conductivity elements from a total of 2304 measurement data generated at 10 MHz frequency. For all methods, the maximum number of iterations was set to $k_{max} = 20$ to avoid the possibility of being stuck in an infinite loop. Using the RGNM, image reconstruction was carried out with several values for the regularisation parameter λ in an attempt to identify the band inside which the best convergence can be achieved, and eventually the ensemble $(10^{-1}, 10^{-2}, 10^{-3}) \times \lambda_0$ was selected. For the sake of comparison, image reconstruction was repeated with these values using LMM and PDLM. However, as explained in section 4.2.4 the regularisation parameter for DGNM is involved in a damping process and the algorithm is flexible with regard to the initial value as long as a large value is chosen as a starting point, thus λ is chosen equal to λ_0.

In a second simulation, the image reconstruction protocol was repeated with the same example (P1), but this time data was generated from Maxwell 3D, (a commercial FE software package by Ansoft Corp). This is a good stepping stone to generate simulated data that emulate real experimental data, where the noise may not follow a priori specified distribution. When compared with noise free data, the mean value of the noise was evaluated to be 2.36%. This figure is entirely caused by all sources of error due to meshing and field calculations.

4.2.7 Results and discussion

4.2.7.1 Convergence of the objective function

For the standard RGNM, Figure 4.17 shows the optimum convergence was achieved with the regularisation parameter value ($\lambda = 10^{-2} \lambda_0$), whereas with $\lambda = 10^{-1} \lambda_{0,}$ a weaker convergence was recorded and the optimisation failed with the $\lambda = 1e^{-3} \lambda_0$. However, using the LMM, DGNM and the PDLM, minor improvement was observed for all values of the regularisation parameter and the best convergence is similar in all of them (Figure 4.19, Figure 4.23, Figure 4.26). Unlike the RGNM, all the optimisations with LMM and PDLM were successful, which reflect their superiority in providing stability in the solution.

For the second simulation with simulated data from Ansoft, similar observations as to the first experiment can be made in comparing the optimisation methods. The LMM and the PDLM (Figure 4.31, Figure 4.36) produced similar performance, which appears to be better relative to the RGNM (Figure 4.29). As can be seen in Figure 4.34, DGNM, however, produced a remarkable convergence compared with all other methods. Another interesting remark comparing the two computational experiments can be drawn, wherein all algorithms appear to provide better convergence with Maxwell simulated data than with artificial data, although the noise level is larger in the former. This brings into light that not only the noise level affects image reconstruction, but also the type of its distribution.

4.2.7.2 Convergence of the solution error

While the convergence error of the objective function is an available criterion to assess how efficient nonlinear optimization methods are in minimizing the least squares problem $\widetilde{F}$, the conductivity solution error is the major criterion with the ultimate answer to which optimization method is robust to produce a minimiser $\boldsymbol{\sigma}^*$ closer to the true distribution $\boldsymbol{\sigma}_{\text{true}}$. Although this answer cannot be granted in reality but for comparison the true conductivity distribution is assumed to be known in order to analyse the efficiency of the proposed optimisation methods. Figure 4.17 and Figure 4.18 depict the relative solution error norm over iteration and the conductivity maps of the conductivity vector argument that produces the smallest minimum of the objective function using the RGNM. When comparing with the LMM (Figure 4.19, Figure 4.22) and PDLM (Figure 4.26) the minimum recorded solution error is comparable in all of them to approximately 50%, which is obtained with $\lambda = 10^{-2}\ \lambda_0$. However, this latter value does not correspond to the curve that produced the minimum value of the objective function in case of the LMM and the PDLM. Indeed, with this image reconstruction experiment, the convergence error of the objective function does not correlate well with the solution (image) error in case of the LMM and the PDLM, and the reconstructed images that should practically be given are illustrated by Figure 4.21 and Figure 4.28 obtained with $\lambda = 10^{-3}\ \lambda_0$. With regard to the DGNM, the best solution error norm is roughly the same compared with the RGNM in case of $\lambda = 10^{-2}\ \lambda_0$ and the results are displayed in Figure 4.23 and Figure 4.25. Similar to the LMM and the PDLM, the actual reconstructed conductivity that must be validated in the DGNM is shown in Figure 4.24.

For the second experiment with data obtained by Maxwell, a different scenario can be observed, whereby the trend exhibited by the objective function value is now a good indicator of the minimum of the solution error in all cases of the proposed nonlinear optimisation methods. In fact, from the solution error graphs (Figure 4.29; Figure 4.31 and Figure 4.36) we observe that the LMM and the PDLM achieve smaller solution error compared with the RGNM. More interestingly, the DGNM (Figure 4.34) with its damping strategy applied to the regularisation parameter records the most superior solution error convergence with approximately 46%. This is manifested with a noticeable quantitative convergence on the corresponding conductivity maps shown in

Figure 4.35 where the reconstructed conductivity for the inclusion is approximately 0.7 Sm^{-1}, i.e. ≈155% improvement compared to the LMM and the PDLM, and ≈ 200% relative to the RGNM. All algorithms, however, were able to recover the inclusion (stroke) feature, except that DGNM provided the sharpest images and the RGNM images are of relatively low resolution with a dominating blur.

4.2.7.3 Stability of the optimisation

Stability of the image reconstruction algorithms is another important aspect. The LMM and the PDLM are shown to provide better stability among the optimisation methods. Usually instability in optimisation methods is manifested when small changes in data are reconstructed with large conductivity changes, a process which is usually encountered in the final stage of the iterative process when the algorithm passes near to the local minimiser and diverges away. Using the damping and trust region techniques explained in section (4.2.1), the algorithms provide good control by being able to switch between the Newton's method and the steepest descent method. Clearly this effect is noticeable in the final stage of the iteration where the LMM and the PDLM switch to small step sizes, which infers the steepest descent becomes dominant. This means that when the minimiser ($\boldsymbol{\sigma}^*$) has been reached, the methods avoid divergence from the minimiser by converting the algorithm to usage of small steps that are terminated by the stopping criterion. Although the DGNM employs similar damping process like the LMM, it is not a hybrid method and hence cannot benefit from the steepest descent method. However, the algorithm controls the stability by increasing the regularisation weight which seems to be a satisfactory approach.

4.2.7.4 Robustness of the stopping criteria

The LMM and the PDLM employs an endpoint strategy to their iterative procedure which functions such that the iteration stops when the change in the conductivity solution i.e. $\delta\boldsymbol{\sigma}_k$ is small (see section 4.2.3). Since the LMM and PDLM eventually convert to using small steps for updating conductivity as described in the previous section, this stopping strategy is theoretically adequate and reasonable. The performance of such stopping mechanism is illustrated in (Figure 4.20, Figure 4.27, Figure 4.32). For the RGNM and the DGNM, this stopping criterion cannot be applied since the methods are not guaranteed to switch to small step sizes toward the end of the iterative procedure. Hence, a stopping technique that terminates the iteration when the descending condition for the objective function $\widetilde{F}$ described by (4.38) is not met is employed. The main difference between the conventional RGNM and the DGNM in this respect is the latter employs the special damping strategy whereby the regularisation parameter is increased in a series in order to obtain a descent direction, and if after a number of times (iterations) this is not achieved, the algorithm stops. This stopping approach appears to function reasonably well as illustrated by the plots of the solution error norm discussed earlier.

4.2.7.5 Sensitivity to the choice of the regularisation parameter

For solving the MIT conductivity inverse problem, the LMM and the PDLM require the specification of two parameters: the damping variable γ and the constant regularisation parameter λ. From the results on the convergence of the objective function and the solution error the methods provided different convergence trends for different values of the regularisation parameter. Hence, it may be deduced that the methods are sensitive to the choice of such parameter, which infers a proper parameter selection method is required. However, the DNGM employs only one variable, i.e. the regularisation parameter which is updated in a similar way to γ. The DGNM is not sensitive to the choice of initial value of the hyper-parameter λ_1 as long as it is sufficiently large to provide a smooth image, since it will be reduced through the iterations. In this respect, the DGNM is better than the LMM and the PDLM since it is less complex (employs less parameters) and is not sensitive to the choice of the regularisation parameter.

RGNM:

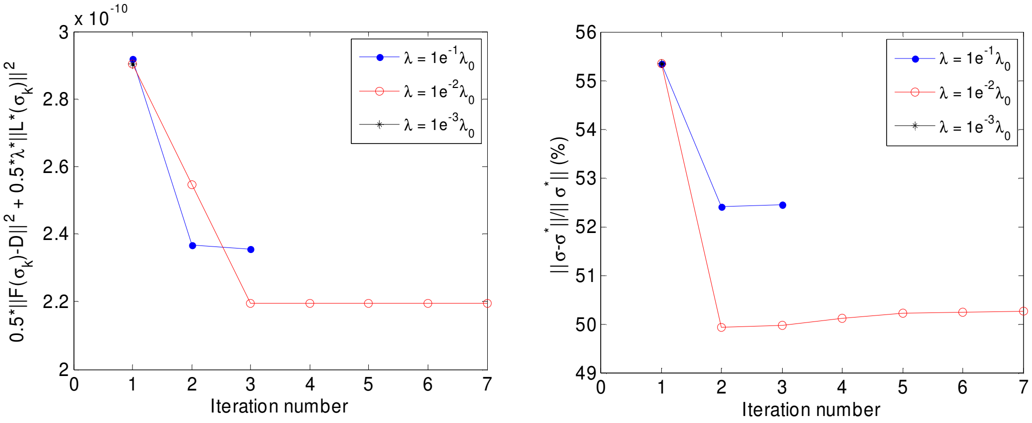

Figure 4.17: Convergence plot of the objective function (left) and relative solution error (right) versus iteration with regularised Gauss Newton method (example (P1); data with 2% Gaussian noise).

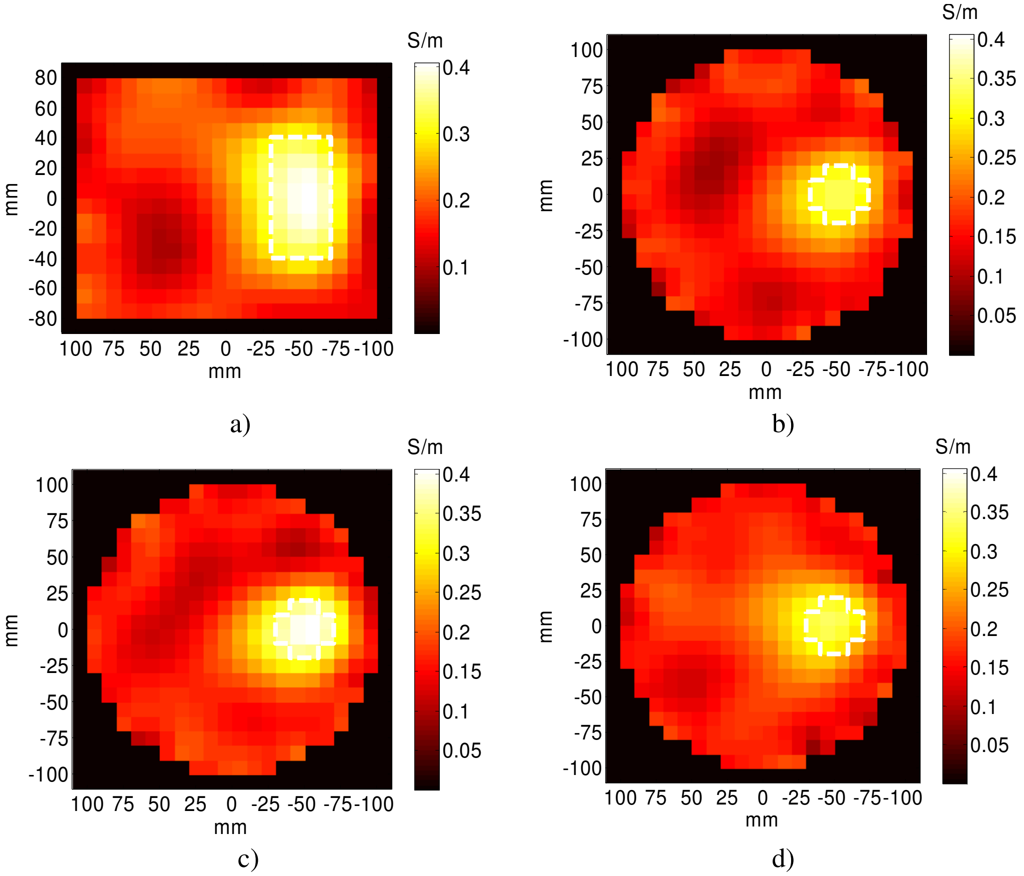

Figure 4.18: Reconstruction of conductivity distribution showing a) vertical slice (*x*=0) mm, [b); c); d)] horizontal slices in different *z* levels (*z*=-40*;* *z*=0*;* *z*=40) mm, with the regularised Gauss Newton method (example (P1); data with 2% Gaussian noise; $\lambda = 10^{-2}\,\lambda_0$)

LMM:

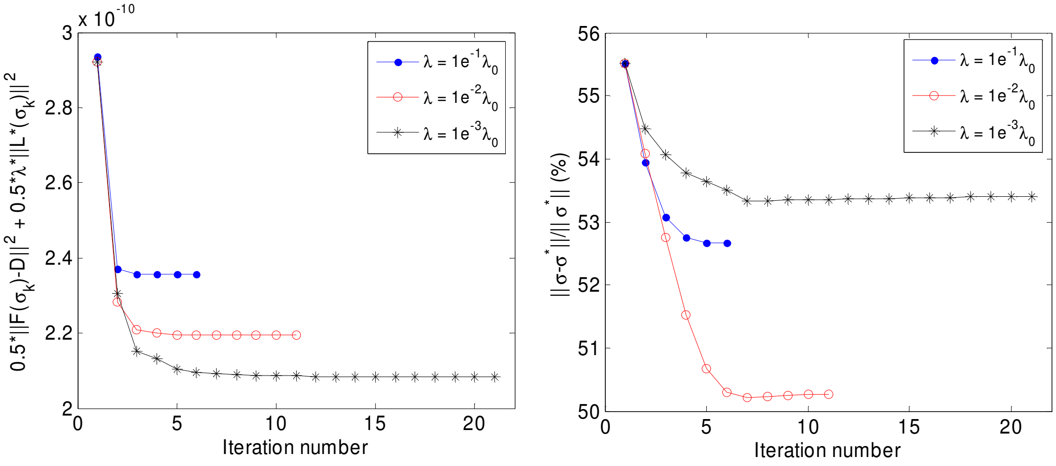

Figure 4.19: Convergence plot of the objective function (left) and relative solution error (right) versus iteration with LM method (example (P1); data with 2% Gaussian noise).

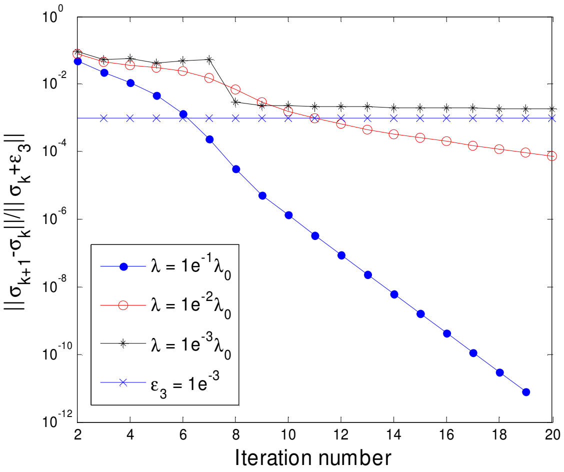

Figure 4.20: Performance of the stopping criterion for the LM method (example (P1); data with 2% Gaussian noise).

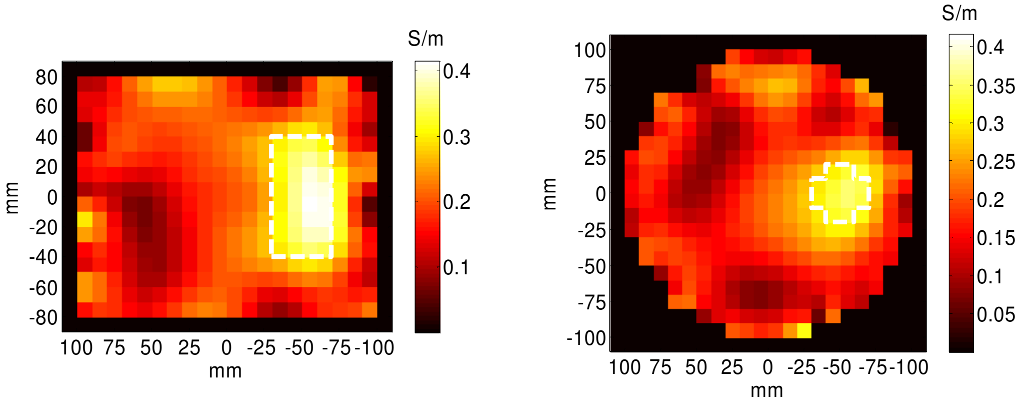

a)

b)

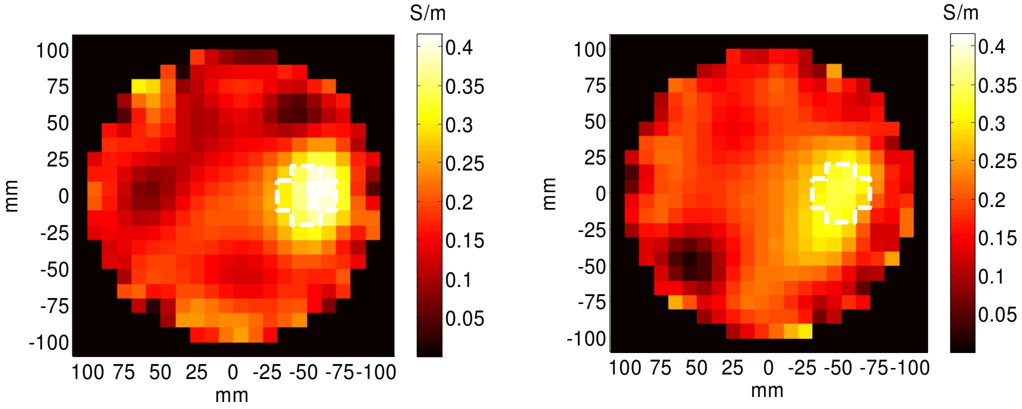

c) d)

Figure 4.21: Reconstruction of conductivity distribution showing a) vertical slice (*x*=0) mm, [b); c); d)] horizontal slices in different *z* levels (*z*=-40*;* *z*=0*;* *z*=40) mm, with the Levenberg Marquardt method (example (P1); data with 2% Gaussian noise; $\lambda = 10^{-3}\ \lambda_0$).

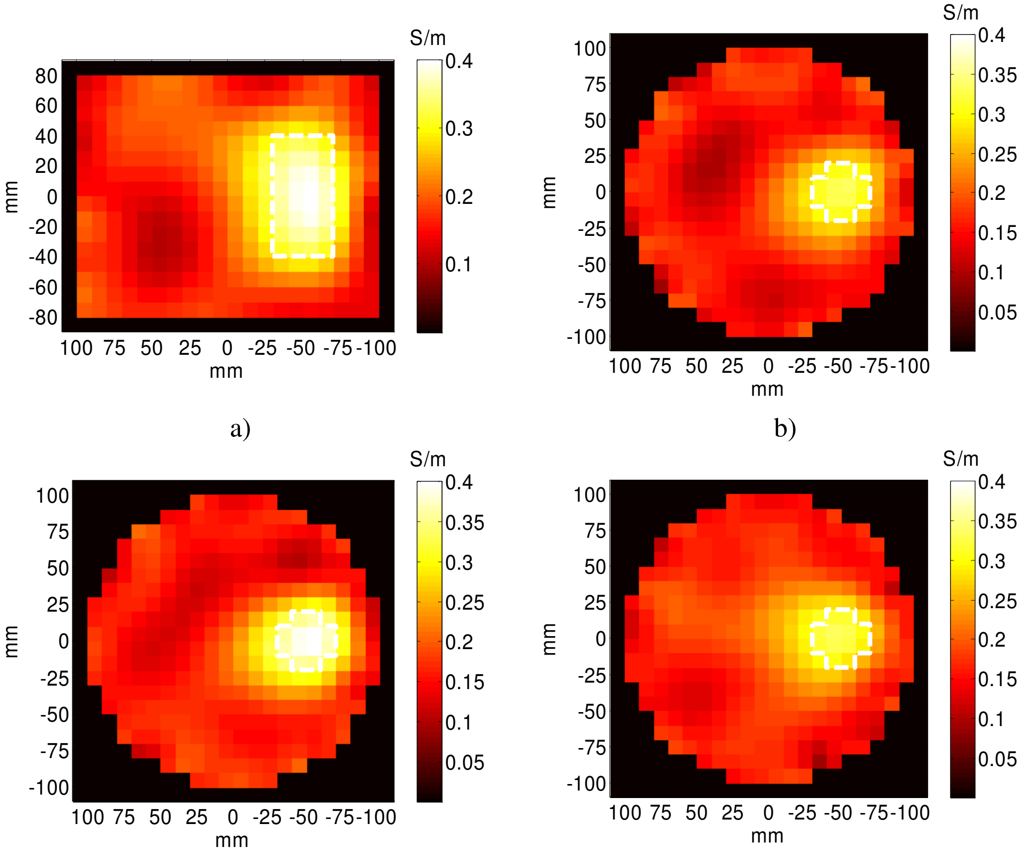

a) b)

c) d)

Figure 4.22: Reconstruction of conductivity distribution showing a) vertical slice (*x*=0) mm, [b); c); d)] horizontal slices in different *z* levels (*z*=-40*;* *z*=0*;* *z*=40) mm, with the Levenberg Marquardt method (example (P1); data with 2% Gaussian noise; $\lambda = 10^{-2}\ \lambda_0$).

DGNM:

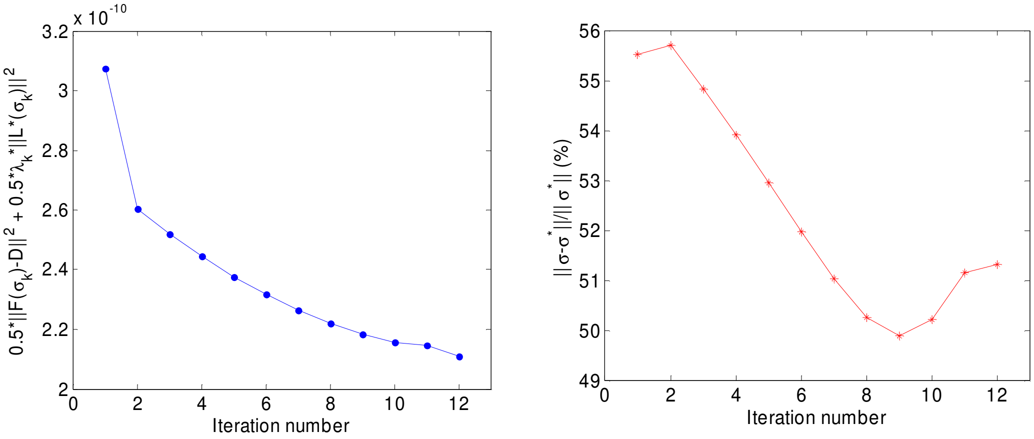

Figure 4.23: Convergence plot of the objective function (left) and relative solution error (right) versus iteration with damped Gauss Newton method (example (P1); data with 2% Gaussian noise).

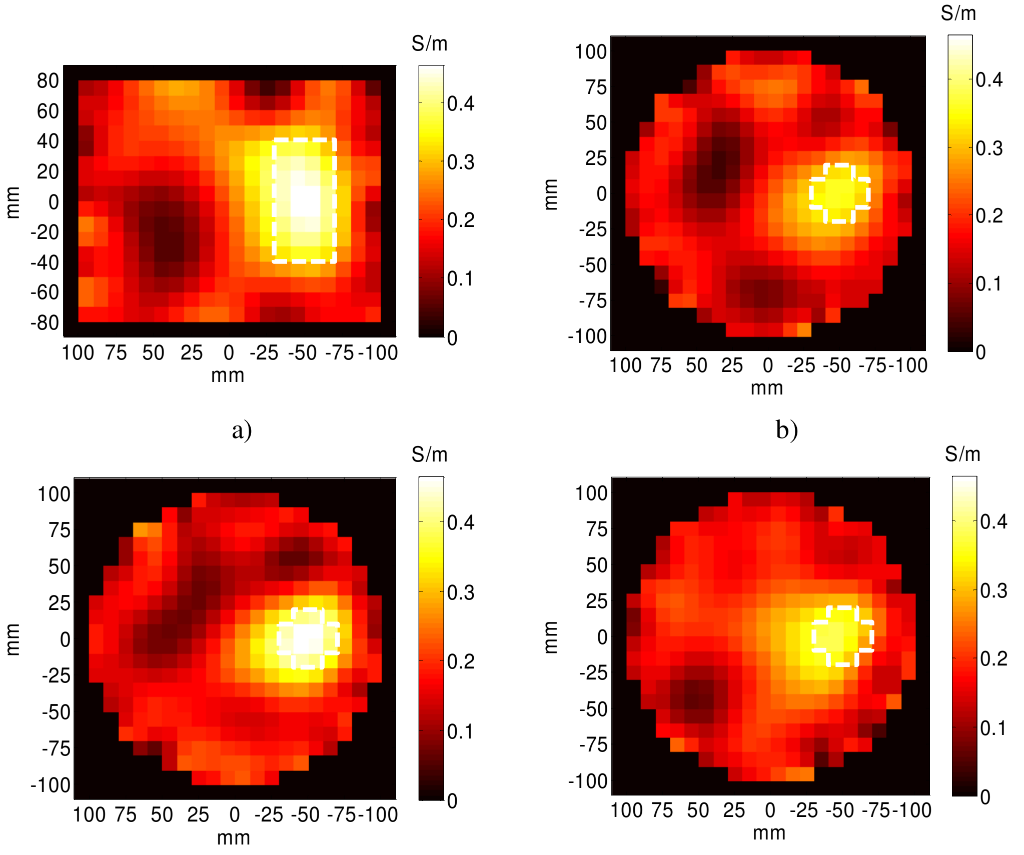

a)

b)

c)

d)

Figure 4.24: Reconstruction of conductivity distribution showing a) vertical slice (*x*=0) mm, [b); c); d)] horizontal slices in different *z* levels (*z*=-40*;* *z*=0*;* *z*=40) mm, with the damped Gauss Newton method (example (P1); data with 2% Gaussian noise).

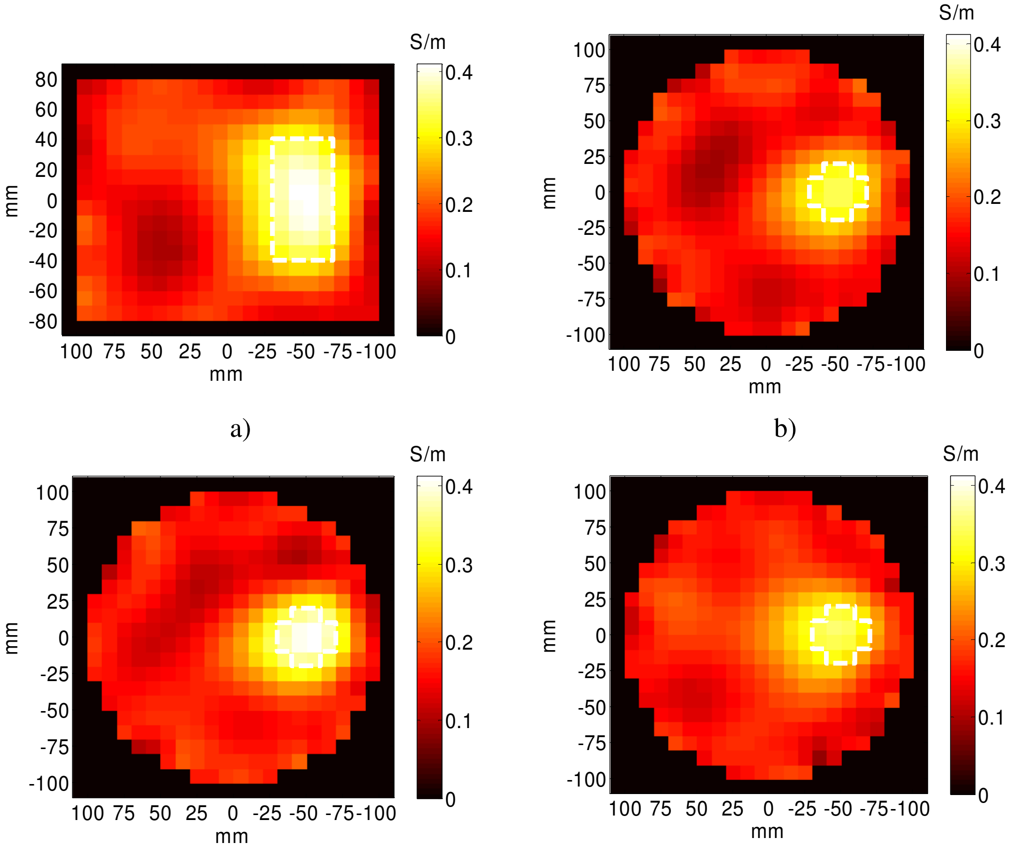

a)

b)

c)

d)

Figure 4.25: Reconstruction of conductivity distribution showing a) vertical slice (*x*=0) mm, [b); c); d)] horizontal slices in different *z* levels (*z*=-40*;* *z*=0*;* *z*=40) mm, with the damped Gauss Newton method (example (P1); data with 2% Gaussian noise).

PDLM:

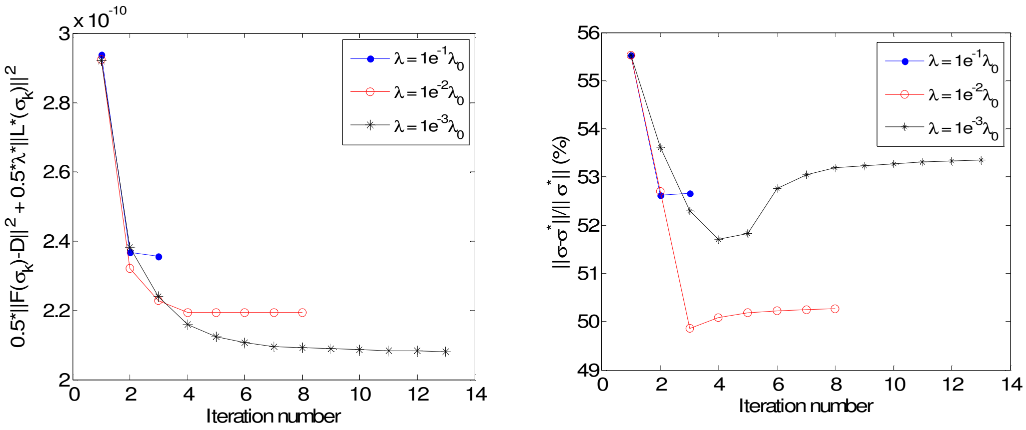

Figure 4.26: Convergence plot of the objective function (left) and relative solution error (right) versus iteration with Powell Dog Leg method (example (P1); data with 2% Gaussian noise).

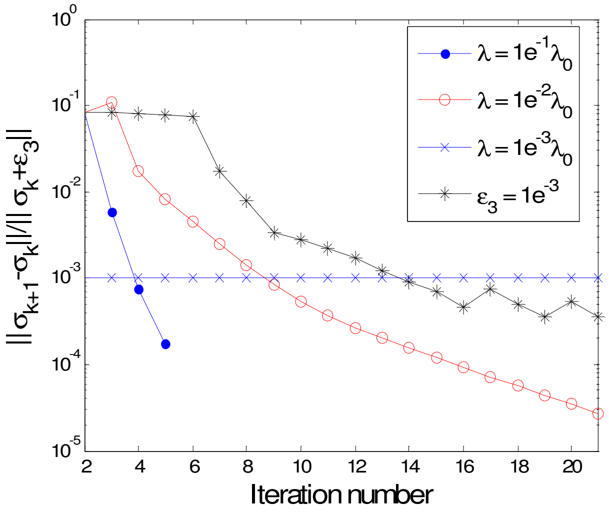

Figure 4.27: Performance of the stopping criterion for the PDL method (example (P1); data with 2% Gaussian noise).

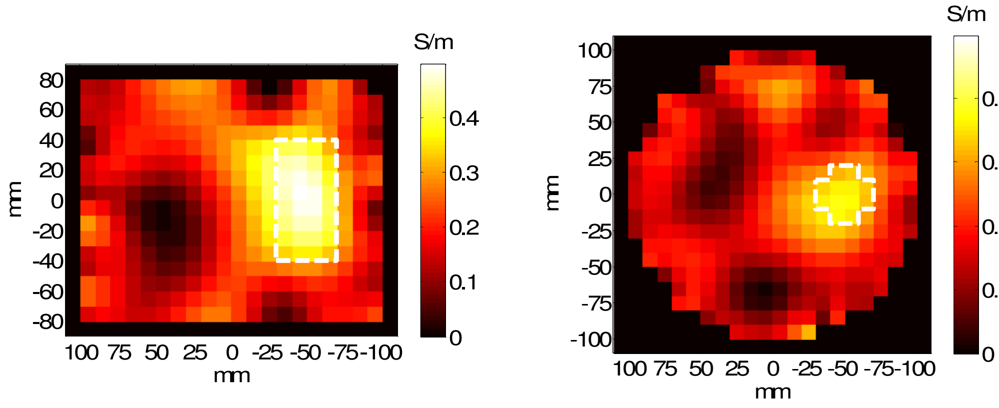

a) b)

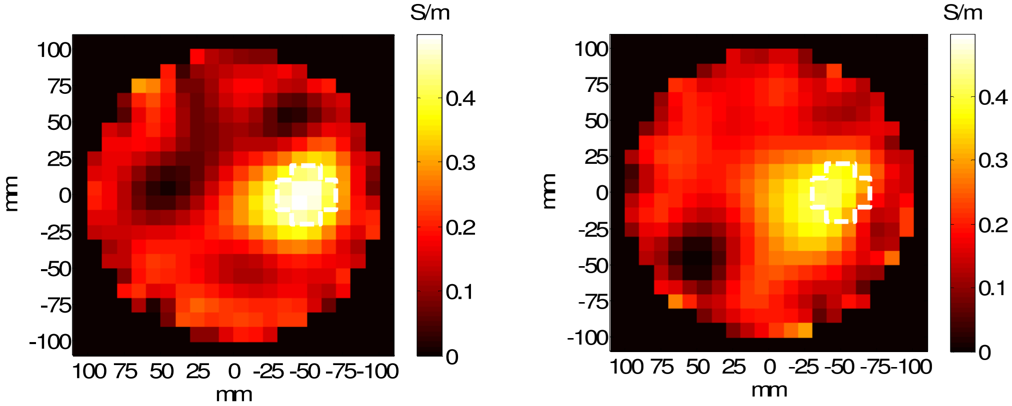

c) d)

Figure 4.28: Reconstruction of conductivity distribution showing a) vertical slice (x=0) mm, [b); c); d)] horizontal slices in different z levels (z=-40; z=0; z=40) mm, with the Powell Dog Leg method (example (P1); data with 2% Gaussian noise; $\lambda = 10^{-3}\lambda_0$).

RGNM:

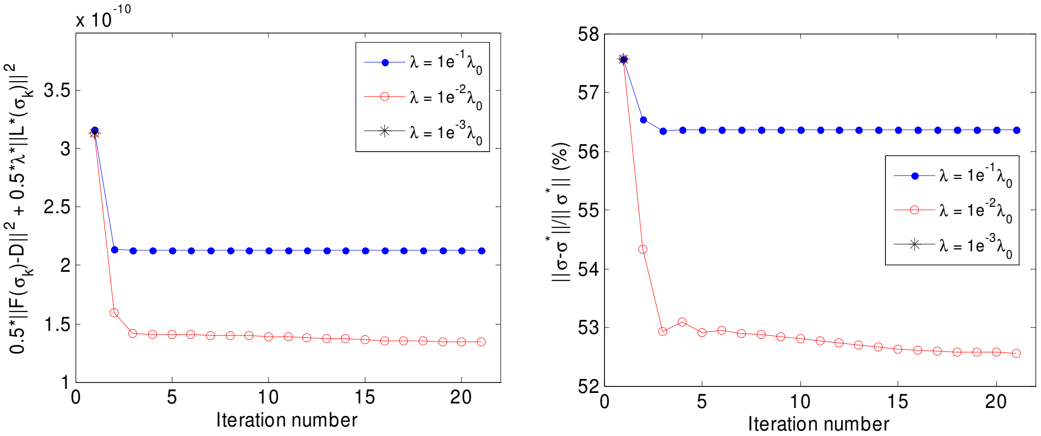

Figure 4.29: Convergence plot of the objective function (left) and relative solution error (right) versus iteration with regularised Gauss Newton method (example (P1); simulated data from Ansoft).

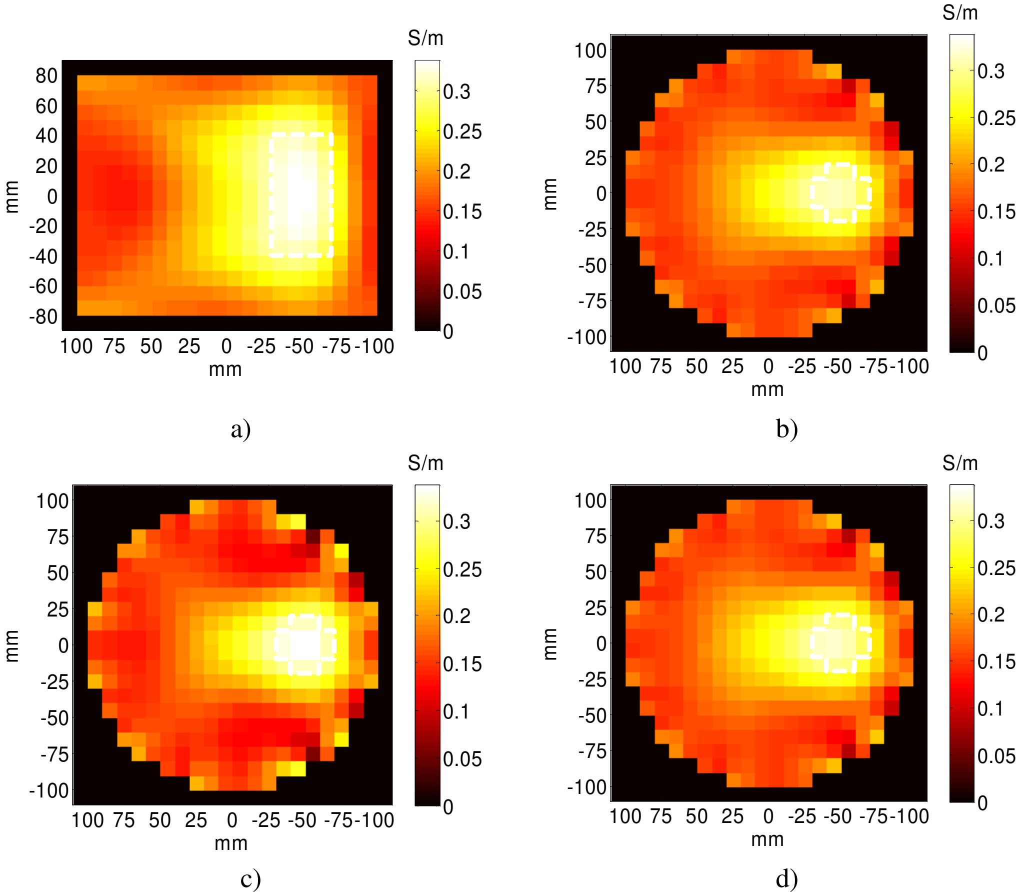

a)

b)

c)

d)

Figure 4.30: Reconstruction of conductivity distribution showing a) vertical slice (x=0) mm, [b); c); d)] horizontal slices in different z levels (z=-40; z=0; z=40) mm, with regularised Gauss Newton method (example (P1); simulated data from Ansoft; $\lambda = 10^{-2}\lambda_0$).

LMM:

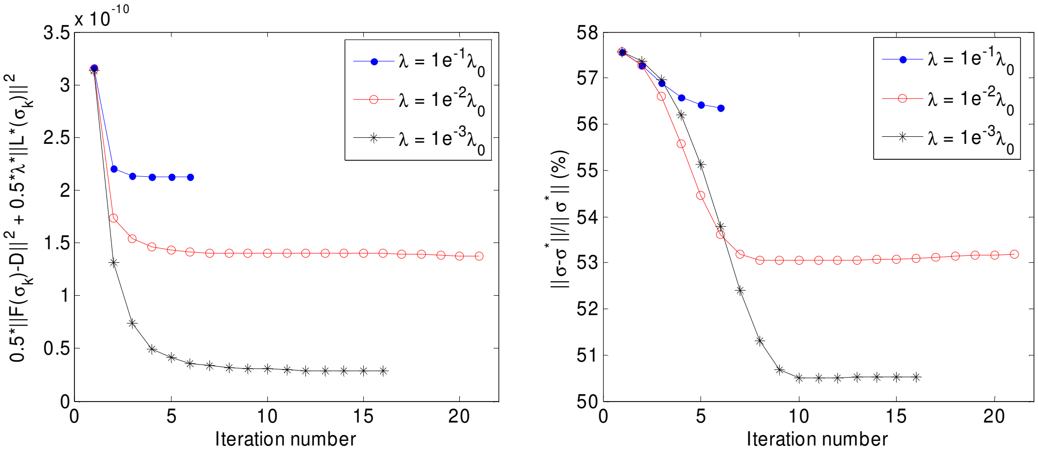

Figure 4.31: Convergence plot of the objective function (left) and relative solution error (right) versus iteration with Levenberg Marquardt method (example (P1); simulated data from Ansoft).

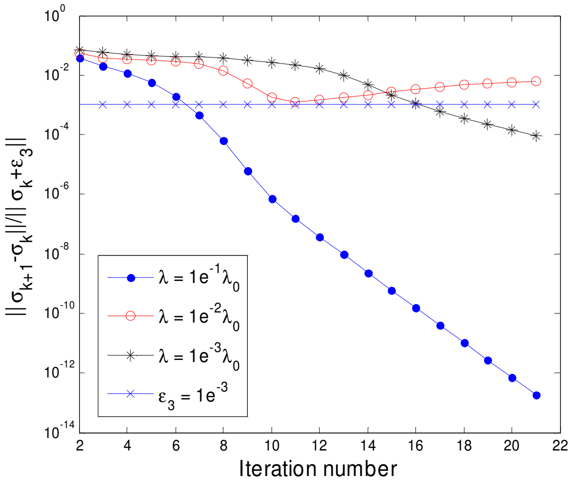

Figure 4.32: Performance of the stopping criterion for the LM method (example (P1); data with 2% Gaussian noise).

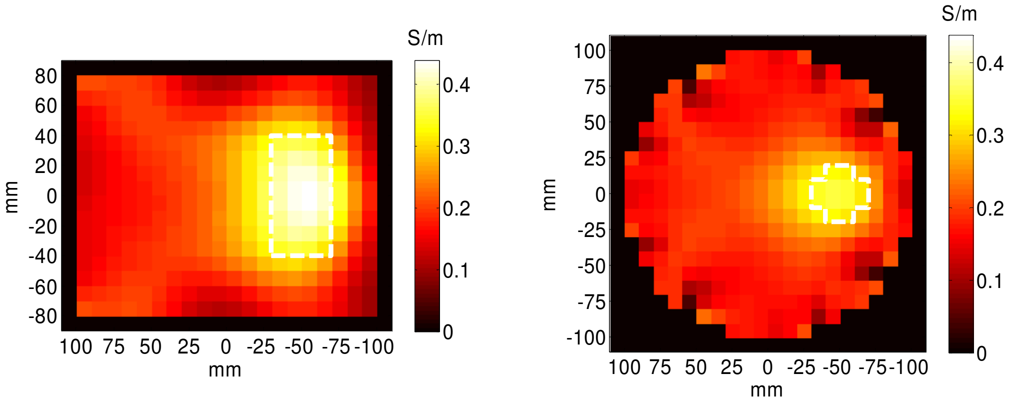

a)

b)

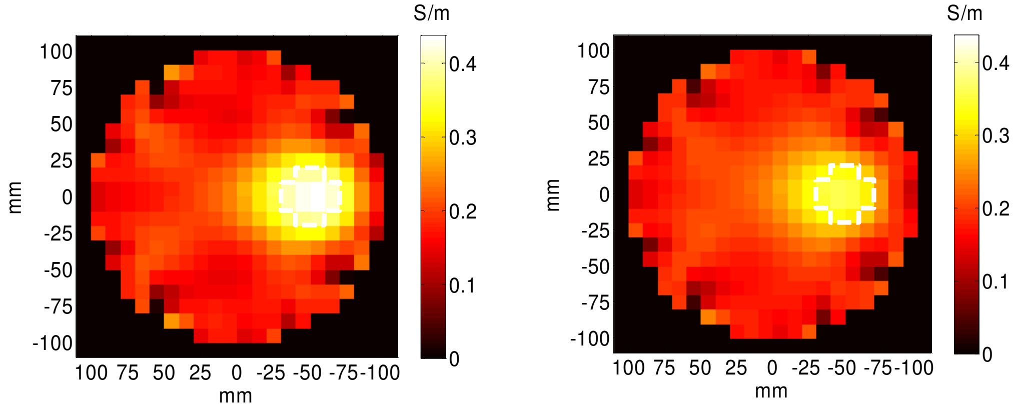

c) d)

Figure 4.33: Reconstruction of conductivity distribution showing a) vertical slice (*x*=0) mm, [b); c); d)] horizontal slices in different *z* levels (*z*=-40; *z*=0; *z*=40) mm, with Levenberg Marquardt method (example (P1); simulated data from Ansoft; $\lambda = 10^{-3}\ \lambda_0$).

DGNM:

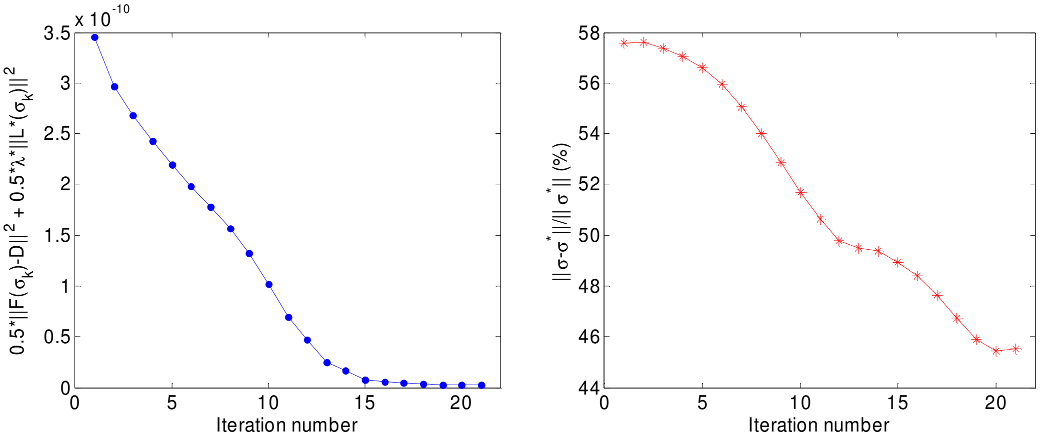

Figure 4.34: Convergence plot of the objective function (left) and relative solution error (right) versus iteration with damped Gauss Newton method (example (P1); simulated data from Ansoft).

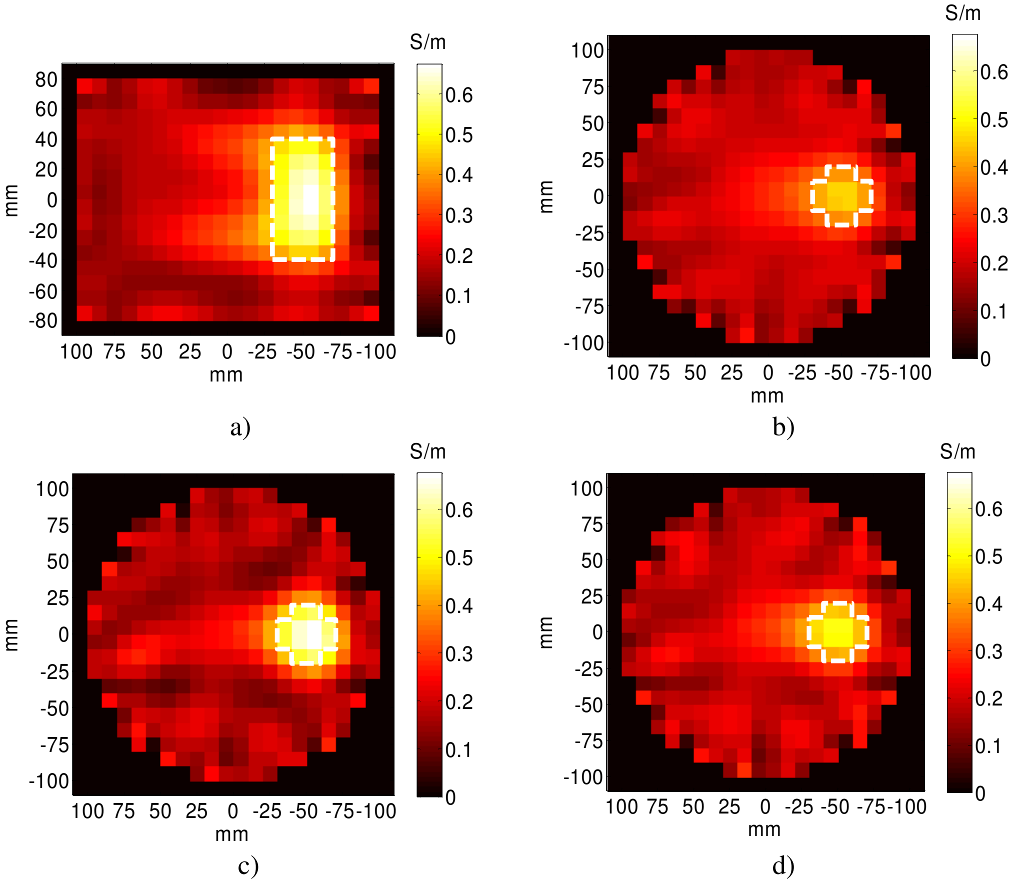

Figure 4.35: Reconstruction of conductivity distribution showing a) vertical slice (*x*=0) mm, [b); c); d)] horizontal slices in different *z* levels (*z*=-40*;* *z*=0*;* *z*=40) mm, with damped Gauss Newton method (example (P1); simulated data from Ansoft).

PDLM:

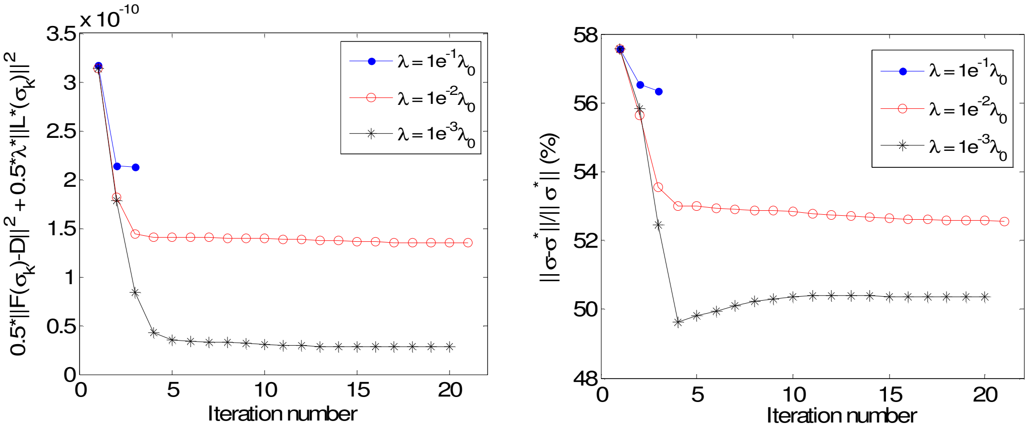

Figure 4.36: Convergence plot of the objective function (left) and relative solution error (right) versus iteration with Powell Dog Leg method (example (P1); simulated data from Ansoft).

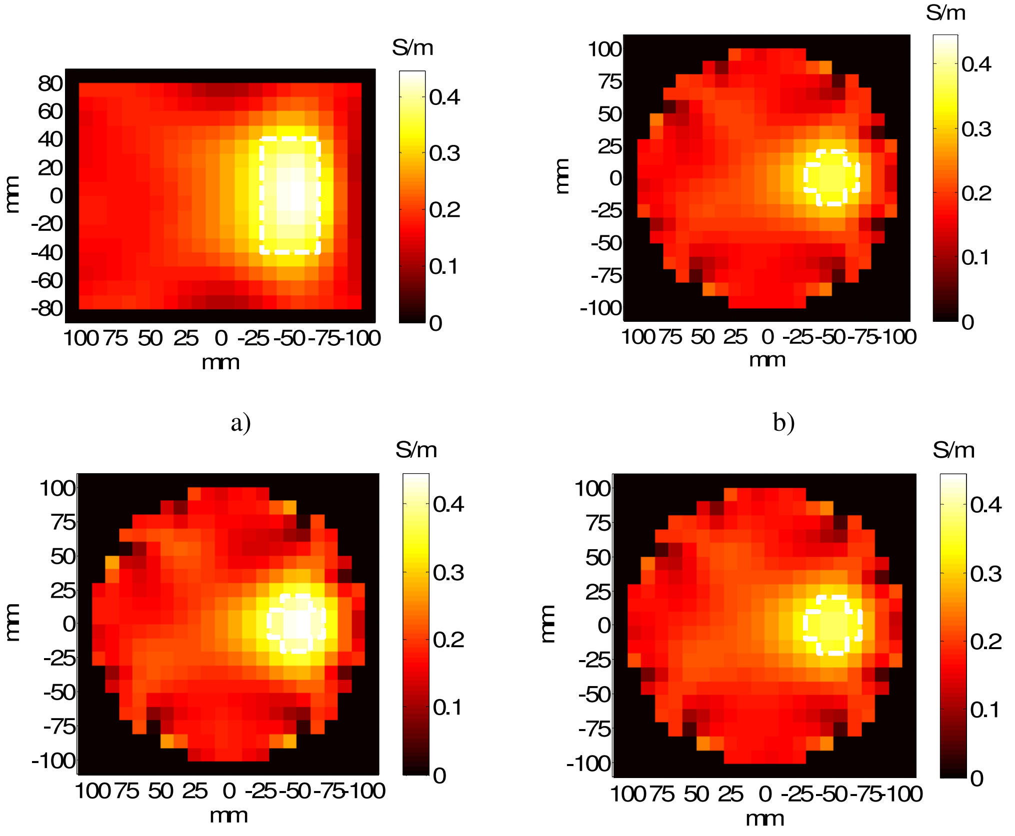

a)

b)

c)

d)

Figure 4.37: Reconstruction of conductivity distribution showing a) vertical slice (*x*=0) mm, [b); c); d)] horizontal slices in different *z* levels (*z*=-40*;* *z*=0*;* *z*=40) mm, with Powell Dog Leg method (example (P1); simulated data from Ansoft; ; $\lambda = 10^{-3}\ \lambda_0$).

4.3 Krylov sub-space methods for large scale problems

As discussed in the previous chapter, a nonlinear inverse problem is usually solved in an iterative scheme where in each iteration, three dimensional modelling of the forward problem is needed. Since the eddy current problem is often solved in high resolution, approaches have been suggested to deal with the associated high computational and memory demands. In some applications, the MIT inverse problem is solved with smaller number of unknown conductivity elements, which produces low resolution images. However in medical MIT applications like imaging local conductivity shifts (e.g. cerebral stroke) in the brain, which constitutes a topic of investigation in this thesis, the inverse problem may need to be solved with large number of degrees of freedom, if the solutions seeks to recover the shape of the stroke and estimate its volume, and/or if structural regularisation information is incorporated in the solution procedure. In order to make the problem less underdetermined, a large number of measurement data is collected. As a result, an outsized Hessian is formed and the task of computing the conductivity vector via direct inversion Newton based methods presented in section (4.2) is extremely computationally demanding. Furthermore, since the matrix is full, it is difficult to handle even matrix multiplication, which raises the enquiry about development of special numerical methods to handle this challenge.

In this section, the application of special numerical techniques based on the Krylov sub-space methods, which can be used for the efficient calculation of large scale problems, is presented. Among these methods, the Conjugate Gradient (CG) optimisation technique has been successfully implemented in medical EIT. Originally the method was proposed by Hestnes and Stiefel in the 1950s as an iterative method for solving linear systems of the following form:

$$\boldsymbol{A}\,\boldsymbol{x} = \boldsymbol{y} \tag{4.59}$$

where $\boldsymbol{A} \in \mathbb{R}^{n \times n}$ is a symmetric positive definite matrix. Thus, the linear CG can be applied directly to the MIT forward problem since the coefficient matrix holds these properties and is sparse. While direct inversion methods solve (4.59) via factorisation and multiplication, the CG iteration projects the problem with its dimension into a lower dimension Krylov sub-space. Using an iterative scheme, the method reduces the original problem into a sequence of lower dimension matrix problems. When applied to solve (4.59) the solution obtained by the *n*th iteration will lie in the associated Krylov subspace generated by $\boldsymbol{A}$ and $\boldsymbol{y}$, like:

$$\begin{aligned}&\boldsymbol{x}_n \in K_n(\boldsymbol{A};\boldsymbol{y}) \text{ where}\\ &K_n(\boldsymbol{A};\boldsymbol{y})=\text{span}\left\{\boldsymbol{y},\boldsymbol{A}\boldsymbol{y},\boldsymbol{A}^2\boldsymbol{y},\boldsymbol{A}^3\boldsymbol{y},...,\boldsymbol{A}^{n-1}\boldsymbol{y}\right\}.\end{aligned} \tag{4.60}$$

This approach makes the CG method computationally efficient to handle large scale problems. The CG algorithm applied to the system (4.59) is presented below:

```
$\boldsymbol{r} = \boldsymbol{y} - \boldsymbol{A}\boldsymbol{x}_0$
while $\|\boldsymbol{r}_n\| / \|\boldsymbol{r}_0\| > tol$ do
   $n = n + 1$
   if $n = 1$
     $\boldsymbol{p} = \boldsymbol{r}$
   else
     $\beta_n = \|\boldsymbol{r}_{n-1}\|^2 / \|\boldsymbol{r}_{n-2}\|^2$                                        (4.61)
     $\boldsymbol{p}_n = \boldsymbol{r}_{n-1} + \beta_n \boldsymbol{p}_{n-1}$
   end
   $\alpha_n = \|\boldsymbol{r}_{n-1}\|^2 / (\boldsymbol{p}_n^{\mathrm{T}} \boldsymbol{A}\boldsymbol{p}_n)$
   $\boldsymbol{x}_n = \boldsymbol{x}_{n-1} + \alpha_n \boldsymbol{p}_n$
   $\boldsymbol{r}_n = \boldsymbol{r}_{n-1} - \alpha_n \boldsymbol{A}\boldsymbol{p}_n$
end
```

where $\boldsymbol{x}_0$ is an initial guess of the solution $\boldsymbol{x}$, $\boldsymbol{r}$ is the residual vector, $\boldsymbol{p}$ is the search direction and α is the step size. Here, β is a calibration scalar that is determined to enforce the special "conjugacy property" of the CG iteration, which requires the search direction vectors $\boldsymbol{p}_{n-1}$ and $\boldsymbol{p}_n$ to be $\boldsymbol{A}$ conjugate. This means that the set of vectors produced by the CG iterations $\{\boldsymbol{p}_0,\boldsymbol{p}_1,\boldsymbol{p}_2,...,\boldsymbol{p}_{n-1}\}$ are found to be $\boldsymbol{A}$ orthogonal as:

$$\boldsymbol{p}_i^{\mathrm{T}}\boldsymbol{A}\boldsymbol{p}_j = 0 \quad \text{for all } i \neq j \tag{4.62}$$

4.3.1 Nonlinear Conjugate Gradient method

Recall that the MIT inverse problem is treated through the minimisation of the nonlinear least squares problem:

$$\widetilde{F}(\boldsymbol{\sigma}) = \frac{1}{2}\left\|\boldsymbol{F}(\boldsymbol{\sigma}) - \boldsymbol{D}\right\|^2 + \frac{1}{2}\lambda\left\|\boldsymbol{L\sigma}\right\|^2$$

Fletcher and Reeves proposed the nonlinear variant of the CG method (NLCG) in the 1960s which has later been applied successfully to solve the EIT conductivity inverse problem [117]. The NLCG algorithm is presented below:

```
$\boldsymbol{d}_0 = -\nabla\widetilde{F}(\boldsymbol{\sigma}_0) = -\boldsymbol{g}(\boldsymbol{\sigma}_0)$ , $k$=0;
while $\nabla\widetilde{F}(\boldsymbol{\sigma}_k) > tol$ do
    $k = k + 1$
    Compute $\alpha_k$ (line search)
    $\boldsymbol{\sigma}_k = \boldsymbol{\sigma}_{k-1} + \alpha_k \boldsymbol{d}_{k-1}$
    $\beta_k^{FR} = \left(\nabla\widetilde{F}(\boldsymbol{\sigma}_k)^{\mathrm{T}}\nabla\widetilde{F}(\boldsymbol{\sigma}_k)\right) / \left(\nabla\widetilde{F}(\boldsymbol{\sigma}_{k-1})^{\mathrm{T}}\nabla\widetilde{F}(\boldsymbol{\sigma}_{k-1})\right)$
    $\boldsymbol{d}_k = -\nabla\widetilde{F}(\boldsymbol{\sigma}_k) + \beta_k \boldsymbol{d}_{k-1}$
End
```

(4.63)

where the scalar β_k^{FR} is calculated using a formula suggested by Fletcher and Reeves. k is the iteration number of the optimisation method. An alternative expression has been proposed later by Polak and Ribiere which is given by the pair of equations:

$$\beta_k^{PR} = \nabla\widetilde{F}(\boldsymbol{\sigma}_k)^{\mathrm{T}}\left(\nabla\widetilde{F}(\boldsymbol{\sigma}_k)\text{-}\nabla\widetilde{F}(\boldsymbol{\sigma}_{k-1})\right) / \left(\nabla\widetilde{F}(\boldsymbol{\sigma}_{k-1})^{\mathrm{T}}\nabla\widetilde{F}(\boldsymbol{\sigma}_{k-1})\right) \tag{4.64}$$

$$\beta_k^{PR} = \max\left\{\beta_k^{PR}, 0\right\} \tag{4.65}$$

where (4.65) enforces the condition that when β_k^{PR} is negative, the new search direction $\boldsymbol{d}_k$ is chosen to be the steepest decent direction i.e. $-\nabla\widetilde{F}(\boldsymbol{\sigma}_k)$. Hence, this condition ensures that new direction is always descent. There are many variants for determining β, but numerous references suggest that the Polak-Ribiere is the most robust and efficient variant [58, 104].

4.3.2 Damped Gauss Newton Krylov method

Since the NLCG employs only 1st order derivative information in calculating the direction step, the convergence of the method is slow. As a result, a large number of iterations may be required to achieve a satisfactory optimisation. Since the 3D forward problem is recomputed every time the model is updated, the computational time can be a major obstacle. In order to deal with this problem Vauhkonen [117] and Polydorides [119] applied the special block NLCG in EIT originally developed for optical diffuse tomography, which is based on the idea of splitting the inverse problem with its original dimension into sub-problems with smaller dimensions. In doing so, the original Jacobian $\boldsymbol{J} \in \mathbb{R}^{m \times n}$ is partitioned into sub-blocks by splitting the measurement data into smaller subsets, and using this approach the inverse problem is solved with a single data subset. After each update of the model, a different subset of data is selected to calculate the next iteration conductivity distribution. Although the iteration time and memory storage is significantly reduced via this approach, the method would still need a larger number of iterations. Since iterative inversion methods which employ 2nd order information converge faster than methods employing 1st order derivative information, Horesh [120] and Polydorides [121] implemented another variant of the CG method which employs 2nd order derivative of the objective function $\widetilde{F}$. In the Gauss Newton search direction the nonlinear inverse problem is linearised locally, i.e. the nonlinear inverse problem is decomposed into a series of linearly approximated steps. The linear iterative CG method described by (4.61) can be applied to estimate the linearised step $\boldsymbol{d}_{dGN-K}$ used to update the iterate $\boldsymbol{\sigma}_k$ within the Gauss Newton algorithm by substituting:

$$\boldsymbol{x}_n \leftarrow K_n(\boldsymbol{A}\,;\boldsymbol{y})$$

With:

$$\boldsymbol{d}_{dGN-K} \leftarrow K_n\left(\underbrace{(\boldsymbol{J}_k{}^{\mathrm{T}}\boldsymbol{J}_k + \lambda_k \boldsymbol{L}^{\mathrm{T}}\boldsymbol{L})}_{\boldsymbol{H}}\;;\; \underbrace{-\left(\boldsymbol{J}_k{}^{\mathrm{T}}(\boldsymbol{F}(\boldsymbol{\sigma}_k)\text{-}\boldsymbol{D}) + \lambda_k \boldsymbol{L}^{\mathrm{T}}\boldsymbol{L}\boldsymbol{\sigma}_k\right)}_{-\boldsymbol{g}} \right) \tag{4.66}$$

While the iterative CG approach produces an approximation to the Newton direct inverse of the Hessian, the problem related to the explicit formulation of the immense approximated regularised Hessian $(\boldsymbol{J}_k{}^{\mathrm{T}}\boldsymbol{J}_k + \lambda_k \boldsymbol{L}^{\mathrm{T}}\boldsymbol{L})$ would still impose computational and memory storage difficulties in large scale problems. In order to deal with this problem all matrix-vector product operations comprised within the CG iteration in which the explicit Hessian is involved are modified as follows:

$$\boldsymbol{H}_k \boldsymbol{d}_n = \left(\boldsymbol{J}_k{}^{\mathrm{T}}\left(\boldsymbol{J}_k \boldsymbol{d}_n\right) + \lambda_k \boldsymbol{L}^{\mathrm{T}} \boldsymbol{L}\left(\boldsymbol{d}_n\right)\right) \tag{4.67}$$

As can be seen, the brackets surrounding the product $\boldsymbol{J}_k \boldsymbol{d}_n$ results in a vector, which is then multiplied by $\boldsymbol{J}_k{}^{\mathrm{T}}$, so the immense term of $\boldsymbol{J}_k{}^{\mathrm{T}} \boldsymbol{J}_k$ is never explicitly formed. The product $\boldsymbol{H}_k \boldsymbol{d}_n$ for explicit Hessian formulation requires u^3 floating point operations, whereas the implicit formulation requires $u^2v+ uv^2$ (assuming that the computational cost of $\boldsymbol{L}^{\mathrm{T}} \boldsymbol{L}\left(\boldsymbol{d}_n\right)$ is negligible since $\boldsymbol{L}^{\mathrm{T}} \boldsymbol{L}$ is a sparse matrix). Therefore, Horesh [120] explains this way of implicitly forming the Hessian is more efficient whenever $v < \left(\sqrt{5}-1\right)/2u$. For large scale problems as considered in this section, $v \ll u$, and therefore this formulation is favoured.

In order to further optimise the convergence and stability of the CG iterative scheme, preconditioning of the approximate Hessian can be an advantage since the distribution of the singular values of this matrix can impact on the quality of this convergence. Favourably, the singular values should be clustered around a fixed positive number, and therefore fewer iterations are required to reach the convergence of the CG. Using an appropriate pre-conditioner $\varTheta$, the system (4.60) has a solution identical to the one of the preconditioned system given by:

$$\boldsymbol{x}_n \leftarrow K_n(\varTheta^{-1}\boldsymbol{A};\ \varTheta^{-1}\boldsymbol{y}) \tag{4.68}$$

Several preconditioning matrices have been proposed in the literature, but in this section the following pre-conditioner will be employed:

$$\varTheta = diag\left(\sum_{j=i} \boldsymbol{J}_{ji} + \lambda_k\right) \tag{4.69}$$

and the algorithm (4.61) using the proposed pre-conditioner is modified to form the CG Krylov iterative scheme presented below used to calculate an approximation for the step $\boldsymbol{d}_{dGN}$ obtained via the inversion based damped Gauss Newton method. When employing this iterative scheme (inner iterations) within the iterative (outer iteration) damped Gauss Newton, the method is called the damped Gauss Newton Krylov (DGN-K) method

```
$\boldsymbol{r}_0 = -\boldsymbol{g}_k - \boldsymbol{H}_k \boldsymbol{d}_0$; $n$=0
while $\|\boldsymbol{r}_n\| / \|\boldsymbol{r}_0\| > tol$ do
    $n = n + 1$
    $\boldsymbol{z} = \boldsymbol{\Theta} \backslash \boldsymbol{r}$
    if $n = 1$
        $\boldsymbol{p} = \boldsymbol{z}$
    else
        $\beta_n = \left(\boldsymbol{r}_{n-1}^{\mathrm{T}} \boldsymbol{z}_{n-1}\right) / \left(\boldsymbol{r}_{n-2}^{\mathrm{T}} \boldsymbol{z}_{n-2}\right)$
        $\boldsymbol{p}_n = \boldsymbol{z}_{n-1} + \beta_n \boldsymbol{p}_{n-1}$
    end
    $\alpha_n = \left(\boldsymbol{r}_{n-1}^{\mathrm{T}} \boldsymbol{z}_{n-1}\right) / \left(\boldsymbol{p}_n^{\mathrm{T}} \boldsymbol{H}_k \boldsymbol{p}_n\right)$
    $\boldsymbol{d}_n = \boldsymbol{d}_{n-1} + \alpha_n \boldsymbol{p}_n$
    $\boldsymbol{r}_n = \boldsymbol{r}_{n-1} - \alpha_n \boldsymbol{H}_k \boldsymbol{p}_n$
end
```

(4.70)

where tol is specified by the user, for instance, $tol = 1 \times 10^{-3}$ appears to be a reasonable choice for the cases considered here. Note, *n* is the iteration index for the CG method and *k* denotes the index for the outer iteration for the iterative image reconstruction.

4.3.3 Simulations

In order to test the accuracy and the computational efficiency of the proposed DGN-K method, the following problems with different numbers of unknown conductivity elements (DoFs) are considered as follows:

a) Example (P1) (Cylindrical background and an inclusion) comprising 5056 DoFs
b) Head model (H1) (White matter and large stroke) comprising 9012 DoFs
c) Head model (H2) (White matter and large stroke) comprising 30405 DoFs

The two employed head models were obtained from an FE head model that was created by Holder *et al* from University College London who applied 53,336 FEs in the head cavity to simulate 7 different biological tissues. Since the scale (size) of the problem is the main focus of this investigation, two tissues were considered for simplicity namely: white matter (0.16 Sm^{-1}) and the stroke (1.1 Sm^{-1}) as shown in

Figure 4.38. For image reconstruction, 2304 simulated measured data was collected and absolute images for the three conductivity models were generated from the iterative DGN-K optimisation method. In order to examine the computational benefits of this method, the same image reconstruction was carried out with the inversion based DGN method and comparisons were made according to the following criteria a) Convergence of the objective function and the solution error norm, b) image quality, and c) Computation time.

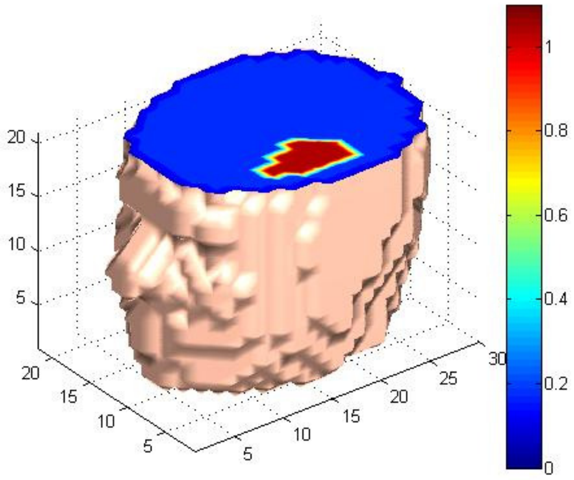

Figure 4.38: Head model (white matter and large peripheral stroke) (9012 DoFs)

4.3.4 Results and Discussion

4.3.4.1 Convergence of the objective function and the solution error norm

Figure 4.39 shows the convergence of the objective function and the solution error norm for the image reconstruction of the head model (H1) using the DGN-K and the DGN methods. Clearly, similar degree of convergence is attained using both methods, which infers that there is no loss of accuracy caused by the application of the Krylov sub-space method in combination of the Damped Gauss Newton method

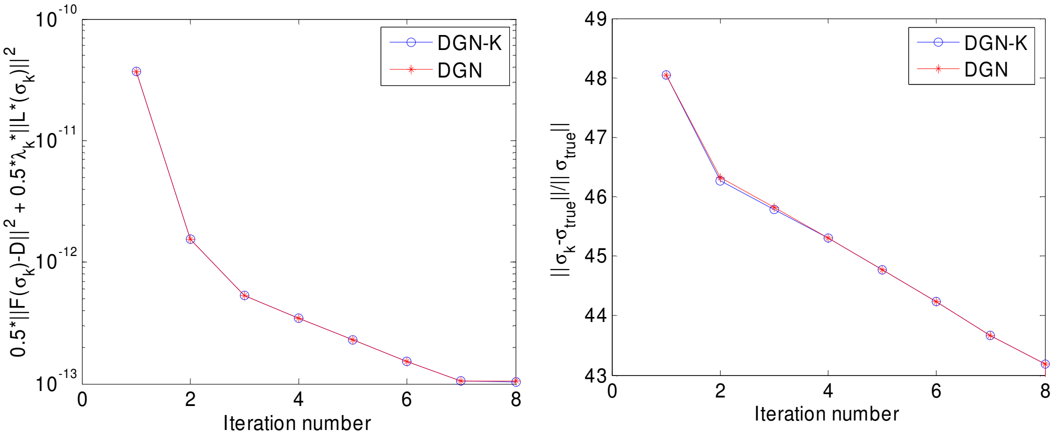

Figure 4.39: Plot of the convergence of the objective function (left), and the solution error (right)

4.3.4.2 Image quality

Figure 4.40 shows the cutaway plane displaying the reconstructed conductivity distribution using the DGN-K and the DGN methods. Again, the reconstructed images resemble each other, which infers there is no loss in the image quality using the proposed CG method.

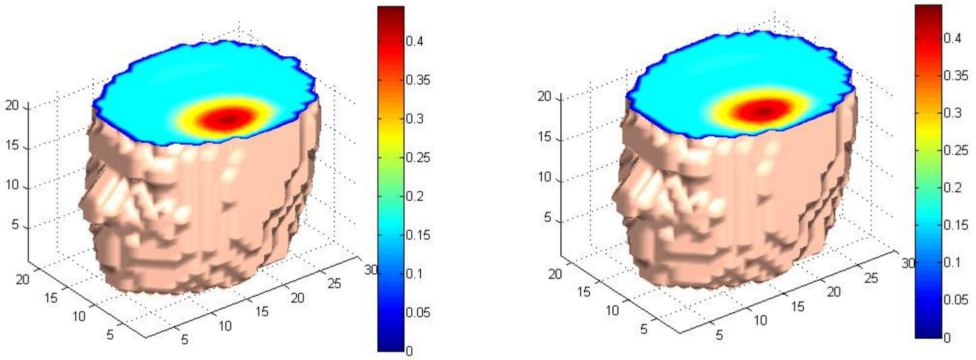

Figure 4.40: Reconstructed images for the large scale head model (H1), using the DGN-K method (left) and the DGN method (right)

4.3.4.3 Computation time

In order to assess the computational cost saving using the DGN-K method compared to its counterpart candidate, the Newton version DGN method, the average time per iteration was calculated for the three problems with different resolutions. From Figure 4.41, it can be shown that as the problem size increases in scale, the computation time is reduced for the DGN-K. For the Head model with 30k elements, the DGN-K is 8 times faster than the DGN method.

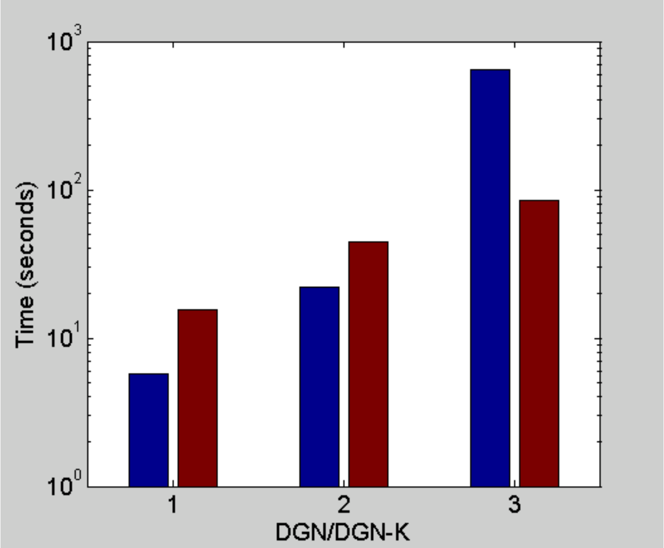

Figure 4.41: Average computation time per iteration for (1: example (P1); 2: head model (H1); 3 head model (H2))

5 Regularisation methods in Magnetic Induction Tomography

5.1 Introduction

In Chapter 4, a class of nonlinear optimisation methods was investigated for use in image reconstruction of volumetric material properties using MIT. In order to compare the stability and convergence performance of these methods the same a-priori knowledge about the solution or the regularisation operator was employed. This consisted of a 2nd order Laplacian operator which penalises large changes in material properties (i.e. conductivity) of the object. Other than the regularisation matrix being common, the algorithms employed numerical mechanisms to control the convergence and maintain the stability of the solution throughout the iteration process. In summary, on the one hand, it was shown that all the proposed methods provided noticeable improvement in different respects of nonlinear optimisation of the ill-posed MIT inverse problem compared to the standard regularised Gauss Newton method (RGNM). On the second hand, the regularised Levenberg Marquardt method (LMM) and the trust region Powell Dog Leg method (PDLM) exhibited similar performance characteristics of which they demonstrated an outstanding stability toward the end of the iterative process by keeping away from unwanted divergence. The newly introduced damped Gauss Newton method (DGNM) was able to produce better quantitative convergence but is relatively more prone to instability at the last stage of the iterations especially if the data is heavily contaminated with noise. As a result of this assessment, in this chapter the (LM) method has been chosen to approach the investigation of regularisation in MIT.

For image reconstruction in MIT, regularisation operators holding a-priori information about the object structure and the noise distribution in the data are introduced to help the solution of the underdetermined, ill-posed inverse problem. In Chapter 2, a detailed numerical analysis was presented, which demonstrates how such operators tend to filter noise form the data and correlate the solution toward some given prior. One of the very classical regularisation approaches in tomography is standard Tikhonov regularisation which uses the identity matrix. This approach employs uniform weights to penalise the magnitude of the MIT data. However, due to the soft field effect that is typical of MIT, the sensitivity varies spatially and increases towards the periphery of the object, hence a common disadvantage associated with this operator is that the centre will be largely penalised and the noise will be pushed towards the border in the reconstructed image. With the introduction of the so called "generalised Tikhonov regularisation" several regularisation operators can be utilised with different prior information that suit a particular inspection application. In addition to the smoothing 2nd order difference operator the objective in this chapter is to investigate three other regularisation matrices with different prior characteristics. The benefits and the limitations of such regularisation schemes in the MIT image reconstruction are examined for two low conductivity applications. The first considers the 3D reconstruction of a stroke in a simple target and a realistic shaped head. The second consists of inspecting the water fraction in water/oil pipelines via 2.5D image reconstruction. Three flow regimes are approached: stratified, annular and bubble flows.

5.2 Regularisation priors

Regularisation priors are numerical tools for treatment of ill-conditioned inverse problems as those encountered in EIT or MIT. They can provide probabilistic information about the conductivity values of the image elements and their correlation. Several regularisation operators have been proposed in the literature. Most commonly applied priors in electrical tomography include: smoothing operators, edge preserving priors and structural information based priors. Smoothing operators assume the conductivity distribution in the object is largely smooth. Hence they penalise large changes in the conductivity values of elements losing information about internal material boundaries and edges. In EIT, Hua *et al* [122] implemented two forms of smoothing operators: first (Neighbouring matrix) and second order Laplacian operators and concluded the second order operator is most effective in filtering noise at the expense of smoothing the image. Another regularisation approach proposed by Cheney *et al* [123] called NOSER consists of scaling the uniform weights of the identity matrix with the diagonal elements of the sensitivity coefficient matrix such that $[\boldsymbol{R}]_{i,i} = [\boldsymbol{J}^{\mathrm{T}}\boldsymbol{J}]_{i,i}$. The image conductivity elements are then regularised using different weights according to their associated sensitivities. This approach can be more effective than the identity matrix regularisation since it accounts for the soft field nature of MIT where the sensitivity is a function of position. Dai *et al* [124] proposed other variants of NOSER by taking the exponent (p) of the sensitivity diagonal elements giving ($[\boldsymbol{R}]_{i,i} = [\boldsymbol{J}^{\mathrm{T}}\boldsymbol{J}]_{i,i}^{p}$). The choice of the exponent is heuristic compromise between reducing the noise in the centre (p = 0) or in the boundary (p = 1). On the other hand, Casanova *et al* [125] demonstrated an edge preserving technique [126] using linear image reconstruction, which can be used in MIT for detecting large variations in conductivity. Vauhkonen *et al* [42] proposed a regularisation method which takes into account prior information about the conductivity distribution in the object.

In this chapter, the performance of four regularisation methods is investigated using the LM image reconstruction algorithm. These priors are described below:

NOSER:

$$\boldsymbol{R} = \mathrm{diag}\left(\mathrm{diag}(\boldsymbol{J}_k^{\;T}\boldsymbol{J}_k)\right)^{1/2}$$

Second order Laplacian prior:

$$\boldsymbol{L} = \boldsymbol{N} \mid N_{(u,v)} = \begin{cases} \Sigma_n & \text{for } u = v \\ -1 & \text{for } u \text{ and } v \text{ are neighbours} \\ 0 & \text{otherwise} \end{cases}$$

$$\boldsymbol{R} = \boldsymbol{L}^{\mathrm{T}}\boldsymbol{L}$$

Edge preserving regularisation:

$$\boldsymbol{L} = \begin{cases} (1,-1) \text{ for two voxels } j \text{ sharing a facet } i \\ 0 \qquad \text{otherwise} \end{cases}$$

$$\boldsymbol{G} = \boldsymbol{L} * \boldsymbol{\sigma}$$

$$\boldsymbol{E} = \frac{1}{\boldsymbol{G}^2 + \beta}$$

$$\boldsymbol{R} = \boldsymbol{L}^T * diag(\boldsymbol{E}) * \boldsymbol{L}$$

Subspace regularisation method:

A learning set of conductivity distributions is constructed:

$$\boldsymbol{\sigma} = \left(\boldsymbol{\sigma}_1, \boldsymbol{\sigma}_2, ..., \boldsymbol{\sigma}_Q\right)$$

Given that the approximation for the correlation matrix $\boldsymbol{corr}_{\boldsymbol{\sigma}}$ can be calculated as:

$$\boldsymbol{corr}_{\sigma} = \sum_{i=1}^{Q} \zeta_i \boldsymbol{\sigma}_i \boldsymbol{\sigma}_i^T$$

We assume the relative probabilities for the conductivity distribution are uniform, Hence:

$$\boldsymbol{corr}_{\sigma} = Q^{-1} \boldsymbol{\sigma}_i \boldsymbol{\sigma}_i^T$$

Having the matrix $\boldsymbol{corr}_{\sigma}$, the eigenvalues σ_i (note that σ_i are different from the conductivity vectors $\boldsymbol{\sigma}_i$) and the corresponding eigenvectors υ_i are computed.

A subspace K_υ is constructed by taking the first M eigenvectors corresponding to the largest eigenvalues.i.e. $K_\upsilon = span\left\{\upsilon_i \mid 1 \le i \le M\right\}, M \ll Q$

The orthogonal projector onto the subspace K_υ can be written as $\boldsymbol{P} = \boldsymbol{U}\boldsymbol{U}^{\mathrm{T}}$, where

$$\boldsymbol{U} = \left(\upsilon_1, ..., \upsilon_M\right) \in \mathbb{R}^{N \times M}$$

$$\boldsymbol{L} = \boldsymbol{I} - \boldsymbol{U}\boldsymbol{U}^{\mathrm{T}}$$
$$\boldsymbol{R} = \boldsymbol{L}^T \boldsymbol{L}$$

5.3 Simulations

A series of simulations has been devised to test the LM method and analyse the performance of the regularisation techniques for two low conductivity applications:

5.3.1 Imaging cerebral stroke

In a first test, the application of the proposed regularisation priors within the LMM was tested with a simple image reconstruction problem, the dimensions and the electrical properties of which have already been described in section 4.2.2. The problem (Figure 5.1 (a)) consists of a cylindrical background assigned a conductivity of 0.16 Sm^{-1} and a small perturbation with conductivity of 1.1 Sm^{-1}, altogether crudely approximating a head with white matter and a stroke modelled as blood. This seems a reasonable starting point to enable us to explore the regularising properties of the priors before moving to structures which are realistic of the actual problem.

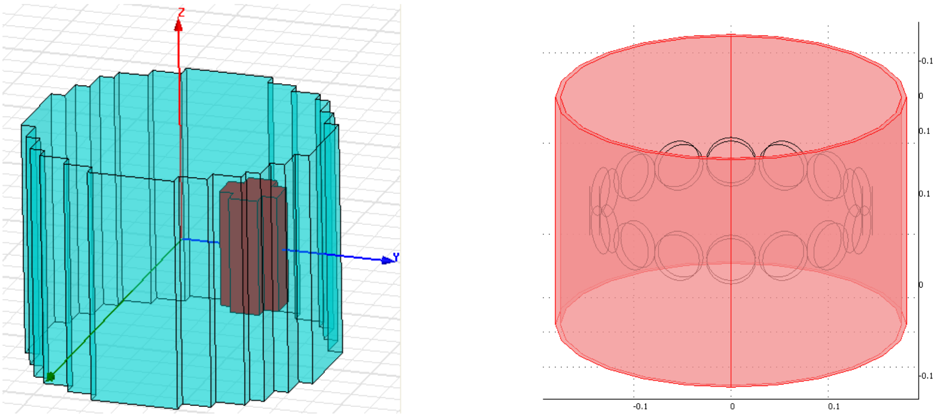

a) b)

Figure 5.1: a) Phantom (P1) and b) the MIT system model

For image reconstruction the 16 channel MIT system Mark 1 (Figure 5.1(b)) presented and employed in Chapters 3 and 4 was used to simulate the data used for inversion. A dataset of 2034 induced voltages was compiled from 9 planes of projections achieved by scanning the object at different equally spaced positions (20 mm displacements) in the vertical (z axis) direction. This process was carried out to obtain good sensitivity around the 3D object volume and increase the size of independent data. For mesh generation, the object was discretised into 5056 cubic voxels, of which 96 elements were allocated in the perturbation. The operating frequency was set to 10 MHz. The data was disturbed by adding a voltage data dependent Gaussian white noise with 1% variance and zero mean giving an SNR of 40 dB. This noise is assumed to model the integral of various possible sources of noise namely: instrumentation noise, positioning and geometrical inaccuracies and numerical discretisation errors. The initial guess was obtained using a direct (single step) inversion of the data (see algorithm Figure 4.7) using the 2nd order Laplacian as a regularisation matrix and a regularisation parameter λ_0 chosen to be 10^{-8}. In the iterative procedure, the damping parameter was initialised to $\gamma_{(k=0)} = 1\times10^{-3}\,\lambda_0$ (k is the iteration index) and then has been dynamically varied in every iteration according to the gain in the reduction of the objective function value compared to that of the quadratic model function. The amount by which the damping parameter is increased or decreased follows the Levenberg Marquardt updating strategy described by (4.23). The regularisation parameter λ was kept constant.

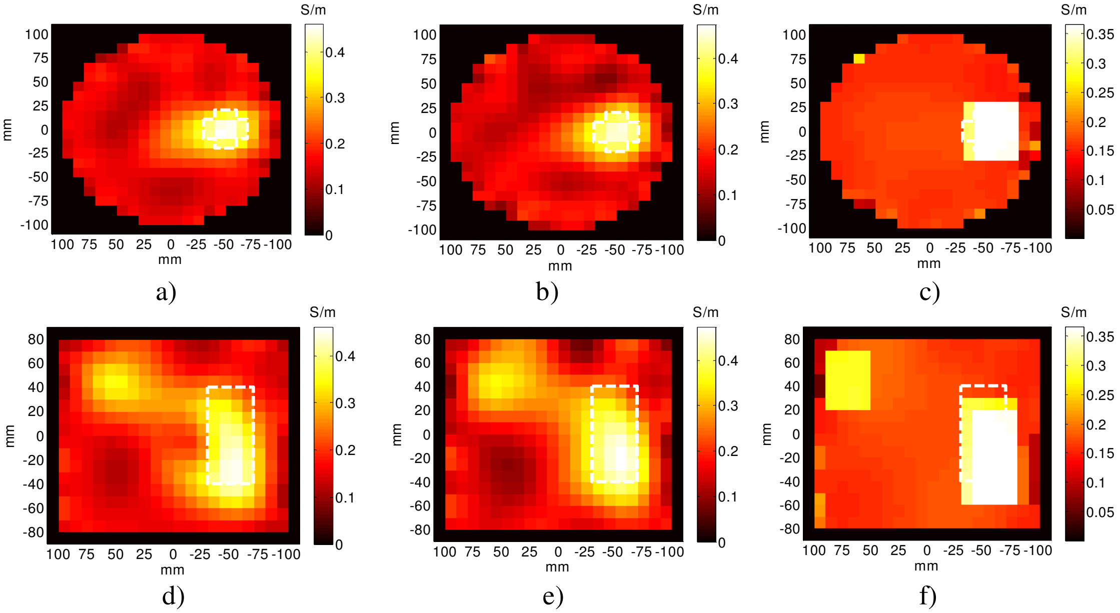

a)
b)
c)
d)
e)
f)

Figure 5.2: Case of simple phantom (one perturbation (1.1 Sm^{-1}) in a homogenous background (0.16 Sm^{-1})). Reconstructed images using a)-d) NOSER, b)-e) 2nd Order Laplacian, c)-f) Edge preserving regularisation.

Figure 5.2 shows horizontal and vertical slices of the 3D reconstructed object using the LMM algorithm with three types of regularisation, namely NOSER, 2nd order Laplacian matrix and edge preserving prior. The results show the LMM algorithm with the NOSER and the 2nd order Laplacian operator produced more or less similar quality of reconstruction, where both were able to recover the perturbation, but at the expense of some spatial artefacts. In addition, the perturbation is fairly well positioned within its original boundaries (dashed line) but with noticeable smoothing. On the other hand, we can clearly see the effect of edge preserving regularisation in marking the edges of the perturbation while smoothing the background region. However, such features of this prior also undesirably led to more or less recovering the edges of an artefact on the top left hand corner.

In medical applications, a priori information about the internal anatomical structure of the head tissues and the initial state of the stroke may become available after a single high resolution MRI or CT scan. In this case, this structural prior information can be utilised and MIT may be considered for monitoring changes in the condition of the stroke. Vauhkonen *et al* [42] presented the so called "Sub-space regularisation method (SSRM)" which employ anatomical structural information and probabilistic techniques, and has demonstrated its application for imaging of the thorax. Here, SSRM is implemented in MIT for head imaging and is used to predict the current state of the stroke as part of the continuous monitoring. The advantage of SSRM is that it is capable to produce a reasonable estimate of the material distribution even when the employed prior information is incompatible to some extent with the true internal structure of the object. This is because the minimisation process is not entirely biased to the prior information within the SSRM operator, but is also dependent on adjusting the reconstructed model to fit the actual measured data.

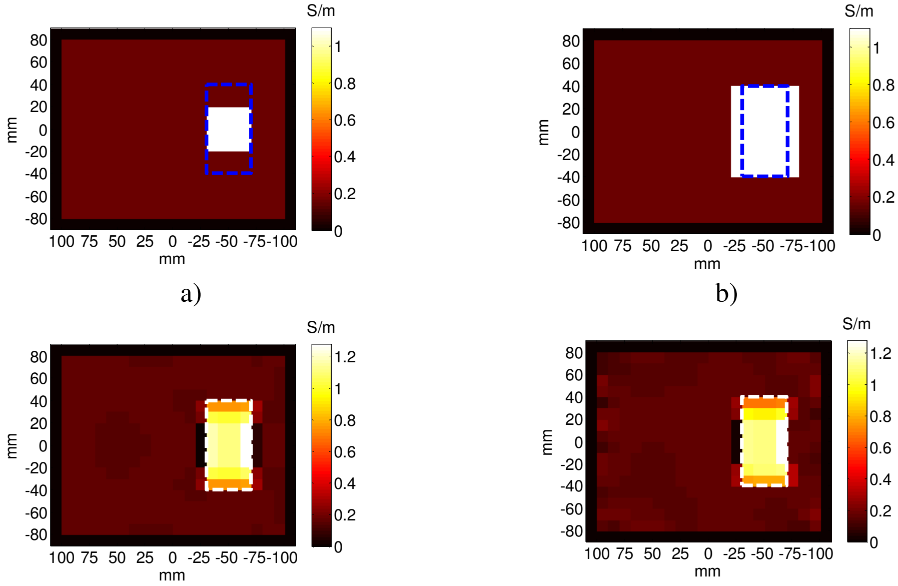

a)

b)

c)

d)

Figure 5.3: Case of simple phantom (one perturbation (1.1 Sm^{-1}) in a homogenous background (0.16 Sm^{-1})). a) Minimal state of the perturbation, b) Maximal state of the perturbation, c) Reconstructed perturbation from noise free data, d) Reconstructed perturbation using SSRM from data with 1% added random noise.

A brief description of the SSRM algorithm is shown in section 5.2, and for more details see [63]. Given the initial state of the perturbation by Figure 5.3 (a) let us assume the expected maximal state (development) of the perturbation is depicted by Figure 5.3 (b). The actual state of the perturbation to be reconstructed at the current time is shown by the dashed frame. A learning set of 21 possible conductivity distributions was constructed to simulate different states of the perturbation randomly chosen between the minimal and maximal states. Using principal component analysis, the first 5 eigenvectors in the SVD of the covariance matrix were used in the computation of the regularisation matrix. The initial guess for image reconstruction was assumed to be a homogenous background (white matter: $\sigma = 0.16$ Sm^{-1}) and the initial regularisation parameter λ_0 was chosen to be 1×10^{-12}. Figure 5.3 (c) and (d) shows the reconstructed images without and with noise added to data. The method was able to recover the actual boundaries of the current state of the perturbation and was able to handle noise effectively.

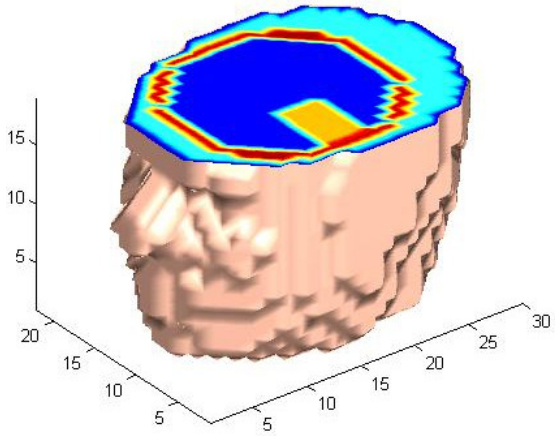

Figure 5.4: Simulated Target (Head and stroke)

In a second simulation arrangement, a model with the shape of a head was employed. A spherical layer crudely approximating the CSF was added together with a rectangular perturbation simulating the abnormality (Figure 5.4). The head was meshed into 9012 cubic voxels of 7.5 mm^3 resolution, which were distributed as (white matter: 7900, CSF: 1008, stroke region: 104) elements. The internal tissues were assigned conductivities as (white matter: 0.16, CSF: 1.5, stroke region: 1.1) Sm^{-1}. Note the CSF conductivity has been reduced to 1.5 Sm^{-1} from the value reported in the literature [26] of 2 Sm^{-1} in order to compensate for the increased thickness caused by mesh resolution. Figure 5.5(a) shows a sagittal plane view of the original image. For image reconstruction, the starting image was obtained using a single step inversion with 2nd order Laplacian operator and regularisation parameter $\lambda_0 = 1\times10^{-9}$. Using the LMM algorithm images were reconstructed from noise free data using NOSER, 2nd order Laplacian and edge preserving priors as displayed by Figure 5.5 (b)-(c) and (d) respectively. The results show the LMM algorithm with the cited regularisation mechanisms produced poor image reconstruction. The reason is the signal response is dominated by the signal contribution of the CSF located around the periphery of the head with the highest conductivity. It can be deduced that none of the a-priori information featuring smoothing or edge preserving priors proves to be useful to recover the stroke region.

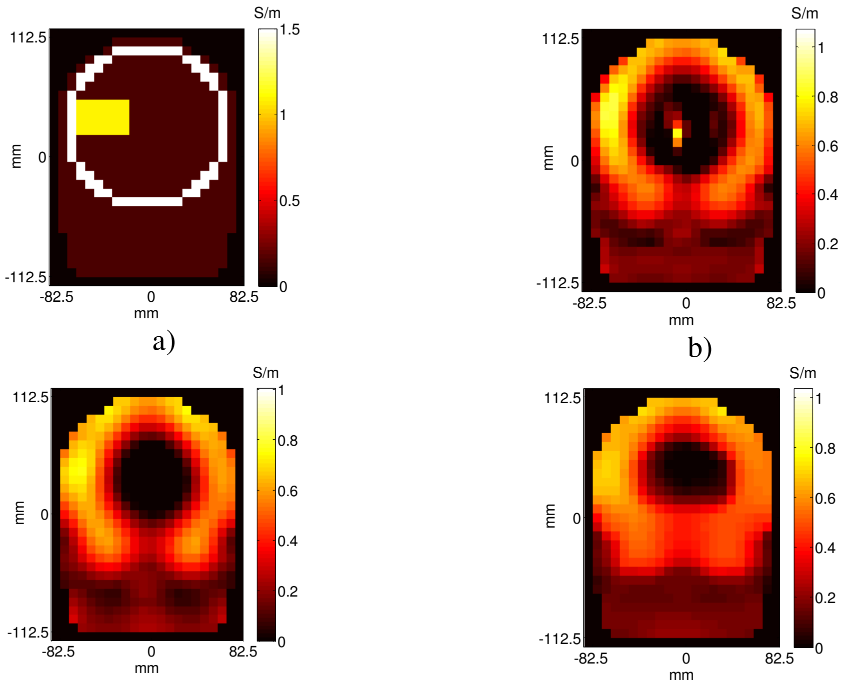

a) b) c) d)

Figure 5.5: Case of head with two tissues (white matter: 0.16,CSF: 1.5) Sm^{-1} and stroke region (blood: 1.1) Sm^{-1}. a) True image. Reconstructed conductivity distribution using b) NOSER, c) 2nd order Laplacian, d) Edge preserving regularisation from noise free data.

The image reconstruction procedure was repeated using SSRM for regularisation. The initial conductivity distribution was assumed to be uniform (0.16 Sm^{-1}) and λ_0 = 1×10^{-12}. A series of 21 conductivity estimates simulating random contours of stroke region were taken between the minimal and maximal states of the stroke depicted by Figure 5.6 (a-b). Figure 5.6 (c) shows the SSRM was able to produce reasonable reconstruction of the current status of the stroke. Hence, this regularisation method proves to be promising for image reconstruction of the stroke region in an anatomically realistic head. To further test the method's robustness, an extra tissue simulating the SCALP (skin and muscle) was modelled with conductivity of 0.6 Sm^{-1}. Two different states of the stroke region have been attempted as shown by Figure 5.7 (a) and (b). In case (a) this time a learning set of 84 conductivity estimates was constructed, which simulates 21 different states and 4 different conductivities of the stroke region. In this example the selected conductivities of the stroke region were calculated based on different percentages of blood in the affected white matter according to Table 5-1. For case (b) random noise with 1 % of rms value of the absolute voltage was added to the measurement data. Figure 5.7 (c) and (d) show the actual state of the stroke has been reasonably reconstructed when compared with the true distributions.

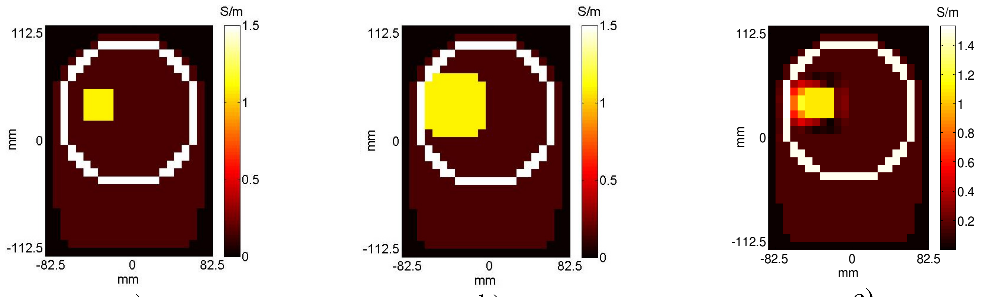

a) b) c)

Figure 5.6: a) Minimal state of the stroke, b) Maximal state of the stroke, c) Reconstructed stroke conductivity from noise free data.

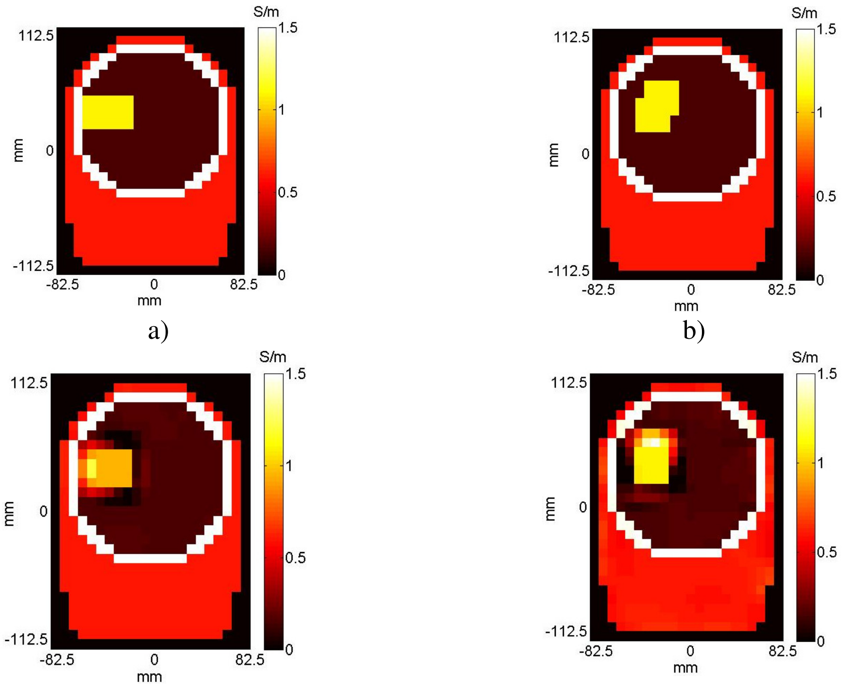

a) b)

c) d)

Figure 5.7: Case of head with three tissues (SCALP: 0.6, CSF: 1.5, white matter: 0.16) Sm^{-1} and stroke (blood: 1.1) Sm^{-1}. a)-b) True images. c) reconstructed image from 84 conductivity and state estimates-d) reconstructed image from noise contaminated data (SNR = 40 dB)

Table 5-1: Conductivity estimates of the stroke region

	70% blood and 30% white matter	80% blood and 20% white matter	90% blood and 10% white matter	100% blood
Stroke (σ)Sm^{-1}	0.81	0.91	1	1.1

5.3.2 Imaging oil / process water flow

The application of MIT for monitoring the water fraction in multiphase flows has been reported in [35, 127]. Recently, work in partnership with the Universities of Swansea and Glamorgan conducted experimental and simulation studies using a 16 channel MIT system to attempt imaging the saline water component in phantoms representing idealized conductivity distributions of stratified, annular and bubble flow regimes [57]. Two dimensional absolute conductivity reconstructions of cross sections of the phantoms were performed using linear Tikhonov and Landweber methods. Results showed that the isolated regions of conductivity in stratified flow regime were reasonably represented in the images; however local variations in conductivity found in annular and bubble flow types were difficult to resolve. This work concluded that the use of linear optimization algorithms in image reconstruction of the flow type might be a convincing reason to justify the inability to produce reasonable images for these types where the flow structures involved low conductivity features bounded by high conductive saline water. From the hardware side, it was later found the noise produced by the employed tomography system and in particular from the geometrical and positioning errors was not good enough to meet the low noise requirements of an absolute imaging algorithm. Consequently, two questions needed to be answered, which are the theme of this chapter:

a) *Can an absolute nonlinear image reconstruction algorithm be capable of recovering the internal structure in annular and bubble flow regimes using simulated data*?

b) *Will it be possible to generate a fairly clean data from the new instrumentation system (Mark 2a) so as a successful absolute image reconstruction can be obtained*?

In dealing with the first question, three phantoms representing stratified, annular and bubble flow models were simulated as shown in Figure 5.8 I)-II)-III). The simulated pipes (20 cm diameter and 50 cm depth) were filled with process water with conductivity of 5 Sm^{-1} and oil was assigned an infinitesimal conductivity of 0.013 Sm^{-1}. For continuous monitoring of industrial flow applications fast image reconstruction is required, hence one projection plane of sensor array was used to acquire data and a nonlinear 2.5D image reconstruction was considered. In this case, the cross sectional conductivity distribution on the sensor array plane was assumed to be invariant along the pipe axis. Hence, images are reconstructed in 2D and the forward problem is solved for the full 3D model. The Jacobian matrix was calculated by summing the sensitivity coefficients along the pipe axis. The coils were sequentially driven with unit excitation at a frequency of 1 MHz. This frequency was found suitable in order to have an efficient field penetration across the pipe volume and to reduce the impact of the skin effect. Images were reconstructed from noise free data and data with 1 % added random noise. The LM method was used to reconstruct the simulated data. For the stratified and the annular flow, the regularisation parameter λ was chosen 10^{-9} and for the bubble flow 10^{-10} was found suitable. Bear in mind the regularisation matrices for the NOSER and the edge preserving priors are normalized to the maximum value.

Figure 5.8 below shows the images for three flow types reconstructed with three regularisation priors, NOSER, 2nd order Laplacian matrix and edge preserving regularisation. Results show image reconstructions with all regularisation priors were successful in recovering the oil phase within the conductive process water, at the expense of some artefacts and some smoothing effects. For the stratified flow, the images were almost identical using the different regularisation priors. Regularisation using 2nd order Laplacian and NOSER produced better image reconstruction for the annular flow, whereas the edge preserving method outperformed its other counterparts in the case of the bubble flow. In order to further process the images and remove the smoothing effect, thresholding was applied and the second set of results is also depicted in Figure 5.8. Overall it can be deduced that nonlinear absolute image reconstruction with the three priors was successful in producing reasonable estimates of the conductivity distribution in all the flow types considered.

True Image

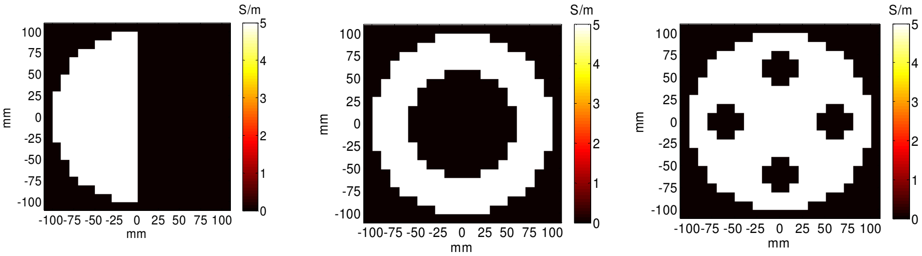

I) II) III)

NOSER

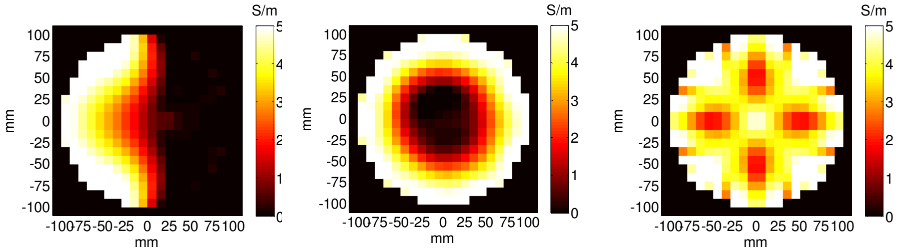

a) b) c)

2nd Order Laplacian

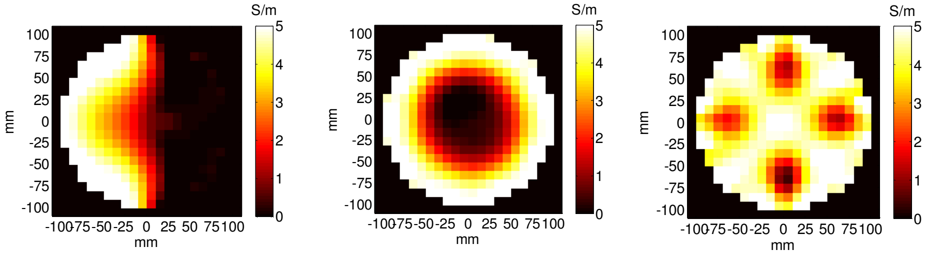

d) e) f)

Edge preserving

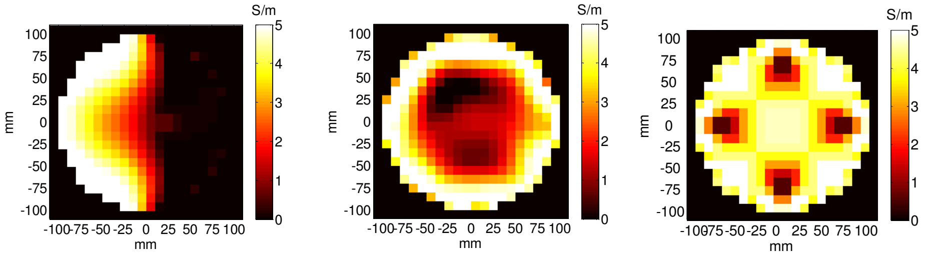

g) h) i)

NOSER

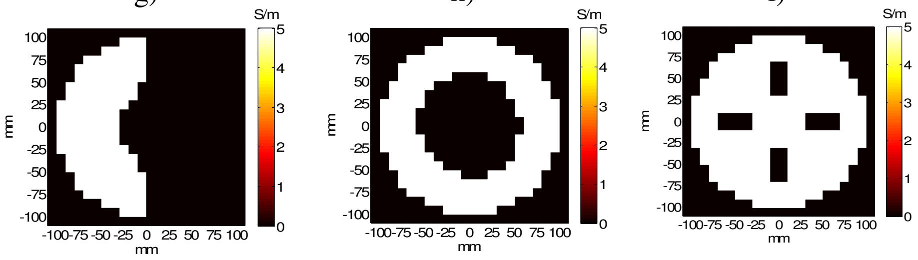

a’) b’) c’)

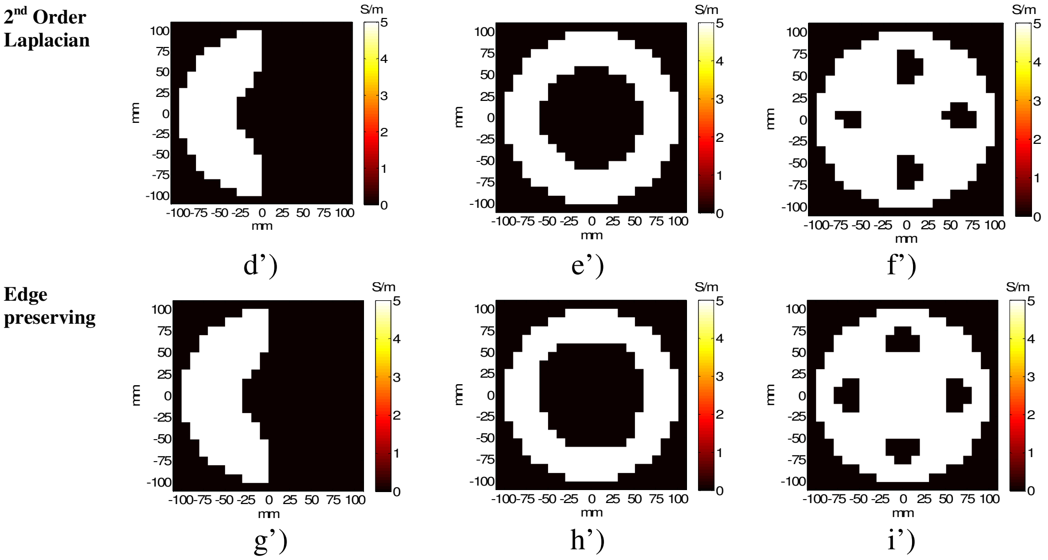

Figure 5.8: Non linear 2.5D image reconstruction of idealised models of three flow regimes: I) stratified, II)Annular and III) bubble. a)-b)-c)-d)-e)-f)-g)-h)-i) are reconstructed from noise free data. a')-b')-c')-d')-e')-f')-g')-h')-i') are reconstructed from data with 1% added random noise.

5.4 Practical experiments

Recall from [57] on the initial MIT studies for oil/water pipeline inspection, stratified type flow was not a major issue and basic linear type image reconstruction algorithms produced reasonable results. Hence, in this practical study the other two flow types (i.e. the annular and the bubble flow regimes), which constituted a real challenge, were approached. In order to overcome this challenge, a new 14 channel tomography system (Mark 2a) was developed by Glamorgan University, South Wales. An obvious difference between this system and the Mark 1 coil arrays is that in the former the excitation and receiver coils are not coaxial, instead they are arranged in two planes with one above the other. The rationale behind this arrangement is to decrease the empty space primary linkage and hence increase the dynamic range of the secondary field which carries information about the target. The system is also reported to achieve a measurement phase noise of less than a 1 m^0 for a time constant of 1 s for frequencies in the range 1-14 MHz [128]. This is compared to 17 m^0 recorded with the previous (Mark 1) system whose electronic design and noise specification can be found in [129].

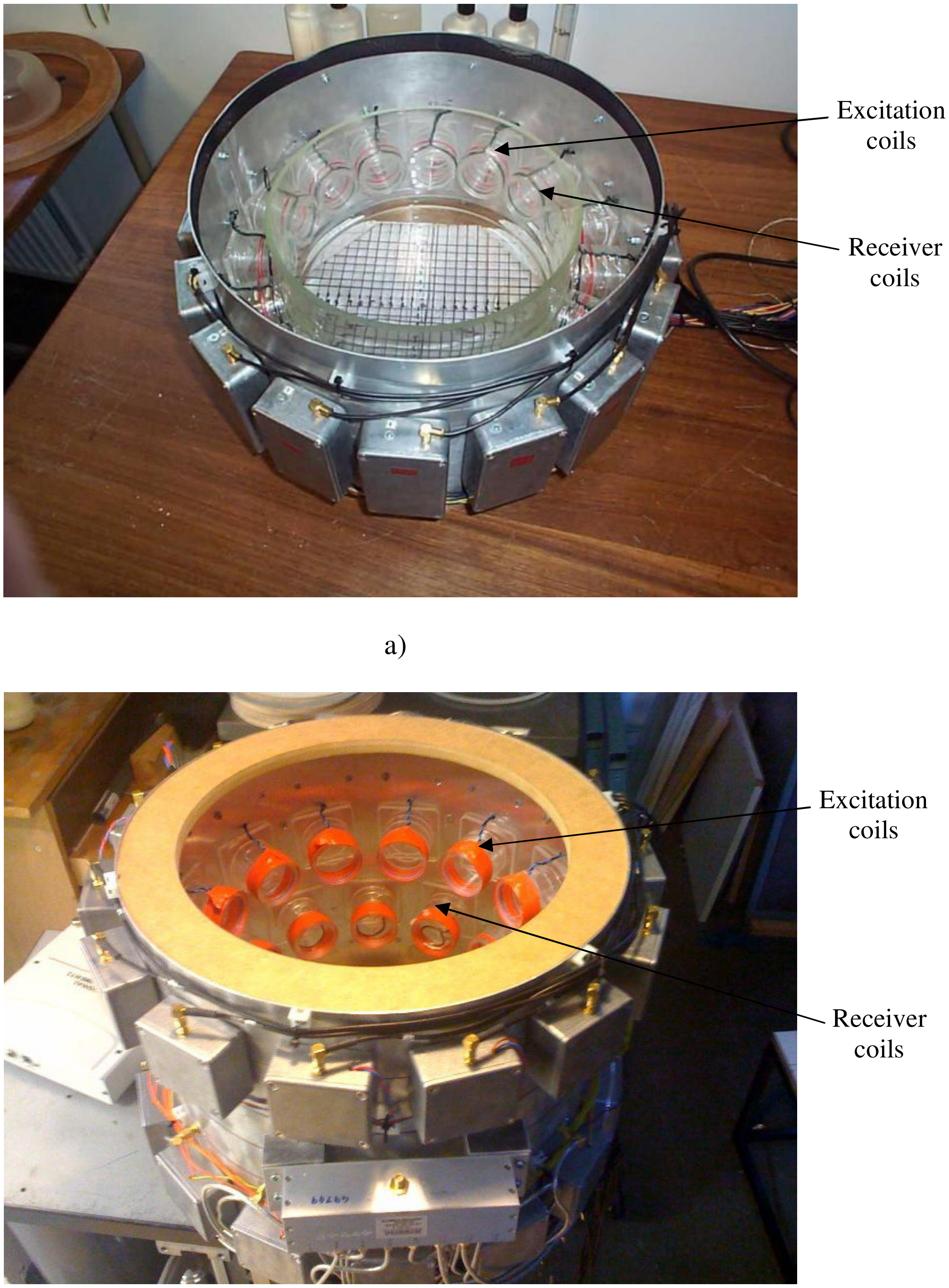

a)

b)

Figure 5.9: MIT tomography systems a) 16 channel Mark 1 b) 14 channel Mark 2a, courtesy University of Glamorgan

In an attempt to create a representation of an annular flow regime, a pipeline phantom (internal diameter 194 mm and height 494 mm – see Figure 5.10) was placed vertically and an annulus of oil/gas was created by inserting one plastic cylinder filled with tap water within the pipe. The remaining volume of the phantom was then filled with saline to a height of 494 mm. Because the experiment has been conducted with an operating frequency of 10 MHz, a conductivity of about 0.1 Sm^{-1} has been used for the 'seawater' in order to keep the skin depth large so that the quasi-static model will be accurate. This choice of conductivity was suggested by our partner, with the intent to rerun the test with the conductivity of 5 Sm^{-1} typical of sea water at a later stage in the future, and obviously with a lower operating frequency (e.g. 1 MHz). For the oil/gas, the conductivity of the tap water was measured and found to be around 0.01 Sm^{-1}. Seven measurements were taken for various representations of annular flow by choosing different diameters and positions for the oil/gas annulus cylinders. Table 5-2 explains the geometrical arrangement for each measurement set carried out.

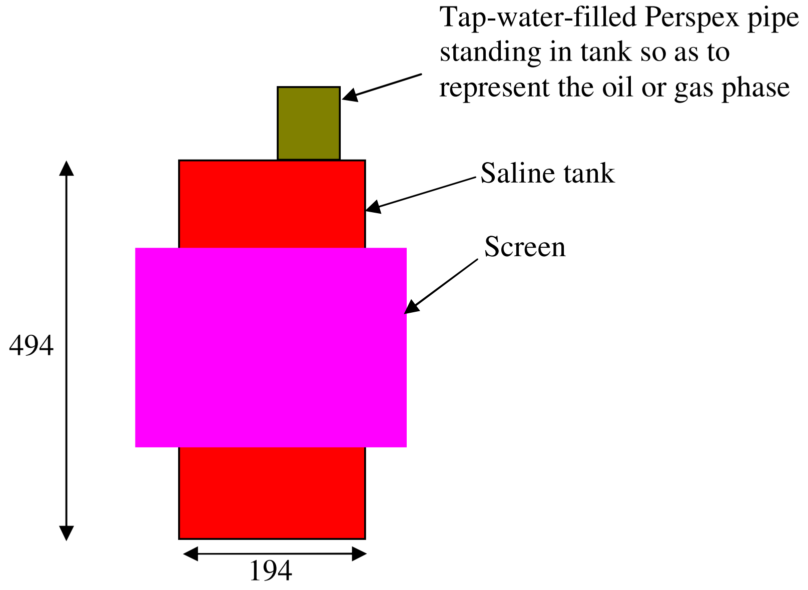

Figure 5.10: Schematic of the experimental arrangement

For the bubble flow regime, a water continuous phantom representing oil and/or gas bubbles was constructed by inserting hollow cylinders of diameter 36 mm and height 494 mm filled with tap water into the pipe phantom which was filled with saline (0.1 Sm^{-1}) to a height of 494 cm (Figure 5.10). The cylinders were inserted according to a template which allowed for 8 different positions, labelled A to H, shown in Figure 5.11. Four different combinations of cylinders were placed within the pipe representing mainly unsymmetrical configurations. Table 5-3 describes the different bubble flow tests performed.

For all the experiments performed in this study, two measurement sets were taken for each case with one measurement set taken with the tank all filled with saline (homogenous case) and the second measurement set was collected for when the Perspex pipes filled with tap water were inserted inside the tank (Actual case). This allows the possibility for difference imaging to be a viable option.

Given that the tomography system consists of 14 pairs of exciter-receiver coils, the Mark 2a should in principle provide 196 measurement data points. However, because of an outstanding fault associated with one receiver channel (Rx3) that was causing noticeable drift the measurements associated with such channel were neglected. Hence, only 182 data were employed for image reconstruction. The saline tank was discretised to a 5 mm^3 resolution and 2.5D image reconstruction was considered. To recall, this latter assumption infers that the forward problem is computed for the full 3D tank and the inverse problem is solved in 2D to reconstruct the cross sectional plane of the tank which amounts to 1201 unknown conductivity elements or DoFs. Now, let us recall the question already posed earlier in the chapter:

A test was performed involving rotating a tank of saline around the array showed large fluctuations (tens of millidegrees) in the measured data. These errors could probably be due to non-cylindrical symmetry in the set-up, such as if the tank is not quite circular in cross section or if its ends are not machined square. Because these errors were reproducible and unavoidable, although the reported electronic noise is $1m^0$, the geometrical errors associated with the set up were much larger and absolute imaging was not a feasible option at this stage. Hence, difference imaging relative to the full tank was tested since such errors can be well cancelled.

Table 5-2: Annular flow measurements protocol

Case	Description of measurement
A	70 mm outer diameter column of ‘oil/gas’ positioned approximately centrally in tank = Perspex pipe containing water 0.012 Sm^{-1}.
B	Same pipe in tank but moved towards Receiver (Rx10) so that distance to wall of tank = 41mm
C	Same pipe but now brought right against the tank’s wall.
D	110 mm outer diameter column of ‘oil/gas’ positioned approximately centrally in tank = Perspex pipe containing water 0.012 Sm^{-1}.
E	Same pipe in tank but moved towards Rx10 so that distance to wall of tank = 15mm
F	150 mm outer diameter column of ‘oil/gas’ positioned approximately centrally in tank
G	Same pipe but now brought towards Rx10. Distance to wall of tank = 4 mm.

Table 5-3: Bubble flow measurements protocol

Case	Description of measurement
H	2 tubes, A and C
I	2 tubes, A and H
J	Now just 4 tubes, A, C, H and F.
K	8 tubes, A-H, all in place

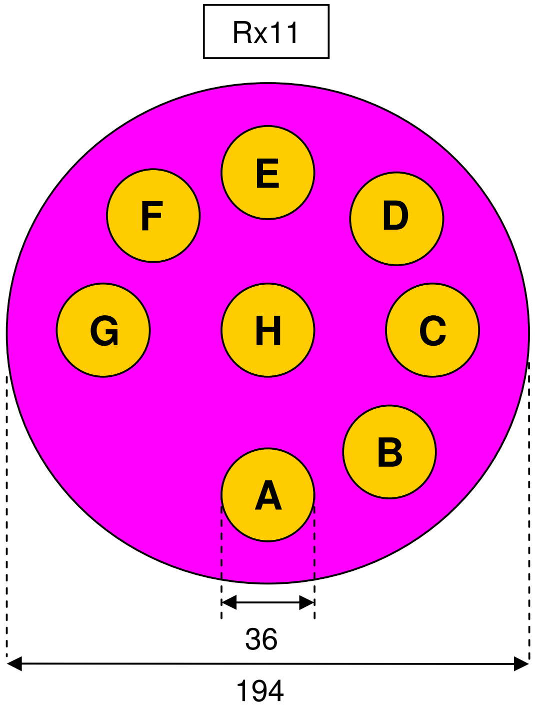

Figure 5.11: Position template for oil/gas bubble cylinders

Figure 5.12 and Figure 5.13 present the images reconstructed from the measurement data corresponding to the annular and the bubble flow regimes respectively. For image reconstruction, a single step Tikhonov method (column I) and iterative LM reconstruction algorithm (column II) were tried. In the inversion, a 2nd order Laplacian operator was used to obtain a regularised solution. In order to determine the amount of regularisation, Tikhonov solution was obtained by choosing the regularisation parameter $\lambda = 10^{-2}$. For the LM method, the regularised Tikhonov solution is chosen as the first guess and the initial value for the dynamic damping parameter is selected as $\gamma_0 = 10^{-3}\ \lambda$. Image reconstruction is repeated for different regularisation parameter values within the range $[10^{-1}, 10^{-6}]\times\lambda_0$ to achieve best optimised reconstructed solution. Further regularisation was implemented in the Tikhonov and within the LM iterations by constraining the reconstructed conductivity maps to lower and upper bounds. At the lower end, non-negativity bound was applied while at the upper bound conductivity elements were restricted assuming the difference between the saline and the tap water conductivities are a priori known. The sensitivity maps were calculated relative to homogenous full saline tank.

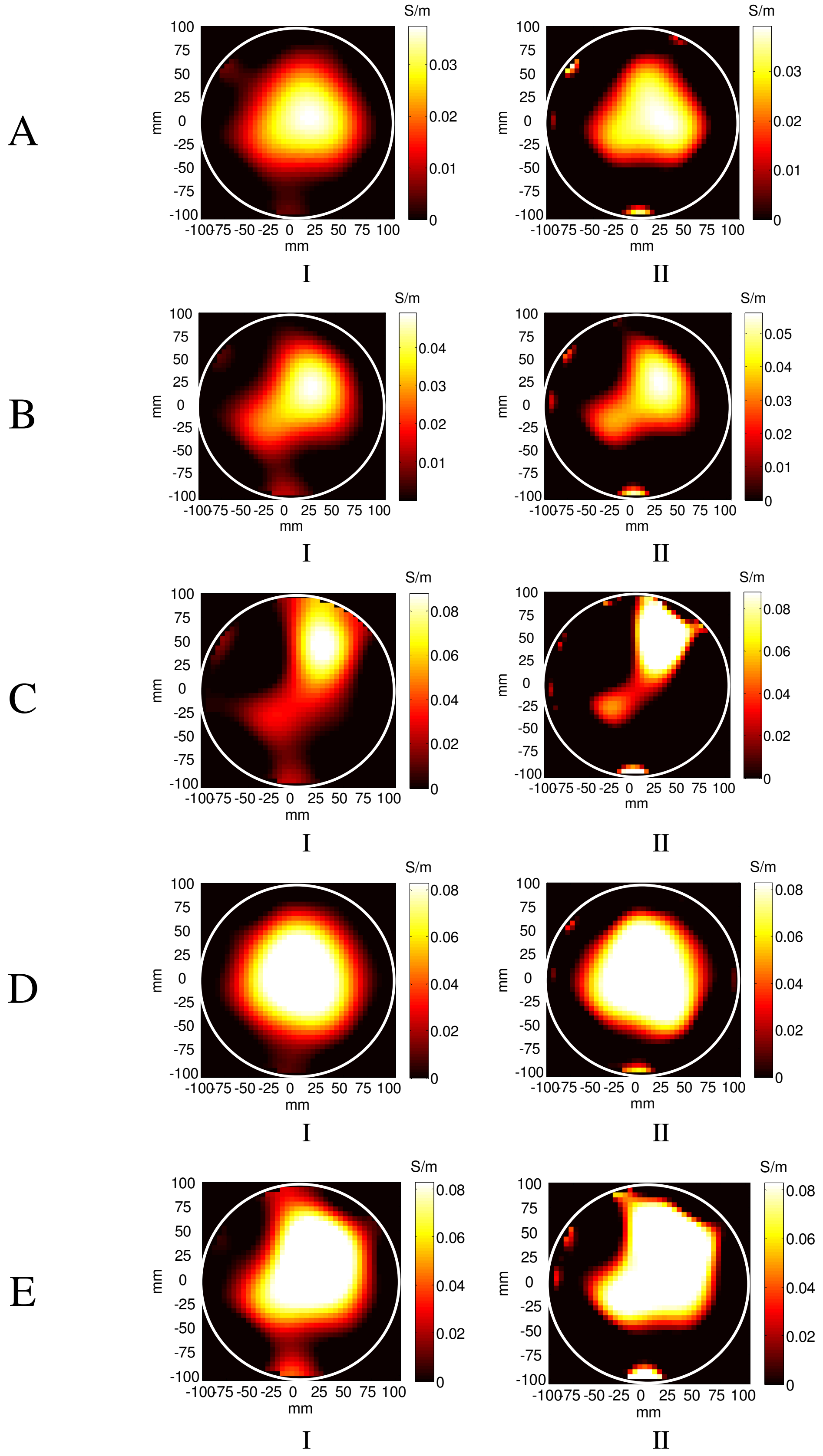
A
B
C
D
E
I
II
S/m
mm
100
75
50
25
0
-25
-50
-75
-100
0.01
0.02
0.03
0.04
0.05
0.06
0.08

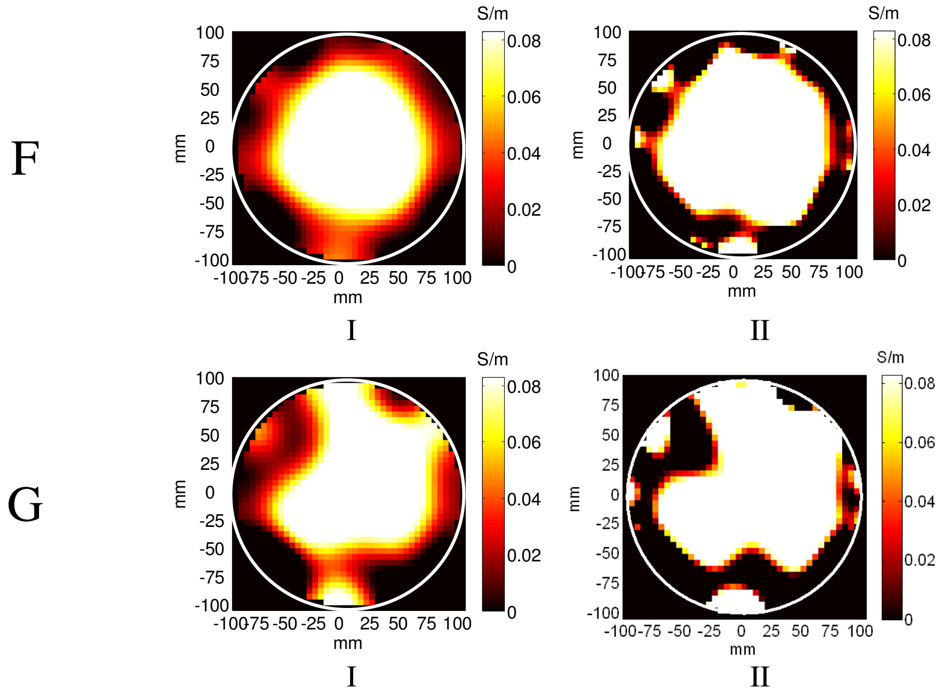

Figure 5.12: 2.5 D image reconstruction of idealised models of annular flow regimes from real experimental data using difference imaging relative to full tank, I: Single step, II: Iterative method

From Figure 5.12, the following results can be observed:

- The tap water annulus representing the oil phase was fairly reconstructed by the single step Tikhonov method for cases A to F, and the linear iterative LM method appear to be able to improve the regularised Tikhonov solution, by reducing the smoothing and increasing the sharpness of the annulus feature.
- The centralised tap water annular test cases (A, D and F) were reconstructed better than the annular cases shifted toward the periphery. For instance, as the 70 mm annulus is brought near to the tank edge (A.B and C (I-II)), the reconstructed annulus become increasingly distorted toward the centre of the tank.
- A quantitative comparison shows as the annulus is shifted toward the edge, the conductivity of the reconstructed tap water annulus grow near the true realistic value.
- By increasing the diameter of the tap water annulus from 70 mm to 150 mm, noticeable artefacts appear as the low conductive annulus grows closer to the tank edge.

- The images also show a common artefact present in all cases near the channel Rx3. Its presence can be justified by the lack of eddy current information around that region caused by dismissing the Rx3 data from the reconstruction data set.

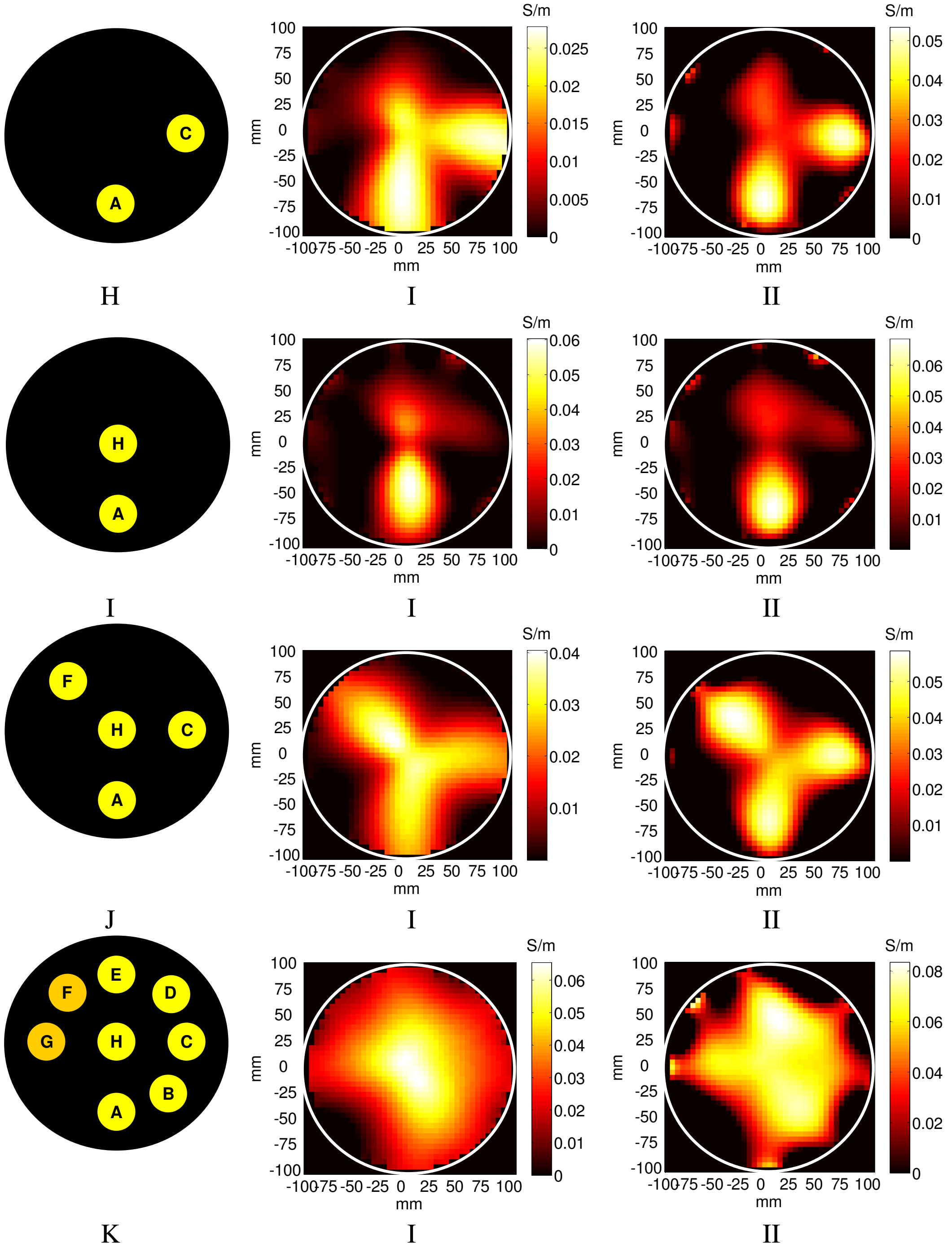

Figure 5.13: 2.5D image reconstruction of idealised models of bubble flow regimes from real experimental data using difference imaging relative to full tank, I: Single step, II: Iterative method.

With regards to the bubble flow reconstruction test cases, the following observations can be drawn from Figure 5.13:

- Again fair reconstruction of some test cases was achieved with both the direct Tikhonov inversion and the LM algorithms, especially for cases H and J. Similar observation made for the annular flow regarding the improvement made by the LMM over the basic single step Tikhonov applies here.
- Test cases involving bubbles located in the central region appear to go more or less lost in the reconstructed images (I, J, K), which can be justified with a compromise in the sensitivity in the central region compared to the periphery. The employed sensitivity maps are computed for a homogenous background; hence they are the cause of such problem and cannot be suitable for recovering features in the centre especially if these are accompanied with bubbles near the edge.
- As the number of bubbles increases, it becomes difficult for the employed algorithm to discriminate between the reconstructed bubbles as can be seen in case K. Again, a number of factors can be associated with this difficulty, of note the sensitivity becomes increasingly unrepresentative of the true distribution, the a-priori information assuming smooth variations in the conductivity turn to be not suitable and the number of independent data is much smaller than that of the unknown conductivity elements.

6 Frequency difference imaging of cerebral stroke

6.1 Introduction

Frequency difference imaging is another differential imaging technique that can be applied in MIT to reconstruct changes in the conductivity distribution inside a test object. While state difference imaging functions by mapping local conductivity changes of interest, relative to a given conductivity background (i.e. a reference state), frequency difference imaging exploits the spectral behaviour of the materials inside the object in order to map the conductivity changes from measurements taken at different frequencies.

In medical imaging of cerebral stroke, state difference imaging cannot be applied since it requires one of the two datasets to be taken from the patient prior to the formation of the stroke. Clinical applications where state difference imaging can practically be useful could include monitoring lung activity by detecting conductivity changes between inspiration and respiration. Therefore, since all biological tissues have conductivities which are frequency dependents, frequency difference imaging is the only applicable differential imaging method for detecting conductivity changes related to the stroke. Nevertheless, initial reports on stroke imaging using MIT approached the state difference technique mainly to investigate the feasibility of detecting the stroke. For instance, Merwa *et al* [101] simulated MIT measurements at 100 kHz on a human brain model comprising three tissue types, namely CSF, grey matter, white matter, and a spherical perturbation modelling the stroke. Difference images were reconstructed. Similar study was conducted by Zolgharni *et al* [130] using a more realistic head model consisting of 7 tissue types. Reconstructed images from phase changes at 10 MHz showed a large peripheral stroke (49 cm^3) can be recovered from data contaminated with 17 m^0 phase noise, which is characteristic of the Mark 1 MIT system employed in this thesis. In other modelling papers, Merwa *et al* [10] and Dekdouk *et al* [131] continued using the same technique to evaluate the sensitivity of the MIT coil channels to the stroke, and hence estimate the required noise level of MIT systems needed for possible detection of the lesion. Based on the noise level characteristics obtained from MIT systems they employed, results showed centrally located strokes with radii of 20 mm and 27 mm, respectively, could be detected. Early work on stroke imaging using differential multi-frequency MIT measurements was presented in Brunner *et al* [100] who conducted a simulated and an experimental study to reconstruct the conductivity spectra of a vegetable material, which represents a perturbation, immersed inside a saline tank and compared it against parametric conductivity spectra obtained from a Cole model. Results showed good agreement between reconstructed and real data inferring that MIT spectroscopy and possibly frequency difference MIT can be a promising road to take toward detecting the stroke in a real human brain.

For image reconstruction, Brunner *et al* [100] derived a linear formulation relating the change in the conductivity distribution to the difference between the data obtained at dissimilar frequencies. This formulation is given below:

$$\boldsymbol{\Delta D} = \left(\boldsymbol{D}_{\mathrm{f}_1} - \left({}^{\mathrm{f}_1}\!/_{\mathrm{f}_2} \right)^2 \boldsymbol{D}_{\mathrm{f}_2} \right) \tag{6.1}$$

$$\Delta\boldsymbol{\sigma} = \left(\boldsymbol{J}_{\mathrm{Ref}}^{\mathrm{T}} \boldsymbol{J}_{\mathrm{Ref}} + \lambda \boldsymbol{R} \right)^{-1} \boldsymbol{J}_{\mathrm{Ref}}^{\mathrm{T}} \Delta\boldsymbol{D} \tag{6.2}$$

where $\boldsymbol{\Delta D} \in \mathbb{R}^m$ is the vector of the difference between the induced voltages $\boldsymbol{D}_{\mathrm{f}_1}$ and $\boldsymbol{D}_{\mathrm{f}_2}$ at the test frequencies f_1 and f_2. $\boldsymbol{\Delta\sigma} \in \mathbb{R}^n$ are the reconstructed conductivity changes. $\boldsymbol{J}_{\mathrm{Ref}} \in \mathbb{R}^{m \times n}$ denotes the Jacobian at the reference conductivity map σ_{Ref}.

This formulation assumes the measurement signals are linearly proportional to the square of the frequency, hence inferring that the sensitivity is quadratic dependent on frequency. This assumption is only valid in situations where the penetrating depth of the electromagnetic field is much larger than the object dimensions. Brunner showed that reconstructed difference images based on this formulation exhibit a fairly well localised perturbation but with noticeable smearing and smoothing caused by the linear nature of the algorithm. In what follows, this formulation will be further tested in MIT on simple models with a single perturbation as well as on phantoms approximating the realistic structure of a head with a stroke region.

6.2 Simulations

6.2.1 Simple cylindrical model with perturbation

The first test considers the image reconstruction of a single perturbation placed in different positions within a homogenous conductive background. The background is cylindrical with 200 mm diameter and 160 mm height and has been assigned a conductivity of white matter. The inner perturbation is a small cylinder of 40 mm diameter and 40 mm height and is assumed to have the conductivity of blood. The properties assumed for white matter and blood are given in Table 7.1. Four test cases have been considered namely L1-L4 as shown in Figure 6.1. The simulated data are generated using the Mark 1 MIT setup described earlier in section 3.3. From this image reconstruction example, we intend to test the ability of the frequency difference formulation to recover the perturbation within the homogeneous region in symmetrical and unsymmetrical arrangements.

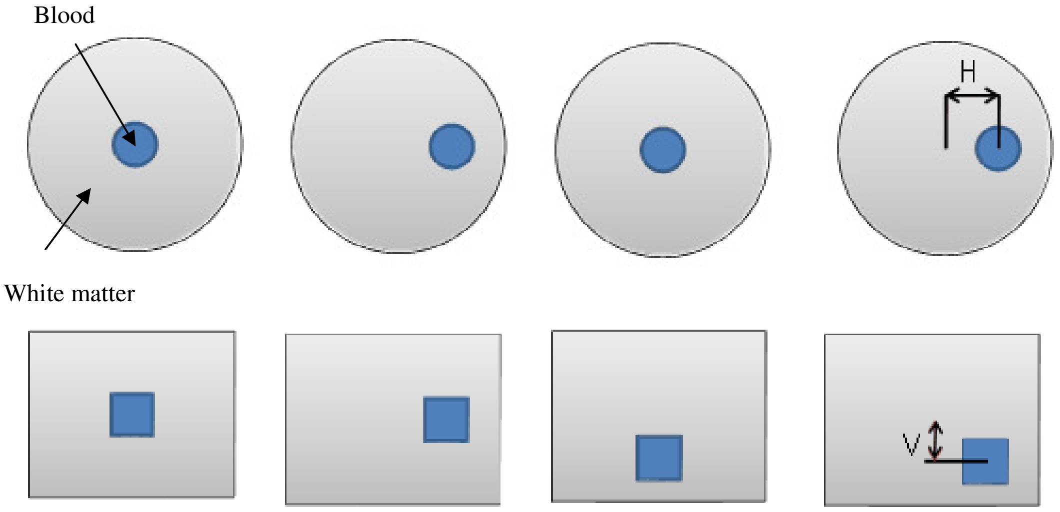

(H = 0, V = 0) mm L1

(H = 50, V = 0) mm L2

(H = 0, V = -40) mm L3

(H = 50, V = -40) mm L4

Figure 6.1: Positions of the perturbation phantoms. H and V correspond to the horizontal and vertical displacements of the perturbation away from the centre of the phantom.

For frequency difference imaging, the measurements are simulated at frequencies of 1 MHz (reference frequency) and 10 MHz. In this range, the change in the conductivity of blood is about 5 times higher than that of white matter. Thus, from a theoretical point of view there is a chance for frequency difference imaging to recover the blood perturbation. With regard to the choice of the frequency range, we are restricted with frequencies up to 10 MHz as an upper bound limit since the frequency formulation considered assumes the sensitivity map does not change with frequency, which is only true for weak perturbations of the primary magnetic field. In Chapter 3 (sections 3.6 and 3.6.2) we have investigated the error due to this approximation and concluded the assumption will not hold valid for frequencies larger than 10 MHz. On the other side, the current system limitations with regard noise level does not facilitate going below 1 MHz because the received signals becomes too small. So far, we have not developed models taking into account the change of the sensitivity with frequency.

Table 6-1: Conductivities of blood and white matter tissues in the frequency range 100 k-100 MHz (From [26])

	100 kHz	1 MHz	10 MHz	100 MHz
$\sigma_{(\text{Blood})}$ Sm^{-1}	0.7	0.8	1.1	1.2
$\sigma_{(\text{White matter})}$ Sm^{-1}	0.08	0.1	0.16	0.32

Simulated voltages were generated by solving Maxwell's equations using the custom forward program that has been presented in Chapter 3. Nine equally spaced planes of measurements are simulated to form each dataset. Position of the planes relative to the background is shown in Figure 6.2, where the central axes of the of coils lie on each plane. It is also assumed that the location of the coil arrays relative to the shielding screen remains fixed. In total, 2304 induced voltages were collected for each frequency.

For image reconstruction, the phantoms were discretised into cubic voxels with size of 10 mm, resulting in total 5056 unknown elements (i.e. conductivities) of which 48 are allocated in the perturbation. In order to simulate modelling errors and instrumentation noise picked by the receiver coils, white noise was simulated and added to the obtained simulated voltages. In this respect, two ways of adding the noise were considered:

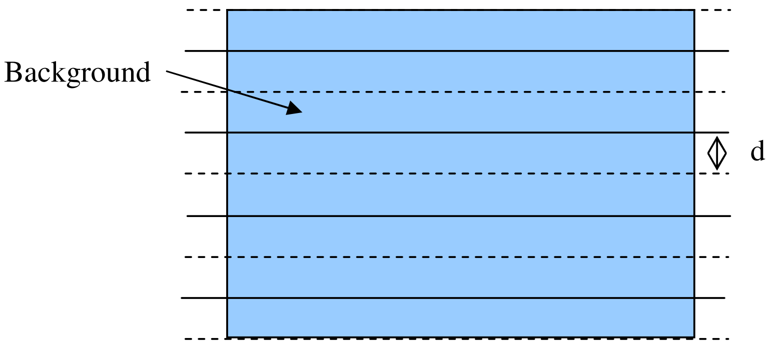

Figure 6.2: Position of the measurement planes relative to the background cylinder (d = 20 mm)

Case 1:

White noise with 0.01 % of the rms value of the induced voltages simulated at 10 MHz was added to the data at 10 MHz and at 1 MHz. This approach assumes noise does not scale with frequency and is rather a pessimistic approach since the induced voltages at 1 MHz will be over contaminated due to the quadratic dependence of the data with frequency.

Case 2:

White noise with 1% of the rms value of the difference between the two datasets of induced voltages at 10 MHz and 1 MHz is added to the difference set. This is quite an optimistic method which considers the noise to scale perfectly with frequency.

6.2.2 Head model with a peripheral stroke

A model of the head (Figure 6.3) consisting of 7 biological tissues (Scalp, Skull, CSF, grey matter, white matter, spinal/optic nerves, and eye balls) was considered. The tissue conductivities were obtained from [26]. For the forward and inverse problems, the head was meshed into 9012 cubic voxels with a side length of 7.5 mm, of which 119 elements were occupied by the stroke. Hence, the simulated stroke has a volume of about 50 ml. The vector of measurement voltages has been constructed from 11 planes of projections interspaced with 20 mm and arranged parallel to each other along the z axis, i.e. the axis of the circular coil array, amounting to 2816 induced voltages. This data was contaminated with Gaussian noise synthesized in a similar fashion to the previous problem.

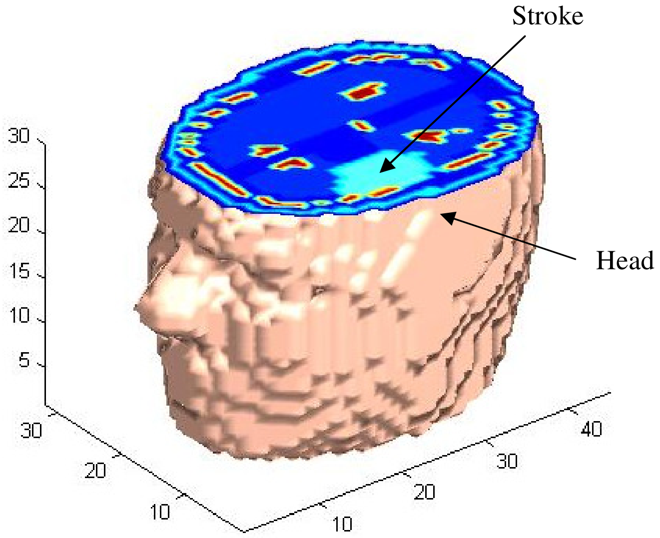

Figure 6.3: A model of a head with a stroke.

Image reconstruction was carried out using single step Tikhonov method to generate the initial guess. Then, this guess was fed into a linear scheme using the LM method to produce an iterative estimate of the conductivity distribution. For regularisation, a 2nd order Laplacian matrix taking the 2nd order derivative between neighbouring voxels was employed.

6.3 Results and Discussion

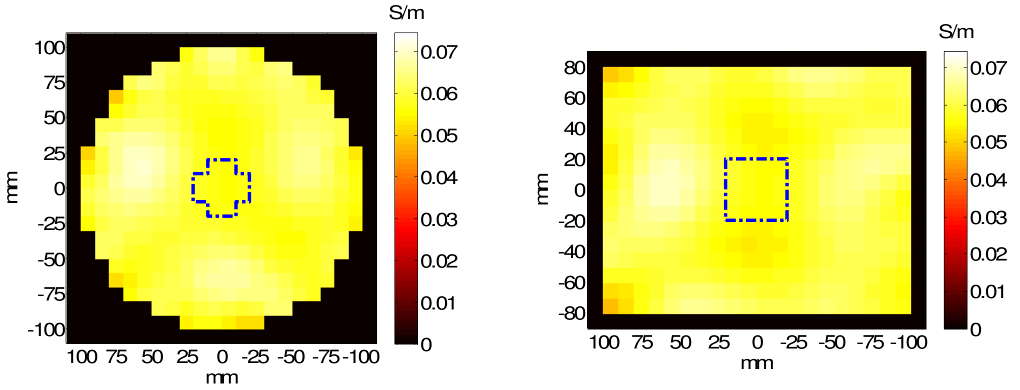

L1-H

L1-V

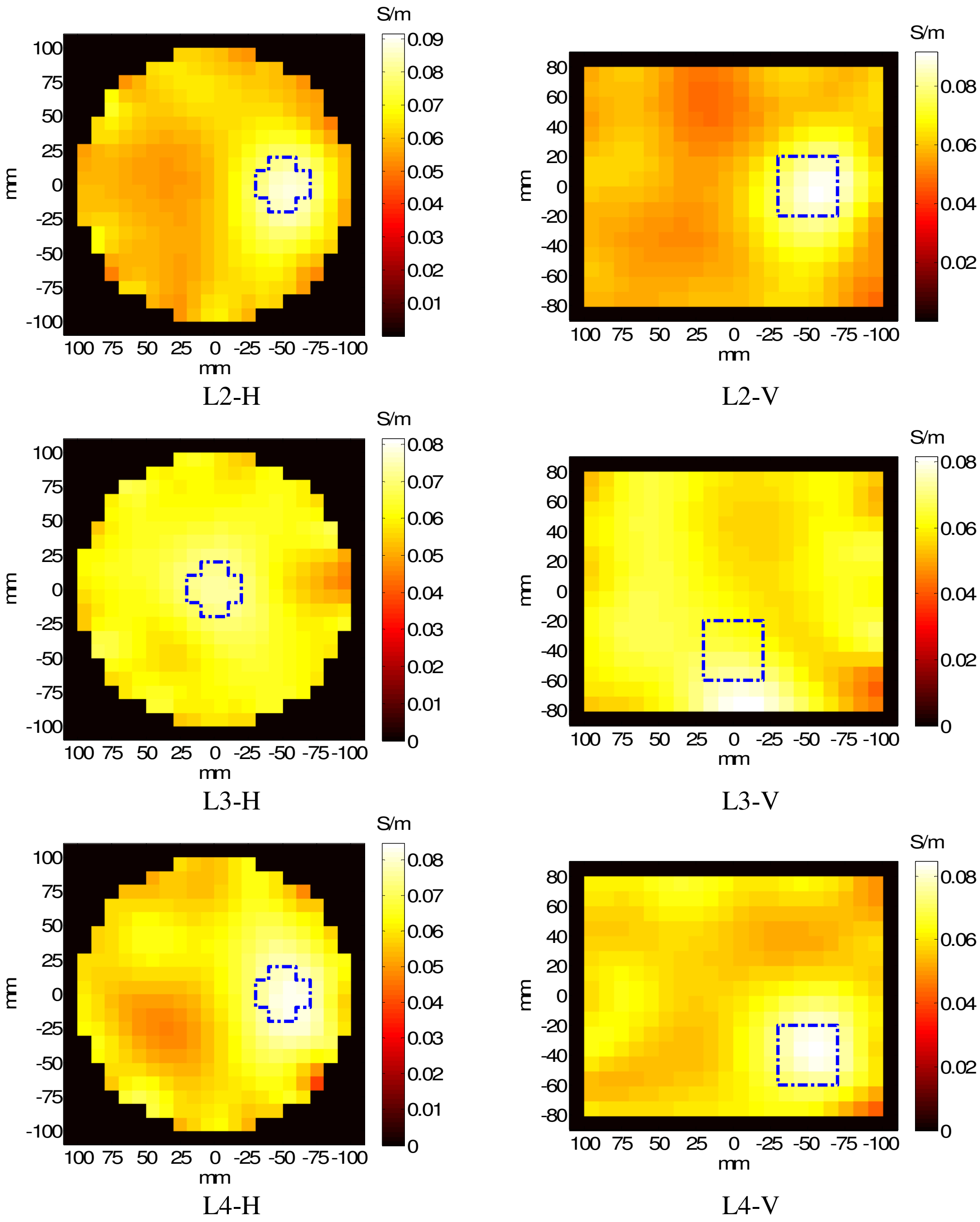

Figure 6.4: Frequency difference images of reconstructed $\Delta\sigma$ from simulated data with noise (case 1). Four different positions of the perturbation: L1-L4. The Dotted line shows the true boundaries of the perturbation. Test frequencies: 10 MHz – 1 MHz

Figure 6.4 shows the reconstructed images of the conductivity change $\Delta\boldsymbol{\sigma}$ from the differential measurements taken at the test frequencies of 1 MHz and 10 MHz. The pictures display the sagittal (right column) and the transversal (left column) cross sections of the cylinder, which are selected so as they contain the centre of the perturbation. The cases L1-L4 for the different positions of the perturbation are distributed over the rows. The results show the perturbation was recovered in cases L2 and L4, with fair positioning but with considerable smoothing. Quantitatively speaking, the perturbation was recovered with a maximum that is about 4 times smaller than the true value. These negative aspects related to the low resolution and poor convergence of the reconstructed images are, to some extent, caused by the linear nature of the reconstruction algorithm. With a nonlinear reconstruction algorithm that allows the search direction and the step length to be optimized a further improvement can be achieved. However, it is not now clear how to synthesize such an algorithm in the framework of differential multi-frequency reconstruction. In case L3, the perturbation has been recovered, but has been shifted away from its original boundaries towards the edge. Lastly, the reconstruction completely failed in case L1. Hence, even with a simple model of a cylindrical homogenous background and a perturbation, it is unlikely to recover a perturbation in the centre than if it is near the edge. This conforms to a classical observation in MIT that the central regions suffer from low sensitivity. Therefore, it can be deduced that it would be impossible to see a stroke feature in the centre with such linear algorithm for more realistic head phantoms. The reconstructed data included random noise of 0.1% of the rms value of the data at 10 MHz, which had been added to the data at 10 and 1 MHz. This infers the data at 1 MHz is more disturbed than 10 MHz, with computed SNRs of 40 and 80 dB respectively. The second set of images reconstructed in Figure 6.5 corresponds to the 2nd case in which 1% of random noise was added to the difference data, which assumes noise scales with frequency. More or less similar observations can be made on the results shown below, except that a slight improvement on the reconstructed images can be observed in cases L2 and L3.

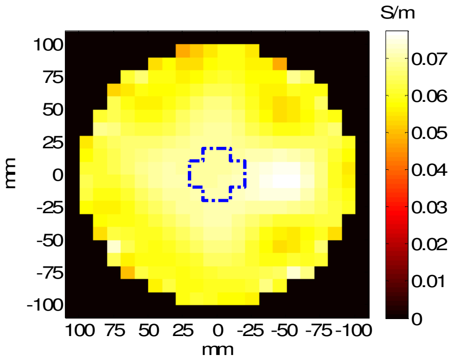

L1-H

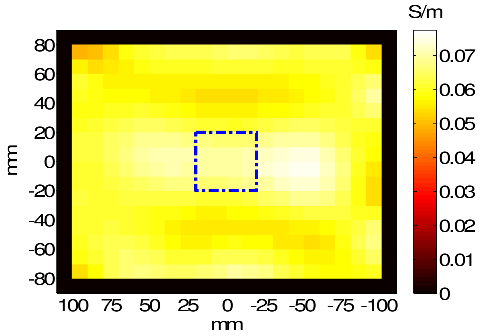

L1-V

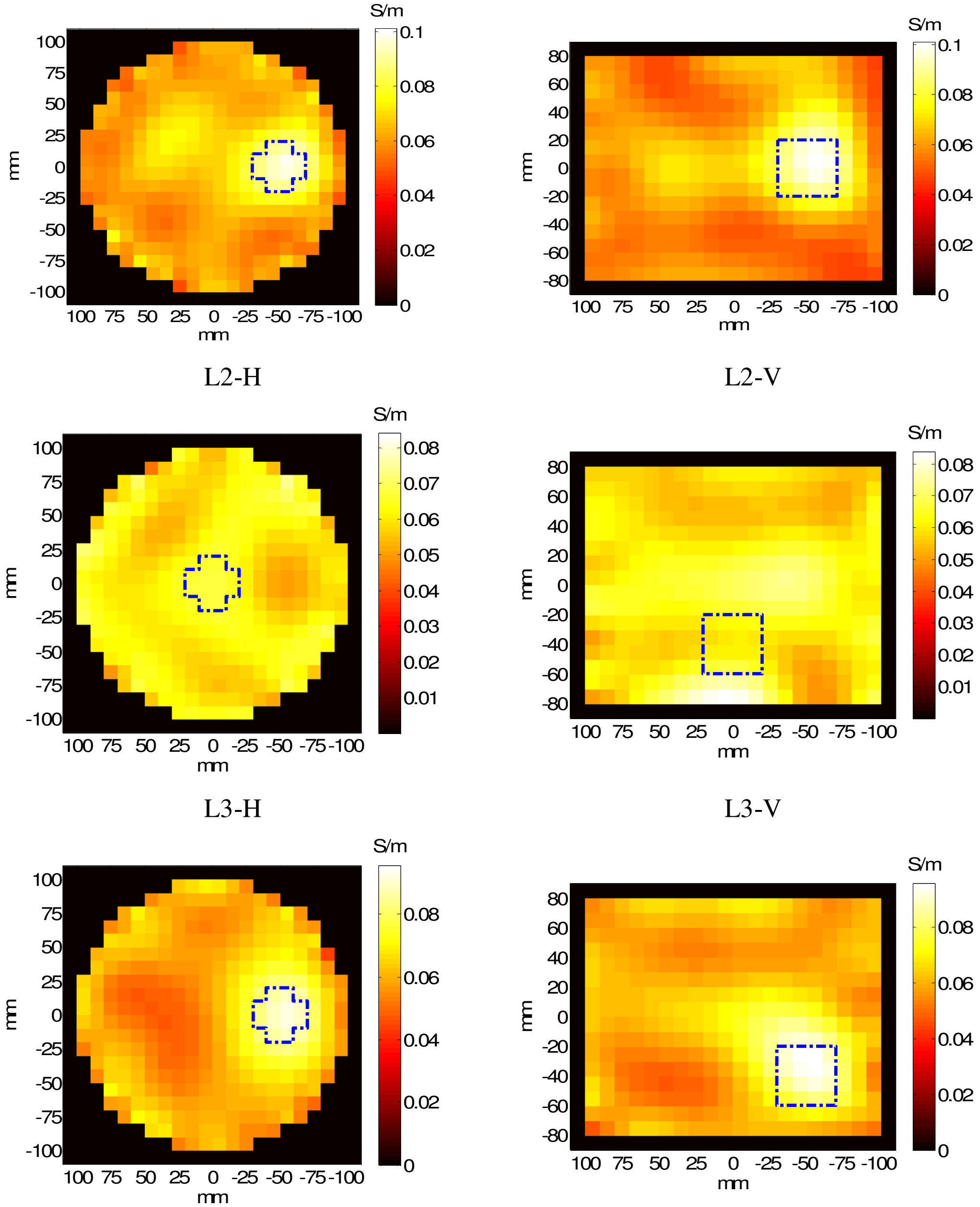

L2-H

L2-V

L3-H

L3-V

L4-H

L4-V

Figure 6.5: Frequency difference images of reconstructed $\Delta\sigma$ from simulated data with noise (case 2). Four different positions of the perturbation: L1-L4. The Dotted line shows the true boundaries of the perturbation. Test frequencies: 10 MHz – 1 MHz

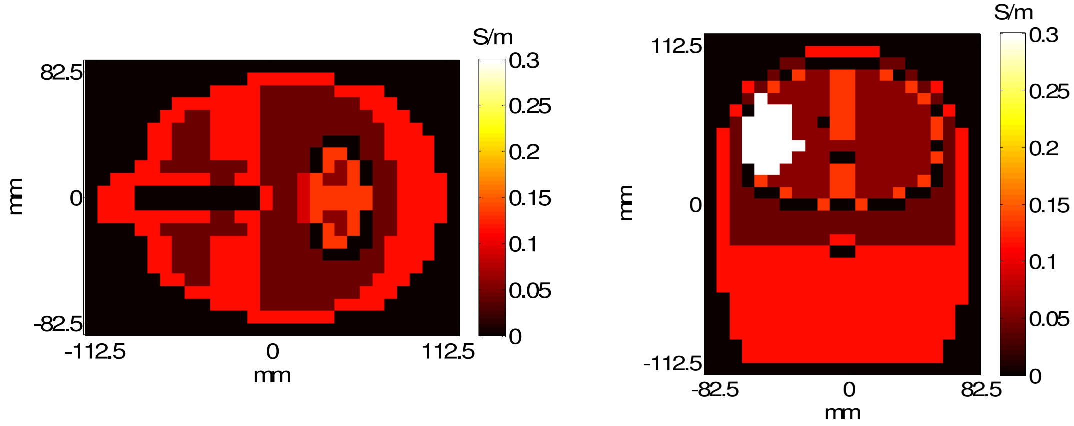

a) b)

Figure 6.6: Transversal a) and Sagittal b) cross sections of the true difference conductivity distribution $\Delta\sigma$ between the test frequencies 1 MHz and 10 MHz

Figure 6.6 (a) and (b) depict pictures of the transversal and sagittal cross sections of the head respectively illustrating the conductivity difference between the maps estimated at 1 MHz and 10 MHz. Figure 6.6 (b) also shows a peripheral stroke modelled as blood clot which exhibits the largest conductivity change estimated as 0.3 Sm^{-1}. Figure 6.7 (a) shows the corresponding reconstructed image with the single step Tikhonov formulation, where it is clear the stroke was not recovered. Instead, the region occupied by the neck, which consists of the scalp, appears with a larger reconstructed conductivity and includes an artefact with a conductivity of about 0.2 Sm^{-1}. As can be seen from Figure 6.6 (a-b), the scalp (muscle) exhibits a considerable conductivity change ($\Delta\boldsymbol{\sigma}_{\text{SCALP/Muscle}} = 0.12\ \text{Sm}^{-1}$) after the stroke ($\Delta\boldsymbol{\sigma}_{\text{Stroke}} = 0.3\ \text{Sm}^{-1}$) and the eye balls ($\Delta\boldsymbol{\sigma}_{\text{eye balls}} = 0.18\ \text{Sm}^{-1}$). In addition, the scalp occupies an enormous part of the head and some parts of which are very close to the coil array like the nose and back of the head. Consequently, the received signal is dominated by the signal from the scalp. In order to reduce this problem, a further regularisation posterior to the Newton inversion has been applied, which constrains the scalp to an upper bound conductivity value since it is a-priori known that the stroke cannot evolve in parts such as the neck, the nose or the mouth. Figure 6.7 (b) shows the results when the reconstructed conductivity of the scalp in image (a) is constrained to a threshold of 0.12 Sm^{-1}. This process subsequently reveals the stroke with a maximum of 0.16 Sm^{-1} on the exact top left corner of the head.

When contaminating the data according to case 2 with 1 % random noise, and repeating the same reconstruction procedure, the advantages of constraining the scalp can be seen where the stroke emerges clearly from Figure 6.8 (a) to (b). Another important remark concerns the way the random noise is added, where in Figure 6.8 (b) the stroke is reconstructed better than in Figure 6.7 (b), inferring there is a benefit when the noise is scaled (i.e. to be dependent) with frequency. When we follow case 2 and decrease the noise level to 0.01 %, we improve the SNR from 40 dB to 80 dB, which is a figure that has been published in the recent developed MIT system (Mark 2a) [128] . The corresponding reconstructed image shows the stroke better localised.

The ability to recover the stroke feature using the single step linear formulation and the posterior regularisation can be regarded as an achievement in the sense that a stroke with the volume 50 ml was reconstructed from within head model with complex shape and multiple tissues. Even with low resolution and poor localisation, these results are encouraging since they constitute one of the first reports to demonstrate the potential feasibility of image reconstruction of stroke in MIT on a head model with an approximation to realistic anatomical structure. However, clearly it would be extremely difficult to achieve such results in practice for the following reasons:

- There will be numerous sources of error that will increase the noise level much beyond the applied value, which can be classified into two subsets namely, a) geometrical errors, such as positioning errors, registration of the outer shape boundary. b) modelling errors related to discretisation of the head tissues. c) Spectral errors which are linked with the quantification of noise with changing the applied frequency.
- A satisfactory representative model of human head would require a very dense mesh with a fine resolution. This means a large number of degrees of freedom to solve, which will make the linear system of equations very much underdetermined. Hence this will accentuate the ill-posedness by increasing the condition number and making the system difficult to stabilise.

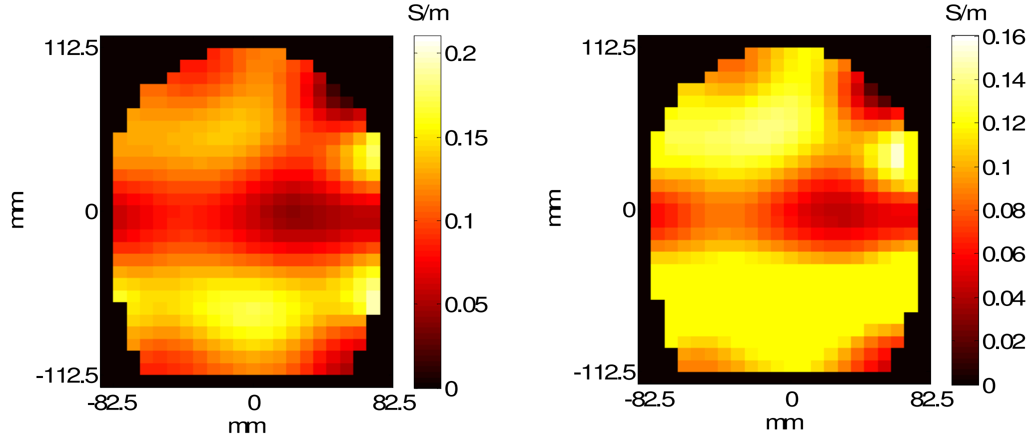

a) b)

Figure 6.7: Sagittal images of reconstructed $\Delta\sigma$ from simulated data with added Gaussian noise (case 1). a) Single step reconstruction. b) Single step reconstruction with constraining

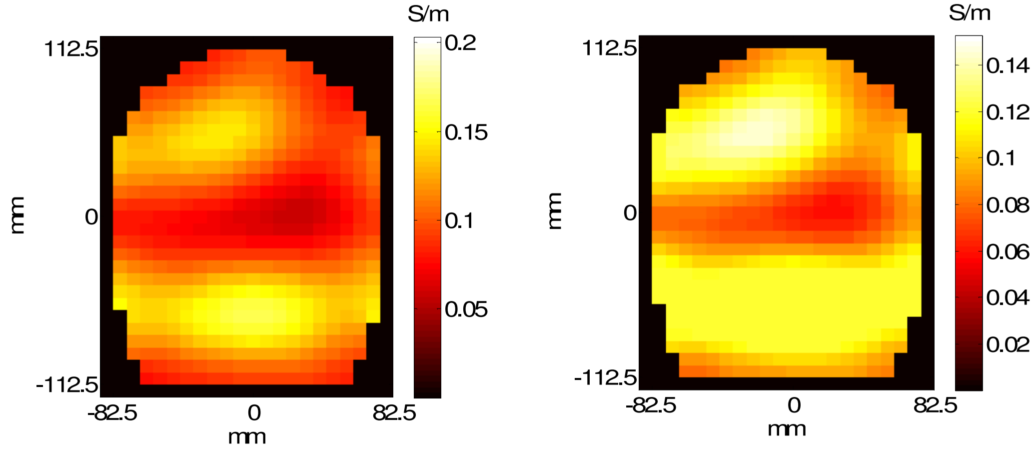

a) b)

Figure 6.8: Sagittal images of reconstructed $\Delta\sigma$ from simulated data with added Gaussian noise (case 2 with 1% noise). a) Single step reconstruction. b) Single step reconstruction with constraining

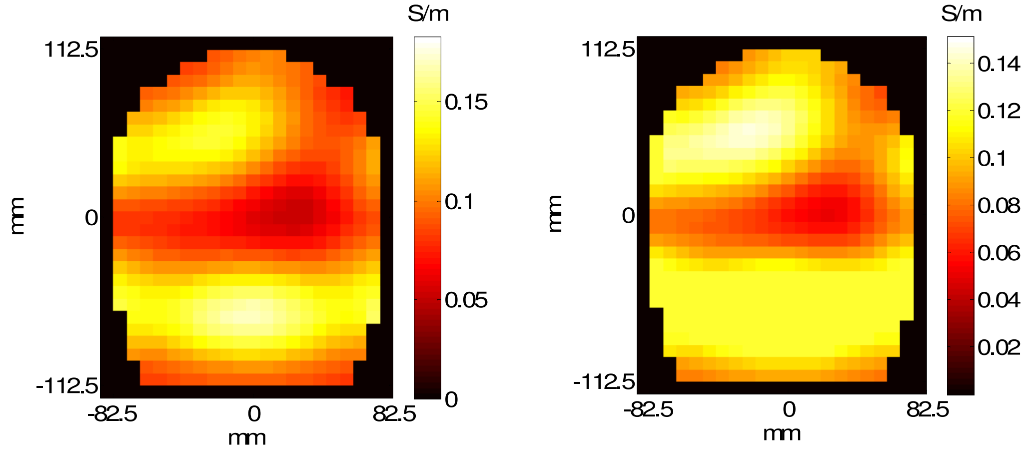

a) b)

Figure 6.9: Sagittal images of reconstructed $\Delta\sigma$ from simulated data with added Gaussian noise (case 2 with 0.01% noise). a) Single step reconstruction. b) Single step reconstruction with constraining.

7 Conclusions and Future Work

7.1 Conclusions

The thesis has approached the image reconstruction problem in MIT for three dimensional imaging of, low conductivity materials not exceeding a few Siemens per meter.. The investigation constituted a subset of a large EPSRC funded project aimed at developing MIT for screening medical and industrial process applications with low conductivity profiles. The thesis covered four chief objectives:

a) Formulate a new fast and memory efficient forward model to make nonlinear iterative optimisation of the MIT inverse problem a feasible method to adopt in practice.
b) Investigate the feasibility of detecting cerebral stroke using numerical and analytical solutions of the eddy current problem
c) Implement advanced optimisation techniques equipped with control and monitoring tools to further stabilise the MIT ill-posed inverse problem and achieve optimum convergence
d) Investigate different regularisation methods for image reconstruction and in particular study their suitability for the medical and industrial process applications considered in this thesis.
e) Conduct further analysis on the feasibility of detecting stroke using difference imaging based on multi-frequency measurements.

Based on the results presented in this thesis, the following conclusions can be drawn:

With regard to the forward modelling in MIT, a custom forward solver based on the impedance method was constructed. In order to efficiently implement the impedance method, nodal analysis has been selected among other circuit analysis techniques mainly because it requires relatively far less number of equations, and it is suitable for analysing three dimensional eddy current problems. In addition, initial testing of the impedance method based on this technique with two dimensional structures have shown that nodal analysis produces similar results compared to the branch current and mesh analysis techniques, which agrees with theory. For modelling 3D objects, validation tests involving the computation of the eddy current distribution in a homogeneous conductive sphere subject to magnetic excitation from a single coil showed the constructed custom eddy current solver generates results matching those of commercial software packages (i.e. Ansoft, COMSOL and TLM) as well as coded analytical solution. Furthermore, the custom forward solver adopted a weakly coupled field assumption which, for objects of the size of the human head, appeared to be a valid approximation for low frequencies up to 10 MHz and low conductivity materials in the range of biological tissues (<0.5 Sm^{-1}). Using the approximation, the custom forward solver exhibited considerable computational efficiency in speed and memory demands compared to commercial FEM solvers, which suggested that full 3D inversion using nonlinear MIT image reconstruction can be possible.

With regard to the study on the feasibility of detecting cerebral stroke, results based on an analytical evaluation of the induced voltage in an opposite coil pair for a multilayer spherical head model showed that a central spherical stroke with 27 mm radius could possibly be detected above noise level reported on the Mark 1 prototype. This is using absolute imaging and is provided that the background field can be perfectly eliminated. From a clinical perspective such a stroke is very large, which infers noise levels have to be reduced much below current characteristics in order to increase the potential of detecting a central stroke. In a second numerical study on examining the effects of systematic errors which are experienced with the Mark 1 system as well as those related to movement of the head, results showed the signal due to a large stroke located near the periphery of a realistic anatomical head is comparable to such effects. Exploiting the spectroscopic behaviour of biological tissues and performing frequency differential measurements does not cancel such errors. Therefore, it can be deduced that system optimisation is required to make MIT feasible for stroke detection and calibration of such errors in image reconstruction could be helpful.

The subsequent study was set to implement efficient optimisation techniques to solve the MIT inverse problem. A selection of nonlinear optimisation techniques has been investigated in MIT namely LMM, DGNM and PDLM. Within the functionality of these methods, stability control tools were exploited; namely the damping mechanism and the trust region technique. Performance tests to detect a perturbation in a homogeneous background using simulated data contaminated with noise have been carried out to compare the efficiency of these methods against that of classical RGNM. From the results, it can be concluded that the LMM and the PDLM offer satisfactory stability especially toward the end of the optimisation by converting to small step sizes calculated by the steepest descent method. Hence, these two methods can be useful to achieve a guaranteed stable solution for reconstruction problems with data incorporating large errors. On the other hand, DGNM provided finer convergence compared to its counterparts and requires the specification of a lesser number of parameters. However, this method does not employ the steepest descent method. Hence, it may become unstable and cannot be guaranteed to remain near the objective function minimiser in the final stage of the iterative process.

Since large scale inverse problems can be expected in future work on cerebral stroke imaging especially when more realistic head models will be deployed, initial work to deal with the inversion of large systems have been carried out by implementing Krylov subspace techniques in MIT. An algorithm denoted DGN-KM has been presented, which implements the linear preconditioned CG iterative scheme into the DGN method to replace the inversion operation. Simulations tests using three problems of different scales showed that as the problem scale grows the DGN-K method becomes more computationally efficient than its counterpart DGNM. Since DGN-KM employs 2nd order derivative information like DGNM for calculating the length and the search direction of the step, comparison tests show there is no noticeable loss in the accuracy level of the DGN-KM solution.

In connection with the study on regularisation, four regularisation priors, namely: NOSER, 2nd order Laplacian, Edge preserving and SSRM have been implemented within the LM image reconstruction to solve the MIT inverse problem for a medical and an industrial process application.

For the stroke imaging application, images reconstructed from a head phantom with two tissues and a perturbation showed the prior information implicit in the cited smoothing and edge preserving regularisation matrices is not good enough to produce reasonable absolute images of the stroke especially in the existence of the CSF layer which appears to dominate the measurement data. SSRM, however for the first time has been applied to MIT, and appears promising in enabling MIT to monitor the stroke provided that structural information of the tissues is obtained a priori through high resolution medical scanners.

In a second example of using MIT for imaging the water component in oil / process water pipelines, results showed that reasonable low resolution absolute reconstructions using simple smoothing and edge preserving regularisation priors can be obtained from simulated data disturbed with Gaussian noise. From the practical tests two flow regimes namely annular and bubble flow were considered. Using the new 14 channel MIT system to generate the data, and difference imaging using the LM algorithm and 2nd order Laplacian operator reasonable reconstructions were obtained,for several cases which have been unsolvable with previous MIT systems and image reconstructed algorithms. However, reconstructions showed problems related to spatial resolution and artefacts which can be mitigated by addressing the outstanding hardware issues and increasing the number of independent of measurements.

On the feasibility of detecting stroke using frequency difference imaging, a linear formulation has been implemented to examine the ability of the algorithm to recover a perturbation in different positions from inside a saline cylindrical model. Based on the results from simulated data with added synthetic noise it can be deduced that a peripheral perturbation (volume: 50 ml) is easier to discriminate by virtue of a large sensitivity in the region whereas a perturbation in the centre remains a challenging case. In another simulation test involving a realistic head model and a peripheral stroke (50 ml), application of the linear direct Tikhonov method with smoothing regularisation and non-negativity constraining was not successful and the images showed a large conductivity artefact in the scalp which prevented the stroke feature from standing out. The application of further regularisation by constraining the scalp’s reconstructed conductivity appeared to reveal a large conductivity feature in the location associated with the stroke. However, even if the feature relates to the stroke the quality of the reconstructed images is compromised. Thus, frequency difference reconstruction for this application may be improved with nonlinear algorithms.

7.2 Future Work

From the work and research carried out in this thesis, it seems MIT has long way to go before it can successfully be introduced in the hospitals or the industry for imaging objects with low conductivity materials. From the applications investigated it also seems, MIT has got more potential to be used for imaging water fraction in oil pipelines than to be employed for discriminating between ischemia and haemorrhage, or even detecting a stroke in general. The reasons are quite obvious: a) the human head is extremely complex in outer shape and interior structure, b) the actual application imposes constraints such as the impossibility to utilize difference imaging because of the unavailability of data prior to the stroke formation, c) the small volume of the stroke and d) the limitation on the excitation field intensity.

Indeed, MIT has been proposed as a possible medical imaging application for imaging the stroke just recently over the last decade, which infers MIT is still immature and requires further research. However, one might also see that MIT shares many features in common with EIT which has been researched for three decades and still has not been established clinically. *So do we think MIT needs more research in order to be used for detecting or monitoring the stroke*? Furthermore, a substantial focus has been devoted to investigate MIT for imaging the stroke in particular, compared to other medical applications because the stroke is an emergency condition which could benefit from a fast scanning modality like MIT. Hence this latter could replace low time resolution established imaging techniques like MRI in the future. However, one might also say, MIT is also restrained in time by image reconstruction and by the time a substantial research is invested into MIT, the limitations of the other established techniques, notably the cost and the time resolution could be tackled. *So could MIT have a role in the future, or will the ill-posedness and the sensitivity limitation of MIT remain major problems*? In the author's view, in order to increase the chances for MIT to become an imaging technique in the medical field or the low conductivity industry, a substantial investment of research, preferably a *multidisciplinary* research is required to address the missing ingredients and the research gaps before making any conclusions with regard to this modality. The work presented in this thesis contributed to this aim and progress has been achieved. In what follows, the strategy to address the future work is outlined.

Regarding the image reconstruction in MIT, two major computational procedures are encountered: the forward problem and the inverse problem:

The evaluation of the forward problem to produce computed data aimed at fitting the measured data as well as possible requires efficient numerical methods and accurate modelling.

a) For stroke imaging, high definition head models should be used in the future. Hence, efficient meshing of the models is required to accurately represent the thin tissue structures which lead to large systems of equations. Direct methods will no longer become time and memory efficient and iterative methods such as the CG method based on the Krylov subspace technique or a similar alternative can be employed to solve the forward problem faster and accurately with low tolerance error.
b) The head model incorporates irregular outer shape and is important to be modelled accurately because MIT is most sensitive to peripheral regions. Any errors in modelling the outer boundaries would hamper the minimization process of the objective function and make the inverted solution highly unstable to noise because of the MIT ill-posedness. Both the FEM based on tetrahedral and FDM based on cubic voxels may be suitable for implementation. In [78], a technique has been presented to trim the cubic voxels to accurately model curved boundaries using the FIM. If models are to be generated from practical head phantoms, appropriate technologies such as high definition optical scanners have to be developed for accurate registration of outer boundaries. In section (3.8), on examining the feasibility of detecting the stroke using analytical solution for a multilayer spherical head model, the results showed a 1.2 mm error in determining the outer boundaries is equivalent to the system noise exhibited by the Mark 1. Hence, shape scanners with resolution of sub-millimetres need to be developed.

c) The developed forward model takes only the real part (the conductivity) of the biological tissues to compute the simulated data. The imaginary part caused by the permittivity can be taken into account especially at high frequencies. The inclusion of the imaginary dielectric component can be straightforward in the developed forward solver. Another issue of concern is the anisotropic nature of biological tissues. So far, the forward solver assumed tissues are isotropic and the software can be extended to model anisotropic tissues which should be important in clinical experiments.

In connection with the inverse problem, the thesis presented a new class of nonlinear optimization techniques to solve the MIT inverse problem. To stabilize the inverse solution and optimize convergence, the techniques employed dynamic damping parameter and trust region radius, as well as the implementation of a dynamic regularisation parameter. These techniques showed better performance than the standard Gauss Newton method and are generic. i.e. they can be employed in other applications where they can show more success. However, what could be done in continuation on stroke imaging is as follows:

a) The sensitivity to the perturbation (i.e. the stroke) plays an essential role to the success of the image reconstruction. From the thesis, we can infer it would be reasonable to focus or make MIT work on imaging peripheral stroke (e..g Subarachnoid or Subdural) since MIT is more sensitive near the border than to the centre of the test object. Peripheral stroke cannot be identified without an initial diagnosis using a high resolution scanning method like MRI or CT. Hence, MIT can be found valuable in monitoring the development of the stroke instead of detecting or identifying its type. It would also be necessary to ask clinicians whether peripheral stroke could develop toward the centre or just spread around the periphery. It may also be possible to investigate time difference imaging to detect changes in the stroke. Another issue of importance is to increase the sensitivity around the brain, hence the requirement for developing coil arrays which conform to the head shape. Recently, a helmet coil array (Mark 2b) has been developed by our academic partner in Glamorgan University and showed an improvement of sensitivity.

b) There is much work can still be done on regularisation of the inverse problem. Defining regularisation as a method to incorporate a priori knowledge about the noise variation and the expected solution, existing regularisation matrices like smoothing and edge preserving priors were not successful in absolute imaging of the stroke because they did not hold representative information. In fact, the assumed information does not correlate to the head structure which features a complicated 3D distribution conductivity and also contain some large contrasts notably in the CSF region. In addition, the noise distribution between the MIT channels is assumed to be uniform, i.e. the coefficient matrix inside the Hessian ($\boldsymbol{J}^{\mathrm{T}}\boldsymbol{J}$) is scaled with identity. In the future we would expect the second assumption to hold valid with the advances of high specification acquisition systems and coil arrays. With regard to the first assumption, the implementation of regularisation matrix incorporating structural prior information (e.g. SSRM) of biological tissues was demonstrated to help the absolute image reconstruction. It would therefore seem reasonable to suggest that further work should be invested to research statistical methods to improve this regularisation method. As an immediate task, this regularisation should be investigated with high resolution head models obtained from MRI, and assign a margin of error to all tissues conductivities. With regard to the regularisation parameter, it would be interesting to research, implement and analyse different selection methods. Regularisation can also be done posteriori to the inversion of the Hessian in the form of constraining. Hence, image processing tools can be added to the algorithm to include a-priori knowledge based on the analysis of the inverted solution.

c) Multi-frequency differential imaging can also be further investigated for stroke imaging. In order to exploit the full spectral behaviour of the biological tissues in the selected frequency range for example 1-10 MHz, difference frequency images can be reconstructed for different test frequencies and reference frequencies within the frequency range. From the results, spectral conductivity curves can be plotted and fitted against frequency differential Cole models to infer tissue types. In doing this, the spectral behaviour of biological tissues can be well exploited and the MIT image reconstruction becomes less underdetermined.

With regard to the application of MIT for imaging the sea water for oil/water applications, the thesis presented successful images reconstructed from a practical experiment. Future work should involve repeating the experiment for the true conductivity value of the sea water. The experiments should then be carried at low frequency of 1 MHz. In the long term, if the method is successful, work could continue with more realistic flow regimes and fast image capture rates

To this end, the efforts devoted to further develop image reconstruction in MIT for imaging the stroke or the process water in oil pipelines should be transferred to other applications. For instance, in the medical field there are areas which seem easier than stroke imaging and MIT can have a successful role for example: monitoring lung activity. In this application state difference imaging with its benefits in cancelling geometrical errors and systematic hardware noise can be employed

8 References

[1] A. J. Peyton, Z. Z. Yu, G. Lyon, S. AlZeibak, J. Ferreira, J. Velez, F. Linhares, A. R. Borges, H. L. Xiong, N. H. Saunders, and M. S. Beck, "An overview of electromagnetic inductance tomography: Description of three different systems," *Measurement Science & Technology,* vol. 7, pp. 261-271, 1996.

[2] H. Griffiths, "Magnetic induction tomography," *Measurement Science & Technology,* vol. 12, pp. 1126-1131, 2001.

[3] H. S. Tapp and A. J. Peyton, "A state of the art review of electromagnetic tomography," in *3rd World Congress on Industrial Process Tomography*, 2003, pp. 340–346.

[4] X. A. Ma, A. J. Peyton, R. Binns, and S. R. Higson, "Imaging the flow profile of molten steel through a submerged pouring nozzle," in *Proc. 3rd world Congress on Industrial Process Tomography (WCIPT3)*, Banff, Canada, 2003.

[5] X. D. Ma, A. J. Peyton, R. Binns, and S. R. Higson, "Electromagnetic techniques for imaging the cross-section distribution of molten steel flow in the continuous casting nozzle," *IEEE Sensors Journal,* vol. 5, pp. 224-232, 2005.

[6] X. Ma, A. J. Peyton, S. R. Higson, A. Lyons, and S. J. Dickinson, "Hardware and software design for an electromagnetic induction tomography (EMT) system for high contrast metal process applications," *Measurement Science & Technology,* vol. 17, pp. 111-118, 2006.

[7] X. Ma, A. J. Peyton, S. R. Higson, and P. Drake, "Development of multiple frequency electromagnetic induction systems for steel flow visualization," *Measurement Science & Technology,* vol. 19, 2008.

[8] M. H. Pham, Y. B. Hua, and N. B. Gray, "Imaging the solidification of molten metal by eddy currents: I," *Inverse Problems,* vol. 16, pp. 469-482, 2000.

[9] M. H. Pham, Y. B. Hua, and N. B. Gray, "Imaging the solidification of molten metal by eddy currents: II," *Inverse Problems,* vol. 16, pp. 483-494, 2000.

[10] R. Merwa, K. Hollaus, B. Oszkar, and H. Scharfetter, "Detection of brain oedema using magnetic induction tomography: a feasibility study of the likely sensitivity and detectability," *Physiological Measurement,* vol. 25, pp. 347-354, 2004.

[11] R. Merwa, K. Hollaus, P. Brunner, and H. Scharfetter, "Solution of the inverse problem of magnetic induction tomography (MIT)," *Physiological Measurement,* vol. 26, pp. S241-S250, 2005.

[12] W. A. Wan-Daud, H. S. Tapp, C. Ktistis, and A. J. Peyton, "A 3D Imaging system for measuring the shape and volume of the human body," in *Proc. 3rd World Congress on Industrial Process Tomography*, Banff, Canada, 2003, pp. 358-63.

[13] H. S. Tapp, D. Goss, R. Mackin, E. Crescenzo, W. A. Wan-Daud, C. Ktistis, and A. J. Peyton, "A combined digital camera - EMT system to measure human body composition," in *Proc. 3rd World Congress on Industrial Process Tomography*, Banff, Canada, 2003, pp. 358-63.

[14] C. Ktistis, "Electromagnetic induction tomography techniques for low conductivity biomedical application " in *School of Electrical and Electronic Engineering* Manchester: The University of Manchester, 2007.

[15] M. Steffen, K. Heimann, N. Bernstein, and S. Leonhardt, "Multichannel simultaneous magnetic induction measurement system (MUSIMITOS)," *Physiological Measurement,* vol. 29, pp. S291-S306, 2008.

[16] A. R. J. Borges, E. de Oliveira, J. Velez, C. Tavares, F. Linhares, and P. A.J., "Development of electromagnetic tomography (EMT) for industrial applications, Part 2: image reconstruction and software framework," in *1st World Congress on Industrial Process Tomography*, Buxton, Greater Manchester, 1999.

[17] H. Griffiths, W. R. Stewart, and W. Gough, "Magnetic induction tomography - A measuring system for biological tissues," *Electrical Bioimpedance Methods: Applications to Medicine and Biotechnology,* vol. 873, pp. 335-345, 1999.

[18] M. Soleimani, "Image and shape reconstruction methods for magnetic induction and electrical impedance tomography, PhD Thesis." vol. PhD: University of Manchester, 2005.

[19] K. R. Foster and H. P. Schwan, "Dielectric properties of tissues and biological materials - A critical review," *Critical Reviews in Biomedical Engineering,* vol. 17, pp. 25-104, 1989.

[20] R. Pethig and D. B. Kell, "The passive electrical properties of biological systems - Their significance in physiology, biophysics and biotechnology," *Physics in Medicine and Biology,* vol. 32, pp. 933-970, 1987.

[21] L. A. Geddes and L. E. Baker, "Specific resistance of biological material - a compendum of data for biomedical engineer and physiologist," *Medical & Biological Engineering,* vol. 5, pp. 271-&, 1967.

[22] M. A. Stuchly and S. S. Stuchly, "Dielectric properties of biological substances - Tabulated," *Journal of Microwave Power and Electromagnetic Energy,* vol. 15, pp. 19-26, 1980.

[23] C. H. Durney, C. C. Johnson, P. W. Barber, H. Massoudi, M. F. Iskander, S. J. Allen, and J. C. Mitchell, "Descriptive summary - Radiofrequency radiation dosimetry handbook - 2nd edition," *Radio Science,* vol. 14, pp. 5-7, 1979.

[24] F. A. Duck, *Physical Properties of Tissue: A Comprehensive Reference Book*: London: Academic, Harcourt Brace Jovanovich, 1990.

[25] C. Gabriel, S. Gabriel, and E. Corthout, "The dielectric properties of biological tissues .1. Literature survey," *Physics in Medicine and Biology,* vol. 41, pp. 2231-2249, 1996.

[26] S. Gabriel, R. W. Lau, and C. Gabriel, "The dielectric properties of biological tissues .2. Measurements in the frequency range 10 Hz to 20 GHz," *Physics in Medicine and Biology,* vol. 41, pp. 2251-2269, 1996.

[27] S. Gabriel, R. W. Lau, and C. Gabriel, "The dielectric properties of biological tissues .3. Parametric models for the dielectric spectrum of tissues," *Physics in Medicine and Biology,* vol. 41, pp. 2271-2293, 1996.

[28] R. H. Bayford, "Bioimpedance tomography (Electrical impedance tomography)," *Annual Review of Biomedical Engineering,* vol. 8, pp. 63-91, 2006.

[29] H. P. Schwan, "Dielectric properties of biological tissue and biophysical mechansims of EM-Field interation," *Abstracts of Papers of the American Chemical Society,* vol. 179, pp. 68-PHYS, 1980.

[30] The NHS Confederation, "The National stroke strategy," 2008.

[31] F. C. Vinas, "Bedside invasive monitoring techniques in severe brain-injured patients," *Neurological Research,* vol. 23, pp. 157-166, 2001.

[32] http://www.medmovie.com/.

[33] R. Guardo, S. Trudelle, A. Adler, S. Boulay, and P. Savard, "Contactless recordings of cardiac related thoracic conductivity changes," in *Engineering in Medicine and Biology* Canada, 1995, pp. 1581–2.

[34] A. Richer and A. Adler, "Eddy current based flexible sensor for contactless measurement of breathing," in *IMTC Instrumentation and Measurement*, Ottawa, Canada, 2005.

[35] R. A. Albrechtsen, Z. Z. Yu, and A. J. Peyton, "Preliminary experiments on the investigation of the inductive technique for measuring water content in multi-phase flow," in *European Concerted Action on Process Tomography*, Bergen, Norway, 1995, pp. 205 - 213.

[36] M. Soleimani and W. R. B. Lionheart, "Absolute conductivity reconstruction in magnetic induction tomography using a nonlinear method," *IEEE Transactions on Medical Imaging,* vol. 25, pp. 1521-1530, 2006.

[37] D. W. Marquardt, "Generalized inverses, ridge regression, biased linear-estimation, and non-linear estimation," *Current Contents/Engineering Technology & Applied Sciences,* pp. 20-20, 1983.

[38] R. Aster, B. Brochers, and C. Thurber, *Parameter Estimation and Inverse Problems*: Academic Press, 2004.

[39] P. C. Hansen, *Rank-Deficient and Discrete Ill-Posed Problems: Numerical Aspects of Linear Inversion*. Philadelphia: SIAM, 1998.

[40] N. G. Gencer and M. N. Tek, "Electrical conductivity imaging via contactless measurements," *IEEE Transactions on Medical Imaging,* vol. 18, pp. 617-627, 1999.

[41] C. CohenBacrie, Y. Goussard, and R. Guardo, "Regularized reconstruction in electrical impedance tomography using a variance uniformization constraint," *IEEE Transactions on Medical Imaging,* vol. 16, pp. 562-571, 1997.

[42] M. Vauhkonen, D. Vadasz, P. A. Karjalainen, E. Somersalo, and J. P. Kaipio, "Tikhonov regularization and prior information in electrical impedance tomography," *IEEE Transactions on Medical Imaging,* vol. 17, pp. 285-293, 1998.

[43] W. Q. Yang and L. H. Peng, "Image reconstruction algorithms for electrical capacitance tomography," *Measurement Science & Technology,* vol. 14, pp. R1-R13, 2003.

[44] V. A. Morozov, "Solution of functional equations by regularization method " *Doklady Akademii Nauk Sssr,* vol. 167, pp. 510-&, 1966.

[45] P. C. Hansen, "Analysis of discrete ill-posed problems by means of the L-Curve," *Siam Review,* vol. 34, pp. 561-580, 1992.

[46] G. Wahba, "Spline Models for Observational Data," in *CBMS-NSF Regional Conference Series in Applied Mathematics, SIAM*, Philadelphia, PA 1990, p. 169.

[47] H. Rutishuser, *Once again: The least squares problem*: Linear Algebra Applications, 1968.

[48] A. Borsic, "Regularisation Methods for Imaging from Electrical Measurements," in *School of Engineering*
Oxford Brookes University, 2002.

[49] M. Soleimani and W. R. B. Lionheart, "Nonlinear image reconstruction for electrical capacitance tomography using experimental data," *Measurement Science & Technology,* vol. 16, pp. 1987-1996, 2005.

[50] W. F. Fang, "A nonlinear image reconstruction algorithm for electrical capacitance tomography," *Measurement Science & Technology,* vol. 15, pp. 2124-2132, 2004.

[51] M. Soleimani, W. R. B. Lionheart, A. J. Peyton, X. D. Ma, and S. R. Higson, "A three-dimensional inverse finite-element method applied to experimental eddy-current imaging data," *IEEE Transactions on Magnetics,* vol. 42, pp. 1560-1567, 2006.

[52] V. Kolehmainen, S. R. Arridge, W. R. B. Lionheart, M. Vauhkonen, and J. P. Kaipio, "Recovery of region boundaries of piecewise constant coefficients of an elliptic PDE from boundary data," *Inverse Problems,* vol. 15, pp. 1375-1391, 1999.

[53] A. Tamburrino and G. Rubinacci, "A new non-iterative inversion method for electrical resistance tomography," *Inverse Problems,* vol. 18, pp. 1809-1829, 2002.

[54] M. Bruhl, "Explicit characterization of inclusions in electrical impedance tomography," *Siam Journal on Mathematical Analysis,* vol. 32, pp. 1327-1341, 2001.

[55] T. F. Chan and X. C. Tai, "Level set and total variation regularization for elliptic inverse problems with discontinuous coefficients," *Journal of Computational Physics,* vol. 193, pp. 40-66, 2004.

[56] W. Q. Yang, D. M. Spink, T. A. York, and H. McCann, "An image-reconstruction algorithm based on Landweber's iteration method for electrical-capacitance tomography," *Measurement Science & Technology,* vol. 10, pp. 1065-1069, 1999.

[57] S. Watson, C. Ktistis, B. Dekdouk, D. W. Armitage, A. J. Peyton, R. J. Williams, and H. Griffiths, "Development of MIT for oil industry applications," in *5th World Congress on Industrial Process Tomography*, Bergen, Norway, 2007, pp. 1045-1050.

[58] C. Vogel, *Computational methods for inverse problems*: Frontiers in Applied Mathematics, 2002.

[59] H. L. Xiong and L. A. Xu, "Electromagnetic tomography (EMT): Theoretical analysis of the forward problem," *Applied Mathematics and Mechanics-English Edition,* vol. 21, pp. 1034-1044, 2000.

[60] G. Dassios, S. N. Giapalaki, A. N. Kandili, and F. Kariotou, "The exterior magnetic field for the multilayer ellipsoidal model of the brain," *Quarterly Journal of Mechanics and Applied Mathematics,* vol. 60, pp. 1-25, 2007.

[61] A. Gonzalez-Nakazawa, W. Q. Yang, and K. Hennessey, "An analytical approach for modelling electro-magnetic tomography sensor," *Sensor Review,* vol. 28, pp. 212-221, 2008.

[62] Breckon. W. R., "Image reconstruction in electrical impedance tomography," University of Manchester, 1990.

[63] M. Vauhkonen, "Electrical impedance tomography and prior information, PhD thesis," University of Kuopio 1997.

[64] M. Molinari, "High fidelity imaging in electrical impedance tomography, PhD Thesis." vol. PhD Thesis: University of Southampton, 2003.

[65] K. Hollaus, C. Magele, R. Merwa, and H. Scharfetter, "Fast calculation of the sensitivity matrix in magnetic induction tomography by tetrahedral edge finite elements and the reciprocity theorem," *Physiological Measurement,* vol. 25, pp. 159-168, 2004.

[66] M. Soleimani., W. R. B. Lionheart., C. H. Riedel., and O. Dössel., "Forward Problem in 3D Magnetic Induction Tomography (MIT)," in *3rd World Congress on Industrial Process Tomography*, Banff, Canada, 2003, pp. pp. 275-280.

[67] D. W. Armitage, H. H. Leveen, and R. Pethig, "Radiofrequency induced hyperthermia - Computer simulation of specific absorption rate distributions using realistic anatomical models," *Physics in Medicine and Biology,* vol. 28, pp. 31-42, 1983.

[68] A. Morris, H. Griffiths, and W. Gough, "A numerical model for magnetic induction tomographic measurements in biological tissues," *Physiological Measurement,* vol. 22, pp. 113-119, 2001.

[69] M. H. Pham and A. J. Peyton, "A model for the forward problem in magnetic induction tomography using boundary integral equations," *IEEE Transactions on Magnetics,* vol. 44, pp. 2262-2267, 2008.

[70] M. Zolgharni, P. D. Ledger, D. W. Armitage, D. S. Holder, and H. Griffiths, "Imaging cerebral haemorrhage with magnetic induction tomography: numerical modelling," *Physiological Measurement,* vol. 30, pp. S187-S200, 2009.

[71] P. B. Johns, "On the relationship between TLM and Finite Difference Methods for Maxwell's equations " *IEEE Transactions on Microwave Theory and Techniques,* vol. 35, pp. 872-873, 1987.

[72] O. Biro, "Edge element formulations of eddy current problems," *Computer Methods in Applied Mechanics and Engineering,* vol. 169, pp. 391-405, 1999.

[73] O. Biro, K. Preis, and K. R. Richter, "On the use of the magnetic vector potential in the nodal and edge finite element analysis of 3D magnetostatic problems," *IEEE Transactions on Magnetics,* vol. 32, pp. 651-654, 1996.

[74] R. Merwa, K. Hollaus, B. Brandstatter, and H. Scharfetter, "Numerical solution of the general 3D eddy current problem for magnetic induction tomography (spectroscopy)," *Physiological Measurement,* vol. 24, pp. 545-554, 2003.

[75] R. Merwa, P. Brunner, A. Missner, K. Hollaus, and H. Scharfetter, "Solution of the inverse problem of magnetic induction tomography (MIT) with multiple objects: analysis of detectability and statistical properties with respect to the reconstructed conducting region," *Physiological Measurement,* vol. 27, pp. S249-S259, 2006.

[76] O. Biro and K. Preis, "On the use of the magnetic vector potential in the Finite Element Analysis of 3 dimensional eddy currents " *IEEE Transactions on Magnetics,* vol. 25, pp. 3145-3159, 1989.

[77] M. V. K. Chari, A. Konrad, M. A. Palmo, and J. Dangelo, "3-Dimensional vector potential analysis for machine field problems," *IEEE Transactions on Magnetics,* vol. 18, pp. 436-446, 1982.

[78] Van Rienen. U., *Numerical methods in computational electrodynamics, Linear systems in pratical applications*: Springer, 2001.

[79] S. Watson, R. J. Williams, H. Griffiths, W. Gough, and A. Morris, "Magnetic induction tomography: phase versus vector-voltmeter measurement techniques," *Physiological Measurement,* vol. 24, pp. 555-564, 2003.

[80] W. R. B. Lionheart, M. Soleimani, and A. J. Peyton, "Sensitivity analysis of 3D Magnetic Induction Tomography (MIT)," in *3rd World Congress on Industrial Process Tomography*, Banf, Canada, 2nd-5th Sept 2003

[81] J. R. Mortarelli, "A generalization of the Geselowitz relationship useful in impedance plethysmographic field calculations," *IEEE Transactions on Biomedical Engineering,* vol. 27, pp. 665-667, 1980.

[82] O. P. Gandhi and G. Kang, "Calculation of induced current densities for humans by magnetic fields from electronic article surveillance devices," *Physics in Medicine and Biology,* vol. 46, pp. 2759-2771, 2001.

[83] J. Cheng, M. A. Stuchly, C. Dewagter, and L. Martens, "Magnetic field induced currents in a human head from use of portable appliances," *Physics in Medicine and Biology,* vol. 40, pp. 495-510, 1995.

[84] O. P. Gandhi and X. Bin Chen, "Specific absorption rates and induced current densities for an anatomy-based model of the human for exposure to time-varying magnetic fields of MRI," *Magnetic Resonance in Medicine,* vol. 41, pp. 816-823, 1999.

[85] D. G. Wu, R. Qiang, J. Chen, S. Seidman, D. Witters, and W. G. Kainz, "Possible overexposure of pregnant women to emissions from a walk through metal detector," *Physics in Medicine and Biology,* vol. 52, pp. 5735-5748, 2007.

[86] J. M. Ivison, *Electric circuit theory*: Van Nostrand Reinhold Company Ltd, 1977.

[87] Boylesland R. L., *Introductory circuit analysis*, 9th ed.: Prentice Hall, 2000.

[88] Alexander. C. K. and Sadiku. M. N. O., *Fundamentals of electric circuits*, 2nd ed.: McGraw-Hills, 2003.

[89] P. J. Dimbylow, "Induced current densities from low-frequency magnetic fields in a 2 mm resolution, anatomically realistic model of the body," *Physics in Medicine and Biology,* vol. 43, pp. 221-230, 1998.

[90] M. Z. Abdullah, "Simulation of an inverse problem in electrical impedance tomography using resistance electrical network analogues," *International Journal of Electrical Engineering Education,* vol. 36, pp. 311-324, 1999.

[91] M. Vauhkonen, M. Hamsch, and C. H. Igney, "A measurement system and image reconstruction in magnetic induction tomography," *Physiological Measurement,* vol. 29, pp. S445-S454, 2008.

[92] W. R. Smythe, *Static and dynamic electricity*, 3rd Edition ed.: McGraw-Hill, 1968.

[93] C. V. Dodd and W. E. Deeds, "Analytical solutions to eddy-current probe-coil problems," *Journal of Applied Physics,* vol. 39, pp. 2829-&, 1968.

[94] A. Tizzard, L. Horesh, R. J. Yerworth, D. S. Holder, and R. H. Bayford, "Generating accurate finite element meshes for the forward model of the human head in EIT," *Physiological Measurement,* vol. 26, pp. S251-S261, 2005.

[95] L. Horesh, O. Gilad, A. Romsauerova, and D. S. Holder, "Stroke type detection by Multi-Frequency Electrical Impedance Tomography (MFEIT) - a feasibility study " in *VI International Conference on Biomedical Applications of Electrical Impedance Tomography*, London, UK, 2005

[96] A. Romsauerova, A. McEwan, L. Horesh, R. Yerworth, R. H. Bayford, and D. S. Holder, "Multi-frequency electrical impedance tomography (EIT) of the adult human head: initial findings in brain tumours, arteriovenous malformations and chronic stroke, development of an analysis method and calibration," *Physiological Measurement,* vol. 27, pp. S147-S161, 2006.

[97] A. P. Bagshaw, A. D. Liston, R. H. Bayford, A. Tizzard, A. P. Gibson, A. T. Tidswell, M. K. Sparkes, H. Dehghani, C. D. Binnie, and D. S. Holder,

"Electrical impedance tomography of human brain function using reconstruction algorithms based on the finite element method," *Neuroimage,* vol. 20, pp. 752-764, 2003.

[98] L. Fabrizi, A. McEwan, T. Oh, E. J. Woo, and D. S. Holder, "A comparison of two EIT systems suitable for imaging impedance changes in epilepsy," *Physiological Measurement,* vol. 30, pp. S103-S120, 2009.

[99] D. Gursoy and H. Scharfetter, "Reconstruction artefacts in magnetic induction tomography due to patient's movement during data acquisition," *Physiological Measurement,* vol. 30, pp. S165-S174, 2009.

[100] P. Brunner, R. Merwa, A. Missner, J. Rosell, K. Hollaus, and H. Scharfetter, "Reconstruction of the shape of conductivity spectra using differential multi-frequency magnetic induction tomography," *Physiological Measurement,* vol. 27, pp. S237-S248, 2006.

[101] R. Merwa and H. Scharfetter, "Magnetic Induction Tomography: A feasibility study of brain oedema detection using a finite element human head model," in *13th International Conference on Electrical Bioimpedance and the 8th Conference on Electrical Impedance Tomography*, 2007, pp. 480-483.

[102] W. Yin and A. J. Peyton, "A planar EMT system for the detection of faults on thin metallic plates," *Measurement Science & Technology,* vol. 17, pp. 2130-2135, 2006.

[103] R. Binns, A. R. A. Lyons, A. J. Peyton, and W. D. N. Pritchard, "Imaging molten steel flow profiles," *Measurement Science & Technology,* vol. 12, pp. 1132-1138, 2001.

[104] J. Nocedal and S. J. Wright, *Numerical optimization*: Springer, 1999.

[105] E. Polak, *Optimization. Algorithms and Consistent Approximations*: Springer, 1997.

[106] P. E. Frandsen, K. Jonasson, H. B. Nielsen, and O. Tingleff, *Unconstrained Optimization*, 3rd Edition ed.: IMM, DTU, 2004.

[107] K. Madsen, H. B. Nielsen, and O. Tingleff, "Methods for non -linear least sqaures problems," 2nd ed, 2004.

[108] C. Wang, R. G. Liu, F. Fu, F. S. You, X. T. Shi, and X. Z. Dong, "Image reconstruction for Magnetic Induction Tomography and preliminary simulations on a simple head model," *2007 Annual International Conference of the IEEE Engineering in Medicine and Biology Society, Vols 1-16,* pp. 4406-4409, 2007.

[109] D. W. Marquardt, "An algorithm for least-squares-estimation of nonlinear parameters," *Journal of the Society for Industrial and Applied Mathematics,* vol. 11, pp. 431-441, 1963.

[110] H. B. Nielsen, "Damping parameter in Marquardt's Method," IMM, DTU 1999.

[111] R. Fletcher and M. J. D. Powell, "A rapidly convergent descent method for minimization," *Computer Journal,* vol. 6, 1963.

[112] C. G. Broyden, "The convergence of a class of double-rank minimization algorithms," *J. Inst. Maths. Applics.,* vol. 6, pp. 76-90, 1970.

[113] R. Fletcher, "A new approach to variable metric algorithms," *Computer Journal* vol. 13, pp. 317-322, 1970.

[114] D. Goldfarb, "A family of variable metric methods derived by variational means," *Mathematics of Computation,* vol. 24, pp. 23-26, 1970.

[115] D. F. Shanno, "Conditioning of quasi-Newton methods for function minimization," *Mathematics of Computation,* vol. 24, 1970.

[116] K. Levenberg, "A Method for the Solution of Certain Non-Linear Problems in Least Squares," *The Quarterly of Applied Mathematics 2,* pp. 164–168, 1944.

[117] P. J. Vauhkonen, "Image reconstruction in electrical impedance tomography," Kuopio, Finland: PhD Thesis University of Kuopio, 2004.

[118] M. Goharian, A. Jegatheesan, and G. R. Moran, "Dogleg trust-region application in electrical impedance tomography," *Physiological Measurement,* vol. 28, pp. 555-572, 2007.

[119] N. Polydorides, "Image Reconstruction Algorithms for Soft-Field Tomography ": PhD Thesis, UMIST, 2002.

[120] L. Horesh, "Some Novel Approaches in Modelling and Image Reconstruction for Multi-Frequency Electrical Impedance Tomography of the Human Brain," PhD Thesis, UCL, 2006, pp. 137-173.

[121] N. Polydorides, W. R. B. Lionheart, and H. McCann, "Krylov subspace iterative techniques: On the detection of brain activity with electrical impedance tomography," *IEEE Transactions on Medical Imaging,* vol. 21, pp. 596-603, 2002.

[122] P. Hua, J. G. Webster, and W. J. Tompkins, "A regularised electrical impedance tomography reconstruction algorithm," *Clin Phys Physiol Meas,* vol. 9 Suppl A, pp. 137-41, 1988.

[123] M. Cheney, D. Isaacson, J. C. Newell, S. Simske, and J. Goble, "NOSER: An algorithm for solving the inverse conductivity problem," *Int. J. Imag. Syst., Technol,* vol. 2 pp. 66–75, 1990.

[124] T. Dai, M. Soleimani, and A. Adler, "Four-dimensional regularization for Electrical Impedance Tomography imaging," *13th International Conference on Electrical Bioimpedance and the 8th Conference on Electrical Impedance Tomography 2007,* vol. 17, pp. 408-411, 2007.

[125] R. Casanova, A. Silva, and A. R. Borges, "MIT image reconstruction based on edge-preserving regularization," *Physiological Measurement,* vol. 25, pp. 195-207, 2004.

[126] P. Charbonnier, L. BlancFeraud, G. Aubert, and M. Barlaud, "Deterministic edge-preserving regularization in computed imaging," *IEEE Transactions on Image Processing,* vol. 6, pp. 298-311, 1997.

[127] E. A. Hammer and C. Fossdal, "A new water-in-oil monitor based on high frequency magnetic field excitation," in *Proc. 2nd International Symposium Process Tomography*, Wroclaw, Poland, 2002.

[128] H. C. Wee, S. Watson, R. Patz, H. Griffiths, and R. J. Williams, "A Magnetic Induction Tomography system with sub-millidegree phase noise and high long-term phase stability," in *4th European Conference of the International Federation for Medical and Biological Engineering*, 2009, pp. 744-747.

[129] S. Watson, R. J. Williams, W. Gough, and H. Griffiths, "A magnetic induction tomography system for samples with conductivities below 10 Sm^{-1}," *Measurement Science & Technology,* vol. 19, 2008.

[130] M. Zolgharni, H. Griffiths, and D. S. Holder, "Imaging haemorrhagic cerebral stroke by frequency-difference magnetic induction tomography: numerical modelling," in *IFMBE Proceedings*, Antwerp, Belgium 2009.

[131] B. Dekdouk, M. H. Pham, D. W. Armitage, C. Ktistis, M. Zolgharni, and A. J. Peyton, "A feasibility study on the delectability of Edema using Magnetic Induction Tomography using an Analytical Model," in *4th European Congress for Medical and Biomedical Engineering*, Antwerp, Belgium, Nov 2008.